Understanding Middle Atmospheric Composition Variability from the Solar Occultation for Ice Experiment Instrument and Other Datasets

Saswati Das

Dissertation submitted to the Faculty of
the Virginia Polytechnic Institute and State University
in partial fulfillment of the requirements for the degree of

Doctor of Philosophy
in
Electrical Engineering

Scott M Bailey
Scott L England
Jeffrey H Reed
Wayne A Scales
Yizheng Zhu

September 22, 2022
Blacksburg, Virginia

Keywords: Ozone, Atomic Oxygen, Nitric Oxide, Sudden Stratospheric Warming, Stratosphere, Mesosphere-Lower Thermosphere, SOFIE, Composition, and Dynamics

Understanding Middle Atmospheric Composition Variability from the Solar Occultation for Ice Experiment Instrument and Other Datasets

Saswati Das

(**ABSTRACT**)

This dissertation comprises multiple studies surrounding the middle atmosphere's chemistry, composition, and dynamics. The middle atmosphere refers to the region from ~ 10 km to ~ 100 km and consists of the Stratosphere, Mesosphere, and Lower Thermosphere. The Stratosphere, Mesosphere, and Thermosphere are bounded by pauses where the strongest changes in chemical composition, movement, density, and thermal behavior take place. While several studies in the past have investigated the chemical composition of the middle atmosphere and quantified the distribution of various species from the stratosphere to the lower thermosphere, seasonal variations and redistribution of species resulting from transport events make it important to continuously monitor the middle atmosphere. Dynamic events such as Sudden Stratospheric Warmings (SSW) impact the temperature gradient and the zonal mean wind pattern in the stratopause. Descent events triggered by SSWs result in enhanced transport of species from the lower thermosphere to the stratosphere. Temperature increments during SSWs have an important impact on Polar Stratospheric Clouds (PSCs), resulting in Antarctic ozone enhancement and a smaller ozone hole. The middle atmosphere is, thus, home to a diverse range of dynamics and chemistry, making it a critical subject that warrants attention from the science community. The continuous monitoring of the middle atmosphere is important to this end. Several satellite missions in the past have been dedicated to monitoring the middle atmosphere and collecting data for decades. However, continual revisions and revaluations of measurement approaches and the introduction of novel

space instruments are necessary to compensate for the limitations associated with existing missions, expand the extant specimen database, and improve phenomenon-centric observations.

The Solar Occultation for Ice Experiment (SOFIE) is one of the two instruments on the Aeronomy of Ice in the Mesosphere (AIM) spacecraft. The studies presented in this dissertation primarily focus on the use of SOFIE observations combined with results from other science missions, an atmospheric model, and other datasets.

Chapter I is an overview of the research goals and the motivations that propelled this research. In Chapter II, a validation study of the Version 1.3 SOFIE ozone data against the Atmospheric Chemistry Experiment (ACE) and the Michelson Interferometer for Passive Atmospheric Sounding (MIPAS) ozone data is presented. The SOFIE-ACE and SOFIE-MIPAS data pairs demonstrate similar variability in the ozone vertical profile. SOFIE vertical ozone profiles agree best with ACE from 30 - 70 km and MIPAS from 30-64 km. The mean difference values averaged over all seasons and both hemispheres are typically $< 24\%$ with ACE and $< 20\ \%$ with MIPAS.

Atomic oxygen is an important species in the mesopause region (~ 80 – 100 km) that impacts the region's ozone photochemistry and radiative balance. In Chapter III, SOFIE ozone measurements used to derive daytime atomic oxygen are compared to coincident retrievals from the Sounding of the Atmosphere using Broadband Emission Radiometry (SABER) instrument and the Naval Research Laboratory Mass Spectrometer Incoherent Scatter radar (NRLMSIS 2.0) model. The datasets agree qualitatively. Results indicate a strong seasonal variation of atomic oxygen with summer and wintertime maxima at ~ 84 km and 94 km, respectively.

The middle atmospheric composition is redistributed by the transport of species during SSWs. In Chapter IV, the 2019 SSW in the northern hemisphere that triggered a large transport event from

the lower thermosphere to the stratosphere is evaluated using SOFIE, ACE, and the Modern-Era Retrospective analysis for Research and Applications (MERRA-2) observations. The event was similar to the major SSW-triggered descent events in the northern hemisphere since 2004 and led to the enhancement of nitric oxide produced by Energetic Particle Precipitation, attributed to unusual meteorology. The transport peak descended by ~ 5-6 km every 10 days.

An SSW event occurred in the southern hemisphere in 2019 and led to enhanced ozone in the stratosphere. In Chapter V, satellite instruments, ground station data, and measurements from NASA Ozone Watch are used to conclude that large temperature increments evaporated PSCs, resulting in the lower conversion of halogen reservoir species into ozone-destroying forms. Thus, a large ozone enhancement was recorded in 2019.

Chapter VI concludes all findings and Chapter VII summarizes future work.

Understanding Middle Atmospheric Composition Variability from the Solar Occultation for Ice Experiment Instrument and Other Datasets

Saswati Das

(**GENERAL AUDIENCE ABSTRACT**)

The middle atmosphere is the region between ~ 10 and 100 km in the atmosphere and is comprised of the Stratosphere, Mesosphere, and Lower Thermosphere. The middle atmosphere is a dynamic region, and the chemistry of this region is subject to variations occurring naturally or those triggered by anomalous events such as Sudden Stratospheric Warmings (SSW). Several species in the middle atmosphere need to be measured continuously or reevaluated for improved understanding. Dynamical events in the middle atmosphere are responsible for transporting and redistributing species in the middle atmosphere. Thus, the continuous monitoring of the middle atmosphere is necessary. Novel approaches with improved techniques and approaches are thus important to explore the middle atmosphere and quantify the chemistry of the region.

The Solar Occultation for Ice Experiment (SOFIE) instrument is an instrument onboard the Aeronomy of Ice in the Mesosphere (AIM) spacecraft. SOFIE typically measures at high latitudes and looks at a wide range of wavelengths. This dissertation uses SOFIE and other datasets to evaluate the varying chemistry and dynamics of the middle atmosphere. The dissertation addresses four research problems and assimilates them to evaluate the middle atmosphere.

Ozone is an important species in the middle atmosphere, which is present in the highest quantity in the stratosphere, followed by the lower thermosphere (~ 85 – 100 km). Ozone is important as it absorbs ultraviolet radiations and impacts the stratospheric radiative balance. Missions in the past have monitored ozone in the middle atmosphere. Novel approaches and improved observation

techniques to compensate for the limitations of past missions and the continuous measurement of ozone are necessary. Thus, ozone retrievals from SOFIE are validated against independent and established datasets to demonstrate the robustness and usability of the SOFIE ozone data product within the atmospheric science community.

Atomic oxygen is an important species in the mesopause region (~ 80 – 100 km) because of its role in ozone photochemistry and impact on the radiative balance of the region. It is technologically challenging to make direct measurements of atomic oxygen; thus, most conventionally, derived measurements and model results are used. To this date, atomic oxygen has been understood in a limited capacity with several inaccuracies. To improve the understanding of atomic oxygen and fill the current knowledge gaps, atomic oxygen is derived from SOFIE ozone measurements during the daytime using the Chapman equations for ozone photochemistry. Further, the derived atomic oxygen is compared to other established datasets from satellite instrument-derived measurements and model predictions. The seasonal variability of atomic oxygen is evaluated with a focus on the difference in its behavior during summer and winter. Lastly, inter-hemispheric differences in atomic oxygen distribution are evaluated.

Apart from the natural atmospheric variation in species, SSW-triggered transport events redistribute species in the atmosphere. The 2019 SSW event in the northern hemisphere was similar to those in 2004, 2006, 2009, and 2013. Large quantities of nitric oxide were transported from the lower thermosphere to the stratosphere. Air poor in water vapor and methane was also transported. Atomic oxygen was transported from the lower thermosphere to several kilometers below in amounts higher than usual. The increased nitric oxide concentration in the stratosphere due to the transport catalytically destroyed the ozone in the region. The vertical transport rates

were calculated to understand the speed of the descent. The low geomagnetic index in 2019, like in all years besides 2004, indicates that these events are attributed to unusual meteorology.

An SSW event took place in the southern hemisphere in 2019 during the Antarctic winter. This led to a large increase in temperature, which evaporated the Polar Stratospheric Clouds (PSCs). PSCs provide their surface for converting halogen reservoir species into ozone-destroying reactive forms. The absence of PSCs during and immediately after the SSW event led to a lower conversion of halogen reservoir species into reactive forms. Satellite instrument measurements agree with theoretical expectations. The 2002 SSW in the SH led to similar outcomes and are compared to the 2019 event. Large enhancements in ozone in 2019 led to the smallest ozone hole since ~ 1982.

Acknowledgments

I have had the fond honor of working with and learning from so many great people through the journey of my Ph.D. that I could not possibly list them all. I am thankful for the friendships and professional relationships that have inspired me to be a better researcher, and I will list as many as I can here.

My career as a graduate student and this dissertation would not have been possible without the unwavering support of my advisor, Dr. Scott Bailey. He introduced me to the wonderful world of sounding rockets and atmospheric-balloon experiments, presented me with tremendous opportunities to pursue the research I loved, and, most importantly, showed me how not to let my mistakes weigh me down. I am grateful for his kindness and support. Dr. Bailey's research career has inspired me to be more perseverant and determined to accomplish my goals. The wisdom gained from Dr. Bailey during the Polar NOx Rocket Mission and learning about his journey through overcoming impediments during previous flights will continue to motivate me throughout my scientific career.

I thank Dr. Scott England for providing valuable feedback on my work as a part of my doctoral committee. Through the years of my Ph.D., I was taught two courses by Dr. England that he wonderfully developed. I am grateful to Dr. England for his patience, and kindness, and for being a wonderful teacher, which helped me pave my way to be more confident than the disillusioned graduate student that had walked into his class.

I thank my committee members Dr. Jeffrey Reed, Dr. Wayne Scales, and Dr. Yizheng Zhu, for reading my dissertation and providing their invaluable time and feedback.

This dissertation would not have been possible without the guidance of Dr. Brentha Thurairajah, Dr. Mark Hervig, and Dr. Benjamin Marshall from the Aeronomy of Ice in the Mesosphere (AIM) team. I thank them for providing valuable comments that helped me improve my work. Several great scientists from the AIM team have inspired me with their research, and I am grateful to have known them. They are Dr. James Russell, Dr. Cora Randall, Dr. Lynn Harvey, Dr. David Siskind, and Dr. Mike Stevens. I thank them for their encouragement and wonderful conversations.

My mentors in the rocket work include Dr. William McClintock and Dr. Justin Carstens. I am grateful for their guidance with the rocket mission and patience with all my questions. I will always treasure our memories from the rocket launch in Alaska. In addition, I thank Mr. Weston Allen and Mr. Brett Poche for their insightful teachings and for being wonderful people to work with.

A tremendous number of people were involved in the Polar NOx rocket and GLO balloon launches. I thank all the people at Wallops Flight Facility, Poker Flat Research Range, LASP, Space Dynamics Lab, NRL, and Columbia Scientific Balloon Facility.

I thank Dr. Anne Smith at NCAR for providing valuable feedback on my work and helping me with my questions. I am grateful to her, and Dr. Daniel Marsh for inspiring me with their research that laid the foundation of my doctoral work.

I am thankful to Dr. Michael Kiefer at Karlsruhe Institute of Technology for several helpful conversations and his support with data acquisition from the Michelson Interferometer for Passive Atmospheric Sounding (MIPAS) instrument, and to Dr. Manuel López Puertas at Instituto de Astrofísica de Andalucía for providing guidance on the MIPAS data. I thank Dr. Peter Bernath and Dr. Jeff Crouse for their support with the Atmospheric Chemistry Experiment (ACE) instrument data.

I would like to thank my family and friends for their constant support and encouragement. I thank Dr. Mihir Rimjha for his unconditional support and for showing me that patience and perseverance go a long way. I thank my parents for their encouragement and support and my late grandparents for their blessings.

Finally, I thank all those who have provided my work with constructive criticism over the years, which has propelled me to improve my research and strive for better.

Table of Contents

List of Figures

List of Tables

1. Introduction

The Solar Occultation for Ice Experiment (SOFIE) (*Gordley et al.,* 2009) is an instrument on the Aeronomy of Ice in the Mesosphere (AIM) (*Russell et al.,* 2009) spacecraft. SOFIE uses the satellite solar occultation technique to measure solar energy passing through the limb of the earth's atmosphere at sun rises and sets relative to the spacecraft. SOFIE has a field-of-view of ~ 1.6 km and, using 16 spectral regions, covers wavelengths from 0.29 μm to 5.26 μm. SOFIE typically makes high latitude measurements poleward of 65^{o} N/S. SOFIE measurements are used to retrieve temperature, an abundance of five gases, Polar Mesospheric Cloud (PMC) extinction, and meteoric smoke extinction (*Hervig et al.,* 2009; Marshall et al., 2011; *Rong et al.,* 2011, 2016). SOFIE is a relatively new instrument within the science community compared to the flight heritage of other satellite instruments. SOFIE's ability to continuously look at high latitudes is an advantage in understanding the wintertime dynamics in these regions. SOFIE measurements compensate for the limitations associated with existing measurements and help expand the existing science database. SOFIE measurements are available from April 2007 until late 2020 in both hemispheres. Measurements in the northern hemisphere are available to the present day. Using SOFIE in combination with other datasets, including satellite instruments, model, reanalysis, and ground station data, this study investigates the varying chemistry, composition, and dynamics of the middle atmosphere.

The middle atmosphere is a dynamic region between ~ 10 and 100 km. The middle atmosphere can be divided into the stratosphere, mesosphere, and lower thermosphere. These regions are different in the distribution of atmospheric species, where seasonal variations and anomalous events trigger the transport and redistribution of the atmospheric species. The stratosphere is abundant in ozone, with its largest concentration in the entire atmosphere. A secondary ozone

maximum is present in the atmosphere between ~ 85 and 95 km (*Smith et al.,* 2005, 2009). Ozone is an important species due to its ability to absorb ultraviolet radiation and its impact on the stratospheric radiative balance. Stratospheric ozone varies seasonally, with a maximum observed during the spring and a minimum in the autumn. The continuous observation of middle atmospheric ozone is necessary to this end. Several space missions in the past have been able to accomplish this (*Cunnold et al.,* 1989; *Russell et al.,* 1993; *Lucke et al.,* 1999; *Bernath.,* 2001; *Fischer et al.,* 2008). However, new, and improved approaches need to be taken to compensate for past missions' limitations and expand the extant ozone database. The validation of SOFIE ozone retrievals against independent datasets is thus necessary to establish its robustness and usability within the space science community.

Chapter II presents a validation study of the ozone data retrieved by the SOFIE instrument against two independent datasets - the Atmospheric Chemistry Experiment (ACE) and the Michelson Interferometer for Passive Atmospheric Sounding (MIPAS). The ozone retrievals from SOFIE are compared seasonally to the other datasets from ~ 20 to 100 km for both hemispheres, and a thorough analysis of the differences and biases is done. The seasonal ozone variation in the stratosphere is particularly emphasized, and the maximum and minimum in ozone concentration during the spring and late autumn, respectively, are evaluated. The variation of SOFIE ozone compared to other instruments seasonally and inter-hemispherically are quantified, and reasons for the points of disagreement are evaluated.

Atomic oxygen is a critical species in the mesopause region (~80 – 100 km) and plays a vital role in the ozone photochemistry alongside impacting the radiative balance of the mesopause (*Mlynczak and Solomon,* 1993; *Mlynczak et al.,* 2013). While the role of atomic oxygen is crucial in the mesopause, its measurement through in-situ and remote sensing techniques is

technologically challenging and not devoid of complexities (*Siskind and Sharp.,* 1990; *Patterson,* 2005). Thus, the only suitable conventional recourse is derived atomic oxygen measurements and model predictions (*Smith et al.,* 2010; *Mlynczak et al.,* 2013; *Picone et al.,* 2002; *Emmert et al.,* 2020). Despite these alternatives, the atmospheric science community does not fully understand atomic oxygen. Using new approaches and datasets is thus necessary to address existing knowledge gaps. Atomic oxygen measurements derived from SOFIE ozone using ozone photochemistry defined by the Chapman (*Chapman.,* 1930) equations and their comparison to coincident profiles from independent atomic oxygen datasets are thus necessary. SOFIE's ability to (typically) continuously look at high latitudes overcomes the limitations of other satellite measurements that do not focus particularly on high latitudes (*Russell et al.,* 1999). The seasonal variation of atomic oxygen and its distribution in both hemispheres also needs further understanding to explore this species in greater detail.

In Chapter III, SOFIE-derived vertical profiles of atomic oxygen are compared to coincident retrievals from the Sounding of the Atmosphere using Broadband Emission Radiometry (SABER) instrument and the Naval Research Laboratory Mass Spectrometer Incoherent Scatter radar (NRLMSIS 2.0) model. The seasonal variation of atomic oxygen is observed, and the role of eddy diffusion is evaluated in its transport during the wintertime. Further, the altitudes at which atomic oxygen attains its maximum during the summer and winter are estimated, and the differences in its inter-hemispheric variation are analyzed.

Anomalous events in the stratosphere trigger descent events from the lower thermosphere to the stratosphere (*Randall et al.,* 2009; *Bailey et al.,* 2014). Sudden Stratospheric Warming (SSW) events indicated by the high-temperature gradients and reversal in the zonal mean wind at 10 hPa and 60^{o} N results in an elevated stratopause (*Andrews et al.,* 1987; *Scherhag.,* 1952; *WMO,* 1978;

McInturff., 1978; *Labitzke.,* 1981). Although many SSW events have occurred in the northern hemisphere, descent events have been reported for only specific SSW events (*Randall et al.,* 2006, 2009; *Bailey et al.,* 2014). In 2004, 2006, 2009, and 2013, large amounts of nitric oxide were transported to the stratosphere from the lower thermosphere during the Arctic winter (*Randall et al.,2005,* 2006, 2009; *Pérot et al.,* 2014). A similar descent was observed in 2019 (*Pérot and Orsolini.,* 2021). The nitric oxide produced due to Energetic Particle Precipitation (EPP) was transported by the large tongues of air after the SSW. All years except 2004 reported low geomagnetic activity suggesting that the enhanced nitric oxide was associated with unusual meteorology. Ozone in the stratosphere is catalytically destroyed by nitric oxide rendering it important to verify if the 2019 event exhibited this trend. Comparing the descent events in all five years, determining their strength and reach into the stratosphere are important to quantify their impact on the middle atmosphere, alongside estimating their vertical transport rates (*Bailey et al.,* 2014).

Chapter IV evaluates the major SSWs that triggered large transport events from 2004 until 2019 using SOFIE, ACE, and the Modern-Era Retrospective analysis for Research and Applications (MERRA-2) observations. Large amounts of nitric oxide were carried from the lower thermosphere to the stratosphere during the Arctic winters of 2004, 2006, 2009, 2013, and 2019. The descent during these five years is tracked from January to April, and nitric oxide concentration entering the stratosphere is quantified. Water vapor and methane are also tracked during the same time, and the descent strengths of the years are estimated using the negative correlation with water vapor. Derived atomic oxygen measurements from simultaneous ozone retrievals indicate that it was transported below ~ 80 km in quantities larger than usual. Further, the catalytic destruction of stratospheric ozone by nitric oxide upon entering the stratosphere is evaluated. Descent profiles of

the recent 2019 event suggest that nitric oxide traveled the farthest that year. Vertical transport rates using tracer measurements are calculated for all years. Strong descent events during all years with low geomagnetic activity (except in 2004) indicate that the events are strongly attributed to unusual meteorology.

SSW events are a rare occurrence in the southern hemisphere. A major SSW event was recorded in 2002 (*Varotsos,* 2003; *Cho et al.,* 2004) and a minor one in 2010 (*Eswaraiah et al.,* 2016, 2017, 2018). In 2019, an SSW event was reported in the southern hemisphere, which by World Meteorological Organization's definition (*WMO/IQSY,* 1964) is classified as a minor event, although its behavior was similar (*Eswaraiah et al.,* 2020; *Safieddine et al.,* 2020) to the event in 2002. During polar winters in the southern hemisphere, Polar Stratospheric Clouds (PSCs) (*Tritscher et al.,* 2021) play a critical role in ozone destruction and, thus, ozone hole formation. PSCs provide their surface for converting chlorine reservoir species into reactive ozone-destroying forms (*Solomon et al.,* 1986; *Solomon,* 1999). Further, they delay chlorine deactivation through the removal of gas-phase nitric acid and water by the sedimentation of large nitric acid tetrahydrate (NAT), which leads to prolonged ozone depletion in the stratosphere (*Tritscher et al.,* 2021). High temperatures during SSWs lead to the evaporation of PSCs and, thus, decrease ozone loss by creating an absence of a site for the conversion of chlorine reservoir species into reactive forms. In 2019, high-temperature increments during the SSW event in the stratosphere led to similar occurrences, leading to large ozone enhancements and thus, resulting in an ozone hole smallest since ~ 1982. Further investigations are needed to understand the stratosphere's chemistry, composition, and variability during the 2019 SSW in the southern hemispheric winter. It is thus necessary to investigate the 2019 SSW-triggered ozone enhancement with multiple

complementary instrument data and evaluate the event, comparing it to the 2002 major SSW in the southern hemisphere.

In Chapter V, polar cap ozone and ozone hole area from 1979 to 2021 using NASA Ozone Watch data are evaluated. The results indicate that the ozone hole size in 2019 was the smallest since ~ 1982. MERRA-2 observations suggest that although the 2019 SSW was a minor one, its characteristics were comparable to the 2002 SSW, the only major event recorded in the southern hemisphere in recent times. High temperatures in 2019 compared to previous years' average indicate that PSC evaporation occurred during the SSW event. PSCs provide their surface to convert halogen reservoir species into ozone-destroying reactive forms. PSC data from Dumont d'Urville station indicate the gradual decrease in PSC concentration coinciding with periods of increased temperature. The absence of PSCs led to the lower conversion of halogen reservoirs into their reactive forms. Measurements from SOFIE, ACE, and the Sub-Millimeter Radiometer (SMR) instrument suggest large ozone enhancements compared to previous years' average. Increased amounts of halogen reservoir species and lower concentrations of their reactive forms compared to previous years' average agree well with theoretical expectations. Further, the ozone enhancement in 2002 is compared to 2019, with large similarities in the chemistry and dynamics of both years.

In Chapter VI, the findings of all chapters are combined, and future work is described in Chapter VII. While the focus of each study of this dissertation has been on a particular atmospheric species, phenomenon, or phenomenon-triggered variation in species' distribution, understanding the varying chemistry and dynamics qualitatively and quantitatively is the key thrust. The middle atmosphere is associated with a wide range of altitudes and is, thus, subject to continuous change from the various simultaneous occurrences in the region. Thus, the goal of developing diverse

investigative studies presented in each chapter of this dissertation is an effort toward collectively understanding the variation of the middle atmosphere. While the results answer individual research problems, the individual components come together to build a holistic picture of the middle atmosphere.

References

Andrews, D.G., Holton, J.R. and Leovy, C.B., 1987. Middle atmosphere dynamics (No. 40). Academic press.

Bailey, S.M., Thurairajah, B., Randall, C.E., Holt, L., Siskind, D.E., Harvey, V.L., Venkataramani, K., Hervig, M.E., Rong, P. and Russell III, J.M., 2014. A multi tracer analysis of thermosphere to stratosphere descent triggered by the 2013 Stratospheric Sudden Warming. *Geophysical Research Letters*, 41(14), pp.5216-5222. https://doi.org/10.1002/2014GL059860

Bernath, P., 2001. Atmospheric chemistry experiment (ACE): An overview. *Spectroscopy from Space*, pp.147-160. DOI: 10.1007/978-94-010-0832-7_9

Chapman, S., 1930. XXXV. On ozone and atomic oxygen in the upper atmosphere. *The London, Edinburgh, and Dublin Philosophical Magazine and Journal of Science*, 10(64), pp.369-383. https://doi.org/10.1080/14786443009461588

Cho, Y.M., Shepherd, G.G., Won, Y.I., Sargoytchev, S., Brown, S. and Solheim, B., 2004. MLT cooling during stratospheric warming events. *Geophysical Research Letters*, 31(10). https://doi.org/10.1029/2004GL019552

Cunnold, D.M., Chu, W.P., Barnes, R.A., McCormick, M.P. and Veiga, R.E., 1989. Validation of SAGE II ozone measurements. *Journal of Geophysical Research: Atmospheres*, 94(D6), pp.8447-8460.https://doi.org/10.1029/JD094iD06p08447

Eswaraiah, S., Kim, Y.H., Hong, J., Kim, J.H., Ratnam, M.V., Chandran, A., Rao, S.V.B. and Riggin, D., 2016. Mesospheric signatures observed during 2010 minor stratospheric warming at King Sejong Station (62 S, 59 W). *Journal of Atmospheric and Solar-Terrestrial Physics*, 140, pp.55-64. https://doi.org/10.1016/j.jastp.2016.02.007

Eswaraiah, S., Kim, Y.H., Liu, H., Ratnam, M.V. and Lee, J., 2017. Do minor sudden stratospheric warmings in the Southern Hemisphere (SH) impact coupling between stratosphere and mesosphere–lower thermosphere (MLT) like major warmings?. *Earth, Planets and Space*, 69(1), pp.1-8. https://doi.org/10.1186/s40623-017-0704-5

Eswaraiah, S., Kim, Y.H., Lee, J., Ratnam, M.V. and Rao, S.V.B., 2018. Effect of Southern Hemisphere sudden stratospheric warmings on Antarctica mesospheric tides: First observational study. *Journal of Geophysical Research: Space Physics*, 123(3), pp.2127-2140. https://doi.org/10.1002/2017JA024839

Eswaraiah, S., Kim, J.H., Lee, W., Hwang, J., Kumar, K.N. and Kim, Y.H., 2020. Unusual changes in the Antarctic middle atmosphere during the 2019 warming in the Southern Hemisphere. *Geophysical Research Letters*, 47(19), p.e2020GL089199. https://doi.org/10.1029/2020GL089199

Emmert, J.T., Drob, D.P., Picone, J.M., Siskind, D.E., Jones Jr, M., Mlynczak, M.G., Bernath, P.F., Chu, X., Doornbos, E., Funke, B. and Goncharenko, L.P., 2021. NRLMSIS 2.0: A whole-atmosphere empirical model of temperature and neutral species densities. *Earth and Space Science*, 8(3), p.e2020EA001321. https://doi.org/10.1029/2020EA001321

Fischer, H., et al. "MIPAS: an instrument for atmospheric and climate research." *Atmospheric Chemistry and Physics* 8.8 (2008): 2151-2188. DOI:10.5194/acp-8-2151-2008

Gordley, L.L., Hervig, M.E., Fish, C., Russell III, J.M., Bailey, S., Cook, J., Hansen, S., Shumway, A., Paxton, G., Deaver, L. and Marshall, T., 2009. The solar occultation for ice experiment. *Journal of Atmospheric and Solar-Terrestrial Physics*, 71(3-4), pp.300-315. doi:10.1016/j.jastp.2008.07.012

Hervig, M.E., Gordley, L.L., Stevens, M.H., Russell III, J.M., Bailey, S.M. and Baumgarten, G., 2009. Interpretation of SOFIE PMC measurements: Cloud identification and derivation of mass density, particle shape, and particle size. *Journal of atmospheric and solar-terrestrial physics*, 71(3-4), pp.316-330. doi:10.1016/j.jastp.2008.07.009

Labitzke, K., 1981. Stratospheric-mesospheric midwinter disturbances: A summary of observed characteristics. *Journal of Geophysical Research: Oceans*, 86(C10), pp.9665-9678. https://doi.org/10.1029/JC086iC10p09665

Lumpe, J., Bevilacqua, R., Randall, C., Nedoluha, G., Hoppel, K., Russell, J., Harvey, V.L., Schiller, C., Sen, B., Taha, G. and Toon, G., 2006. Validation of Polar Ozone and Aerosol Measurement (POAM) III version 4 stratospheric water vapor. *Journal of Geophysical Research: Atmospheres*, 111(D11). DOI:10.1029/2005JD006763

Marshall, B.T., Deaver, L.E., Thompson, R.E., Gordley, L.L., McHugh, M.J., Hervig, M.E. and Russell III, J.M., 2011. Retrieval of temperature and pressure using broadband solar occultation: SOFIE approach and results. *Atmospheric Measurement Techniques*, 4(5), pp.893-907. doi:10.5194/amtd-3-5743-2010.

McInturff, R.M., 1978. Stratospheric warmings: Synoptic, dynamic and general-circulation aspects (No. NASA-RP-1017). Document ID: 19780010687

Mlynczak, M.G. and Solomon, S., 1993. A detailed evaluation of the heating efficiency in the middle atmosphere. *Journal of Geophysical Research: Atmospheres*, 98(D6), pp.10517-10541. https://doi.org/10.1029/93JD00315

Mlynczak, M.G., Hunt, L.H., Mertens, C.J., Marshall, B.T., Russell III, J.M., López Puertas, M., Smith, A.K., Siskind, D.E., Mast, J.C., Thompson, R.E. and Gordley, L.L., 2013. Radiative and energetic constraints on the global annual mean atomic oxygen concentration in the mesopause region. *Journal of Geophysical Research: Atmospheres*, 118(11), pp.5796-5802., doi:10.1002/jgrd.50400.

Patterson, P.L., 2005. In situ measurements of upper atmospheric atomic oxygen: The ATOX resonant fluorescence/absorption sensor. Utah State University.

Pérot, K., Urban, J. and Murtagh, D.P., 2014. Unusually strong nitric oxide descent in the Arctic middle atmosphere in early 2013 as observed by Odin/SMR. *Atmospheric Chemistry and Physics*, 14(15), pp.8009-8015. https://doi.org/10.5194/acp-14-8009-2014

Pérot, K. and Orsolini, Y.J., 2021. Impact of the major SSWs of February 2018 and January 2019 on the middle atmospheric nitric oxide abundance. *Journal of Atmospheric and Solar-Terrestrial Physics*, 218, p.105586. https://doi.org/10.1016/j.jastp.2021.105586

Picone, J.M., Hedin, A.E., Drob, D.P. and Aikin, A.C., 2002. NRLMSISE-00 empirical model of the atmosphere: Statistical comparisons and scientific issues. *Journal of Geophysical Research: Space Physics*, 107(A12), pp.SIA-15. https://doi.org/10.1029/2002JA009430

Randall, C.E., Harvey, V.L., Singleton, C.S., Bernath, P.F., Boone, C.D. and Kozyra, J.U., 2006. Enhanced stratospheric NOx in 2006 linked to strong Arctic vortex. *Geophys. Res. Lett*, 33, p.L18811., doi:10.1029/2006GL027160.

Randall, C.E., Harvey, V.L., Siskind, D.E., France, J., Bernath, P.F., Boone, C.D. and Walker, K.A., 2009. NOx descent in the Arctic middle atmosphere in early 2009. *Geophysical Research Letters*, 36(18). doi:10.1029/2009GL039706.

Rong, P., Russell III, J.M., Gordley, L.L., Hervig, M.E., Deaver, L., Bernath, P.F. and Walker, K.A., 2010. Validation of v1. 022 mesospheric water vapor observed by the Solar Occultation for Ice Experiment instrument on the Aeronomy of Ice in the Mesosphere satellite. *Journal of Geophysical Research: Atmospheres*, 115(D24). doi:10.1029/2010JD014269.

Rong, P.P., Russell III, J.M., Marshall, B.T., Siskind, D.E., Hervig, M.E., Gordley, L.L., Bernath, P.F. and Walker, K.A., 2016. Version 1.3 AIM SOFIE measured methane (CH4): Validation and seasonal climatology. *Journal of Geophysical Research: Atmospheres*, 121(21), pp.13-158. doi:10.1002/2016JD025415.

Russell III, J.M., Mlynczak, M.G., Gordley, L.L., Tansock Jr, J.J. and Esplin, R.W., 1999, October. Overview of the SABER experiment and preliminary calibration results. *In Optical spectroscopic techniques and instrumentation for atmospheric and space research III* (Vol. 3756, pp. 277-288). SPIE. DOI: 10.1117/12.366382

Russell III, J.M., Bailey, S.M., Horanyi, M., Gordley, L.L., Rusch, D.W., Hervig, M.E., Thomas, G.E., Randall, C.E., Siskind, D.E., Stevens, M.H. and Summers, M.E., 2009. Aeronomy of ice in the mesosphere. *J. Atmos. Solar-Terr. Phys*. doi:10.1016/j.jastp.2008.08.011

Safieddine, S., Bouillon, M., Paracho, A.C., Jumelet, J., Tence, F., Pazmino, A., Goutail, F., Wespes, C., Bekki, S., Boynard, A. and Hadji-Lazaro, J., 2020. Antarctic ozone enhancement during the 2019 sudden stratospheric warming event. *Geophysical Research Letters*, 47(14), p.e2020GL087810. https://doi.org/10.1029/2020GL087810

Scherhag, R., 1952. Die explosionartigen stratospharenwarmungen des spatwinters 1951-1952. *Ber. Deut. Wetterd.*, 6, pp.51-63. CRID:1573950399672518528

Siskind, D.E. and Sharp, W.E., 1990. A vibrational analysis of the O2 (A3Σ+ u) Herzberg I system using rocket data. *Planetary and space science*, 38(11), pp.1399-1408. https://doi.org/10.1016/0032-0633(90)90115-7

Smith, A.K. and Marsh, D.R., 2005. Processes that account for the ozone maximum at the mesopause. *Journal of Geophysical Research: Atmospheres*, 110(D23). https://doi.org/10.1029/2005JD006298

Smith, A.K., López-Puertas, M., García-Comas, M. and Tukiainen, S., 2009. SABER observations of mesospheric ozone during NH late winter 2002–2009. *Geophysical Research Letters*, 36(23). https://doi.org/10.1029/2009GL040942

Smith, A.K., Marsh, D.R., Mlynczak, M.G. and Mast, J.C., 2010. Temporal variations of atomic oxygen in the upper mesosphere from SABER. *Journal of Geophysical Research: Atmospheres*, 115(D18). doi:10.1029/2009JD013434.

Solomon, S., Garcia, R.R., Rowland, F.S. and Wuebbles, D.J., 1986. On the depletion of Antarctic ozone. *Nature*, 321(6072), pp.755-758. https://doi.org/10.1029/RG026i001p0013110.1038/321755a0

Solomon, S., 1999. Stratospheric ozone depletion: A review of concepts and history. *Reviews of Geophysics*, 37(3), pp.275-316. https://doi.org/10.1029/1999rg900008

Tritscher, I., Pitts, M.C., Poole, L.R., Alexander, S.P., Cairo, F., Chipperfield, M.P., Grooß, J.U., Höpfner, M., Lambert, A., Luo, B. and Molleker, S., 2021. Polar stratospheric clouds: Satellite observations, processes, and role in ozone depletion. *Reviews of geophysics*, 59(2), p.e2020RG000702. https://doi.org/10.1029/2020RG000702

Varotsos, C., 2003. What is the lesson from the unprecedented event over Antarctica in 2002. *Environmental science and pollution research*, 10(2), pp.80-81. https://doi.org/10.1007/BF02980093

WMO/IQSY. (1964). International Years of the Quiet Sun (IQSY) 1964-65. Alert messages with special references to stratwarms. WMO/IQSY Report No 6, Secretariat of the World Meteorological Organization, Geneva, Switzerland. World Meteorological Organization.

2. Validation of Version 1.3 Ozone Measured by the SOFIE Instrument

Das, Saswati, et al. "Validation of Version 1.3 Ozone Measured by the SOFIE Instrument." *Earth and Space Science (Under Review)*

2.1 Abstract

Solar Occultation for Ice Experiment (SOFIE) is one of the instruments onboard the Aeronomy of Ice in the Mesosphere (AIM) spacecraft. SOFIE uses solar occultation to retrieve ozone (O_3) profiles from ~ 20 to 100 km. This study evaluates SOFIE O_3 profiles from 2008 to 2014. SOFIE O_3 is compared with independent satellite measurements from the Atmospheric Chemistry Experiment Fourier Transform Spectrometer (ACE-FTS) and the Michelson Interferometer for Passive Atmospheric Sounding (MIPAS) instruments. In general, SOFIE shows quantitative agreement with both data sets in terms of mean seasonal climatology and variability across seasons and altitudes. When averaged over all seasons and hemispheres, the mean difference between SOFIE and ACE is less than 30 % between ~ 30 - 90 km, except between ~ 76 - 80 km where the mean difference is higher than 30 %. The values are less than 18 % in most of these cases. The mean difference between SOFIE and MIPAS is less than 20 % between 30 – 64 km. The mean difference values over all hemispheres, seasons, and datasets show that SOFIE is biased low at most altitudes and more strongly in the lower stratosphere (~ 20 km) and upper mesosphere (80 km and 100 km, but not at 90 km). The uncertainties in the measurements are attributed to the systematic and random errors in each data set and the seasonal distribution of the coincidences between the datasets.

2.2 Plain Language Summary

Ozone is an important species in the middle atmosphere that requires continuous and high-quality measurements. Novel measurements from new satellite instruments are important to this end. The

Solar Occultation for Ice Experiment (SOFIE) instrument measures the solar energy passing through the limb of the Earth's atmosphere at sunrise and sunset (relative to the spacecraft) that is used for retrieving ozone profiles. The profiles are compared to coincident profiles from other satellite instruments seasonally and in both hemispheres. The agreement between SOFIE and the correlative datasets over both hemispheres and all seasons is the best between ~ 30 – 64 km. SOFIE measurements capture the seasonal variation in ozone profiles.

2.3 Introduction

Ozone (O_3) is an important molecule in the middle atmosphere due to its ability to absorb solar ultraviolet (UV) radiation. The primary O_3 maximum lies in the stratosphere's ~ 25 – 40 km altitude range. While the seasonal variability of O_3 concentration depends on the seasonal variation in temperature in the upper stratosphere (~ 40 – 50 km), photochemistry is much slower in the lower stratosphere (~ 25– 40 km) due to the reduced UV flux. Thus, the transport of O_3 is attributed to atmospheric circulations, which drive the seasonal variation of O_3. The primary circulation is upwards in the tropics and poleward/downward in the mid and high latitudes in the lower stratosphere. The dissipation of wave disturbances propagated from the troposphere drives the circulation. During the winter, the dissipation of these waves in the stratosphere leads to downward/poleward circulation. The circulation carries O_3 produced at tropical source regions to high latitudes (*Solomon et al.,* 1985; *Perliski et al.,* 1989). During the winter, stratospheric O_3 is shielded from UV radiation by the O_3 above, and because the solar zenith angle is high in the high latitude winter leading to poor photochemical O_3 loss. The accumulation of O_3 over the winter results in a springtime maximum. In the summer, the position solar zenith angle is smaller, leading to efficient photochemistry. This leads to photochemical loss of O_3 over the summer, and a minimum is attained in late autumn (*Stolarski et al.,* 1991, 1992).

O_3 is abundantly present in a layer in the upper mesosphere and lower thermosphere, known as the secondary O_3 maximum. The altitude of the secondary O_3 maximum during daytime in mixing ratios is 90 - 92 km. While the nighttime O_3 mixing ratios in the secondary maximum region are comparable to what is found in the stratospheric maximum (~ 10 ppm), the daytime mixing ratios are relatively smaller but significantly larger than in the middle and upper mesosphere (*Smith and Marsh.,* 2005; *Smith et al.,* 2008, 2009, 2011, 2013; *Tweedy et al.,* 2013).

In summary, in the stratosphere, O_3 impacts the stratospheric radiative balance. In the upper mesosphere and lower thermosphere, the secondary O_3 maximum (*Smith et al.,* 2005, 2009), is highly variable and so difficult to accurately characterize. Thus, the stratosphere, upper mesosphere, and lower thermosphere are important atmospheric O_3 reservoirs, making it important to have continuous, high-quality O_3 measurements in these atmospheric regions (*Cracknell and Varotsos,* 2012; *Smith et al.,* 2013). Solar occultation measurements are advantageous due to the high signal-to-noise ratio, allowing increased vertical and spectral resolution measurement at higher altitudes. Moreover, solar occultation measurements generally suffer less significant non-LTE effects and are self-calibrating by taking the ratio of the radiances (*Dupuy et al.,* 2009).

The Solar Occultation for Ice Experiment (SOFIE) is on board the Aeronomy of Ice in the Mesosphere (AIM) spacecraft (*Russell et al.,* 2009). SOFIE makes daytime measurements using solar occultation during sunrise and sunset relative to the spacecraft. SOFIE (*Gordley et al.,* 2009) has a resolution of ~ 1.8 km on the limb and typically observes high latitudes (65^o-85^o N/S). The detailed SOFIE measurement approach is explained in Section 2.4.1. Past satellite instruments have measured O_3 in the stratosphere, mesosphere, and lower thermosphere. These include solar occultation satellite-borne instruments such as SAGE II (the Stratospheric Aerosol and Gas Experiment) (*Mauldin III et al.,* 1985; *McCormick et al.,* 1987; *Cunnold et al.,* 1989), SAGE III

(SAGE ATBD Team, 2002a), HALogen Occultation Experiment (HALOE) (*Russell et al.*, 1993), POAM III (Polar Ozone and Aerosol Measurement) (*Lucke et al.,* 1999), SCIAMACHY (SCanning Imaging Absorption spectroMeter for Atmospheric CHartographY) (*Bovensmann et al.,* 1999) and MIPAS (Michelson Interferometer for Passive Atmospheric Sounding) (*Fischer et al.,* 2008). Currently, ACE-FTS (Atmospheric Chemistry Experiment - Fourier Transform Spectrometer) (*Bernath.,* 2001; *Bernath et al.,* 2005) and SABER (Sounding of the Atmosphere using Broadband Emission Radiometry) (*Russell at al.,* 1999) are operational, and observe O_3. SOFIE's ability to typically provide long-term high latitude measurements and observe the stratosphere to the lower thermosphere scan makes its O_3 data an important addition to the existing O_3 database.

In this paper, we validate the most recent publicly released version 1.3 SOFIE O_3 measurements and determine any biases. SOFIE O_3 data is compared to coincidence measurements from ACE-FTS and MIPAS. Section 2.4 describes the SOFIE O_3 measurement approach, retrieval method, and uncertainty analysis. The correlative datasets are described in Section 2.5. Coincidence analysis and the comparisons of the coincident pairs of vertical profiles are in Section 2.6. The summary and conclusions of this study are presented in Section 2.7.

2.4 SOFIE O_3 Measurement Approach, Retrieval, and Uncertainty Analysis

2.4.1 SOFIE Measurement Approach

SOFIE has been operational since May 2007. SOFIE observes at 16 wavelengths. SOFIE data products include the vertical profiles for temperature, five gaseous species (O_3, H_2O, CO_2, CH_4, and NO), polar mesospheric cloud (PMC) extinction, and meteoric smoke extinction (*Gordley et al.,* 2009; *Hervig et al.,* 2009; *Marshal et al.,* 2011). Spacecraft sunsets measurements occurred in

the Southern Hemisphere (SH) with sunrises in the Northern Hemisphere (NH) from 2007-2017. In late 2018 this changed with sunsets switching to the NH. This work uses SOFIE V1.3 data.

SOFIE measures the ratio of the solar intensity through the atmosphere (V = endoatmospheric) to the intensity outside the atmosphere (VO = exoatmospheric), which gives the broadband atmospheric transmission, $\tau = V/VO$ used to calculate geophysical parameters of interest. SOFIE measures the vertical profiles of limb path atmospheric transmission using 16 spectral bands in the 0.29 – 5.32 μm wavelength range.

2.4.2 SOFIE O_3 Retrieval

This study uses data from SOFIE Level 2 processing which retrieves individual profiles of trace species, temperature, and aerosol extinction using SOFIE signals. A signal simulation describes the radiative transfer of sunlight through Earth's atmosphere's limb and accounts for the effects of the instrument. Line-by-line radiative transfer calculations with necessary line parameters (*Gordley et al.,* 1994), assuming a spherically symmetric atmosphere, are used to simulate atmospheric transmissions. An 'onion-peeling' (*Russell and Drayson,* 1972) technique is implemented to retrieve the limb profiles. The volume mixing ratio (VMR) of the target species is inferred in succession through the length of the atmosphere, from top to bottom. Measured signals are compared to simulated transmissions (V/V_O). VMR of the target is adjusted until the measured transmission is successfully reproduced within the noise. Seven individual profiles at 1.4 km spacing are independently processed to obtain a final profile. The seven resulting profiles are combined and undergo smoothing using a 0.7 km full-width Gaussian to decrease random errors. The resulting final profile is reported on a 0.2 km vertical grid.

O_3 is measured using two broadband (~2% filter width) filters centered at 292 and 330 nm wavelength (Bands 1 and 2, respectively), as shown in Figure 1. Note that the Band 2 electronic

response was saturated at launch but came into range by November 2009 due to the normal darkening of the optics with time (*Gordley et al.,* 2009). The 292 nm band is located in a region of strong O_3 absorption to provide enhanced sensitivity to O_3 in the mesosphere. This band provides O_3 measurements from roughly 105 km to 50 km and is opaque at lower heights. The 330 nm band was selected to provide O_3 measurements from ~60 km to the tropopause. Note that O_3 absorption at 330 nm is negligible above ~60 km, and the Band 2 measurements there are used to characterize meteoric smoke (*Hervig et al.,* 2017; *Hervig et al.,* 2017; *Hervig et al.,* 2021) and PMCs during polar summer (*Hervig et al.,* 2009; *Hervig et al.,* 2009). The transmission measurements from Bands 1 and 2 are used separately to retrieve O_3 vertical profiles. The two profiles are then merged to obtain a continuous O_3 product from ~105 km altitude to the tropopause. The retrievals use O_3 simulations based on temperature-dependent O_3 cross-sections (*Serdyuchenko et al.,* 2014). Rayleigh scattering is the primary interference in the 292 and 330 nm bands. Rayleigh interference is calculated using optical cross-sections from *Bodhaine et al.* (1999) with SOFIE density measurements and removed during the retrieval process. The other interference in the O_3 bands is from stratospheric aerosols below ~35 km (which is not corrected at this time) and from PMCs near 80 - 90 km during polar summer.

PMC (*Hervig et al.,* 2009, 2013, 2016) contamination in the 292 nm O_3 measurements is successfully removed using the PMC extinction retrieved at 330 nm. For this purpose, the 330 nm PMC extinctions are extrapolated in wavelength to 292 nm, based on the modeled wavelength dependence described as the ratio of extinction at 292 nm to that for 330 nm. The extinction ratio varies with PMC particle size, but only by $\pm$10% over the typical range (roughly 15 - 60 nm) of effective radius (r_e). For simplicity, the SOFIE approach assumes the long-term average r_e of 32 nm and accepts the resulting uncertainty (10%) in the O_3 mixing ratios retrieved in PMCs'

presence. Instead, it is possible to use the retrieved r_e from SOFIE in the Band 1 PMC corrections. The retrieved r_e has uncertainties of up to ~25%. However, propagating these uncertainties in the retrieved r_e for each event gives similar errors as assuming the long-term average r_e. Note that the Band 1 O_3 measurements are corrected for PMC interference from November 2009, when the Band 2 measurements became operational.

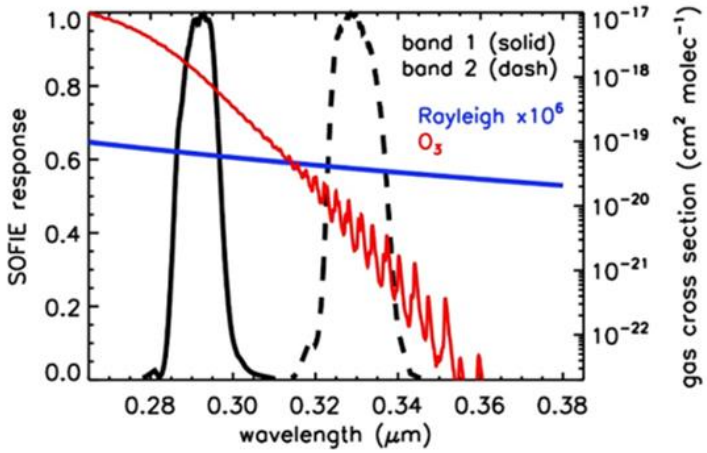

Figure 1. SOFIE spectral response and Rayleigh PMC interference in the O_3 bandpass spectral region. O_3 is measured using the channel 1 pair centered at 0.292 μm and 0.330 μm for strong (solid black curve) and weak (dashed black curve) O_3 bands, respectively.

2.4.3 SOFIE O_3 Uncertainty Analysis

Simulation uncertainties include modeling errors, the representation of instrument characteristics (e.g., relative spectral response), and the description of interfering gases and aerosols. The V1.3 SOFIE O_3 forward model uses the optical cross-sections from *Serdyuchenko et al.*, (2014), which is estimated to have 1% systematic uncertainties. Each error mechanism was imposed in the V1.3 SOFIE retrieval algorithm to determine the resulting uncertainty in retrieved O_3. These errors have been calculated based on the simulated responses to previously known sources of error between 20 – 100 km. The error in the O_3 profile is calculated by using an original presumed unperturbed

profile. The corresponding radiance profile was calculated using the forward model's radiance profile. The radiance profile was then perturbed by introducing errors, and retrievals were performed on the perturbed profiles to predict the O_3 response.

The error sources in retrieved O_3 are summarized in Table 1 for each mechanism over a range of altitudes. The largest O_3 uncertainties are due to errors in the altitude registration and uncertainties in the field of view calibration. Note that altitude registration errors are estimated to be 100 m (*Marshall et al.,* 2010).

Table 1. O_3 mixing ratio uncertainty (%) due to various random (R) and systematic (S) error mechanisms. Retrievals are from Band 1 (292 nm) above ~55 km and Band 2 (330 nm) at lower heights. Note that the uncertainties here do not address stratospheric aerosol or PMC interference

Error Source	**Altitude (km)**								
	20	**30**	**40**	**50**	**60**	**70**	**80**	**90**	**100**
Altitude Registration (S)	5	3	3	3	2	2	2	2	2
Rayleigh Interference (S)	2	1.5	1	2	0.5	1	1	0.5	1
Temperature Bias (S)	1	1	1	1	1	1	2	3	5
O_3 Cross Sections (S)	1	1	1	1	1	1	1	1	1
Field-of-View (S)	1	1	1.5	2	2	3	3	3	3
Forward Model (S)	1	1	1	1	1	1	1	1	1
Signal Noise (R)	0.5	0.1	0.1	0.15	0.1	0.1	0.15	0.2	1
Total (root sum squared)	5.8	3.9	3.9	4.5	3.4	4.1	4.5	4.9	6.5

2.5 Correlative Data Sets

2.5.1 SCISAT ACE-FTS

The ACE-FTS (Atmospheric Chemistry Experiment- Fourier Transform Spectrometer *Bernath.,* 2001; *Bernath et al.*, 2005; *Boone et al.,* 2005) instrument onboard the Canadian SciSat spacecraft is a successor to the ATOMS (Atmospheric Trace Molecule Spectroscopy) experiment (*Gunson*

et al., 1996). ACE uses solar occultation to sense minor species in Earth's atmosphere remotely. ACE was launched to low Earth orbit at 650 km and 74^{o} inclination. ACE measures high-resolution (0.02 cm^{-1}) spectra of the atmosphere in the medium-long infrared range of 2.2 – 13 μm (*Bernath et al.,* 2005). The vertical profiles of temperature, pressure, and VMRs of trace constituents are retrieved from the occultation spectra (*Boone et al.,* 2005). The absence of sufficiently accurate meteorological data for the complete ACE altitude range of observations necessitates the derivation of temperature and pressure directly from the ACE spectra as the first step of the retrieval. These profiles are used to calculate synthetic spectra in the global fitting procedure to retrieve the VMR profiles of the target species in the second phase of the retrieval.

The initial ACE O_3 validation comparisons for Version 1.0 were reported by *Walker et al.,* (2005), *Petelina et al.,* (2005a), *Fussen et al.,* (2005), *McHugh et al.,* (2005), and *Kerzenmacher et al.,* (2005). *Froidevaux et al.,* (2006) used ACE version 2.1 O_3 in earlier validation studies for MLS (Microwave Limb Sounder) on the Aura satellite. In these earlier O_3 retrievals, apparent discrepancies in the spectroscopic data near ~ 5 μm and ~ 10 μm were observed, due to which the vertical profiles near the stratospheric O_3 concentration peak had a consistent low bias of ~ 10% compared to other satellite instrument observations. An updated version 2.2 with improved spectroscopic measurements for O_3 was subsequently introduced and used in various validation studies (*Cortesi et al.,* 2007; *Froidevaux et al.,* 2008; *Dupuy et al.,* 2009). In V2.2, O_3 VMRs are consistently larger than MLS, with O_3 profiles within 5% agreement in the lower stratosphere. However, the agreement deteriorates with altitude and reaches ~ 25% at the upper stratosphere (*Froidevaux et al.,* 2008). *Cortesi et al.,* (2007) compared MIPAS version 4.66 O_3 data with ACE version 2.2, and reported that the relative difference was within ± 10 % between 10-42 km but deteriorated at higher altitudes. In this study, we use ACE O_3 version 4.1 data (*Bernath et al.,*

2021). ACE makes ~ 30 measurements per day, like SOFIE. However, its latitudinal coverage spreads over the globe throughout the year due to the orbit inclination. Thus, there is limited coverage in the polar region.

2.5.2 Envisat MIPAS

The MIPAS instrument onboard the European ENVIronmental SATellite (ENVISAT) was operational from March 2002 until early April 2012. MIPAS was a middle infrared Fourier Transform spectrometer measuring high-resolution spectra of the atmospheric limb emission in five spectral bands (*Fischer et al.,* 2007). ENVISAT was launched on a sun-synchronous polar orbit with 98.55^{o} inclination and at ~800 km altitude.

MIPAS measured in the medium-to-long infrared at a wide spectral range of 4.15 to 14.6 µm in the middle and upper atmosphere. This enabled the detection and spectral resolution of a large number of emission features of major and minor atmospheric constituents. The original spectral resolution of MIPAS was ~0.035 cm^{-1}, but a reduced resolution of ~ 0.0625 cm^{-1} in a new operation mode was introduced in 2005. While the operational Level 2 MIPAS data are processed by ESA/DLR (European Space Agency/ Deutsches Zentrum für Luft- und Raumfahrt); the University of Bologna, Oxford University, and the KIT-IMK/IAA (Karlsruhe Institute of Technology - Institute of Meteorology and Climate Research/Instituto de Astrofísica de Andalucía) are hosts to three other independent research Level-2 processors that rely on the same Level-1b ESA data but use different retrieval schemes. Overall, the four processors show similar performance and use the same Level-1b ESA data, apply global fits, and use microwindows instead of the entire spectrum. Key differences in the processing schemes include the different regularization approaches (leading to a difference in the noise-resolution trade-off, with no clear average advantage to any specific

dataset), the choice of microwindows, the cloud detection threshold, and the approach to treating negative retrieved values.

We use the O_3 data processed by KIT-IMK/IAA. This dataset has been used in several validation and investigative studies (*Glatthor et al.,* 2006; *Steck et al.,* 2007; *von Clarmann et al.,* 2009; *Stiller et al.,* 2012; *Eckert et al.,* 2014; *Laeng et al.,* 2014, 2018; *López-Puertas et al.,* 2018). *Laeng et al.,* (2014) validated MIPAS Version 5.0 (V5R_O3_224) O_3 data. *López-Puertas et al.,* (2018) studied the O_3 in the middle atmosphere and determined the systematic and random errors in the 20-100 km range (at every 10 km). Version V5r_O3_m22 O_3 data in the stratosphere and mesosphere retrieved at 0.0625 cm^{-1} from 2005 to April 2012 in the microwindow of 14.8 μm and 10 μm spectral regions were used for observations made at three middle atmosphere modes (MA-Middle Atmosphere, NLC- Noctilucent and UA- Upper Atmosphere). During the daytime, MIPAS O_3 has an average vertical resolution of 3-4 km under 70 km, 6-8 km at 70-80 km, 8-10 km at 80-90 km, and 5-7 km at the secondary O_3 maximum (90-100 km). *López-Puertas et al.,* (2018) estimated the noise error for daytime to be typically smaller than 2% below 50 km, 2-10% between 50 and 70 km, 10 – 20% at 70 – 90 km, and ~ 30 % above 95 km. They used SABER, ACE, MLS, and SMILES (Superconducting Submillimeter-Wave Limb-Emission Sounder (*Kikuchi et al.,* 2010; *Mitsuda et al.,* 2011; *Baron et al.,* 2011; *Takahashi et al.,* 2011; *Imai et al.,* 2013)) to validate MIPAS O_3 and inferred that MIPAS agreed better than 5% with all instruments (except SABER) below 50 km. At the primary O_3 maximum, the difference was less than 5%. MIPAS measures 10-20% less than SABER between 30 km and 50 km and 5-15% less in the stratospheric O_3 maximum. From 50 km to 65-70 km, MIPAS displays general agreement with all instruments (except SABER at 60-70 km and MLS at 65-70 km altitude ranges during some latitudes/seasons). The difference is less than 5-10 %, with MIPAS displaying higher O_3 values. MIPAS O_3 is smaller (5–10%) than

ACE-FTS in the altitude range of 45–55 km and had up to 20% less O_3 in the daytime than SABER from 50 – 60 km. These differences increase above 60 km. The instruments are in good agreement at the secondary maximum except at certain latitudes/seasons. Overall, through all seasons, latitudes, and hemispheres, the MIPAS (V5r_O3_m22) O_3 during daytime has an accuracy of better than 5% at and below 50 km (with a positive bias of a few percent) and a positive bias of ~ 10% at 50-75 km (possibly due to spectroscopic errors). At 75-90 km, MIPAS shows a large relative positive difference with SMILES (10-20%) and a negative difference (10-50%) with SABER and ACE. MIPAS is accurate within 10-20%. Above 90 km, MIPAS agrees with all instruments by 10%.

This study uses the most recent MIPAS retrieval, version 8.0, processed by KIT-IMK. O_3 VMR vertical distribution was retrieved for version 8 data products using different sets of microwindows above and below 70 km. The structure of the KIT processed MIPAS data is 'spectra version_target species_baseline version' (e.g., V5R_O3_244 means that ESA spectra of version V5R (reduced spectral resolution) in IMK notation were used to retrieve target O_3 while a retrieval setup was used which is identified by the baseline number 244). This study uses baseline version 261 for all comparisons below 70 km and baseline versions 561 and 661 for altitudes above 70 km. While there are significant numbers of data points under baseline 261, the number of data points from versions 561 and 661 is relatively less. Since the Envisat mission ended in 2012, SOFIE measurements have been compared to coincident MIPAS O_3 profiles from 2008 to 2011. The systematic and random errors for MIPAS have been used as estimated by *López-Puertas et al.*, (2018). An older version (Version 5r_O3_m22) of MIPAS was used to predict the error. Revised errors for version 8.0 O_3 were being worked on at the time of this writing.

2.6 Coincidence Analysis

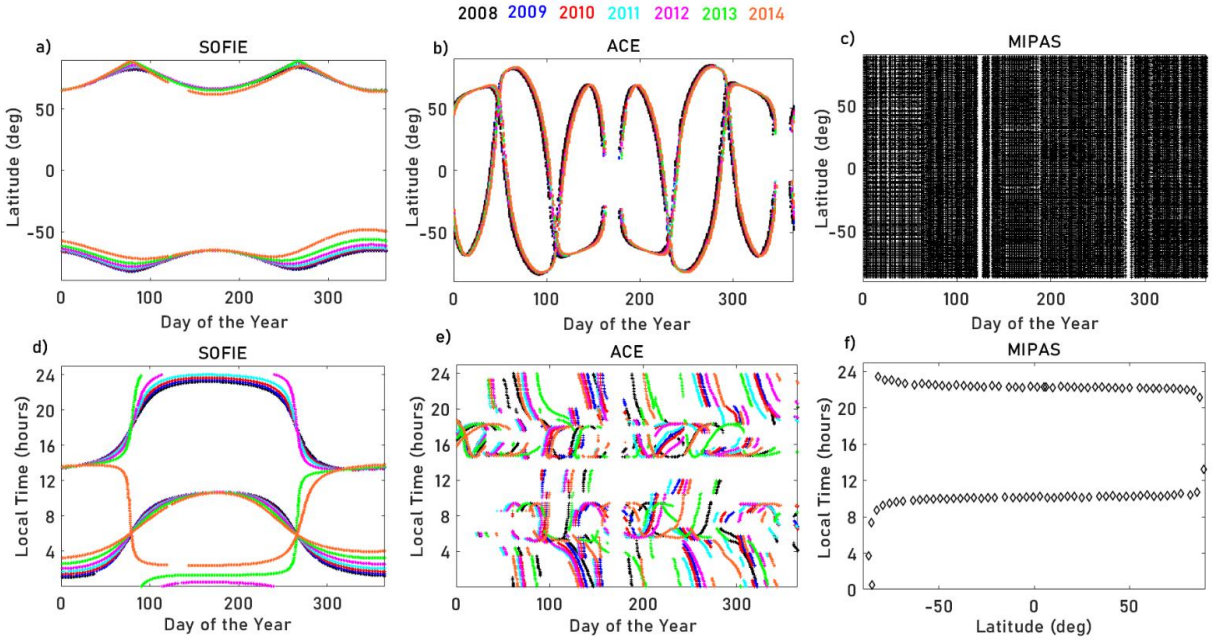

Figure 2. (a) SOFIE latitude coverages during 2008 – 2014 (b) ACE latitude coverages over years 2008 – 2014 (c) MIPAS latitude coverage for 2008, (d) SOFIE local time coverage during 2008 – 2014, (e) ACE local time coverage during 2008 – 2014, and (f) MIPAS local time variation with latitude.

Figure 2a, Figure 2b, and Figure 2c show the SOFIE, ACE, and MIPAS annual latitude coverages, respectively. SOFIE and ACE view a single latitude in each hemisphere on a single day. MIPAS views several latitudes per day. Thus, the latitude coverage in Figure 2c is plotted for 2008 alone. 2009-2011 have a similar annual latitude distribution. Figure 2d and Figure 2e show the SOFIE and ACE annual local time coverages, respectively. These coverages are from 2008 to 2014. Both SOFIE and ACE measure at sunrise and sunset. Figure 2f shows the local time variation of MIPAS with latitude. For each orbit, Envisat's track repeated the same local times (10:00 am/pm); hence, there is no variation in the local time coverage daily or annually. Thus, Figure 2f indicates that there is little latitudinal variation of local time except at high polar latitudes.

2.6.1 Approach

The primary approach behind the O_3 validation process involves using the statistical moments of the near-coincident pairs between SOFIE and correlative data sets ACE-FTS and MIPAS. The spatial and temporal coincidence criteria are a latitude separation of $\pm 5^o$, a longitude difference of $\pm 20^o$, and a time range of 2 hours (hereafter referred to as a coincidence box). During December, January, and February (DJF) in the NH (winter) and SH (summer), there are very few coincidences between SOFIE and MIPAS. Thus, we use a time range of 3 hours during these months.

Figure 3 shows the monthly variation of coincidence numbers in both hemispheres. The number of coincidences depends on the number of profiles that fall into the coincidence box. This figure indicates which months are used most in calculating the seasonal statistics. Figure 3a shows the number of coincident profiles between SOFIE and ACE from 2008 to 2014. Although the number of coincidences per month is inconsistent (e.g., 0 in January and 114 in February in the NH), there are a large number of coincidences for each season. Figure 3b shows the number of coincident profiles between SOFIE and MIPAS from 2008 to 2011. MIPAS typically covers two local times, while SOFIE local time coverage varies throughout the year. This leads to higher coincidence numbers between MIPAS and SOFIE, primarily during mid-year, from April to August. A different set of coincidences for MIPAS above and below 70 km have been calculated (Figure 3b) for reasons described in Section 2.5.2.

SOFIE has the highest vertical resolution compared to both ACE and MIPAS. SOFIE O_3 coincident profiles are linearly interpolated onto corresponding ACE and MIPAS grids. The SOFIE-ACE and SOFIE-MIPAS pairs' profiles are then linearly interpolated onto a common altitude grid of 2 km. A comparison between SOFIE and other correlative data sets is drawn by calculating the statistical moments at the common altitude grid.

The following statistical moments are used for the analysis of coincident O_3 VMR. The relative difference (δrel) is calculated using Equation 1.

$$\delta\text{rel} = \frac{X_{SOFIE} - X_{OTHER}}{(X_{SOFIE} + X_{OTHER})/2} \quad (1)$$

The mean relative difference (Δrel) for N coincident points is calculated using Equation 2.

$$\Delta\text{rel} = \frac{1}{N}\sum_{i} \delta_i \quad (2)$$

The percent relative difference (Δrel(%)) is calculated using Equation 3.

$$\Delta\text{rel}(\%) = \frac{1}{N}\sum_{i} \frac{(X(i)_{SOFIE} - X(i)_{OTHER}) * 100}{(X(i)_{SOFIE} + X(i)_{OTHER})/2} \quad (3)$$

The 1σ standard deviation (SD) of the differences in percent (σ_{rel}) is calculated using Equation 4.

$$\sigma\text{rel} = \sqrt{\left(\frac{1}{N-1}\sum_{i}\left((\delta_i - \Delta_{rel(\%)})^2\right)\right)} \quad (4)$$

The standard error of the mean difference (SEM) is calculated using Equation 5.

$$SEM = \frac{\sigma_{rel}}{N} \quad (5)$$

The random and systematic errors discussed in Section 2.4.3 factor into the statistical moments of combined error prediction. The SEM of the differences combined with the systematic errors of SOFIE and the correlative data set gives the total combined systematic error (Equation 6).

$$\text{ErrorCombined}_{\text{Systematic}} = \sqrt{SEM^2 + Error_{\text{SOFIE}_{\text{Systematic}}}{}^2 + Error_{\text{Correlated}_{\text{Systematic}}}{}^2} \quad (6)$$

Random errors from SOFIE and the correlative data set are considered in calculating the total combined random error (Equation 7) (*von Clarmann*, 2006).

$$\text{ErrorCombined}_{\text{Random}} = \sqrt{Error_{\text{SOFIE}_{\text{Random}}}{}^{2} + Error_{\text{Correlated}_{\text{Random}}}{}^{2}} \qquad (7)$$

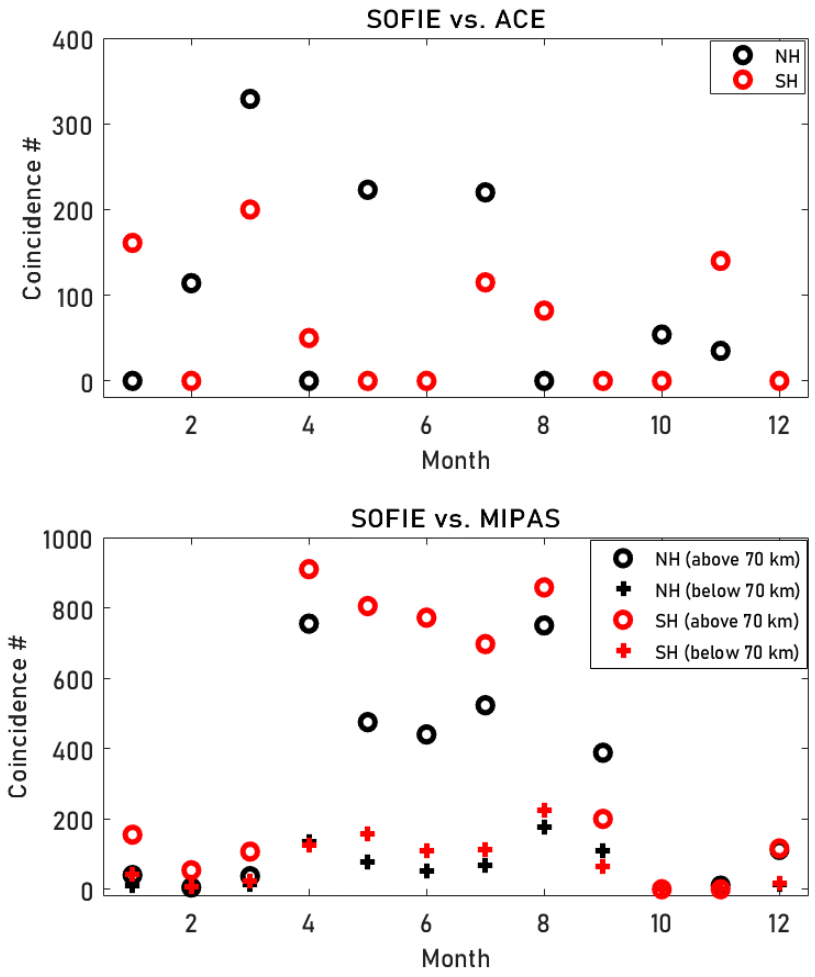

Figure 3. Monthly time series of the number of coincident profiles between (a) SOFIE and ACE for 2008-2014 and (b) SOFIE and MIPAS for 2008-2011. The coincidence box chosen is 20° in longitude x 5° in latitude x 2 hours in time (3 hours for DJF for MIPAS).

2.6.2 Statistics of the Coincidences

2.6.2.1 Winter

2.6.2.1.1 ACE

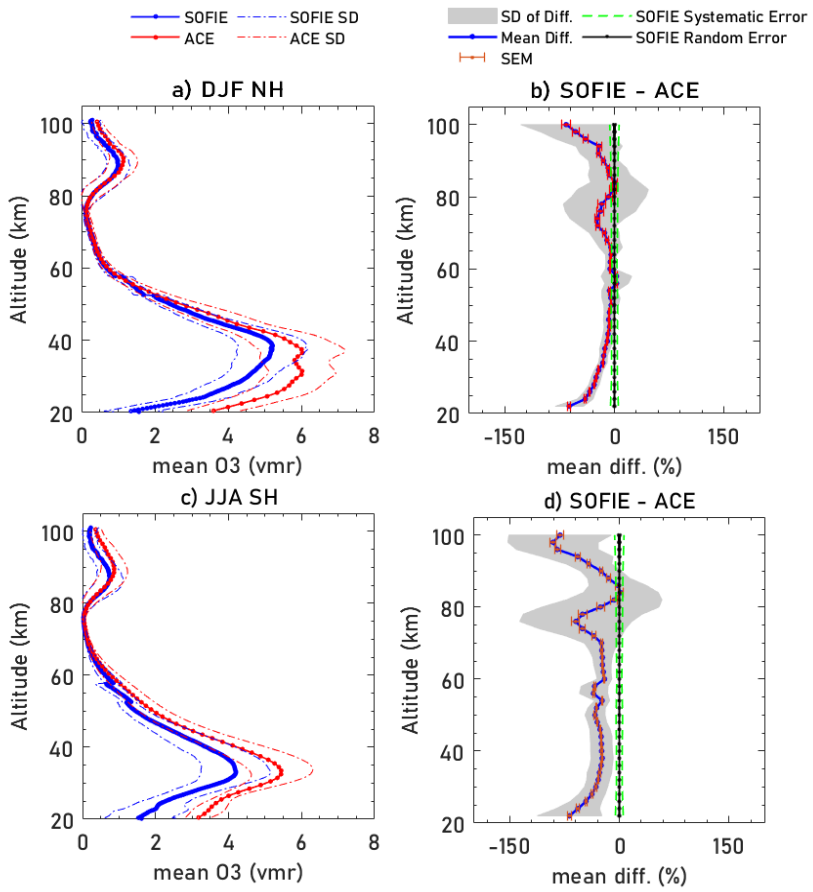

Figure 4. Statistical moments of coincident O_3 profiles from SOFIE and ACE for the winter. NH winter months DJF are plotted in Figures 4a and 4b, and SH winter months JJA are plotted in 4c and 4d. Panels a) and c) indicate the mean values of all coincident profiles (blue for SOFIE and red for ACE). Panels b) and d) for SOFIE-ACE show the mean difference values in percent (solid blue line with dots) with SEM bars and the SD of the differences (gray shade). For SOFIE-ACE, the combined total error (red dashed lines), SOFIE systematic errors (green dashed lines), and SOFIE random errors (solid black line with dots) are plotted. SOFIE-ACE combined total errors are estimated using the standard deviation of individual SOFIE and ACE profiles.

Figure 4 compares SOFIE with ACE during the winter for December, January, and February (DJF) in the NH and for June, July, and August (JJA) in the SH. We note that for Figure 4 through Figure 11, panels a and c indicate the mean values of all coincident profiles and the corresponding standard deviation of individual profiles from the mean, in the NH and SH, respectively. Panels b and d are used to show the statistical parameters calculated in Section 2.6.1 for the profiles shown in panels a and c, respectively. They show the mean difference, SD of the differences (%), and errors. For ACE, SOFIE's systematic and random errors are plotted, as these estimations are not currently reported for ACE. For MIPAS, the combined systematic and random errors are plotted.

In Figure 4a and Figure 4c, the mean O_3 profiles exhibit expected wintertime patterns in the stratosphere in both hemispheres. Patterns of gradual wintertime O_3 accumulations in the stratosphere tending towards a springtime maximum are evident. In the NH, all coincidences fall into February, which is late winter. Thus, all profiles are from the late winter period when the stratospheric O_3 build-up is at its peak. In the SH, the coincidences fall into July and August, with ~ 17 % higher coincidences in July than in August. Thus, the average of all profiles represents the average of mid and late-wintertime O_3. Hence, the accumulated wintertime stratospheric O_3 is better represented in the NH than in the SH.

For the NH, in panel b, the mean difference values between SOFIE and ACE are within 15 % between 36 and 70 km. The values are less than 24 % between 72 and 94 km, with values below 20 % at most altitudes. ACE measurements are typically reported higher than SOFIE. The SD of the differences are within 25 % from 22 to 72 km, with values lying at 10 % or lower at most altitudes.

For the SH, in panel d, the mean difference values are within 35 % between 30 and 72 km, where ACE is always higher than SOFIE. The values are less than 15 % between 72 and 82 km. The SD of the difference is less than 24 % between 26 and 70 km, where values are typically less than 15 %. For both hemispheres, SOFIE systematic and random errors alone are overplotted for the reasons stated above. Figure 4 indicates that the systematic or random errors from SOFIE alone are too small to account for the mean difference or the SD of the differences.

2.6.2.1.2 MIPAS

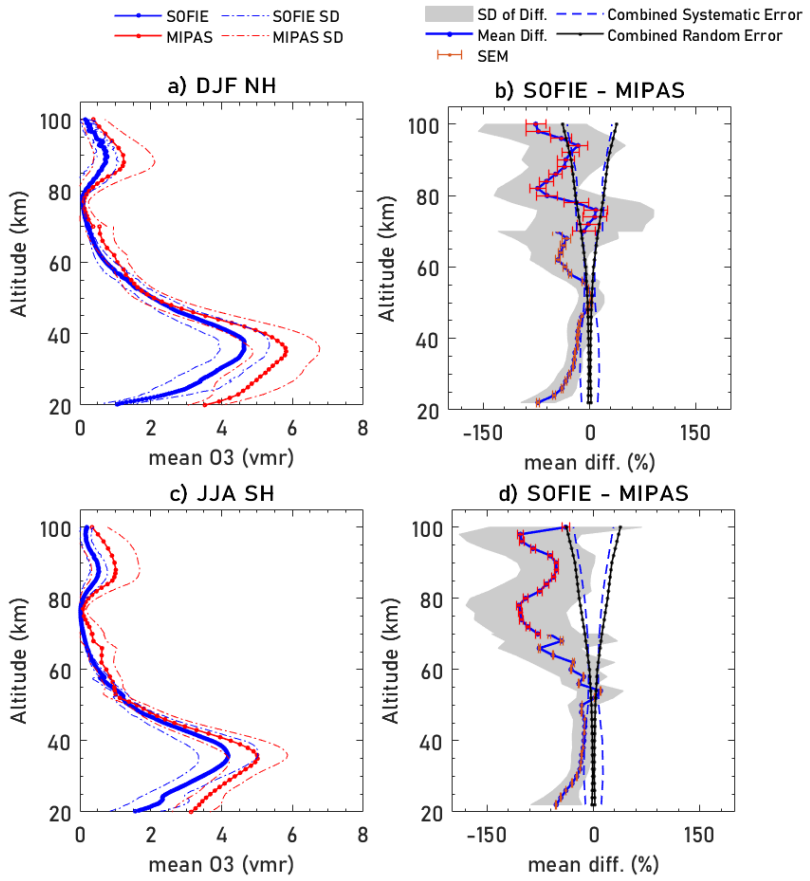

Figure 5. Statistical moments of coincident O_3 profiles from SOFIE and MIPAS for the winter. NH winter months DJF are plotted in Figures 5a and 5b, and SH winter months JJA are plotted in 5c and 5d. Panels a) and c) indicate the mean values of all coincident pro profiles (blue for SOFIE and red for MIPAS). Panels b) and d) for SOFIE-MIPAS show the mean difference values in percent (solid blue line with dots) with SEM bars and the SD of the differences (gray shade). The combined systematic (blue dashed line) and combined random errors (solid black line with dots) are plotted.

In Figure 5, panels a and c show the mean coincident profile during the winter between SOFIE and MIPAS in the NH and SH, respectively. Due to reasons explained in Section 2.5.2, the coincidences for the SOFIE-MIPAS pair are calculated separately above and below 70 km. Below 70 km, ~ 71 % of the coincident profiles are in December and ~ 25% in January, with very few

coincidences in February. Above 70 km, all coincidences are in December. Thus, the observations are biased toward early wintertime in the NH. The SOFIE-MIPAS pair in the NH capture the gradual wintertime enhancement in stratospheric O_3.

The number of coincident profiles in the SH has a relatively even distribution. Below 70 km, ~ 33 % of coincident profiles are in June, ~ 30 % in July, and ~ 37 % in August. Thus, the mean coincident profile is slightly biased towards late winter. Above 70 km, ~ 24 % of coincident profiles are in December, ~ 34 % in July, and ~ 50 % in August. The wintertime stratospheric enhancement is less prominent in the SH than in NH. The limited representation of the wintertime stratospheric O_3 increase in the SH may be because the averaging of the coincident profiles over three months is not equally weighted.

The NH mean difference values (panel b) are within ~ 20 % between 32 and 56 km and less than 16 % between 70 and 78 km. The SD of the differences are within 25 % between 22 and 58 km, with most values less than 20 %. For the SH, in panel d, the mean difference is within 20 % from 28 to 54 km and 90 to 94 km. The mean difference is less than 10 % between 56 and 80 km.

The SD of the difference is within 23 % from 22 to 72 km, where most values are less than 10 %. With a few exceptions, MIPAS measurements are typically higher than SOFIE at most altitudes. The systematic and random errors suggest that the combined systematic and random errors follow a consistent pattern in all seasons. The combined systematic error is less than ~ ± 12 % at ~ 22 km and decreases with altitude until ~ 60 km, where it increases to within ~ ± 7 %. The systematic error increases with altitude and is within ~ ± 32 % at 100 km. The random error follows a similar pattern. It is less than ± 2 % at ~ 22 km and decreases until ~ 60 km, where it is within ± 6%. The

random error increases above this and is less than ± 38 % at 100 km. This pattern for the systematic and random errors is consistent for all seasons and both hemispheres.

2.6.2.2 Spring

2.6.2.2.1 ACE

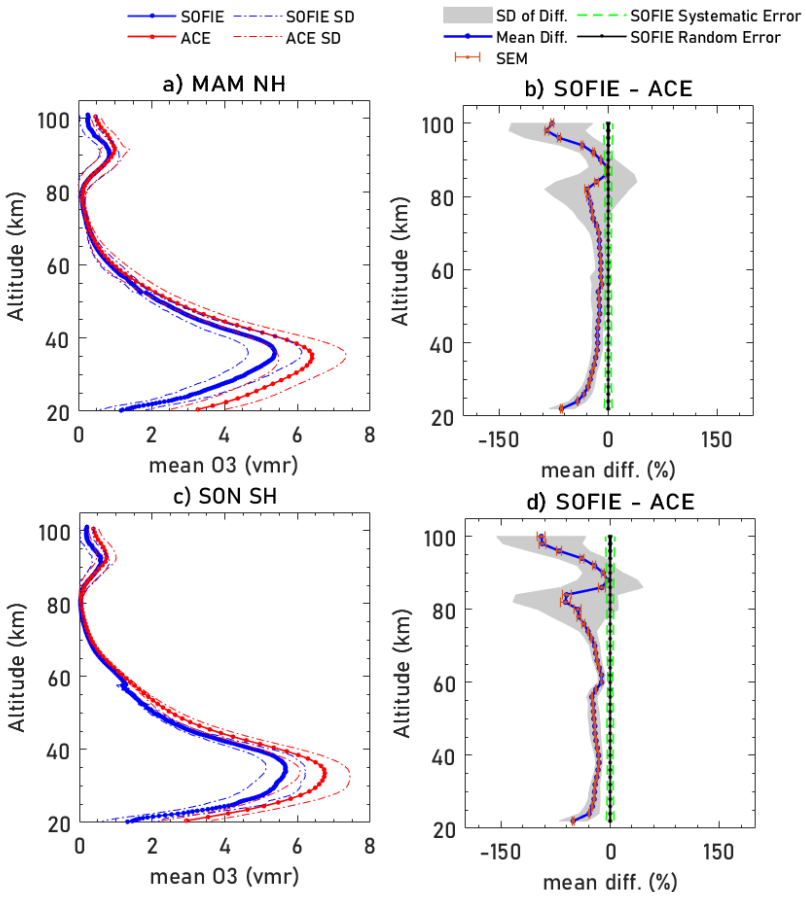

Figure 6. Same as Figure 4, but for the spring.

Figure 6 compares SOFIE with ACE during the spring for March, April, and May (MAM) in the NH and for September, October, and November (SON) in the SH. In panels a and c, the mean O_3 profiles exhibit the expected springtime O_3 maximum in both hemispheres. In the NH, ~ 60 % of the coincident profiles are in March, ~ 40 % in May, and there are no coincidences in April. In the

SH, all coincidences are in November, i.e., late Spring. Both hemispheres thus capture the springtime O_3 maximum.

For the NH, in panel b, the mean difference is within 25 % between 30 and 92 km (except between 80 and 82 km, where the mean difference is slightly higher). In this altitude range, the mean difference is less than ~10 % from 56 to 62 km and 86 to 90 km. The mean difference at altitudes between 30 and 92 km is typically less than 15 %. The SD of the differences is typically within ~ 10 % from 22 to 70 km, except at a few altitudes when the value is less than 15 %. For the SH, in panel d, the mean difference is within 25 % at 26 to 32 km and 46 to 56 km altitude ranges. The mean difference is less than 20 % from 34 to 44 km and 58 to 68 km, and below ~ 12 % from 86 to 90 km. The SD of the difference is within 20 % between 22 and 74 km, with values less than 10 % between 26 and 72 km.

2.6.2.2.2 MIPAS

Figure 7a and Figure 7b show the mean O_3 coincidence profiles during the spring in the NH and SH, respectively. In the NH, the coincident profiles are distributed as ~ 3% in March, ~ 60 % in April, and ~ 37 % in May below 70 km, with a similar distribution above 70 km. In the SH, all coincidences from 22 to 100 km are in September, which is early spring. The SOFIE-MIPAS pair thus fails to capture the increase in springtime O_3 accumulation to its fullest extent in the SH as there are no coincidences during late spring. However, the increase in stratospheric O_3 is evident in the NH, which has a high number of coincidences during late spring.

For the NH, in panel b, the mean difference is within 25 % from 28 to 30 km and 90 to 94 km. The mean difference is less than 20 % in the 32 to 60 km and 70 to 80 km altitude ranges. The SD of the difference is less than 20 % from 22 to 60 km, where it is within 10 % between 26 and 56 km.

For the SH, in panel d, the mean difference is typically below 20 % from 32 to 62 km, and the SD of the difference are below 20 % from 26 to 60 km. While the mean differences are both positive and negative, the values are mostly negative as MIPAS measurements are typically higher than SOFIE.

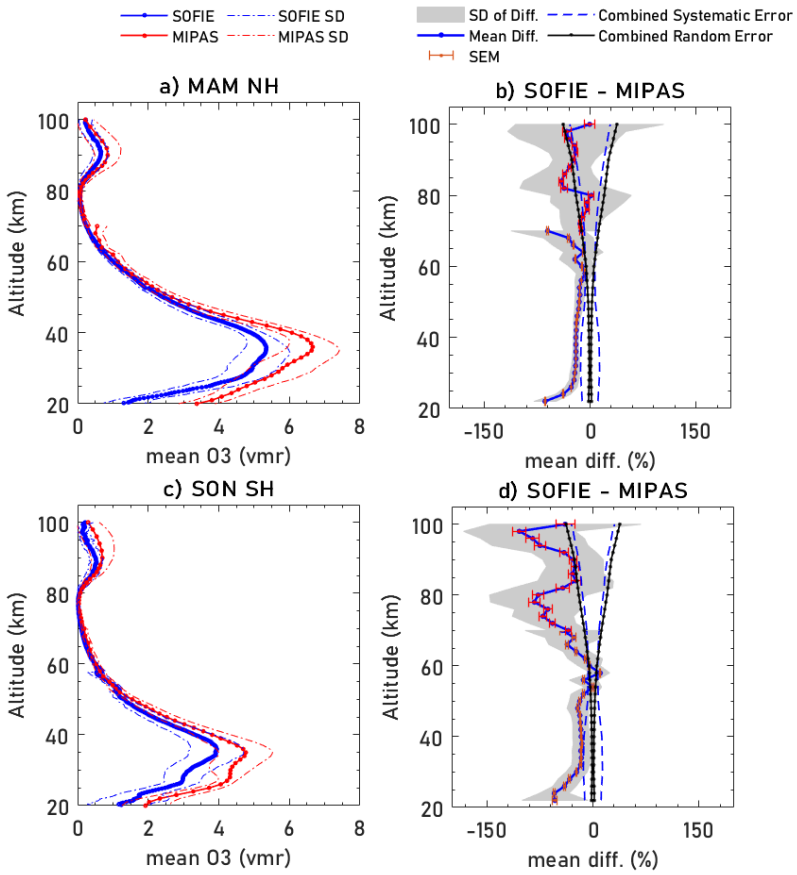

Figure 7. Same as Figure 5, but for the spring.

2.6.2.3 Summer

2.6.2.3.1 ACE

Figure 8 shows a comparison of ACE and SOFIE profiles over the summer during JJA in the NH and DJF in the SH. The destruction of the springtime O_3 maximum in the stratosphere starts in the

summer because of photodissociation. The photodissociation occurs over the entire summer, leading to a prominent decline in O_3 concentration. In the NH and SH, all SOFIE-ACE coincidences fall into July and January, respectively, which are mid-summer periods in the respective hemispheres. Thus, the variation in stratospheric O_3 by late summer is not captured for either hemisphere, resulting in an incomplete picture of summertime O_3 loss.

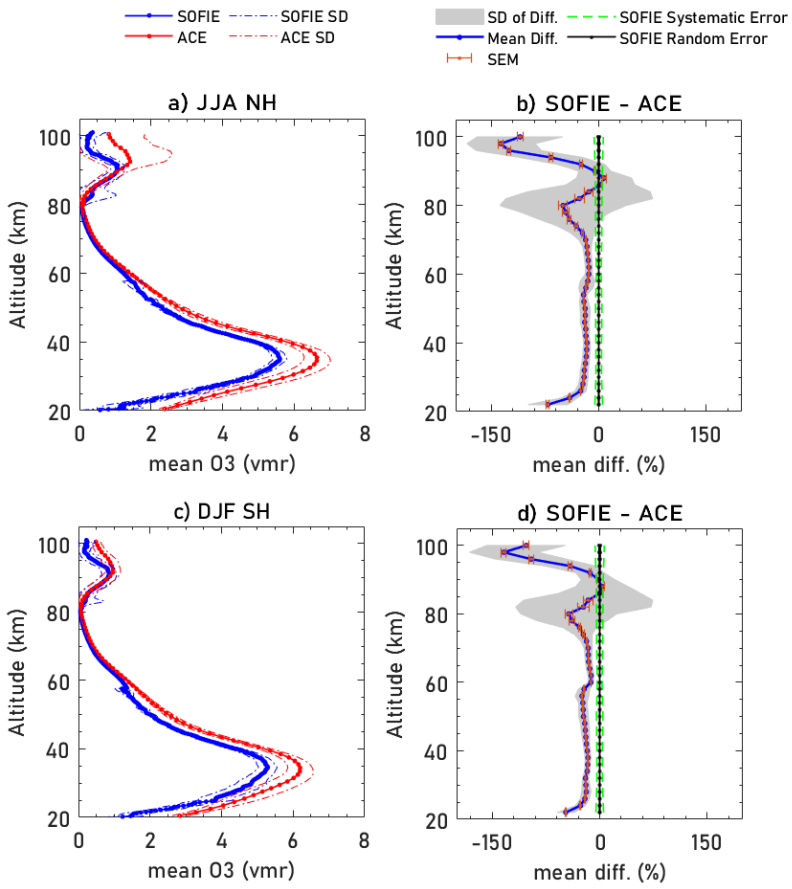

Figure 8. Same as Figure 4, but for the summer.

The mean difference between SOFIE and ACE coincident pairs is less than ~ 25 % between 26 and 72 km in the NH, as shown in panel b, where the values at most altitudes are typically within 20 %. The mean difference between 84 and 90 km is less than 15 %. The SD of the difference is below 10 % from 26 to 70 km in the NH. For the SH, the mean difference is within 25 % from 26

to 74 km, with values typically lower than 20%; and less than 20 % from 84 to 92 km. The SD of the differences is lower than 10 % from 24 to 72 km.

2.6.2.3.2 MIPAS

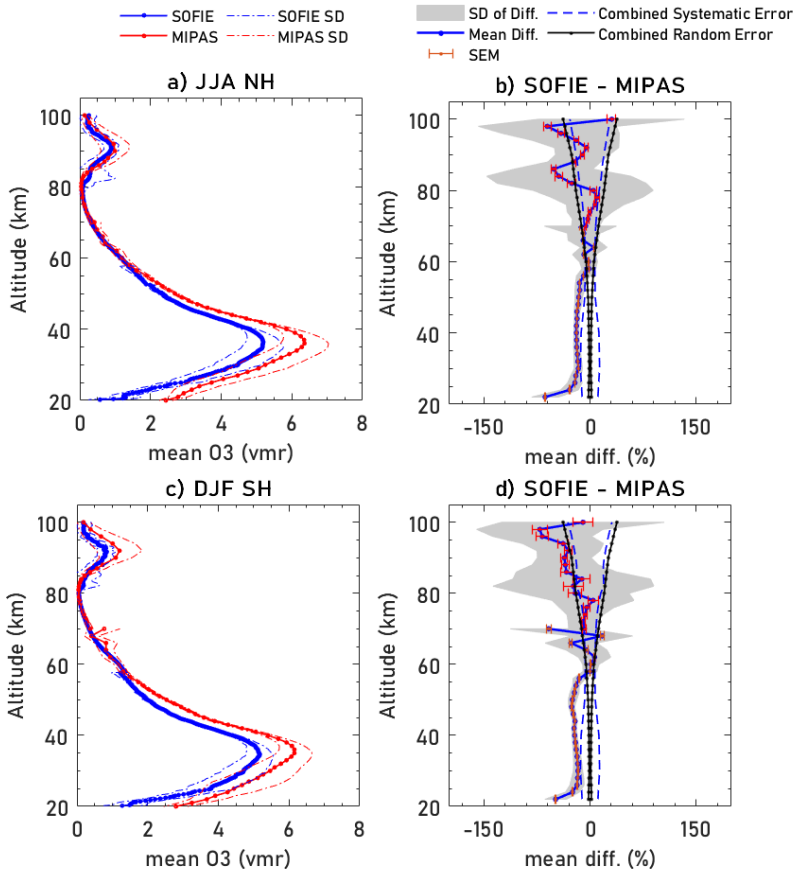

Figure 9. Same as Figure 5, but for the summer.

The mean O_3 coincidence profiles for the NH and SH are shown in Figure 9a and Figure 9b, respectively. For the NH, below 70 km, the coincidences are distributed as ~ 26 % in June, ~ 31 % in July, and ~ 44 % in August. Above 70 km, there are ~ 17 %, ~ 23 %, and ~ 60 % of the total summertime coincidences between MIPAS and SOFIE in June, July, and August, respectively. The expected start of the decrease in stratospheric O_3 is visible in the NH as the late summertime coincidences are high. In the SH, the coincidence distribution falls more into December (~ 35 %)

and January (~ 48 %) than February (~ 17 %), thus limiting the observation of summertime O_3 variability. Above 70 km, the coincidences are distributed similarly: ~ 27 % in December, ~ 62 % in January, and ~ 11% in February.

In the NH, in panel b, the mean difference is below 20 % from 28 to 54 km and 90 to 94 km. The mean difference between 56 and 80 km is less than 10 %. The SD of the difference is within 20 % from 22 to 26 km, 10 % from 28 to 58 km, and 23 % from 60 to 72 km. In panel d, for the SH, the mean difference is below 25 % from 26 to 42 km, 20 % from 56 to 74 km, and 15 % from 84 to 88 km. The SD is less than 20 % in the 22 to 62 km, 70 to 72 km, and 90 to 92 km altitude ranges.

2.6.2.4 Autumn

2.6.2.4.1 ACE

In Figure 10 ACE and SOFIE profiles are compared over the autumn during SON in the NH and MAM in the SH. The gradual summertime O_3 destruction is evident in both hemispheres by the reduction in stratospheric O_3 in the autumn. While a minimum in the O_3 concentration is typically observed during late autumn, there is a distinct reduction from early autumn. In the NH, ~ 61% of the coincidences fall into October and ~ 39 % into November. In the SH, 80 % of coincidences fall into March and 20 % into April. O_3 decreases in the stratosphere in both hemispheres with a minimum in the autumn.

For the NH, panel b shows that the mean difference is within 20 % from 34 to 52 km, with most values less than 15 %. The values are below 10 % from 54 to 70 km and 84 to 88 km. In the altitude range of 72 to 74 km and 90 to 92 km, the values are within 20 %. The SD of differences are within 15 % between 24 and 68 km (except at 32 km) and less than 20 % from 90 to 92 km. For the SH, panel d shows that from 28 to 70 km, the mean difference is less than 20 %, with most values

lower than 10 %. The values are less than 12 % from 86 to 90 km, with most values below 5%. The SD of the difference are within 15% from 22 to 70 km and less than 20 % from 88 to 94 km.

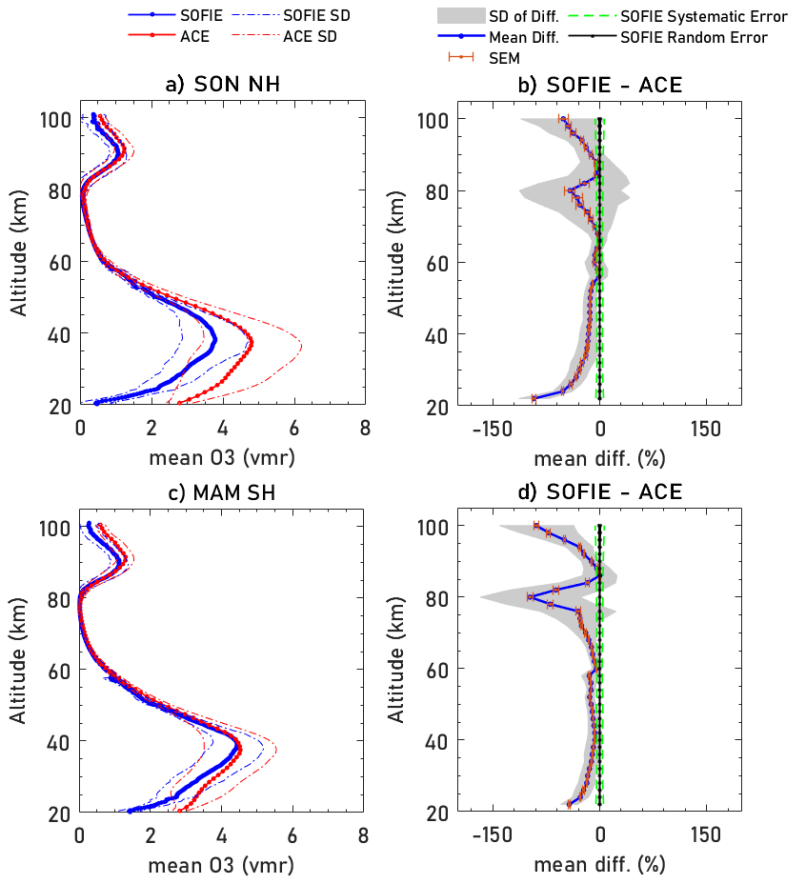

Figure 10. Same as Figure 4, but for the autumn.

2.6.2.4.2 MIPAS

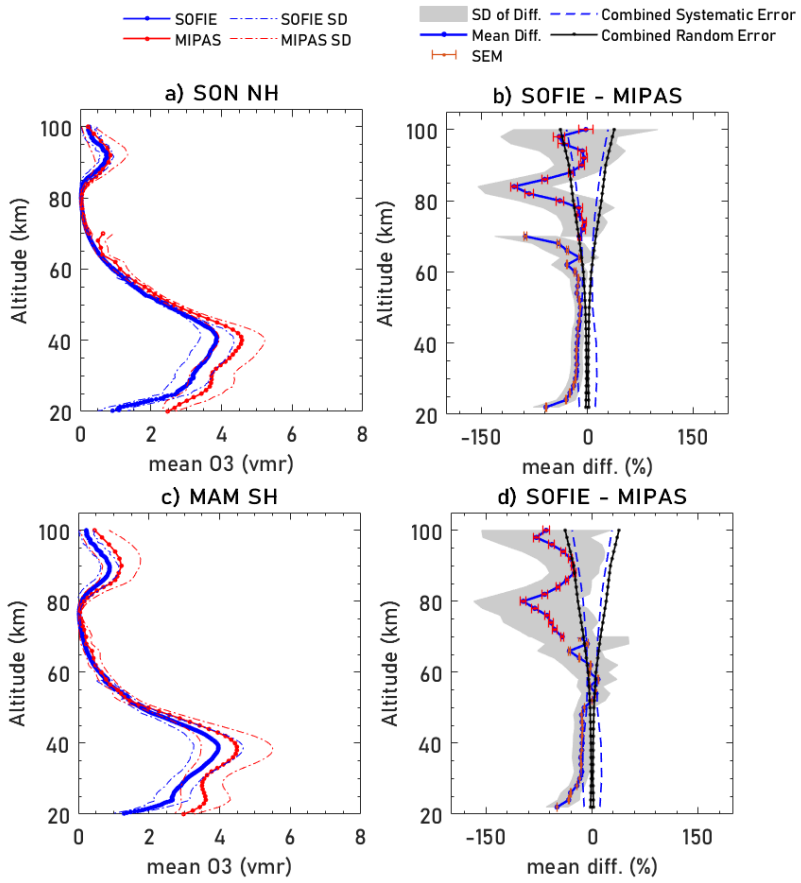

Figure 11. Same as Figure 5, but for the autumn.

Figure 11a and Figure 11c show the mean of the coincidence profiles in the NH and SH, respectively. In the NH, below 70 km, ~ 97 % of coincidence profiles are in September, and the remaining in November. Above 70 km, all coincidences are in September. In the SH, below 70 km, ~ 6% of the coincidences are in March, 50 % in April, and ~ 44 % in May. Above 70 km, ~ 7 % of coincidences are in March, ~ 41 % in April, and ~ 52 % in May. Autumn O_3 concentration is significantly lower in both hemispheres, and a strong decline from the summertime

concentration is observed. The results lean towards an autumn-time minimum in the O_3 concentration.

In the NH, panel b suggests that the mean difference is below 20 % from 28 to 60 km, with most values within 15 %. The values are less than ~ 12 % between 70 and 78 km and less than 10 % from 90 to 94 km. The SD of the difference is within 15 % from 22 to 70 km and below 20 % from 88 to 94 km. In panel d, for the SH, the mean difference is less than 20 % from 30 to 68 km except at 66 km. The values are less than 10 % from 52 to 62 km. The SD of the differences is within 20 % from 22 to 56 km.

2.6.2.5 All Seasons Combined

The averages of the mean difference values between SOFIE and ACE, and SOFIE and MIPAS, over all seasons through the altitude range of ~ 20 – 100 km are summarized in Table 2. The values are shown at 10 km intervals in both hemispheres. The comparisons indicate qualitative and quantitative agreement between SOFIE and ACE or MIPAS O_3 in terms of the mean seasonal climatology and the variability over seasons. SOFIE O_3 typically displays a negative bias through all altitudes (stratosphere, mesosphere, and lower thermosphere), and the average measured value by SOFIE is less than ACE and MIPAS. Comparisons between measurements from SOFIE-ACE and SOFIE-MIPAS for NH and SH indicate that the altitude variability is comparable for both pairs, except at ~ 70 - 80 km in the SH, where MIPAS data deteriorates. High altitude measurements at ~ 100 km also indicate that the agreement at this altitude is not good for both pairs. MIPAS SH values are consistently higher than SOFIE, resulting in larger differences attributed to limited coincidences.

Table 2. The values outside the parenthesis are the mean percent differences, and the values inside the parenthesis are the uncertainties (1 σ standard deviation of the percent differences), relative to SOFIE O_3 for ACE and MIPAS, for different Hemispheres, and altitudes[a] and all seasons averaged

Data Set/ Hemisphere	**Altitude (km)**								
	~ 20	**30**	**40**	**50**	**60**	**70**	**80**	**90**	**100**
1) ACE NH	-72.38 (21.34)	-24.72 (8.40)	-14.06 (8.03)	-12.24 (9.11)	-9.39 (7.89)	-12.92 (16.36)	-31.71 (64.43)	-10.75 (20.33)	-76.07 (59.49)
2) ACE SH	-52.32 (21.92)	-22.42 (9.86)	-16.07 (8.87)	-22.55 (8.73)	-12.30 (5.98)	-20.36 (12.87)	-52.73 (68.13)	-12.17 (23.03)	-91.85 (59.64)
3) ACE NH and SH Combined	-62.35 (21.63)	-23.57 (9.13)	-15.06 (8.45)	-17.40 (8.92)	-10.85 (6.94)	-16.64 (14.61)	-42.22 (66.28)	-11.46 (21.68)	-83.96 (59.56)
4) MIPAS NH	-65.71 (16.10)	-19.06 (9.71)	-16.49 (9.28)	-11.60 (6.00)	-18.04 (22.11)	-9.08 (37.13)	-21.08 (69.39)	-17.02 (41.29)	-9.50 (96.04)
5) MIPAS SH	-51.87 (29.32)	-21.32 (11.66)	-16.88 (11.85)	-18.20 (11.67)	-9.68 (22.20)	-42.04 (38.23)	-64.55 (62.96)	-33.91 (37.00)	-27.25 (87.40)
6) MIPAS NH and SH Combined	-58.79 (22.71)	-20.19 (10.68)	-16.69 (10.57)	-14.90 (8.84)	-13.86 (22.16)	-25.56 (37.68)	-42.81 (66.18)	-25.46 (39.15)	-18.37 (91.72)
All cases (1,2,4 and 5) combined	-60.57 (22.17)	-21.88 (9.91)	-15.88 (9.51)	-16.15 (8.88)	-12.35 (14.55)	-21.10 (26.15)	-42.52 (66.23)	-18.46 (30.41)	-51.17 (75.64)

[a] The percent differences and uncertainties are calculated over all seasons for altitudes at 10 km intervals, starting from ~ 20 km, using the data in Figure 4 - Figure 11 of this paper. All cases combined for the same statistics are shown in the last row.

Table 2 shows that between ~ 30 – 90 km (at every 10 km mark), the mean difference between SOFIE and ACE in the NH is below 30 % (negative bias) and less than 15 % (negative bias) in several of those cases, except at 80 km. The values in the SH are below 30 % (negative bias) between ~ 30 – 72 km and less than 20 % (negative bias) in most cases. The mean difference between SOFIE and MIPAS in the NH is typically below 22 % (negative bias) in the 30-80 km altitude range (except occasional digression between ~ 62 and 68 km). There is less than 21 % negative bias in the SH between 30 - 62 km. Overall, the agreement between SOFIE and ACE,

and SOFIE and MIPAS, is better in the NH than in the SH. The biases are highest in both hemispheres in the lower stratosphere below 30 km and lower thermosphere above 90 km, which are attributed to Polar Stratospheric Cloud (PSC) interference and limited coincidences, respectively.

The mean difference (%) between SOFIE and ACE are similar through the ~ 20 – 100 km altitude range in most seasons in both hemispheres. Mean difference values are typically less than 30 % between 25 and 90 km but tend to increase above ~ 90 km in almost all seasons in both hemispheres. Seasonal differences between SOFIE and ACE are more pronounced in the SH. The mean difference below ~ 25 km is higher than 30 % on several occasions and is attributed to PSCs. The mean difference near ~ 75 km in the winter is higher than 30 %. Better agreement in the NH is also evident in the spring. The mean difference between 80 and 85 km is over 30 % in the SH. In the summer, in both hemispheres, the mean difference exceeds 30 % between ~ 75 and 82 km, and the mean difference values are higher above ~ 90 km in the summer than in other seasons. During the autumn, between ~ 76 and 82 km, the mean difference is higher than 30 %. Thus, typically, in all seasons, the most common region where mean differences exceed 30 % is between ~ 75 and 82 km and above ~ 90 km. Overall, considering both hemispheres, the overall patterns in the agreement are similar for all seasons. SOFIE and ACE coincident data pairs demonstrate seasonal variations in stratospheric O_3 reasonably well, considering the varying number and distribution of coincidences in different months. The wintertime O_3 accumulation is better represented in the NH, while both hemispheres capture the springtime increase in O_3. All coincidences fall into the mid-summer period during the summer; thus, neither hemisphere captures the gradual summertime stratospheric O_3 decrease to its full potential. In the autumn, both hemispheres indicate lowering stratospheric O_3. Thus, the seasonal variation in stratospheric O_3 is

captured reasonably, and the overall patterns in variation of mean O_3 differences are similar for all seasons, with better agreements in the NH than SH.

The mean difference (%) between SOFIE and MIPAS from ~ 20 to 100 km varies in different seasons, typically between ~ 65 and 80 km. In the winter, this is more evident in the SH. There is a better representation of the stratospheric O_3 increase in the NH than in SH. In the spring, the NH shows better overall agreement with mean difference values typically less than 30 %. The springtime O_3 maximum is also better captured in the NH than in the SH. There is an excellent overall agreement between SOFIE and MIPAS in both hemispheres, typically below ~ 90 km in the summer. The NH values exceed 30 % briefly at ~ 86 km, and the SH shows better agreement than the NH. Considering the distribution of coincidences, the extent of the O_3 decrease shown by coincident profiles in the stratosphere is reasonable in both hemispheres and more prominent in the NH. In the autumn, there is an overall agreement between SOFIE and MIPAS. The mean differences exceed 30 % in the ~ 75 - 85 km and ~ 65 - 85 km altitude ranges in the NH and SH, respectively. In the autumn, the gradual O_3 decrease in the stratosphere is captured in both hemispheres. Overall, there is a better agreement in the NH than in the SH between SOFIE and MIPAS.

The last row of Table 2 shows the average values of the NH and SH from SOFIE-ACE and SOFIE-MIPAS data pairs and represents the mean bias irrespective of the season, data set, and hemisphere. The mean bias distribution is relatively high in the lower stratosphere (~ 20 km) and is a possible outcome of interference due to PSCs. At 70 km, the mean difference and SD of less than ~ 26.1% are influenced by the high MIPAS SH values. At 80 km, the mean bias and SD are high due to the high values in the SH displayed by both ACE and MIPAS. At 90 km, the average values are less than 20 % (negative bias). This can be attributed to the low bias values and SD of the difference

in both hemispheres for ACE and in the NH for MIPAS that are included in the average. At 100 km, ACE show high values in both hemispheres, resulting in high mean bias and SD of the difference. In summary, the overall agreement between SOFIE and the other datasets is good in the 30 - 90 km altitude range, except at ~ 80 km and barring a few exceptions.

2.7 Summary and Conclusions

In this study, AIM SOFIE V1.3 O_3 data is validated against ACE-FTS V4.1 O_3 data and Envisat/MIPAS-reprocessed V8.0 O_3 dataset in the altitude range of 20 – 100 km. The statistics of coincident profiles, seasonal climatology, and the variation of the secondary O_3 maximum are investigated. All three datasets demonstrate appreciable seasonal evolution of stratospheric O_3. However, this seasonal evolution is occasionally underestimated due to the number of coincidences that sometimes fall more heavily into a particular month of the season than the others. The summary over all seasons, hemispheres, and profile comparisons for SOFIE-ACE and SOFIE-MIPAS pairs indicates that SOFIE O_3 agrees qualitatively and quantitatively with ACE and MIPAS regarding the mean state and the extent of variability. The mean difference values over both hemispheres, all seasons, and datasets indicate that SOFIE is biased low at all altitudes but more strongly in the lower stratosphere (~ 20 km) and upper mesosphere (80 km and 100 km, but not at 90 km). The agreement is very good, from ~ 30 km to ~ 70 km and typically below 30% except at a few altitudes near ~ 70 km in some seasons. The mean difference improves at ~ 90 km and is less than 19 % averaged over all seasons, hemispheres, and instrument pairs.

For MIPAS, the systematic and random errors (reported by *López-Puertas et al.,* (2018)) are higher than the SOFIE counterparts and more so at high altitudes (~ 70 km – 100 km). The low random error values of SOFIE indicate that the noise levels of SOFIE profiles are very low compared to the MIPAS profiles. The mean difference and SD of the difference for the SOFIE-MIPAS data

pair exceed the combined systematic and random errors more prominently at high altitudes. The agreement between SOFIE and the correlative datasets is overall better in the NH than the SH. SOFIE agrees with ACE and MIPAS comparably between ~ 20 km and ~ 70 km.

There are two aspects of this analysis that need further evaluation. At the lower stratosphere (~ 20 km), the O_3 values from SOFIE are much smaller than the correlative datasets, resulting in large mean differences in both hemispheres. A possible reason for SOFIE's low measurement could be the PSC signals that are not corrected. An alternate explanation is that the destruction of O_3 by PSCs in the lower stratosphere is measured more accurately by SOFIE due to a higher number of near-pole measurements due to its continuous high latitude coverage. These measurements are within the latitude range of $\pm 5^o$ of the coincident profiles. A second irregularity is a sudden increase in the mean difference between SOFIE and the correlative datasets and the low values of SOFIE O_3 near ~ 80 km. SOFIE O_3 data was corrected for polar mesospheric cloud (PMC) interference after 2009. The data prior to 2009 consists of PMC interference during the polar summer (mid-May to late August in the NH and late November to late February in the SH). Thus, 2008 data from SOFIE O_3 during these periods possibly impacted the O_3, leading to higher mean difference values at ~ 80 km. However, the overall data quality is not affected by these biases.

SOFIE O_3 observations agree with ACE and MIPAS overall and exhibit expected seasonal variation in the stratosphere. Seasons with differences from expected behavior are attributed to the limited coincidences in certain months, which biases the observation of seasonal variation. Our results demonstrate the utility and robustness of the SOFIE O_3 data product.

2.8 Acknowledgments

Funding for this research was provided by NASA's Small Explorers Program, which supports the AIM mission. We thank the SOFIE and AIM operation teams for their help and excellent support

with this work. We thank the ACE team for their data. The Canadian Space Agency funds ACE. We thank the Karlsruhe Institute of Technology for providing processed MIPAS data.

2.9 Open Research

The SOFIE Version 1.3 O_3 data and documentation are publicly available at the SOFIE website - http://sofie.gats-inc.com/getdata . ACE Version 4.1 O_3 data are available upon request at the ACE website https://databace.scisat.ca/level2/ace_v4.1_v4.2/ . Processed MIPAS Version 8.0 data are made available by the Karlsruhe Institute of Technology upon request at their website http://imk-asf-mipas.imk.kit.edu/imk/asf/sat/mipas-export/ .

References

Baron, P., Urban, J., Sagawa, H., Möller, J., Murtagh, D.P., Mendrok, J., Dupuy, E., Sato, T.O., Ochiai, S., Suzuki, K. and Manabe, T., 2011. The Level 2 research product algorithms for the Superconducting Submillimeter-Wave Limb-Emission Sounder (SMILES). *Atmospheric Measurement Techniques, 4*(10), pp.2105-2124. https://doi.org/10.5194/amt-4-2105-2011

Bernath, P., 2001. Atmospheric chemistry experiment (ACE): An overview. Spectroscopy from Space, pp.147-160.Bernath, Peter F., et al. "Atmospheric chemistry experiment (ACE): mission overview." *Geophysical Research Letters 32*.15 (2005). https://doi.org/10.1029/2005GL022386

Bernath, P.F., Crouse, J., Hughes, R.C. and Boone, C.D., 2021. The Atmospheric Chemistry Experiment Fourier transform spectrometer (ACE-FTS) version 4.1 retrievals: Trends and seasonal distributions. *Journal of Quantitative Spectroscopy and Radiative Transfer, 259*, p.107409. DOI:10.1016/j.jqsrt.2020.107409

Bodhaine, B.A., Wood, N.B., Dutton, E.G. and Slusser, J.R., 1999. On Rayleigh optical depth calculations. *Journal of Atmospheric and Oceanic Technology, 16*(11), pp.1854-1861. https://doi.org/10.1175/1520-0426(1999)016%3C1854:ORODC%3E2.0.CO;2

Boone, C.D., Nassar, R., Walker, K.A., Rochon, Y., McLeod, S.D., Rinsland, C.P. and Bernath, P.F., 2005. Retrievals for the atmospheric chemistry experiment Fourier-transform spectrometer. *Applied optics, 44*(33), pp.7218-7231.DOI: 10.1364/ao.44.007218

Bovensmann, H., Burrows, J.P., Buchwitz, M., Frerick, J., Noel, S., Rozanov, V.V., Chance, K.V. and Goede, A.P.H., 1999. SCIAMACHY: Mission objectives and measurement modes. *Journal of the atmospheric sciences, 56*(2), pp.127-150. https://doi.org/10.1175/1520-0469(1999)056%3C0127:SMOAMM%3E2.0.CO;2

Charlton, A.J. and Polvani, L.M., 2007. A new look at stratospheric sudden warmings. Part I: Climatology and modeling benchmarks. *Journal of climate, 20*(3), pp.449-469. https://doi.org/10.1175/JCLI3996.1

Cortesi, U., Lambert, J.C., De Clercq, C., Bianchini, G., Blumenstock, T., Bracher, A., Castelli, E., Catoire, V., Chance, K.V., De Maziere, M. and Demoulin, P., 2007. Geophysical validation of MIPAS-ENVISAT operational ozone data. *Atmospheric Chemistry and Physics, 7*(18), pp.4807-4867.DOI : 10.5194/acp-7-4807-2007

Cracknell, A.P. and Varotsos, C., 2012. Remote sensing and atmospheric ozone: Human activities versus natural variability. *Springer Science & Business Media*.

Cunnold, D.M., Chu, W.P., Barnes, R.A., McCormick, M.P. and Veiga, R.E., 1989. Validation of SAGE II ozone measurements. *Journal of Geophysical Research: Atmospheres, 94*(D6), pp.8447-8460.https://doi.org/10.1029/JD094iD06p08447

Dupuy, E., Walker, K.A., Kar, J., Boone, C.D., McElroy, C.T., Bernath, P.F., Drummond, J.R., Skelton, R., McLeod, S.D., Hughes, R.C. and Nowlan, C.R., 2009. Validation of ozone

measurements from the Atmospheric Chemistry Experiment (ACE). *Atmospheric Chemistry and Physics, 9(*2), pp.287-343. doi:10.5194/acp-9-287-2009, 2009.

Eckert, E., von Clarmann, T., Kiefer, M., Stiller, G.P., Lossow, S., Glatthor, N., Degenstein, D.A., Froidevaux, L., Godin-Beekmann, S., Leblanc, T. and McDermid, S., 2014. Drift-corrected trends and periodic variations in MIPAS IMK/IAA ozone measurements. *Atmospheric Chemistry and Physics, 14*(5), pp.2571-2589. https://doi.org/10.5194/acp-14-2571-2014

Fischer, H., Birk, M., Blom, C., Carli, B., Carlotti, M., Von Clarmann, T., Delbouille, L., Dudhia, A., Ehhalt, D., Endemann, M. and Flaud, J.M., 2008. MIPAS: an instrument for atmospheric and climate research. *Atmospheric Chemistry and Physics, 8*(8), pp.2151-2188. DOI:10.5194/acp-8-2151-2008

Froidevaux, L., Livesey, N.J., Read, W.G., Jiang, Y.B., Jimenez, C., Filipiak, M.J., Schwartz, M.J., Santee, M.L., Pumphrey, H.C., Jiang, J.H. and Wu, D.L., 2006. Early validation analyses of atmospheric profiles from EOS MLS on the Aura satellite. *IEEE Transactions on Geoscience and Remote Sensing, 44*(5), pp.1106-1121.DOI:10.1109/TGRS.2006.864366

Hurst, D.F., Lambert, A., Read, W.G., Davis, S.M., Rosenlof, K.H., Hall, E.G., Jordan, A.F. and Oltmans, S.J., 2014. Validation of Aura Microwave Limb Sounder stratospheric water vapor measurements by the NOAA frost point hygrometer. *Journal of Geophysical Research: Atmospheres, 119*(3), pp.1612-1625.DOI:10.1029/2007JD008771

Funke, B., López-Puertas, M., García-Comas, M., Stiller, G.P., Von Clarmann, T., Höpfner, M., Glatthor, N., Grabowski, U., Kellmann, S. and Linden, A., 2009. Carbon monoxide distributions from the upper troposphere to the mesosphere inferred from 4.7 μm non-local thermal equilibrium emissions measured by MIPAS on Envisat. *Atmospheric Chemistry and Physics, 9*(7), pp.2387-2411.https://doi.org/10.5194/acp-9-2387-2009

Fussen, D., Vanhellemont, F., Dodion, J., Bingen, C., Walker, K.A., Boone, C.D., McLeod, S.D. and Bernath, P.F., 2005. Initial intercomparison of ozone and nitrogen dioxide number density profiles retrieved by the ACE-FTS and GOMOS occultation experiments. *Geophysical research letters, 32*(16).https://doi.org/10.1029/2005GL022468

Glatthor, N., Von Clarmann, T., Fischer, H., Funke, B., Gil-López, S., Grabowski, U., Höpfner, M., Kellmann, S., Linden, A., López-Puertas, M. and Mengistu Tsidu, G., 2006. Retrieval of stratospheric ozone profiles from MIPAS/ENVISAT limb emission spectra: a sensitivity study. *Atmospheric Chemistry and Physics, 6*(10), pp.2767-2781. https://doi.org/10.5194/acp-6-2767-2006

Gordley, L.L., Marshall, B.T. and Chu, D.A., 1994. LINEPAK: Algorithms for modeling spectral transmittance and radiance. *Journal of Quantitative Spectroscopy and Radiative Transfer, 52*(5), pp.563-580.DOI: 10.1016/0022-4073(94)90025-6

Gordley, L.L., Hervig, M.E., Fish, C., Russell III, J.M., Bailey, S., Cook, J., Hansen, S., Shumway, A., Paxton, G., Deaver, L. and Marshall, T., 2009. The solar occultation for ice

experiment. *Journal of Atmospheric and Solar-Terrestrial Physics, 71(*3-4), pp.300-315. doi:10.1016/j.jastp.2008.07.012

Gordley, L., Burton, J., Marshall, B.T., McHugh, M., Deaver, L., Nelsen, J., Russell, J.M. and Bailey, S., 2009. High precision refraction measurements by solar imaging during occultation: results from SOFIE. *Applied optics*, *48*(25), pp.4814-4825. https://doi.org/10.1364/ AO. 48.004814

Gunson, M.R., Abbas, M.M., Abrams, M.C., Allen, M., Brown, L.R., Brown, T.L., Chang, A.Y., Goldman, A., Irion, F.W., Lowes, L.L. and Mahieu, E., 1996. The Atmospheric Trace Molecule Spectroscopy (ATMOS) experiment: Deployment on the ATLAS space shuttle missions. *Geophysical Research Letters, 23*(17), pp.2333-2336.. https://doi.org/10.1029/96GL01569

Hervig, M.E., Gordley, L.L., Russell III, J.M. and Bailey, S.M., 2009. SOFIE PMC observations during the northern summer of 2007. *Journal of atmospheric and solar-terrestrial physics, 71(*3-4), pp.331-339.doi:10.1016/j.jastp.2008.08.010.

Hervig, M.E., Gordley, L.L., Stevens, M.H., Russell III, J.M., Bailey, S.M. and Baumgarten, G., 2009. Interpretation of SOFIE PMC measurements: Cloud identification and derivation of mass density, particle shape, and particle size. *Journal of atmospheric and solar-terrestrial physics, 71(*3-4), pp.316-330.doi:10.1016/j.jastp.2008.07.009

Hervig, M.E., Berger, U. and Siskind, D.E., 2016. Decadal variability in PMCs and implications for changing temperature and water vapor in the upper mesosphere. *Journal of Geophysical Research: Atmospheres, 121*(5), pp.2383-2392.doi:10.1002/2015JD024439

Hervig, M.E., Bardeen, C.G., Siskind, D.E., Mills, M.J. and Stockwell, R., 2017. Meteoric smoke and H2SO4 aerosols in the upper stratosphere and mesosphere. *Geophysical Research Letters*, *44*(2), pp.1150-1157.doi:10.1002/2016GL072049

Hervig, M.E., Brooke, J.S., Feng, W., Bardeen, C.G. and Plane, J.M., 2017. Constraints on meteoric smoke composition and meteoric influx using SOFIE observations with models. *Journal of Geophysical Research: Atmospheres, 122*(24), pp.13-495.doi:10.1002/2017JD027657

Hervig, M.E., Plane, J.M., Siskind, D.E., Feng, W., Bardeen, C.G. and Bailey, S.M., 2021. New global meteoric smoke observations from SOFIE: insight regarding chemical composition, meteoric influx, and hemispheric asymmetry. *Journal of Geophysical Research: Atmospheres, 126(*13), p.e2021JD035007. https://doi. org/10.1029/2021JD035007

Imai, K., Manago, N., Mitsuda, C., Naito, Y., Nishimoto, E., Sakazaki, T., Fujiwara, M., Froidevaux, L., von Clarmann, T., Stiller, G.P. and Murtagh, D.P., 2013. Validation of ozone data from the Superconducting Submillimeter-Wave Limb-Emission Sounder (SMILES). *Journal of Geophysical Research: Atmospheres, 118*(11), pp.5750-5769. https://doi.org/10.1002/jgrd.50434

Kerzenmacher, T.E., Walker, K.A., Strong, K., Berman, R., Bernath, P.F., Boone, C.D., Drummond, J.R., Fast, H., Fraser, A., MacQuarrie, K. and Midwinter, C., 2005. Measurements

of O3, NO2 and temperature during the 2004 Canadian Arctic ACE Validation Campaign. *Geophysical Research Letters, 32*(16).https://doi.org/10.1029/2005GL023032

Kikuchi, K.I., Nishibori, T., Ochiai, S., Ozeki, H., Irimajiri, Y., Kasai, Y., Koike, M., Manabe, T., Mizukoshi, K., Murayama, Y. and Nagahama, T., 2010. Overview and early results of the superconducting Submillimeter-Wave Limb-Emission Sounder (SMILES). *Journal of Geophysical Research: Atmospheres, 115*(D23).DOI: 10.1029/2010jd014379

Laeng, A., Grabowski, U., Von Clarmann, T., Stiller, G., Glatthor, N., Höpfner, M., Kellmann, S., Kiefer, M., Linden, A., Lossow, S. and Sofieva, V., 2014. Validation of MIPAS IMK/IAA V5R_O3_224 ozone profiles. *Atmospheric Measurement Techniques, 7*(11), pp.3971-3987.https://doi.org/10.5194/amt-7-3971-2014.

Laeng, A., Eckert, E., von Clarmann, T., Kiefer, M., Hubert, D., Stiller, G., Glatthor, N., López-Puertas, M., Funke, B., Grabowski, U. and Plieninger, J., 2018. On the improved stability of the version 7 MIPAS ozone record. *Atmospheric Measurement Techniques, 11*(8), pp.4693-4705. https://doi.org/10.5194/amt-11-4693-2018

Llewellyn, E.J., McDade, I.C., Moorhouse, P. and Lockerbie, M.D., 1993. Possible reference models for atomic oxygen in the terrestrial atmosphere. *Advances in Space Research, 13*(1), pp.135-144.https://doi.org/10.1016/0273-1177(93)90013-2

Llewellyn, E.J. and McDade, I.C., 1996. A reference model for atomic oxygen in the terrestrial atmosphere. *Advances in Space Research, 18*(9-10), pp.209-226. https://doi.org/10.1016/0273-1177(96)00059-2

López-Puertas, M., García-Comas, M., Funke, B., Gardini, A., Stiller, G.P., von Clarmann, T., Glatthor, N., Laeng, A., Kaufmann, M., Sofieva, V.F. and Froidevaux, L., 2018. MIPAS observations of ozone in the middle atmosphere. *Atmospheric Measurement Techniques, 11*(4), pp.2187-2212.doi:10.5194/amt-11-2187-2018

Lucke, R.L., Korwan, D.R., Bevilacqua, R.M., Hornstein, J.S., Shettle, E.P., Chen, D.T., Daehler, M., Lumpe, J.D., Fromm, M.D., Debrestian, D. and Neff, B., 1999. The Polar Ozone and Aerosol Measurement (POAM) III instrument and early validation results. *Journal of Geophysical Research: Atmospheres, 104(*D15), pp.18785-18799.DOI:10.1029/2005JD006763

Marshall, B.T., Deaver, L.E., Thompson, R.E., Gordley, L.L., McHugh, M.J., Hervig, M.E. and Russell III, J.M., 2011. Retrieval of temperature and pressure using broadband solar occultation: SOFIE approach and results. *Atmospheric Measurement Techniques, 4*(5), pp.893-907.doi:10.5194/amtd-3-5743-2010

Mauldin Iii, L.E., Zaun, N.H., McCormick Jr, M.P., Guy, J.H. and Vaughn, W.R., 1985. Stratospheric Aerosol and Gas Experiment II instrument: A functional description. *Optical Engineering, 24*(2), pp.307-312. https://doi.org/10.1117/12.7973473

McCormick, M.P., 1987. SAGE II: an overview. *Advances in space research, 7(*3), pp.219-226. https://doi.org/10.1016/0273-1177(87)90151-7

McHugh, M., Magill, B., Walker, K.A., Boone, C.D., Bernath, P.F. and Russell III, J.M., 2005. Comparison of atmospheric retrievals from ACE and HALOE. *Geophysical Research Letters, 32*(15).https://doi.org/10.1029/2005GL022403

Mitsuda, C., Suzuki, M., Iwata, Y., Manago, N., Naito, Y., Takahashi, C., Imai, K., Nishimoto, E., Hayashi, H., Shiotani, M. and Sano, T., 2011, October. Current status of level 2 product of Superconducting Submillimeter-Wave Limb-Emission Sounder (SMILES). In *Sensors, Systems, and Next-Generation Satellites XV* (Vol. 8176, pp. 177-182). SPIE.DOI:10.1117/12.898135

Perliski, L.M., Solomon, S. and London, J., 1989. On the interpretation of seasonal variations of stratospheric ozone. *Planetary and Space Science, 37*(12), pp.1527-1538.https://doi.org/10.1016/0032-0633(89)90143-8

Petelina, S.V., Llewellyn, E.J., Walker, K.A., Degenstein, D.A., Boone, C.D., Bernath, P.F., Haley, C.S., Von Savigny, C., Lloyd, N.D. and Gattinger, R.L., 2005. Validation of ACE-FTS stratospheric ozone profiles against Odin/OSIRIS measurements. *Geophysical research letters, 32*(15).https://doi.org/10.1029/2005GL022377

Russell III, J.M. and Drayson, S.R., 1972. The inference of atmospheric ozone using satellite horizon measurements in the 1042 cm− 1 band. Journal of Atmospheric Sciences, 29(2), pp.376-390. https://doi.org/10.1175/1520-0469(1972)029<0376:TIOAOU>2.0.CO;2

Russell III, J.M., Gordley, L.L., Park, J.H., Drayson, S.R., Hesketh, W.D., Cicerone, R.J., Tuck, A.F., Frederick, J.E., Harries, J.E. and Crutzen, P.J., 1993. The halogen occultation experiment. *Journal of Geophysical Research: Atmospheres, 98*(D6), pp.10777-10797.DOI: 10.1029/93JD00799

Russell III, J.M., Mlynczak, M.G., Gordley, L.L., Tansock Jr, J.J. and Esplin, R.W., 1999, October. Overview of the SABER experiment and preliminary calibration results. In *Optical spectroscopic techniques and instrumentation for atmospheric and space research III* (Vol. 3756, pp. 277-288). SPIE. https://doi.org/10.1117/12.366382

Russell III, J.M., Bailey, S.M., Gordley, L.L., Rusch, D.W., Horányi, M., Hervig, M.E., Thomas, G.E., Randall, C.E., Siskind, D.E., Stevens, M.H. and Summers, M.E., 2009. The Aeronomy of Ice in the Mesosphere (AIM) mission: Overview and early science results. *Journal of Atmospheric and Solar-Terrestrial Physics, 71*(3-4), pp.289-299. doi: 10.1016/j.jastp.2008.08.011

Serdyuchenko, A., Gorshelev, V., Weber, M., Chehade, W. and Burrows, J.P., 2014. High spectral resolution ozone absorption cross-sections–Part 2: Temperature dependence. *Atmospheric Measurement Techniques, 7*(2), pp.625-636.https://doi.org/10.5194/amt-7-625-2014

Smith, A.K. and Marsh, D.R., 2005. Processes that account for the ozone maximum at the mesopause. *Journal of Geophysical Research: Atmospheres, 110* (D23). https://doi.org/10.1029/2005JD006298

Smith, A.K., Marsh, D.R., Russell III, J.M., Mlynczak, M.G., Martin-Torres, F.J. and Kyrölä, E., 2008. Satellite observations of high nighttime ozone at the equatorial mesopause. Journal of Geophysical Research: Atmospheres, 13(D17).https://doi.org/10.1029/2008JD010066

Smith, A.K., López-Puertas, M., García-Comas, M. and Tukiainen, S., 2009. SABER observations of mesospheric ozone during NH late winter 2002–2009. *Geophysical Research Letters, 36*(23).https://doi.org/10.1029/2009GL040942

Smith, A.K., Marsh, D.R., Mlynczak, M.G., Russell, J.M. and Mast, J.C., 2011. SABER observations of daytime atomic oxygen and ozone variability in the mesosphere. In *Aeronomy of the Earth's Atmosphere and Ionosphere* (pp. 75-82). Springer, Dordrecht. DOI: 10.1007/978-94-007-0326-1_5

Smith, A.K., Harvey, V.L., Mlynczak, M.G., Funke, B., García-Comas, M., Hervig, M., Kaufmann, M., Kyrölä, E., López-Puertas, M., McDade, I. and Randall, C.E., 2013. Satellite observations of ozone in the upper mesosphere. *Journal of Geophysical Research: Atmospheres, 118*(11), pp.5803-5821. https://doi.org/10.1002/jgrd.50445

Solomon, S., Garcia, R.R. and Stordal, F., 1985. Transport processes and ozone perturbations. *Journal of Geophysical Research: Atmospheres, 90*(D7), pp.12981-12989.https://doi.org/10.1029/JD090iD07p12981

Steck, T., Von Clarmann, T., Fischer, H., Funke, B., Glatthor, N., Grabowski, U., Höpfner, M., Kellmann, S., Kiefer, M., Linden, A. and Milz, M., 2007. Bias determination and precision validation of ozone profiles from MIPAS-Envisat retrieved with the IMK-IAA processor. *Atmospheric chemistry and physics, 7*(13), pp.3639-3662.https://doi.org/10.5194/acp-7-3639-2007

Stiller, G.P., Kiefer, M., Eckert, E., Von Clarmann, T., Kellmann, S., García-Comas, M., Funke, B., Leblanc, T., Fetzer, E., Froidevaux, L. and Gomez, M., 2012. Validation of MIPAS IMK/IAA temperature, water vapor, and ozone profiles with MOHAVE-2009 campaign measurements. *Atmospheric Measurement Techniques, 5*(2), pp.289-320. doi:10.5194/amt-5-289-2012

Stolarski, R.S., Bloomfield, P., McPeters, R.D. and Herman, J.R., 1991. Total ozone trends deduced from Nimbus 7 TOMS data. *Geophysical Research Letters, 18*(6), pp.1015-1018. https://doi.org/10.1029/91GL01302

Stolarski, R., Bojkov, R., Bishop, L., Zerefos, C., Staehelin, J. and Zawodny, J., 1992. *Measured trends in stratospheric ozone. Science, 256*(5055), pp.342-349.DOI: 10.1126/science.256.5055.342

Takahashi, C., Suzuki, M., Mitsuda, C., Ochiai, S., Manago, N., Hayashi, H., Iwata, Y., Imai, K., Sano, T., Takayanagi, M. and Shiotani, M., 2011. Capability for ozone high-precision retrieval on JEM/SMILES observation. *Advances in space research, 48*(6), pp.1076-1085.DOI: 10.1016/j.asr.2011.04.038

Tweedy, O.V., Limpasuvan, V., Orsolini, Y.J., Smith, A.K., Garcia, R.R., Kinnison, D., Randall, C.E., Kvissel, O.K., Stordal, F., Harvey, V.L. and Chandran, A., 2013. Nighttime secondary ozone layer during major stratospheric sudden warmings in specified-dynamics WACCM. *Journal of Geophysical Research: Atmospheres, 118*(15), pp.8346-8358.https://doi.org/10.1002/jgrd.50651

Von Clarmann, T., 2006. Validation of remotely sensed profiles of atmospheric state variables: strategies and terminology. *Atmospheric Chemistry and Physics, 6(*12), pp.4311-4320.https://doi.org/10.5194/acp-6-4311-2006

Clarmann, T.V., De Clercq, C., Ridolfi, M., Hoepfner, M. and Lambert, J.C., 2009. The horizontal resolution of MIPAS. *Atmospheric measurement techniques, 2*(1), p.47.DOI: 10.5445/IR/1000041684

Walker, K.A., Randall, C.E., Trepte, C.R., Boone, C.D. and Bernath, P.F., 2005. Initial validation comparisons for the Atmospheric Chemistry Experiment (ACE-FTS). *Geophysical research letters, 32*(16).https://doi.org/10.1029/2005GL022388

3. Atomic Oxygen in the Mesopause Region Using SOFIE Measurements

Das, Saswati, et al. "Atomic Oxygen in the Mesopause Region Using SOFIE Measurements." *Journal of Geophysical Research-Atmospheres (Scheduled for Submission in October 2022)*

3.1 Abstract

Atomic oxygen (O) is critical to the chemistry of the mesopause region (~ 80 - 100 km). It has a strong influence on the energy budget and photochemistry of this region. We present inferred O concentrations from SOFIE (Solar Occultation for Ice Experiment) observations. SOFIE makes sunrise and sunset solar occultation measurements, typically at high latitudes through all seasons of the year and in both hemispheres. O is derived for years 2008 to 2014 from SOFIE's ozone (O_3) product measured at 0.291 μm. We compare the seven-year SOFIE derived O to coincident profiles from the Sounding of the Atmosphere using Broadband Emission Radiometry (SABER) instrument and the Naval Research Laboratory Mass Spectrometer and Incoherent Scatter Radar (NRLMSIS) 2.0 model. Our results show that SOFIE agrees qualitatively with SABER above ~ 85 km and has excellent agreement with the NRLMSIS 2.0 model throughout the mesopause region. We address uncertainties and disagreements between the datasets due to systematic and random errors in individual datasets, sampling differences, and the O derivation algorithm. Further, we investigate the transport of O to altitudes below the mesopause during the winter. This study demonstrates the utility of SOFIE-derived O in filling existing knowledge gaps from satellite measurements and furthering our understanding of O in mesopause chemistry.

3.2 Plain Language Summary

Atomic oxygen (O) is an important species in the mesopause (~ 80 – 100 km) due to its role in the chemistry and energy budget of this region. The existing O measurements are limited in time and space due to the complexities in making direct measurements of O. Derived O measurements from

satellite instruments are thus the most conventional recourse. The inclusion of novel satellite-derived O measurements in the existing O database is important to this end. The Solar Occultation for Ice Experiment (SOFIE) instrument measures the solar energy passing through the limb of the Earth's atmosphere, typically at high latitudes between 65^{o}-85^{o} N/S. SOFIE O_3 retrievals are used to derive O profiles. These profiles are compared to the data from the Sounding of the Atmosphere using Broadband Emission Radiometry (SABER) instrument and the Naval Research Laboratory Mass Spectrometer and Incoherent Scatter Radar (NRLMSIS) 2.0 model. SOFIE derived O data agrees well with that of SABER and the NRLMSIS 2.0 model. SOFIE derived O data capture the seasonal and latitudinal variation in O.

3.3 Introduction

Atomic oxygen (O) is the most abundant reactive trace species in the mesosphere and lower thermosphere (MLT). Its concentration and lifetime vary with increasing altitude. O has a lifetime of several seconds at ~ 50 km but has a long lifetime that spans several months at ~ 100 km. Due to its long lifetime in the mesopause region (~ 80 – 100 km), its seasonal and latitudinal variation result from diffusion, mean circulation, and transport through waves. Other important effects in this region are due to photochemical production and loss. O plays a vital role in the photochemistry of the mesosphere-lower thermosphere (MLT) and is generated by the photolysis of molecular oxygen (O_2) by ultraviolet radiation. Despite its crucial role in the chemical aeronomy (*Mlynczak and Solomon*, 1993; *Mlynczak et al.*, 2013(b)) of the mesopause region, the determination of O concentration at these altitudes is limited, with several inaccuracies (*Siskind and Sharp.*, 1990).

Before the coming of the modern satellite era, O was measured in situ by suborbital rockets through airglow (*Good*, 1976), resonance lamp techniques (*Dickinson et al.*, 1974, 1980), and a combination of both methods (*Ulwick et al.*, 1987). In situ measurements involved measurement-

related challenges associated with the knowledge of mechanisms and rates of the airglow, optical contamination, and shock effects induced by rockets carrying the payloads (*Siskind and Sharp.,* 1990; *Patterson,* 2005). O measurement region through remote sensing techniques at the mesopause is difficult as O makes very few optically active transitions with no vibration and rotation spectra. It emits an optically thick line centered at 63 μm which has been measured in a very limited capacity by space-borne instruments (*Grossmann and Vollmann,* 1997; *Grossmann et al.,* 2000; *Mlynczak et al.,* 2004). It also displays an optically thin line centered at 145 μm which generally requires compound technology. *Ritcher et al.,* (2021) reported direct O measurements in the MLT using the German Receiver for Astronomy at Terahertz Frequencies (GREAT) (*Heyminck et al.,* 2012) instrument onboard the Stratospheric Observatory for Infrared Astronomy (SOFIA) (*Ennico et al*., 2018). SOFIA operates on a modified Boeing 747SP aircraft, limiting continuous spatial and temporal coverage. Typically, indirect methods such as derived measurements from satellite instruments and photochemical models are the most conventional recourse to understanding O in the MLT due to the technical complexity involved with making direct O measurements.

Satellite-derived measurements of nighttime mesospheric O use radiative emissions from the Meinel bands of the hydroxyl (OH) molecule (*Good.,* 1976, *Marsh et al.,* 2006, *Xu et al.,* 2012, *Mlynczak et al.,* 2013(b), *Zhu and Kaufmann,* 2018). *Smith et al*. (2010) used daytime SABER O_3 and measurements to derive O. In the past, day and nighttime O measurements from the Sounding of the Atmosphere using Broadband Emission Radiometry (SABER) instrument (*Russell et al.,* 1999) on the Thermosphere-Ionosphere-Mesosphere Energetics and Dynamics (TIMED) satellite have been reported by several studies (*Marsh et al.,* 2006, *Smith et al.,* 2010, 2013; *Xu et al.,* 2012, *Mlynczak et al.,* 2013(b), 2013(c)). TIMED orbit precesses 180^o in its 60-day yaw period, during

which SABER observations extend close to the pole in one hemisphere and up to ~ 53^{o} in the other. This prevents SABER from looking at high latitudes continuously.

At high latitudes, O mixing ratios are abundant at altitudes as low as 84 km. This is possibly associated with the gravity wave-driven wintertime downwelling circulation (Smith et al., *2010*). *Manney et al.,* (2005, 2008, 2009) and *Siskind et al.,* (2007) noted the unusual circulation and middle atmospheric structure during the latter part of 2004, 2006, and 2009 Northern Hemisphere (NH) winters. These dynamical evolutions during late January and February are attributed to the perturbations that occurred in the recovery phase of Sudden Stratospheric Warmings (SSWs) (*Manney et al.,* 2005, 2008, 2009). *Smith et al.,* (2010) used SABER data and reported that in the NH, the atomic oxygen was particularly high during 2004, 2006, and 2009 from mid-January to mid-March. During these years, the observed downward transport of O is consistent with the transport of other trace gases such as Nitric Oxide (NO), Water vapor (H_2O), and Methane (CH_4) (*Randall et al.,* 2005, 2006, 2009; *Hauchecorne et al.,* 2007; *Jin et al.,* 2005; *Funke et al.,* 2009; *Smith et al.,* 2009). Thus, at high latitudes, the chemistry and dynamics vary strongly during SSWs. The role of O during these times is important to the chemistry of the mesopause region and warrants continuous high latitude measurements, alongside the need to expand the existing O database.

In this study, we use O_3 and temperature measurements from the Solar Occultation for Ice Experiment (SOFIE) (*Gordley et al.,* 2009) instrument on the Aeronomy of Ice in the Mesosphere (AIM) satellite to derive daytime O as described in Section 3.6. We compare our results of derived O measurements from SOFIE to coincident profiles from SABER and the NRLMSISE 2.0 (US Naval Research Laboratory Mass Spectrometer and Incoherent Scatter Radar) model in Section 3.7.1. We analyze the altitudes where the data sets show qualitative agreement and evaluate the

organized differences resulting from the differences in the measuring techniques, sampling, and other factors. We address these discrepancies and uncertainties between the data sets. With the established robustness of SOFIE O, we evaluate its seasonal and latitudinal variation in both hemispheres in Section 3.7.2, and 3.7.3, respectively.

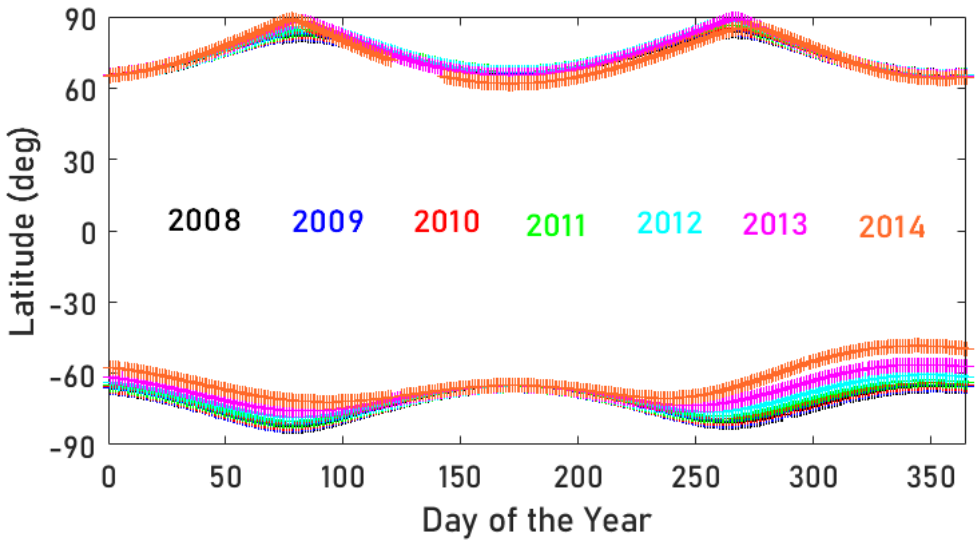

Figure 12. SOFIE latitude coverages over the years 2008 – 2014.

3.4 Correlative Data Sets

3.4.1 SOFIE

SOFIE measures through solar occultation since May 2007 at 16 spectral bands. These measurements are used in the retrieval of temperature, ozone, water vapor, carbon dioxide, methane, nitric oxide, PMC extinction, and meteoric smoke at 0.29 and 5.26 μm wavelengths (*Gordley et al.*, 2009). SOFIE makes 15 measurements each at sunrise and sunset daily. SOFIE's long optical path length (~ 300 km), in combination with the bright solar source and a precise electro-optical system, provides highly sensitive measurements. SOFIE has a high vertical resolution of ~ 1.6 km, and the high precision allows retrievals on the over-sampled 200 m vertical

grid. SOFIE typically measures at high latitudes, between 65°-85° in both hemispheres. Figure 12 shows the latitudes observed by SOFIE from 2008 to 2014. From 2007 to 2017, spacecraft sunsets occurred in the Southern Hemisphere (SH) and sunrises in the NH. This changed in late 2018, with sunsets switching to the NH. In this study, we used SOFIE V1.3 data for O_3 and temperature. *Steven et al.* (2012) validated SOFIE temperature measurements in the upper MLT, and *Smith et al.* (2013) used SOFIE O_3 measurements to compare SABER O_3 in the upper mesosphere. For this study, we use both the NH and SH data from 1 January 2008 through 31 December 2014. Although SOFIE data are available from 2015 to 2017 in both hemispheres, SOFIE views latitudes equatorward of 65° N/S. To be consistent in the use of high latitude measurements, we exclude these years from our analysis.

3.4.2 SABER

SABER began acquiring scientific data in January 2002 to explore the MLT globally from 60 km to 180 km. The TIMED satellited precesses over a 60–65-day yaw period and has data available at almost all local times. SABER O_3 is independently retrieved from two channels measuring different radiances at 9.6 μm (Day/Night measurements) and 1.27 μm (Daytime). In this study, we use the SABER daytime O data product provided by the SABER data team (Smith et al., 2010). This O data was derived by the SABER team using Version 2.0 O_3 retrieved at 9.6 μm. SABER O_3 retrieval uses temperature (*Remsberg et al.,* 2008) and pressure derived from SABER observations. *Rong et al.,* (2009) validated the 9.6 μm O_3 from SABER in the stratosphere and mesosphere (15 - 70 km), and it was used by *Smith et al.,* (2013) to study O_3 in the upper mesosphere. SABER years used in this study are from 2008 to 2014. We derive the SOFIE O from the SOFIE O_3 product using the approach described in *Smith et al.* (2010), discussed in Section 3.6.

3.4.3 NRLMSIS 2.0

Naval Research Laboratory Mass Spectrometer Incoherent Scatter Rada (NRLMSIS-class) empirical models of temperature, composition, and total mass density have been used frequently to describe the upper atmosphere (mesosphere and thermosphere). The NRLMSIS-86 (*Hedin.*,1987) altitude range was upward of 90 km, and NRLMSISE-90 (*Hedin.*, 1991) altitude ranged from the ground to the exobase. The 'E' in NRLMSISE indicates that the model extends through the exosphere from the ground. The NRLMSISE-00 model (*Picone et al.*, 2002) was developed in the late 1990s to upgrade NRLMSISE-90 and focused on the thermosphere with the noteworthy addition of orbital decay data in the NRLMSIS database. The NRLMSISE-00 model incorporated updated temperature measurements and molecular oxygen number density and was extensive in size, spatial range, and time periods. However, one of the inherent limitations of this model was the lack of satellite data to define the composition and structure of the atmosphere under 100 km. An upgrade to this model is the NRLMSIS 2.0 model (*Emmert et al.*, 2020), which includes measurements from many satellite instruments. The model assimilates new measurements and analyses since 2000 for temperature from the troposphere to the mesosphere, O, and atomic hydrogen, among other major changes.

In the MLT, the sensitivity of O to photochemical production and loss, and dynamic transport and diffusion (*Jones et al.*, 2014, 2017; *Smith et al.*, 2010; *Swenson et al.*, 2019) make O distribution very different over a broad range of spatiotemporal scales. Although the NRLMSISE-00 model provided an accurate representation of O using mass spectrometer data, it did not include satellite measurements of O in the MLT. The NRLMSIS 2.0 model includes several rocket profiles to extrapolate the O profiles into the middle atmosphere for estimating O peak values more accurately in the MLT. This model also incorporates SABER and Odin/OSIRIS (Optical Spectrograph and

InfraRed Imager System (*Sheese et al.*, 2011) O data within the MLT region and provides a smoother representation of O data from 50 km through the upper atmosphere. *Emmert et al.* (2020) documented significant differences between NRLMSISE-00 and the incorporated newer data sets. The authors noted the improvement in mesospheric O density predictions compared to NRLMSISE-00, particularly demonstrating a transition from a winter maximum in the upper thermosphere to a summer maximum in the upper mesosphere at mid-latitudes.

3.5 Coincident Profile Calculation

SABER observes multiple latitudes in a single day with coverage ranging from 54°S to 82°N or 82°S to 54°N depending on TIMED's 60-day yaw cycle. In contrast, SOFIE measured only high latitudes from 2008-2014. In Figure 13, SOFIE and SABER latitudes poleward of 60^{o} N/S are plotted against the day of the year from 2008 to 2014.

SOFIE measures a limited range of local time due to its solar occultation technique. SABER operates on a precessing satellite and views a wide range of local times (day/night measurements). Figure 14 shows the distribution of SOFIE and SABER local times against latitude from 2008 to 2014. The yearly distribution of SABER (blue) is over a wide range of local times and latitudes, while SOFIE (red) measures at limited local times and latitudes. The difference in measuring latitudes and local times between SOFIE and SABER results in limited coincidences between the two instruments. Thus, the coincidence criteria are 600 km in horizontal distance and 3 hours in universal time. The geodesic distance is calculated using the latitude and longitude of SOFIE and SABER profiles. The results are discussed in Section 3.7.

Figure 15 shows the number of coincidences between SOFIE and SABER from 2008 to 2014 in both hemispheres indicating higher coincidences in the NH than the SH. The number of coincidences in the NH varies with a minimum of 610 in 2008 and a maximum of 1379 in 2013.

In the SH, the number of coincidences is less than 100 for 2014. In other years, the number of coincidences is between 200 and 400.

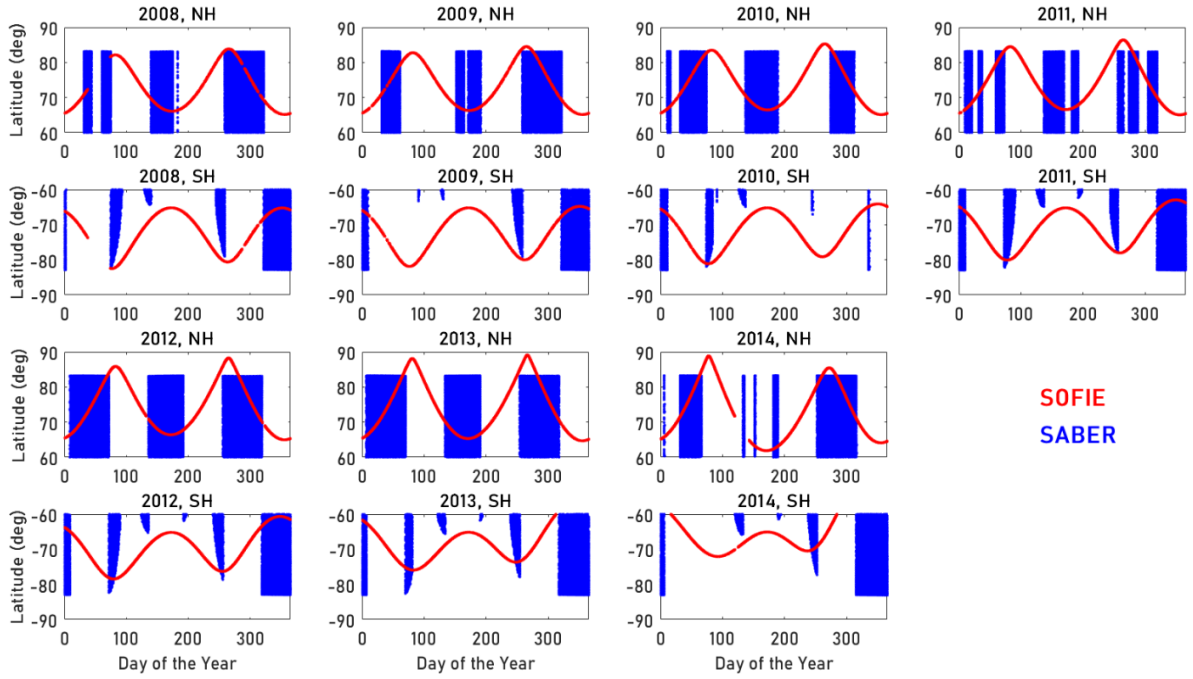

Figure 13. SOFIE and SABER latitude time series for 60º- 90º in both hemispheres for 2008-2014. The blue and red markers indicate SABER and SOFIE distributions, respectively.

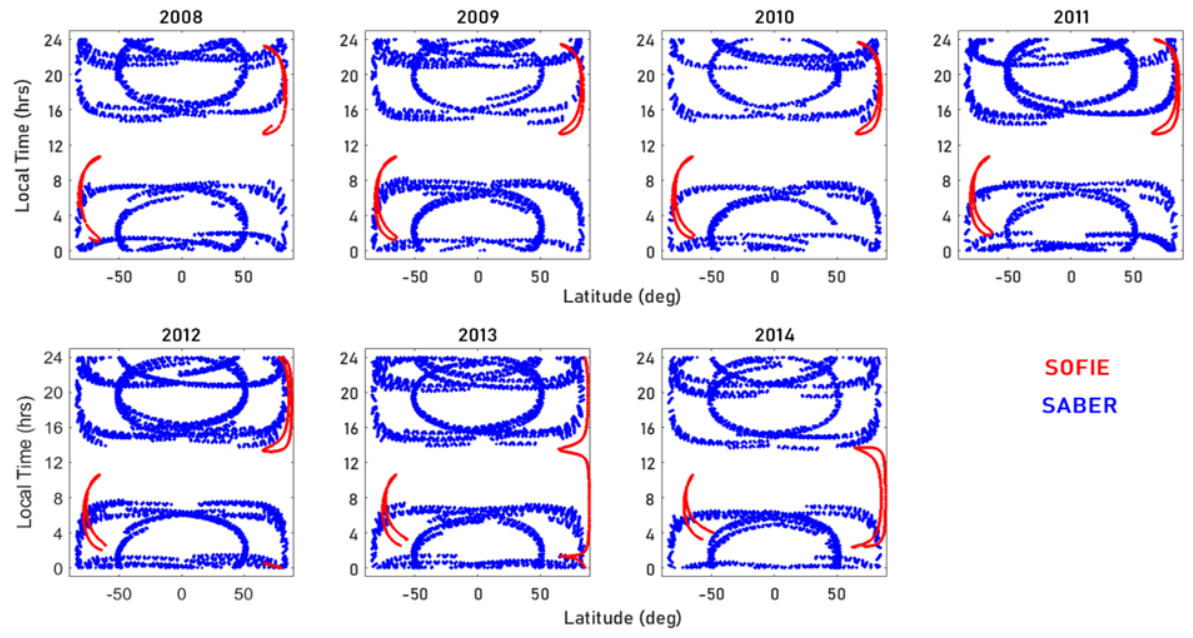

Figure 14. Latitude VS Local Time from SOFIE and SABER for both hemispheres during 2008-2014.The blue and red markers indicate SABER and SOFIE distributions, respectively.

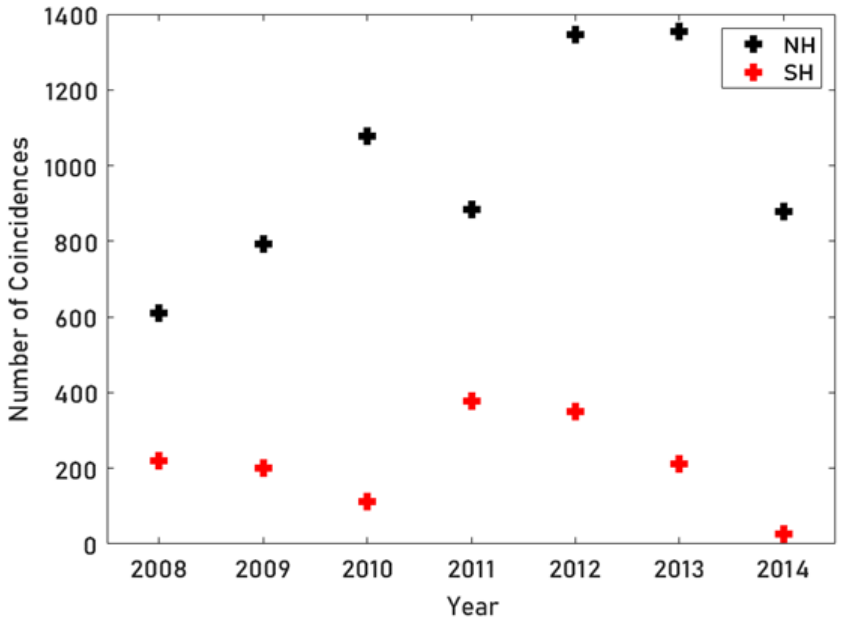

Figure 15. Number of SOFIE and SABER coincident profiles poleward of 60° N/S from 2008 to 2014.

3.6 Determination of Atomic Oxygen and Uncertainties

We use the following method described by *Smith et al.,* (2010) to determine O from SOFIE O_3. First, photochemical equilibrium is assumed (*McDade et al.,* 1985; *Evans et al.,* 1988; *Llewellyn et al.,* 1993; *Llewellyn and McDade,* 1996; *Mlynczak et al.,* 2007). The daytime production and loss formulation as provided by the Chapman mechanism (*Chapman.,* 1930) are then used to derive O in the mesopause. The production and loss of O_3 are determined using equations 1 and 2.

$$O + O_2 + M \rightarrow O_3 + M \quad (1)$$

$$O_3 + hv \rightarrow O + O_2 \quad (2)$$

Due to the photochemical equilibrium between O and O_3 (*Smith and Marsh* 2005), the daytime O_3 is given by

$$O_3 = \frac{\left[k_{o-o_2} * O * O_2.n^2\right]}{J_{O_3}} \quad (3)$$

where O, O_2, and O_3 are the mixing ratios, T is the temperature, and $k_{O\text{-}O2} = 6\times10^{-34}(300/T)^{2.4}$) is the *reaction rate* of the reaction (*Sander et al.,* 2006), J_{O3} is the photolysis rate of O_3 calculated from the TUV (Tropospheric Ultraviolet-Visible) model (*Madronich and Flocke,* 1998). The O_3 photolysis rate is nearly constant because there is very little O_3 above the mesosphere and thus, the atmosphere is optically thin at the ultraviolet wavelengths that are important (*Smith et al.*, 2010). The atmospheric number density, n is calculated using the ideal gas law. The gradient of the O_2 mixing ratio is weak in the mesosphere, and O_2 contribution to O variability is minor. Thus, the O_2 mixing ratio is set to 0.2. O number density is, therefore

$$O_{Daytime} = \left[J_{O_3} * O_3\right] / \left[k_{o-o_2} * O_2.n^2\right] \quad (4)$$

The errors in O estimation are dependent on several factors. SABER O derivations assume the steady-state chemistry of O_3, which indicates that the production and loss rates cancel each other (*Smith et al.,* 2011). The time derivation of O_3 is given by,

$$\frac{d(O_3)}{dt} = 0 = P - L * O_3 \quad (5)$$

where $P = Production\ rate, L = Loss\ rate.$

This equation is not a source of error in itself but makes a difference depending on what is used for P and L. Here, $P = k_{o-o_2} * (O * O_2 * M)$ and $L = J_{O_3}$.

While the production term is accurate, the O_3 loss term is not perfect as it neglects the reactions beyond O_3 photolysis as sources of destruction. Although photolysis is the primary source of O_3 destruction during the day, other reactions that contribute are as below.

$$O_3 + H = O_2 + O * H \quad (6)$$

$$O_3 + O = 2O_2 \quad (7)$$

The omission of equation 6 underestimates the total O, and that of equation 7 introduces non-linearity (mostly above ~ 90 km). However, the regions that show significant differences (in terms of vmr) between the two instruments are typically below ~ 85 km (discussed later) and are potentially uninfluenced by the omission of equation 7. Other sources of error include those due to J_{O_3} and k_{o-o_2} in equation 4, which is temperature-dependent. k_{o-o_2} decreases with increasing temperature and the number density on a pressure surface is inversely proportional to temperature.

Since the process to derive SOFIE O is as described for SABER by *Smith et al.* (2010), we infer that the strongest source of differences between the two datasets is introduced potentially from individual O_3 profiles compared to other sources.

3.7 Results

3.7.1 Comparison of SOFIE-O using coincident profiles

The aim of this study is to compare O in the mesopause from SOFIE to other datasets and explain the major differences. These differences can occur due to a) systematic and random differences between coincident retrieved profiles, including those from retrieval assumptions, and b) differences in the sampling method of each data set. The sampling difference between SOFIE and SABER is primarily driven by SABER's yaw cycle that impacts the viewing latitude, the difference in calendar days, and the measuring techniques (solar occultation vs. precessing) that result in observations at different local times.

SABER has been used in past studies to investigate the diurnal, spatiotemporal, and seasonal variation (*Smith et al.,* 2010, 2011; *Mlynczak et al.,* 2013(c)) of O in the day and night times.

Typically, O_3 and OH (hydroxyl) emission observations are used to derive O during day and night, respectively (*Marsh et al.*, 2006; *Smith et al.*, 2010; *Xu et al*., 2012). In this study, we use coincident profiles from SABER from 2008 to 2014 to compare with SOFIE O calculated using the method described in Section 3.6. We use the NRLMSIS 2.0 model to generate the O profiles at SOFIE parameters (i.e., latitude, longitude, and time).

We compare the SOFIE, SABER, and NRLMSIS 2.0 profiles in terms of volume mixing ratio (VMR) and number density (#/cm^3). While the O_3 data that SABER and SOFIE use for deriving O are reported in vmr (the preferred quantity by the atmospheric science community), the actual O_3 retrievals are done in terms of number density. The comparison of number density profiles in a practical sense is less feasible as it changes by orders of magnitude with altitude. For SOFIE and SABER, O vmr values can be converted to number density using the atmospheric background number density. For NRLMSIS 2.0, O data is made available in terms of number density but is converted to vmr for comparison with SOFIE. In the following comparisons, we emphasize mixing ratio comparisons but also show results in terms of number density.

Figure 16 and Figure 17 show the annual mean O for SOFIE, SABER, and NRLMSIS 2.0 mixing ratios (vmr) in the top panels and the mean number density profiles in the bottom panels for the NH and SH, respectively. The error bars indicate the uncertainty in the O_3 values. In Figure 16 (top panels), the vmr profiles suggest excellent agreement between SOFIE and the other data sets. In all years, all three instruments' profiles closely overlap each other at most altitudes, except in 2009, where SOFIE agrees well with SABER at all altitudes, but the NRLMSIS 2.0 profile digresses below ~ 88 km. The NRLMSIS 2.0 profiles typically strongly overlap with SABER above ~ 90 km, attributed to the incorporation of SABER O data into the NRLMSIS 2.0 model. SOFIE agrees very well with NRLMSIS 2.0 O at altitudes below ~ 95 km but is occasionally

lower between 95 and 100 km in some years. The lower panels representing the number density profiles indicate that a similar trend in O variation between the SOFIE and other data sets is also observed in terms of number density. In most cases, SOFIE values agree very well with NRLMSIS 2.0 under ~ 95 km and are lower than both NRLMSIS 2.0 and SABER measurements above this altitude, except in 2014, where there is excellent agreement between SOFIE and the other data sets above ~ 85 km. NRLMSIS 2.0 and SABER have very good agreement above ~ 90 km, typically. In 2009, the NRLMSIS 2.0 number density profile, like the vmr profile, digresses from SOFIE and SABER (that are in excellent agreement with each other). In 2014, SOFIE number density values are lesser than NRLMSIS 2.0 and SABER between 80 and ~ 83 km. Overall, in the NH, there is a very good agreement between the three data sets where SOFIE has great vmr agreement with SABER at almost all altitudes and with NRLMSIS 2.0 below ~ 95 km. In terms of number density, SOFIE typically agrees well with NRLMSIS 2.0 below ~ 95 km and better with SABER below ~ 90 km than above it.

In Figure 17 (top panels), the vmr profiles suggest that the agreement between SOFIE and NRLMSIS 2.0 is typically very good between ~ 83 and 95 km. 2014 is the only exception to this, where SOFIE indicates better agreement with NRLMSIS 2.0 and SABER above ~ 92 km. Like the NH, in the SH, SABER profiles coincide with NRLMSIS 2.0 at high altitudes, particularly above ~ 92 km, where SOFIE measurements are lower than SABER and NRLMSIS 2.0. In all years, SABER and NRLMSIS 2.0 profiles coincide as an indicator of SABER O data's inclusion in the NRLMSIS 2.0 model. The agreement between all three data sets is very good, between ~ 88 and 95 km in 2010, 2012, and 2013. The lower panels comparing the data sets in terms of number density suggest a trend similar to the vmr. SOFIE and the NRLMSIS 2.0 model indicate good agreement between ~ 83 and 94 km in all years except 2008 and 2014. In 2008, the two data sets

agree better between ~ 84 and 90 km; and in 2014, there is very good agreement from ~ 91 to 100 km. Overall, in the SH, SOFIE shows better agreement with NRLMSIS 2.0 than SABER.

Comparing both hemispheres for all years suggests that the agreement between SOFIE and SABER is much better in the NH, both in terms of vmr and number density. This is strongly attributed to the number of coincidences which are much higher in the NH than in the SH, as seen in terms of latitude and local time overlaps in Figure 13 and Figure 14, respectively. The differences in measurements between SOFIE and SABER are attributed to the sources described in Section 3.6. The difference in the background atmospheric density profiles derived from simultaneous observations from the same instrument introduce a certain amount of error. SABER's atmospheric number density is obtained as a data product from the SABER website, while this parameter is calculated for SOFIE. The difference in the temperature retrievals for both instruments contributes to the uncertainties, alongside differences in sampling and systematic and random errors from both instruments. As both instruments use the same approach to derive O from O_3, major differences are attributed due to errors from O_3 (indicated by error bars in Figure 16 and Figure 17), which are reported as small for SOFIE but significant for SABER. The omission of equation 6 underestimates the O concentration, and that of 7 introduces non-linearity above ~ 90 km, which is a possible explanation for the differences above ~ 90 km.

SOFIE and NRLMSIS 2.0 show excellent agreement in the NH, typically at all altitudes. In the SH, SOFIE shows very good agreement with NRLMSIS 2.0, typically between ~ 83 and 95 km. Although SABER O is incorporated into NRLMSIS 2.0, the inclination of NRLMSIS 2.0 towards SOFIE than SABER over a wider range of altitudes is an indicator that SOFIE also agrees well with the other data sets (OSIRIS and rocket profiles) that have gone into NRLMSIS 2.0 and further

suggests that the disagreements between SOFIE and SABER are attributed more to SABER than SOFIE.

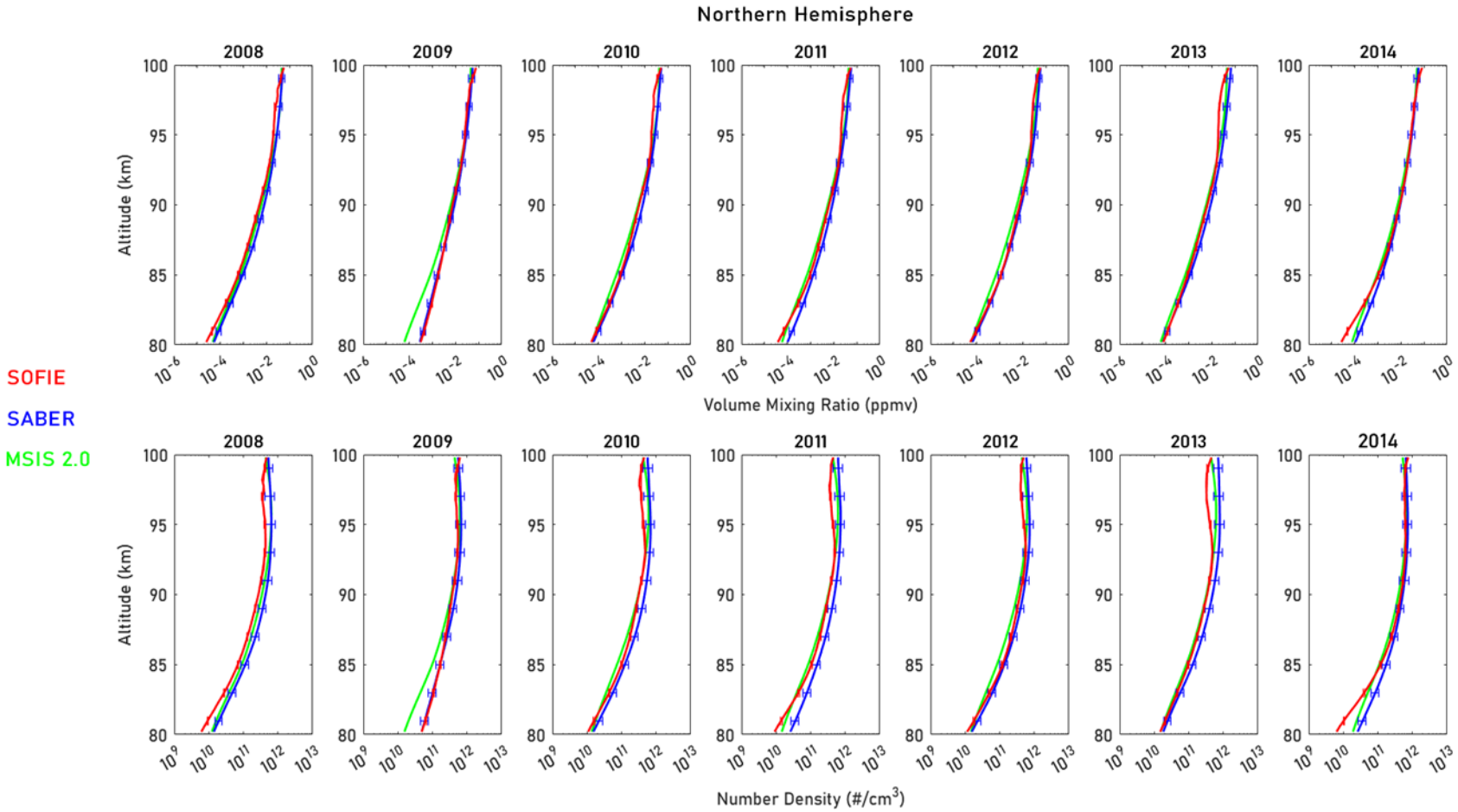

Figure 16. SOFIE, SABER and NRLMSIS 2.0 atomic oxygen vmr (top panels) and number density (#/cm^3) (bottom panels) for 2008-2014 averaged poleward of ~ 60^o N/S in the NH. Red and blue horizontal lines indicate SOFIE and SABER error bars, respectively.

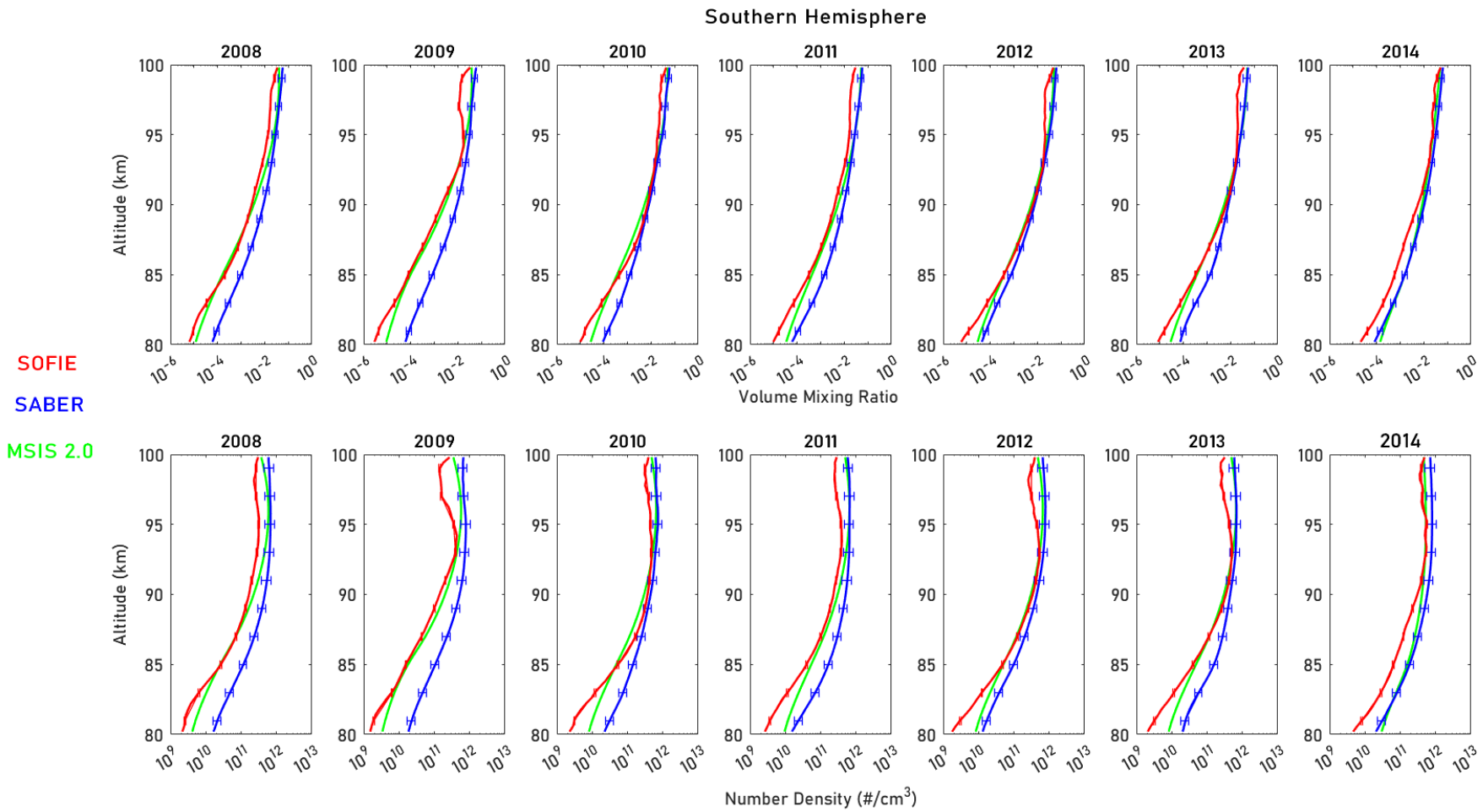

Figure 17. Same as Figure 16, but for the SH.

3.7.2 Seasonal Variation of O

The dynamics of the MLT (~ 60 – 100 km) are strongly dominated by planetary waves, tides, and gravity waves and their effect on the chemistry of this region. Momentum is deposited in the MLT by small-scale gravity waves that drive a summer-to-winter pole circulation in the mesopause. The sources of these waves are located lower in altitude, and the waves continue to increase in magnitude while propagating upwards. Zonal-mean zonal winds are eastward in the winter and westward in the summer in the middle atmosphere. Waves with large amplitudes break and deposit momentum and produce large-scale residual circulations. During the winters in the stratosphere, planetary waves break and drive residual circulation from the equator to the winter pole. In the mesosphere, the gravity waves break, and the dissipation drives the circulation from the summer to the winter pole.

Constituents in the thermosphere are vertically transported through molecular diffusion above 100 km and through eddy diffusion below. While the gravity waves propagate from the lower atmosphere, they break and produce turbulence (*Garcia and Solomon,* 1985; *Fritts and Alexander,* 2003; *Li et al.,* 2005). Turbulence due to convection and shear instabilities, combined with dissipating gravity waves, leads to a large percentage of the disturbances (*Hines,* 1960; *Lübken,* 1997). A mechanical mixing that contributes to diffusive transport is caused by turbulence and damped waves (*Swenson et al.,* 2018). The disturbances caused due to turbulence lead to the eddy diffusion of constituents with respect to the background atmosphere (*Becker & von Savigny,* 2010; *Gardner,* 2018; *Swenson et al.,* 2018).

Eddy transport processes redistribute constituents horizontally and vertically and influence the climatological distribution of the MLT. O distribution was first characterized by *Colgrove et al.,* (1965). O is produced above ~ 100 km through the photodissociation of molecular oxygen. It

diffuses downwards through eddy processes that include dissipating gravity waves and turbulence (*Swenson et al.*, 2018, 2019, 2021).

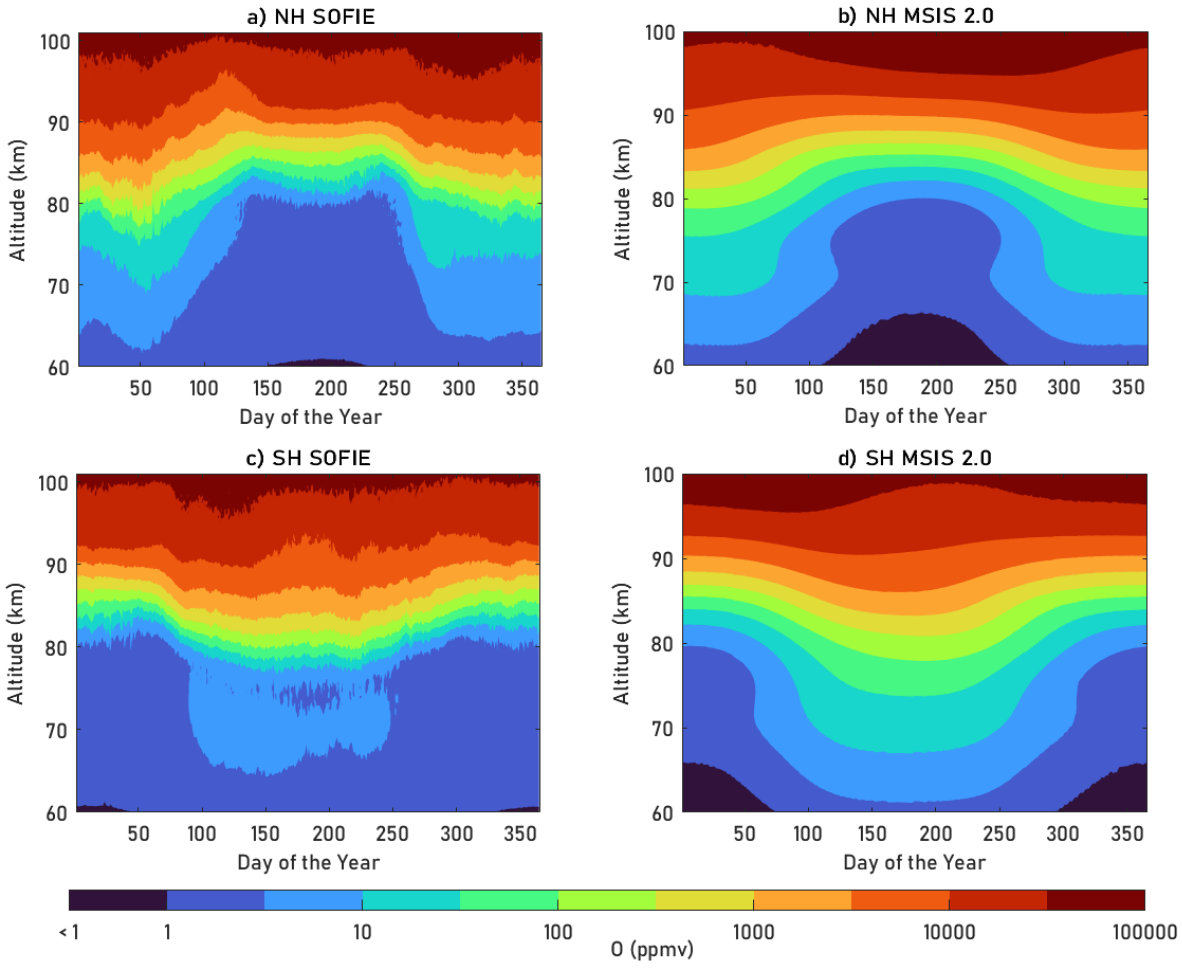

Figure 18. Contour plots of O averaged over 2008 – 2014 from SOFIE in the a) NH and c) SH, and NRLMSIS 2.0 at SOFIE-coincident points in the b) NH and d) SH poleward of 60° N/S.

Figure 18 shows the daily-mean O time series averaged over 2008 to 2014 in both hemispheres for SOFIE and at coincident points for NRLMSIS 2.0. Figure 18a indicates large wintertime descent during the months of December, January, and February (DJF) for SOFIE in the NH. The mesopause region and the altitudes above it are home to large quantities of O. The concentration

reported by SOFIE is ~ 10^5 ppmv at 100 km. Usually, at and below ~ 80 km, the concentration of O is typically low and mostly less than ~ 10 ppmv. However, during wintertime, large amounts of O are transported from the MLT to altitudes lower than 80 km. The transport of O to lower altitudes is triggered by eddy diffusion. Figure 18a suggests that during certain weeks in DJF, the concentration of O just below 80 km is higher than ~ 100 ppmv. The concentration of O continues to decrease as it is transported lower and is less than 10 ppmv at ~ 63 km. During the summertime, there is stable mesopause and no descent activity during June, June, and August in the NH. The concentration of O below ~ 80 km during these months is less than ~ 5 ppmv.

Figure 18b shows results from NRLMSIS 2.0 at the same parameters as SOFIE for Figure 18a. NRLMSIS 2.0 results corroborate the seasonal O descent and variation shown by SOFIE results. During DJF in panel b, a large descent is observed that travels down to ~ 63 km. The vmr distribution shown by NRLMSIS 2.0 is similar to SOFIE. While the concentration of O during the winter is ~ 100 ppmv at ~ 80 km, it is transported due to eddy diffusion, and the concentration is within ~ 10 ppmv at ~ 63 km. During JJA, NRLMSIS 2.0 results indicate stable mesopause and O concentration values less than ~ 5 ppmv below ~ 80 km.

Panel c shows that during the winter in the SH, i.e., JJA, there is a descent similar to the NH but less intense. SOFIE results indicate that like the NH, O concentration in the SH at 100 km is ~ 10^5 ppmv, with concentration reducing with altitude until ~ 80 km. Below ~ 80, the concentration is typically very low (under ~ 5 ppmv), except during the wintertime. Panel c indicates the increase in O around and below ~ 80 km because of eddy diffusion with values close to ~ 100 ppmv. SOFIE indicates that the O concentrations under ~ 10 ppmv were transported to ~ 64 km during JJA. During the SH summer months of DJF, the mesopause layer is stable, and O concentrations are higher only above this altitude.

Panel d shows the SH O distribution for NRLMSIS 2.0. NRLMSIS 2.0 shows a similar distribution pattern as SOFIE during the SH summer and winter. However, NRLMSIS 2.0 reported higher amounts of O between ~ 68 and ~ 80 km than SOFIE during the wintertime in JJA. NRLMSIS 2.0 reports concentrations higher than ~ 10 ppmv until ~ 68 km and reducing concentration further below. The wintertime O descent in JJA reached as low as ~ 61 km.

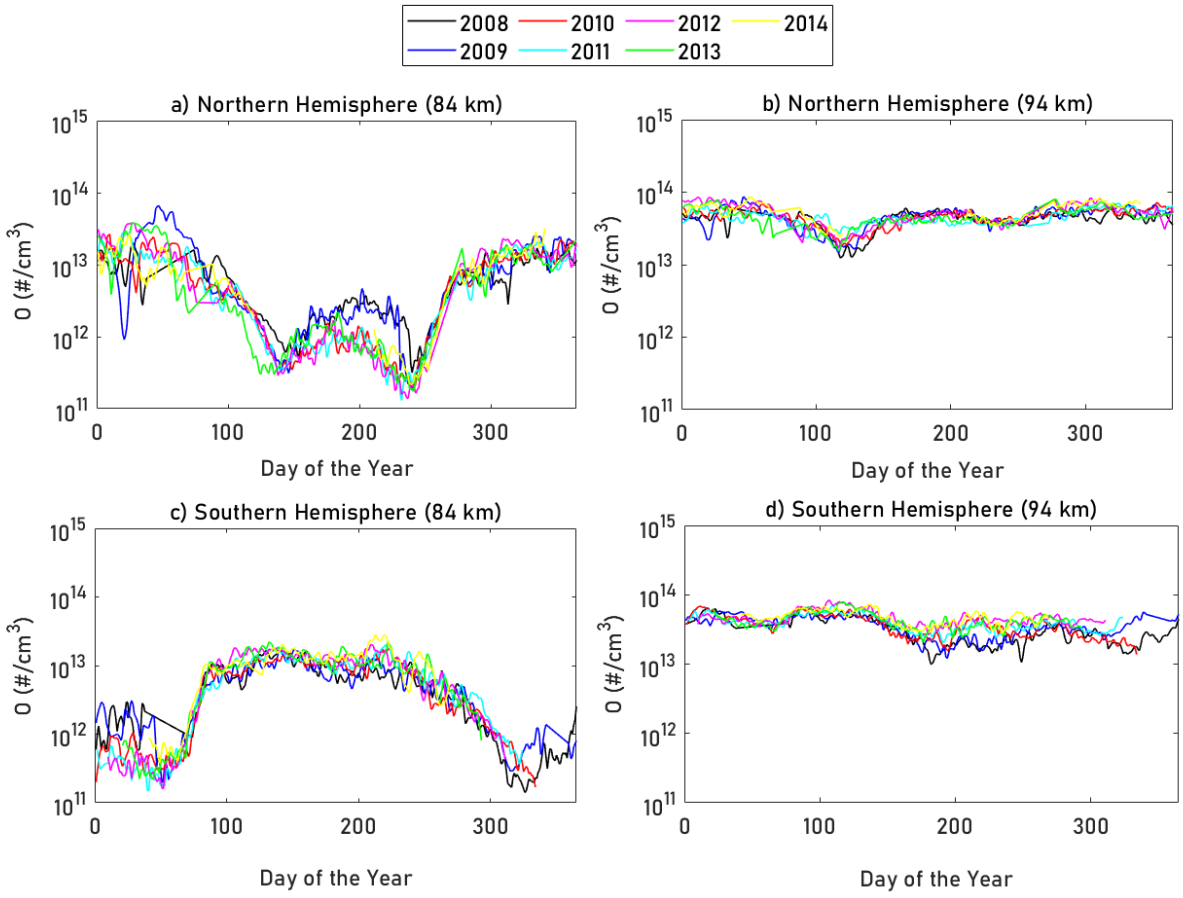

Figure 19. Variation of O at 84 km in the a) NH and c) SH, and at 94 km in the b) NH and d) SH for 2008-2014 averaged poleward of 65° N/S.

Figure 19 shows the annual variation of O during 2008-2014 in both hemispheres (poleward of 65° N/S) at 84 km and 94 km. Figure 19a and Figure 19c show that the O mixing ratio has a wintertime maximum at 84 km at high latitudes, attributed to the gravity wave-driven circulation

during the winter. High peaks during February in 2009 (blue line) and 2013 (green line) in the NH winter (DJF) are consistent with the theoretical expectation of enhanced O at 84 km, particularly during SSWs. In the SH, enhanced O at 84 km during the wintertime (JJA) further corroborates that O attains a wintertime maximum at 84 km at high latitudes. The O maximum is observed at ~ 94 km during summertime, as seen in Figure 19b and Figure 19d. The gravity wave-driven circulation weakens at this altitude during the summer, attributed to wave breaking near the mesopause region (which lies below this altitude at the summer pole). Typically, the summertime mesopause is located by the cold point in the temperature profile and lies in the 83 - 89 km range (*von Zahn et al.,* 1996; *Xu et al.,* 2007). High summertime O at 94 km and above is a potential indicator of the reversal of the normal upwelling circulation in the summer mesosphere and the establishment of a downwelling circulation cell. Molecular diffusion enhances with high temperatures and is another probable cause of high summertime O. Molecular diffusion leads to the mixing of air with thermospheric O higher in volume, resulting in the seasonal O pattern.

3.7.3 Latitudinal Variation of O

Figure 20 shows the averaged O mixing ratio as a function of latitude and altitude, averaged during 2008 – 2014 at all latitudes poleward of 65^{o} in both hemispheres. The O mixing ratio varies by several orders of magnitude in the mesopause region in both hemispheres. Although the concentration of O in the NH is typically higher than the SH at most altitudes, the variation overall is strong and monotonic in altitude. Higher concentrations in the NH, particularly in the 85-90 km range, can be attributed to the inclusion of 2009 and 2013 in the NH average, during which high amounts of SSW-triggered O descent were reported. Between ~ 95 km and 100 km, the O mixing ratio is higher and more widely distributed in the NH than in SH. Overall, O distribution across 65^{o}-85^{o} in the NH and SH is comparable between 80-100 km. Note that SOFIE looks at one latitude

per hemisphere each day. The variation of O is thus not indicated continuously over a fixed location. Hence, the daily variation in O is also a variation in latitude. This explains the daily variation in O concentration at a given altitude over the year(s) and the absence of a pattern in the variation.

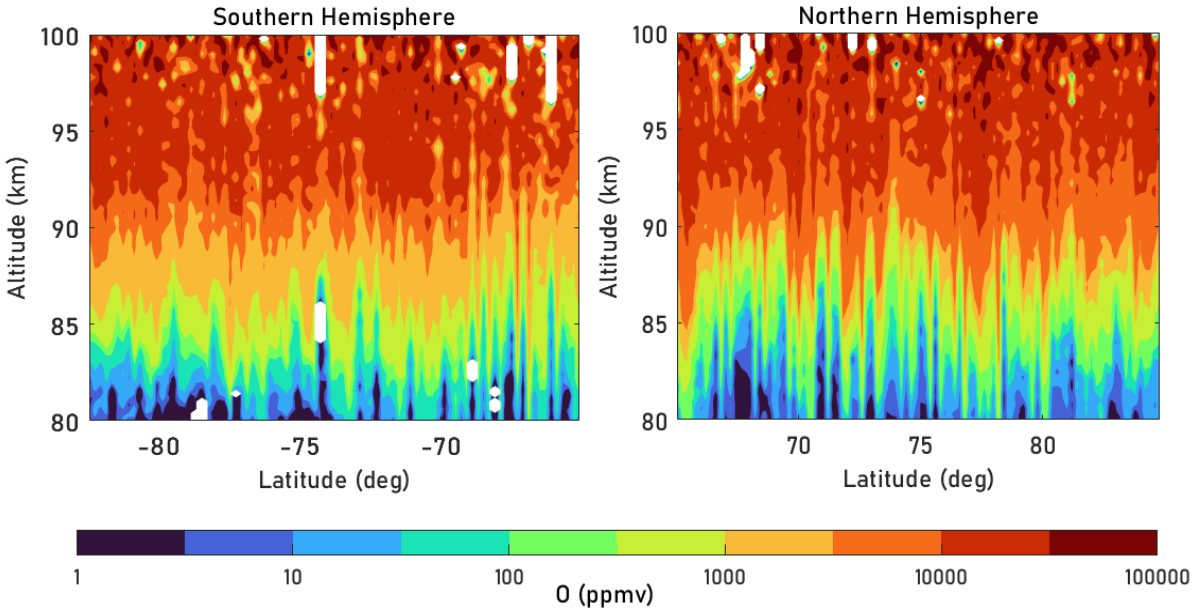

Figure 20. Contour images of latitude vs. altitude of mean O averaged over 2008-2014 poleward of 65^{o} in the (left panel) SH and (right panel) NH.

3.8 Discussion

The measurement of O in the mesopause region through in situ and remote sensing techniques is limited. Past studies have used derived O to assess its vertical distribution and diurnal and seasonal variation. However, the extant O database is limited and requires continuous evaluation and improvement. In this paper, we derived O from SOFIE and evaluated its robustness against established data sets. The SABER O daytime and nighttime data product is the most widely used satellite measurement. However, due to its yaw cycle, SABER looks at different high latitudes every ~ 60 days, thus, limiting a continuous focus on high latitudes. The new and improved

NRLMSIS 2.0 model has made stark improvements over its predecessor with the inclusion of satellite data. We use SOFIE measurements not just to fill existing knowledge gaps by compensating for the limitations of SABER but also to analyze how it compares to the NRLMSIS 2.0 model results and hence, the data sets that are used to develop the NRLMSIS 2.0 O database.

SOFIE profiles, when compared to SABER coincident profiles, indicate excellent agreement typically at all altitudes in the NH in terms of vmr. They indicate very good agreement in terms of number density, typically below ~ 95 km, except in 2011 and 2014, where SOFIE O is distinctly lower than SABER below ~ 84 km. The agreement between the two datasets is excellent, above ~ 95 km in 2009 and 2014. In the SH, the agreement between SOFIE and SABER is lesser than in the NH due to limited coincidences. The vmr profiles typically show good agreement at most altitudes between ~ 87 and 95 km except in 2008 and 2009. SOFIE usually reports lower O than SABER, and there are larger differences in the datasets below ~ 85 km. In 2008 and 2009, the agreement is low between the datasets at all latitudes.

NRLMSIS 2.0 vmr profiles show excellent agreement with SOFIE in the NH except below ~ 85 km in 2009, where SABER and SOFIE have an excellent agreement, but NRLMSIS 2.0 reports lower O than the two datasets. The number density profiles suggest very good agreement between SOFIE and NRLMSIS 2.0 at all altitudes, except in a few years when SOFIE O is distinctly lower above ~ 95 km and below ~ 84 km in 2009 and 2014. In the SH, NRLMSIS 2.0 measurements are inclined towards SOFIE than SABER, typically at altitudes below ~ 95 km for both vmr and number density profiles, except in 2014, where NRLMSIS 2.0 is in better agreement with SOFIE from ~ 90 to 100 km. NRLMSIS 2.0's tendency to align better with SOFIE indicates that SOFIE also agrees with the OSIRIS, rocket measurements, and the other datasets that are used to develop the NRLMSIS 2.0 database. While SABER is one of the datasets used for the NRLMSIS 2.0

database, NRLMSIS 2.0's better agreement with SOFIE than SABER at most altitudes indicates that the differences between SOFIE and SABER are attributed more to the uncertainties associated with SABER. Overall, the agreement between SOFIE and SABER is good, taking into account the coincidences, sampling differences, systematic and random errors, and uncertainties associated with O_3 measurements of the individual datasets, which are higher for SABER than SOFIE. Other sources of error are those from the temperature measurements that are retrieved independently for the two datasets. NRLMSIS 2.0 measurements typically corroborate SOFIE O measurements in both hemispheres. Overall, the SOFIE O vmr profiles show good agreement with SABER (particularly in the NH) and excellent agreement with NRLMSIS 2.0 in the mesopause, with differences that can be justified. However, we believe that further analysis is necessary to narrow down the reasons for discrepancies and uncertainties/error sources (especially those associated with the O retrieval algorithm).

O produced by the breakdown of O_2 has a long life in the MLT and is thus produced in situ or transported from other parts of the atmosphere. The increase in O over what is locally produced is attributed to eddy diffusion that mixes air with thermospheric O, redistributes constituents horizontally and vertically, and influence the climatological distribution of the MLT, resulting in the seasonal O pattern. There is a strong descent of O during the wintertime to altitudes as low as ~ 60 km in both hemispheres. The O layer during summertime is stable and true for both hemispheres. The wintertime maximum in O is observed at 84 km and in the summer at 94 km. Between the two hemispheres, the daytime O is relatively more evenly distributed near ~ 100 km and marginally higher in the NH and an indicator of inter-hemispheric asymmetry. However, both hemispheres observe O variation through several orders of magnitudes with height. An important observation is the lack of a pattern in the daily variation of O at a given altitude which is attributed

to the variation in latitude along with O as SOFIE observes a single latitude in each hemisphere on a given day.

3.9 Conclusion

In this paper, we analyze O measurements derived from the SOFIE O_3 product. Coincident O profiles from SABER and the NRLMSIS 2.0 model are used to analyze results from SOFIE-derived O profiles in terms of vmr and number density. The seasonal and latitudinal variations of O in the mesopause region are evaluated. We summarize the key findings from this study in this section.

The derived O profiles are based on O_3 photochemistry using the Chapman equations. We evaluate the significance of O in the O_3 photochemistry and its impact on the mesopause during the daytime. A comparison of SOFIE O vertical profiles with SABER and the NRLMSIS 2.0 model indicates an overall qualitative agreement with systematic differences and inconsistencies.

SOFIE and SABER agree very well in the NH and typically between ~ 85 km and 95 km in the SH. Disagreements between the datasets are attributed to limited coincidences, sampling differences, systematic and random errors, and uncertainties associated with individual temperature and O_3 retrievals from both instruments. NRLMSIS 2.0 agrees excellently with SOFIE in the NH and is inclined towards SOFIE, typically below ~ 95 km. Investigation of the seasonal O variations from SOFIE and NRLMSIS 2.0 indicate the transport of O from the lower thermosphere to the mesosphere driven by eddy diffusion. NRLMSIS 2.0 results at SOFIE-coincident points indicate great agreement between the datasets in their depiction of seasonal O variation. Wintertime and summertime O maximums occur at 84 km and 94 km (and above), respectively. A latitudinal variation in O is also observed with interhemispheric comparisons indicating that O in the NH is typically slightly larger and more evenly distributed than in the SH, although the overall distribution is comparable between both hemispheres. Larger concentrations of O are transported from 100 km

to ~ 85 km in the NH than in the SH. However, the variation of O through 80 to 100 km occurs over several orders of magnitude in both hemispheres.

While the main thrust of this study has been to compare derived O measurements from SOFIE to other established datasets and understand the variability in O with season and latitude, we also discuss the uncertainties of the retrieval. SOFIE's continuous high latitude coverage provides a holistic understanding of the mesopause, which was limited by SABER's yaw cycle-based latitude coverage. SOFIE's focus on the daytime chemistry and variability of O in the mesopause is an important addition to the extant research on mesopause O, which has mainly focused on nighttime chemistry so far. With a good agreement between SOFIE and SABER and an excellent agreement with NRLMSIS 2.0, we believe that the derived SOFIE-O retrievals are suitable for scientific use. Further investigation is needed to narrow down the uncertainties and understand discrepancies with other data sets to improve the approach for the determination of O in the mesopause region.

3.10 Acknowledgments

This research is funded by AIM through the NASA Small Explorer program. We acknowledge the AIM and SOFIE operation teams for their excellent support with this work. We thank the SABER team for their data. We thank the US Naval Research Laboratory for the NRLMSIS 2.0 model. We acknowledge the University of Colorado Space Weather Technology, Research and Education Center (SWx TREC) for the Pymsis wrapper for NRLMSIS 2.0.

3.11 Open Research

The SOFIE temperature and O_3 data used in this paper to derive O are publicly available on the SOFIE website - http://sofie.gats-inc.com/. SABER O data are publicly available on the SABER website - http://saber.gats-inc.com/. The Python wrapper for the NRLMSIS 2.0 model can be accessed at https://github.com/SWxTREC/pymsis.

References

Bailey, S.M., Thurairajah, B., Randall, C.E., Holt, L., Siskind, D.E., Harvey, V.L., Venkataramani, K., Hervig, M.E., Rong, P. and Russell III, J.M., 2014. A multi tracer analysis of thermosphere to stratosphere descent triggered by the 2013 Stratospheric Sudden Warming. *Geophysical Research Letters*, 41(14), pp.5216-5222. https://doi.org/10.1002/2014GL059860

Baldwin, M.P., Ayarzagüena, B., Birner, T., Butchart, N., Butler, A.H., Charlton-Perez, A.J., Domeisen, D.I., Garfinkel, C.I., Garny, H., Gerber, E.P. and Hegglin, M.I., 2021. Sudden stratospheric warmings. *Reviews of Geophysics*, 59(1), p.e2020RG000708. https://doi.org/10.1029/2020RG000708

Butler, A.H., Seidel, D.J., Hardiman, S.C., Butchart, N., Birner, T. and Match, A., 2015. Defining sudden stratospheric warmings. *Bulletin of the American Meteorological Society*, 96(11), pp.1913-1928. https://doi.org/10.1175/BAMS-D-13-00173.1

Chapman, S., 1930. XXXV. On ozone and atomic oxygen in the upper atmosphere. *The London, Edinburgh, and Dublin Philosophical Magazine and Journal of Science*, 10(64), pp.369-383. https://doi.org/10.1080/14786443009461588

Chandran, A., Collins, R.L., Garcia, R.R., Marsh, D.R., Harvey, V.L., Yue, J. and De La Torre, L., 2013. A climatology of elevated stratopause events in the whole atmosphere community climate model. *Journal of Geophysical Research: Atmospheres*, 118(3), pp.1234-1246. doi: 10.1002/jgrd.50123

Charlton, A.J. and Polvani, L.M., 2007. A new look at stratospheric sudden warmings. Part I: Climatology and modeling benchmarks. *Journal of climate*, 20(3), pp.449-469. https://doi.org/10.1175/JCLI3996.1

De Wit, R.J., Hibbins, R.E., Espy, P.J., Orsolini, Y.J., Limpasuvan, V. and Kinnison, D.E., 2014. Observations of gravity wave forcing of the mesopause region during the January 2013 major Sudden Stratospheric Warming. *Geophysical research letters*, 41(13), pp.4745-4752. https://doi.org/10.1002/2014GL060501

Emmert, J.T., Drob, D.P., Picone, J.M., Siskind, D.E., Jones Jr, M., Mlynczak, M.G., Bernath, P.F., Chu, X., Doornbos, E., Funke, B. and Goncharenko, L.P., 2021. NRLMSIS 2.0: A whole-atmosphere empirical model of temperature and neutral species densities. *Earth and Space Science*, 8(3), p.e2020EA001321. https://doi.org/10.1029/2020EA001321

Ennico, K., Becklin, E.E., Le, J., Rangwala, N., Reach, W.T., Rhodes, A., Roellig, T.L., Sarver, G., Temi, P., Yorke, H.W. and Zavala, E., 2018. An overview of the Stratospheric Observatory for Infrared Astronomy since full operation capability. *Journal of Astronomical Instrumentation*, 7(04), p.1840012. https://doi.org/10.1142/S2251171718400123

Eswaraiah, S., Kim, Y.H., Hong, J., Kim, J.H., Ratnam, M.V., Chandran, A., Rao, S.V.B. and Riggin, D., 2016. Mesospheric signatures observed during 2010 minor stratospheric warming at King Sejong Station (62 S, 59 W). *Journal of Atmospheric and Solar-Terrestrial Physics*, 140, pp.55-64.https://doi.org/10.1016/j.jastp.2016.02.007.

Eswaraiah, S., Kim, Y.H., Liu, H., Ratnam, M.V. and Lee, J., 2017. Do minor sudden stratospheric warmings in the Southern Hemisphere (SH) impact coupling between stratosphere

and mesosphere–lower thermosphere (MLT) like major warmings?. *Earth, Planets and Space*, 69(1), pp.1-8. https://doi.org/10.1186/s40623-017-0704-5.

Eswaraiah, S., Lee, C., Lee, W., Kim, Y.H., Kumar, K.N. and Medineni, V.R., 2021. Temperature tele-connections between the tropical and polar middle atmosphere in the Southern Hemisphere during the 2010 minor sudden stratospheric warming. *Atmospheric Science Letters*, 22(1), p.e1010. https://doi.org/10.1002/asl.1010

Evans, W.F.J., McDade, I.C., Yuen, J. and Llewellyn, E.J., 1988. A rocket measurement of the O2 infrared atmospheric (0–0) band emission in the dayglow and a determination of the mesospheric ozone and atomic oxygen densities. *Canadian Journal of Physics*, 66(11), pp.941-946. https://doi.org/10.1139/p88-151

Funke, B., López-Puertas, M., García-Comas, M., Stiller, G.P., Von Clarmann, T., Höpfner, M., Glatthor, N., Grabowski, U., Kellmann, S. and Linden, A., 2009. Carbon monoxide distributions from the upper troposphere to the mesosphere inferred from 4.7 μm non-local thermal equilibrium emissions measured by MIPAS on Envisat. *Atmospheric Chemistry and Physics*, 9(7), pp.2387-2411. https://doi.org/10.5194/acp-9-2387-2009

Good, R.E., 1976. Determination of atomic oxygen density from rocket borne measurement of hydroxyl airglow. *Planetary and Space Science*, 24(4), pp.389-395. https://doi.org/10.1016/0032-0633(76)90052-0

Gordley, L.L., Hervig, M.E., Fish, C., Russell III, J.M., Bailey, S., Cook, J., Hansen, S., Shumway, A., Paxton, G., Deaver, L. and Marshall, T., 2009. The solar occultation for ice experiment. *Journal of Atmospheric and Solar-Terrestrial Physics*, 71(3-4), pp.300-315. https://doi.org/10.1016/j.jastp.2008.07.012

Grossmann, K.U. and Vollmann, K., 1997. Thermal infrared measurements in the middle and upper atmosphere. *Advances in Space Research*, 19(4), pp.631-638. https://doi.org/10.1016/S0273-1177(97)00156-7

Grossmann, K.U., Kaufmann, M. and Gerstner, E., 2000. A global measurement of lower thermosphere atomic oxygen densities. *Geophysical research letters*, 27(9), pp.1387-1390.doi:10.1029/2000GL003761.

Hauchecorne, A., Bertaux, J.L., Dalaudier, F., Russell III, J.M., Mlynczak, M.G., Kyrölä, E. and Fussen, D., 2007. Large increase of NO2 in the north polar mesosphere in January–February

2004: Evidence of a dynamical origin from GOMOS/ENVISAT and SABER/TIMED data. *Geophysical Research Letters*, 34(3).doi:10.1029/2006GL027628.

Hedin, A.E., 1987. MSIS-86 thermospheric model. *Journal of Geophysical Research: Space Physics*, 92(A5), pp.4649-4662.https://doi.org/10.1029/JA092iA05p04649

Hedin, A.E., 1991. Extension of the MSIS thermosphere model into the middle and lower atmosphere. *Journal of Geophysical Research: Space Physics*, 96(A2), pp.1159-1172.https://doi.org/10.1029/90JA02125

Heyminck, S., Graf, U.U., Güsten, R., Stutzki, J., Hübers, H.W. and Hartogh, P., 2012. GREAT: the SOFIA high-frequency heterodyne instrument. *Astronomy & Astrophysics*, 542, p.L1. https://doi.org/10.1051/0004-6361/201218811

Holton, J.R., 1980. The dynamics of sudden stratospheric warmings. *Annual Review of Earth and Planetary Sciences*, 8, p.169. https://doi.org/10.1146/annurev.ea.08.050180.001125

Jin, J.J., Semeniuk, K., Jonsson, A.I., Beagley, S.R., McConnell, J.C., Boone, C.D., Walker, K.A., Bernath, P.F., Rinsland, C.P., Dupuy, E. and Ricaud, P., 2005. Co-located ACE-FTS and Odin/SMR stratospheric-mesospheric CO 2004 measurements and comparison with a GCM. *Geophysical research letters*, 32(15).doi:10.1029/2005GL022433.

Jones Jr, M., Forbes, J.M. and Hagan, M.E., 2014. Tidal-induced net transport effects on the oxygen distribution in the thermosphere. *Geophysical Research Letters*, 41(14), pp.5272-5279. https://doi.org/10.1002/2014GL060698

Jones Jr, M., Emmert, J.T., Drob, D.P. and Siskind, D.E., 2017. Middle atmosphere dynamical sources of the semiannual oscillation in the thermosphere and ionosphere. *Geophysical Research Letters*, 44(1), pp.12-21.https://doi.org/10.1002/2016GL071741

Kuttippurath, J. and Nikulin, G., 2012. The sudden stratospheric warming of the Arctic winter 2009/2010: comparison to other recent warm winters. *Atmospheric Chemistry & Physics Discussions*, 12(3). doi:10.5194/acpd-12-7243-2012

Labitzke, K., 1981. Stratospheric-mesospheric midwinter disturbances: A summary of observed characteristics. *Journal of Geophysical Research: Oceans*, 86(C10), pp.9665-9678.. doi: 10.1029/JC086iC10p09665

Limpasuvan, V., Orsolini, Y.J., Chandran, A., Garcia, R.R. and Smith, A.K., 2016. On the composite response of the MLT to major sudden stratospheric warming events with elevated

stratopause. *Journal of Geophysical Research: Atmospheres*, 121(9), pp.4518-4537.doi: 10.1002/2015JD024401

Llewellyn, E.J., McDade, I.C., Moorhouse, P. and Lockerbie, M.D., 1993. Possible reference models for atomic oxygen in the terrestrial atmosphere. *Advances in Space Research*, 13(1), pp.135-144. https://doi.org/10.1016/0273-1177(93)90013-2

Llewellyn, E.J. and McDade, I.C., 1996. A reference model for atomic oxygen in the terrestrial atmosphere. *Advances in Space Research*, 18(9-10), pp.209-226. https://doi.org/10.1016/0273-1177(96)00059-2

Madronich, S. and Flocke, S., 1999. The role of solar radiation in atmospheric chemistry. In Environmental photochemistry (pp. 1-26). *Springer, Berlin, Heidelberg*. DOI: 10.1007/978-3-540-69044-3_1

Manney, G.L., Schwartz, M.J., Krüger, K., Santee, M.L., Pawson, S., Lee, J.N., Daffer, W.H., Fuller, R.A. and Livesey, N.J., 2009. Aura Microwave Limb Sounder observations of dynamics and transport during the record-breaking 2009 Arctic stratospheric major warming. *Geophysical Research Letters*, 36(12). https://doi.org/10.1029/2009GL038586

Marsh, D.R., Smith, A.K., Mlynczak, M.G. and Russell III, J.M., 2006. SABER observations of the OH Meinel airglow variability near the mesopause. *Journal of Geophysical Research: Space Physics*, 111(A10).doi:10.1029/2005JA011451.

McDade, I.C., Llewellyn, E.J. and Harris, F.R., 1985. Atomic oxygen concentrations in the lower auroral thermosphere. *Advances in space research*, 5(7), pp.229-232. https://doi.org/10.1016/0273-1177(85)90379-5

McInturff, R.M., 1978. Stratospheric warmings: Synoptic, dynamic and general-circulation aspects (No. NASA-RP-1017).

Mlynczak, M.G. and Solomon, S., 1993. A detailed evaluation of the heating efficiency in the middle atmosphere. *Journal of Geophysical Research: Atmospheres*, 98(D6), pp.10517-10541. https://doi.org/10.1029/93JD00315

Mlynczak, M.G., Martin-Torres, F.J., Johnson, D.G., Kratz, D.P., Traub, W.A. and Jucks, K., 2004. Observations of the O (3P) fine structure line at 63 μm in the upper mesosphere and lower thermosphere. *Journal of Geophysical Research: Space Physics*, 109(A12).doi:10.1029/2004JA010595.

Mlynczak, M.G., Marshall, B.T., Martin-Torres, F.J., Russell III, J.M., Thompson, R.E., Remsberg, E.E. and Gordley, L.L., 2007. Sounding of the Atmosphere using Broadband Emission Radiometry observations of daytime mesospheric O2 (1Δ) 1.27 μm emission and derivation of ozone, atomic oxygen, and solar and chemical energy deposition rates. *Journal of Geophysical Research: Atmospheres*, 112(D15). https://doi.org/10.1029/2006JD008355

Mlynczak, M.G., Hunt, L.H., Mertens, C.J., Marshall, B.T., Russell III, J.M., López Puertas, M., Smith, A.K., Siskind, D.E., Mast, J.C., Thompson, R.E. and Gordley, L.L., 2013a. Radiative and energetic constraints on the global annual mean atomic oxygen concentration in the mesopause

region. *Journal of Geophysical Research: Atmospheres*, 118(11), pp.5796-5802.doi:10.1002/jgrd.50400.

Mlynczak, M.G., Hunt, L.A., Mast, J.C., Thomas Marshall, B., Russell III, J.M., Smith, A.K., Siskind, D.E., Yee, J.H., Mertens, C.J., Javier Martin-Torres, F. and Earl Thompson, R., 2013b. Atomic oxygen in the mesosphere and lower thermosphere derived from SABER: Algorithm theoretical basis and measurement uncertainty. *Journal of Geophysical Research: Atmospheres*, 118(11), pp.5724-5735. https://doi.org/10.1002/jgrd.50401

Mlynczak, M.G., Hunt, L.A., Marshall, B.T., Mertens, C.J., Russell III, J.M., Siskind, D., Thompson, R.E. and Gordley, L.L., 2013c. Radiative constraints on the minimum atomic oxygen concentration in the mesopause region. *Geophysical research letters*, 40(14), pp.3777-3780. https://doi.org/10.1002/grl.50725

Patterson, P.L., 2005. In situ measurements of upper atmospheric atomic oxygen: The ATOX resonant fluorescence/absorption sensor. Utah State University.

Picone, J.M., Hedin, A.E., Drob, D.P. and Aikin, A.C., 2002. NRLMSISE-00 empirical model of the atmosphere: Statistical comparisons and scientific issues. *Journal of Geophysical Research: Space Physics*, 107(A12), pp.SIA-15. https://doi.org/10.1029/2002JA009430

Randall, C.E., Harvey, V.L., Manney, G.L., Orsolini, Y., Codrescu, M., Sioris, C., Brohede, S., Haley, C.S., Gordley, L.L., Zawodny, J.M. and Russell III, J.M., 2005. Stratospheric effects of energetic particle precipitation in 2003–2004. *Geophysical Research Letters*, 32(5).doi:10.1029/2004GL022003.

Randall, C.E., Harvey, V.L., Singleton, C.S., Bernath, P.F., Boone, C.D. and Kozyra, J.U., 2006. Enhanced NOx in 2006 linked to strong upper stratospheric Arctic vortex. *Geophysical Research Letters*, 33(18).doi:10.1029/2006GL027160.

Randall, C.E., Harvey, V.L., Siskind, D.E., France, J., Bernath, P.F., Boone, C.D. and Walker, K.A., 2009. NOx descent in the Arctic middle atmosphere in early 2009. *Geophysical Research Letters*, 36(18). https://doi.org/10.1029/2009GL039706

Remsberg, E.E., Marshall, B.T., Garcia-Comas, M., Krueger, D., Lingenfelser, G.S., Martin-Torres, J., Mlynczak, M.G., Russell III, J.M., Smith, A.K., Zhao, Y. and Brown, C., 2008. Assessment of the quality of the Version 1.07 temperature-versus-pressure profiles of the middle atmosphere from TIMED/SABER. *Journal of Geophysical Research: Atmospheres*, 113(D17). https://doi.org/10.1029/2008JD010013

Richter, H., Buchbender, C., Güsten, R., Higgins, R., Klein, B., Stutzki, J., Wiesemeyer, H. and Hübers, H.W., 2021. Direct measurements of atomic oxygen in the mesosphere and lower thermosphere using terahertz heterodyne spectroscopy. *Communications Earth & Environment*, 2(1), pp.1-9. https://doi.org/10.1038/s43247-020-00084-5

Rong, P.P., Russell III, J.M., Mlynczak, M.G., Remsberg, E.E., Marshall, B.T., Gordley, L.L. and López-Puertas, M., 2009. Validation of Thermosphere Ionosphere Mesosphere Energetics and Dynamics/Sounding of the Atmosphere using Broadband Emission Radiometry

(TIMED/SABER) v1. 07 ozone at 9.6 μm in altitude range 15–70 km. *Journal of Geophysical Research: Atmospheres*, 114(D4). https://doi.org/10.1029/2008JD010073

Russell III, J.M., Mlynczak, M.G., Gordley, L.L., Tansock Jr, J.J. and Esplin, R.W., 1999, October. Overview of the SABER experiment and preliminary calibration results. In *Optical spectroscopic techniques and instrumentation for atmospheric and space research III* (Vol. 3756, pp. 277-288). SPIE. https://doi.org/10.1117/12.366382

Sander, S.P., Friedl, R.R., DeMore, W.B., Golden, D.M., Kurylo, M.J., Hampson, R.F., Huie, R.E., Moortgat, G.K., Ravishankara, A.R., Kolb, C.E. and Molina, M.J., 2000. Chemical kinetics and photochemical data for use in stratospheric modeling. Evaluation Number 13.

Sheese, P.E., McDade, I.C., Gattinger, R.L. and Llewellyn, E.J., 2011. Atomic oxygen densities retrieved from Optical Spectrograph and Infrared Imaging System observations of O2 A-band airglow emission in the mesosphere and lower thermosphere. *Journal of Geophysical Research: Atmospheres*, 116(D1).https://doi.org/10.1029/2010JD014640

Siskind, D.E. and Sharp, W.E., 1990. A vibrational analysis of the O2 (A3Σ+ u) Herzberg I system using rocket data. *Planetary and space science*, 38(11), pp.1399-1408. https://doi.org/10.1016/0032-0633(90)90115-7

Siskind, D.E., Eckermann, S.D., Coy, L., McCormack, J.P. and Randall, C.E., 2007. On recent interannual variability of the Arctic winter mesosphere: Implications for tracer descent. *Geophysical Research Letters*, 34(9).doi:10.1029/2007GL029293.

Siskind, D.E., Sassi, F., Randall, C.E., Harvey, V.L., Hervig, M.E. and Bailey, S.M., 2015. Is a high-altitude meteorological analysis necessary to simulate thermosphere-stratosphere coupling?. *Geophysical Research Letters*, 42(19), pp.8225-8230. doi: 10.1002/2015GL065838

Smith, A.K. and Marsh, D.R., 2005. Processes that account for the ozone maximum at the mesopause. *Journal of Geophysical Research: Atmospheres*, 110(D23).doi:10.1029/2005JD006298.

Smith, A.K., López-Puertas, M., García-Comas, M. and Tukiainen, S., 2009. SABER observations of mesospheric ozone during NH late winter 2002–2009. *Geophysical Research Letters*, 36(23). https://doi.org/10.1029/2009GL040942

Smith, A.K., Marsh, D.R., Mlynczak, M.G. and Mast, J.C., 2010. Temporal variations of atomic oxygen in the upper mesosphere from SABER. *Journal of Geophysical Research: Atmospheres*, 115(D18).doi:10.1029/2009JD013434.

Smith, A.K., Harvey, V.L., Mlynczak, M.G., Funke, B., García-Comas, M., Hervig, M., Kaufmann, M., Kyrölä, E., López-Puertas, M., McDade, I. and Randall, C.E., 2013. Satellite observations of ozone in the upper mesosphere. *Journal of Geophysical Research: Atmospheres*, 118(11), pp.5803-5821. https://doi.org/10.1002/jgrd.50445

Stevens, M.H., Deaver, L.E., Hervig, M.E., Russell III, J.M., Siskind, D.E., Sheese, P.E., Llewellyn, E.J., Gattinger, R.L., Höffner, J. and Marshall, B.T., 2012. Validation of upper mesospheric and lower thermospheric temperatures measured by the Solar Occultation for Ice

Experiment. *Journal of Geophysical Research: Atmospheres*, 117(D16). https://doi.org/10.1029/2012JD017689

Swenson, G.R., Salinas, C.C.J.H., Vargas, F., Zhu, Y., Kaufmann, M., Jones Jr, M., Drob, D.P., Liu, A., Yue, J. and Yee, J.H., 2019. Determination of global mean eddy diffusive transport in the mesosphere and lower thermosphere from atomic oxygen and carbon dioxide climatologies. *Journal of Geophysical Research: Atmospheres*, 124(23), pp.13519-13533. https://doi.org/10.1029/2019JD031329

WMO/IQSY. (1964). International Years of the Quiet Sun (IQSY) 1964-65. Alert messages with special references to stratwarms. WMO/IQSY Report No 6, Secretariat of the World Meteorological Organization, Geneva, Switzerland. World Meteorological Organization.

Xu, J., Liu, H.L., Yuan, W., Smith, A.K., Roble, R.G., Mertens, C.J., Russell Iii, J.M. and Mlynczak, M.G., 2007. Mesopause structure from thermosphere, ionosphere, mesosphere, energetics, and dynamics (TIMED)/sounding of the atmosphere using broadband emission radiometry (SABER) observations. *Journal of Geophysical Research: Atmospheres*, 112(D9).doi:10.1029/2006JD007711

Xu, J., Gao, H., Smith, A.K. and Zhu, Y., 2012. Using TIMED/SABER nightglow observations to investigate hydroxyl emission mechanisms in the mesopause region. *Journal of Geophysical Research: Atmospheres*, 117(D2).doi:10.1029/2011JD016342

Zhu, Y. and Kaufmann, M., 2018. Atomic oxygen abundance retrieved from SCIAMACHY hydroxyl nightglow measurements. *Geophysical Research Letters*, 45(17), pp.9314-9322. https://doi.org/10.1029/2018GL079259

4. Sudden Stratospheric Warming-Triggered Composition Response of the Stratosphere, Mesosphere, and Lower Thermosphere

Das, Saswati, et al. "Sudden Stratospheric Warming-Triggered Composition Response of the Stratosphere, Mesosphere, and Lower Thermosphere." *Journal of Geophysical Research-Atmospheres (Under Review)*

4.1 Abstract

Observations from the SOFIE (Solar Occultation for Ice Experiment) instrument on the Aeronomy of Ice in the Mesosphere (AIM) satellite show that the Arctic winter in 2019 transported enhanced amounts of nitric oxide (NO) from the lower thermosphere to the stratosphere alongside tongues of air poor in water and methane. This transport event was triggered by the Sudden Stratospheric Warming (SSW) on 2 January and was similar to those in 2004, 2006, 2009, and 2013 in terms of chemistry and dynamics. We track the descent in 2019 from January to April (JFMA) and compare the event to the other major descent years. Our results indicate that lower thermospheric air was seen at altitudes below 40 km in 2019. Despite the low geomagnetic activity in 2019, large NO enhancements indicate that they are attributed more strongly to the unusual meteorology. Derived atomic oxygen (O) from ozone measurements during JFMA indicate that O was transported from above the mesopause to the mesosphere during the event. Using SOFIE data, the vertical transport rate from 40 to 90 km shows that the descent rate peaked near ~ 76 km initially, with the peak shifting downwards by ~ 5- 6 km every 10 days. We use data from ACE (Atmospheric Chemistry Experiment) on SciSat for the years SOFIE data is unavailable and for descent intensity comparisons at specific altitudes. Our work demonstrates the utility of SOFIE and ACE measurements in diagnosing the 2019 transport event and comparing it to the previous four major descent events.

4.2 Plain Language Summary

In 2019, large amounts of nitric oxide (NO) were transported from the lower thermosphere to the stratosphere during the winter in the northern hemisphere. This was a result of an anomalous event termed Sudden Stratospheric Warming (SSW) that occurred on 2 January 2019. Poor amounts of water vapor and methane were also transported to the stratosphere. The 2019 SSW event was similar to that of past events from 2004, 2006, 2009, and 2013. The NO transported to the stratosphere led to the catalytic destruction of ozone. Vertical transport rates indicate that the descent peak in 2019 moved by ~ 5 - 6 km every 10 days. The unusual meteorology in 2019, like in other descent years, was responsible for the transport event.

4.3 Introduction

Sudden stratospheric warmings (SSW) are extreme events that can dramatically alter the circulation from the stratosphere through the thermosphere (*Scherhag.,* 1952; *Butler et al.,* 2015). The earliest definition of an SSW event adopted by the World Meteorological Organization (WMO) emphasized two main parameters – the reversal of the temperature gradient poleward of 60° at 10 hPa (*Andrews et al.,* 1987; *Scherhag.,* 1952; *WMO,* 1978) and zonal wind reversal at the 10-hPa pressure level (~30 km), poleward of 60^{o} latitude (*McInturff.,* 1978; *Labitzke.,* 1981; *Charlton and Polvani.,* 2007). SSWs are driven by large-scale topography (like mountains; warm ocean - cold land masses temperature contrasts) that lead to the generation of large-scale planetary waves that propagate into the stratosphere. Upward propagating planetary waves drive the middle atmosphere circulation and their interaction with the mean flow causes SSW events (*Chandran et al.,* 2014; *Matsuno.,* 1971). SSWs trigger major descent events (*Manney et al.,* 2009; *Holt et al.,* 2013) and lead to reformed polar night jet (due to planetary waves (PWs) deceleration) formations that change gravity wave propagation. The breaking of the planetary waves in the stratosphere

leads to the deceleration and perturbation of the polar vortex circulation. This leads to a sudden increase in polar stratospheric temperature. SSWs occur more frequently in the NH due to highly variable topography. After SSW events, the stratopause often reforms at high altitudes (typically between 70 km and 80 km) and descends gradually to its climatological altitude (~50-55 km) in the following weeks (*Manney et al.,* 2008; *Siskind et al.,* 2010; *Baldwin et al.,* 2021). These elevated stratopause events are also more common in the NH and occur approximately in 33% of the NH winters (*Chandran et al.,* 2013, 2014).

Chandran et al. (2013) and *Limpasuvan et al.* (2016) inferred that after SSW events, elevated stratopause formation occurs due to intensified gravity wave forcings that lead to downwelling and adiabatic heating at high altitudes where there is a reformed stratopause. SSWs impact the composition and dynamics of the mesosphere and lower thermosphere (MLT) and lead to high latitude cooling and reversal in zonal winds (*Labitzke.,* 1982; *H. L. Liu & Roble*, 2002; *Hoffmann et al.,* 2007; *Siskind et al.,* 2010; *Limpasuvan et al.,* 2016). The MLT is strongly impacted by gravity wave drag, and the eastward propagation of gravity waves into the MLT (due to the weakening and potential reversal of the zonal mean winds) leads to an increase in the eastward forcing at MLT altitudes once the waves break. This eastward forcing reverses MLT winds and alters the residual circulation at high latitudes from downward to upwards, leading to mesospheric cooling (*H.L.Liu & Roble,* 2002; *Siskind et al.*, 2010; *Limpasuvan et al.,* 2016).

The composition of the stratosphere and mesosphere are altered by the transport of chemical species triggered by the varying dynamics of the upper stratosphere and MLT (*Holt et al.*, 2012). Strong changes in chemistry and enhanced transport of NO_x, H_2O, and CH_4 from the MLT to the stratosphere following elevated stratopause events were reported by *Jin et al.,* (2005); *Hauchecorne et al.,* (2007); *Manney et al.,* (2008a); *Randall et al.,* (2006, 2009); *Funke et al.,*

(2009); *Winnick et al.,* (2009); *Siskind et al.,* (2010); *Salmi et al.,* (2011); *Bailey et al.,* (2014); *Pérot et al.,* (2014); *Orsolini et al.,* (2017). Although NO_x was transported to the stratosphere after minor SSWs, like in 2012 (not shown), the five major SSWs since 2004 that triggered large amounts of NO_x occurred in 2004 (*Randall et al.,* 2005; *López-Puertas et al.,* 2006), 2006 (*Randall et al.,* 2006), 2009 (*Randall et al.,* 2009; *Siskind et al.,* 2010; *Salmi et al.,* 2011), and 2013 (*Bailey et al.,* 2014; *Pérot et al.,* 2014; *Orsolini et al.,* 2017) and 2019 (*Pérot and Orsolini.,* 2021).

During Energetic Particle Precipitation (EPP), triggered by geomagnetic activity (*Barth et al.,* 2004), energetic electrons and protons strike the Earth's atmosphere and channel the production of NO in the mesosphere-lower thermosphere (MLT) region. NO reacts with O_3 during its descent and partly forms NO_2. Both NO and NO_2 are often tracked together as NO_x (NO + NO_2 , assuming negligible N (atomic nitrogen). The lifetime of EPP-produced NO_x (henceforth, EPP-NO_x) in the mesosphere is the longest during polar winters and is transported to the stratosphere during suitable conditions. In the stratosphere, NO_x has a lifetime that lasts months and catalytically destroys O_3 between 25 and ~ 45 km. The decrease in stratospheric O_3 due to the reaction with NOx alters the radiative budget and mid-atmospheric dynamics (*Guttu et al.,* 2020). The transport of EPP-NO_x to the stratosphere during the polar winter is termed the EPP indirect effect (EPP-IE) and has been reported in the past (*Siskind et al.,* 2000; *Randall et al.,* 1998, 2001, 2007; *Funke et al.,* 2005; *Jackman et al.,* 2008). As EPP IE is controlled primarily by meteorology (*Randall et al.,* 2009), high EPP-NO_x descent occurs despite the low geomagnetic Ap index in all years except 2004.

The most recent transport event of 2019 followed a major split-type SSW which occurred on the sixth earliest date (in a total of 26 events) for a major SSW since 1979 (*Lee and Butler,* 2020). This major descent event appears to be triggered by the SSW that occurred on 2 January 2019 and is consistent with the findings of *Holt et al.,* (2013) for other such events from the past. Recent

studies have reported the 2019 SSW using satellite and ground-based observations. *Shi et al.,* (2020) looked at the impacts of the 2019 SSW in comparison to the 2018 SSW at the mid-latitude mesosphere using a microwave radiometer (MWR) at Kharkiv, Ukraine. They quantified the differences in local variability in the zonal wind, temperature, and CO in the stratosphere and mesosphere. *Shephard et al.,* (2020) made contemporaneous multi-instruments (ground-based optical and meteor radar observations) of OH and O_2 airglow, temperature, and neutral winds during the winter of November 2018–February 2019 to study the MLT dynamics. They reported a split-type vortex along with planetary wave activity in the winter MLT region. *Pérot and Orsolini.,* (2021) compared the effects of the 2018 and 2019 SSWs using measurements from SMR (Sub-Millimetre Radiometer) on the Odin satellite and concluded that while the 2018 SSW was dynamically quiet in terms of NO transport from the MLT, the 2019 SSW led to one of the strongest EPP indirect events since 2004, with an NO abundance more than fifty times its usual climatological value. While Shi et al., 2020 and Shephard et al., 2020 did not look at NO transport events from the MLT to the stratosphere, the results demonstrated by *Pérot and Orsolini.,* (2021) from SMR were from data that was not measured continuously through the 2019 winter (Between 26 December 2018 and 25 April 2019, NO measurements were made for 5 days at the beginning followed by 2 consecutive days in a 4-day cycle with a few observation gap periods due to technical problems in the instruments). During the 2019 winter, SOFIE (Solar Occultation for Ice Experiment) made continuous high latitude measurements (typically between 65^{o}- 85^{o}N) at sunset (relative to the spacecraft) and captured the daytime-NO dynamics consistently on all days. Thus, the contribution of SOFIE NO measurements is important in quantifying the composition variation of the MLT and the stratosphere.

In this paper, using measurements from SOFIE (*Gordley et al.,* 2009) on AIM (*Russell et al.,* 2009), we study the transport event of 2019 and compare the results to the major (transport-triggering) SSWs from 2004 onwards. Measurements from ACE-FTS (Atmospheric Chemistry Experiment - Fourier Transform Spectroradiometer) (*Bernath et al.,* 2005) are used to compare with SOFIE and study the descent events in 2004 and 2006 (before the AIM/ SOFIE launch). In addition to NO, SOFIE observes water (H_2O) and methane (CH_4) used as tracers of atmospheric motion in the MLTS. The atomic oxygen (O) derived from ACE and SOFIE O_3 (*Marsh et al.,* 2001; *Smith. et al.,* 2010, 2011, 2013) is used to demonstrate that alongside NO, O was also transported from high altitudes (mesopause region (~ 80 – 100 km)) during the major SSWs to lower altitudes. Using NO, H_2O, and CH_4, we calculate the vertical descent in 2019 and evaluate its standing compared to the other major descent events since 2004.

4.4 Observations

SOFIE uses the solar occultation technique to measure the solar energy passing through the earth's atmosphere's limb at sunrise/sunset relative to the spacecraft. SOFIE measures at typically high latitudes (65^o-85^o N/S) in both hemispheres. Spacecraft sunset measurements were carried out in the Southern Hemisphere (SH) from 2007 to 2017, which changed in late 2018 when sunsets switched to the Northern Hemisphere (NH). Due to this, SOFIE viewed mid-low latitudes between ~ 2017 – 2018. Observations at 16 wavelengths from 0.29 μm to 5.26 μm are used to retrieve the vertical profiles of temperature, O_3, CH_4, NO, H_2O, and CO_2, with a vertical resolution of ~1.8 km. SOFIE measures NO using a broadband filter (~ 2% filter width) centered at 5.32 μm wavelength over altitudes from ~30 to 149 km (*Gomez-Ramirez et al.,* 2013; *Hervig et al.,* 2019). Due to measurement noise and retrieval errors, the SOFIE retrieved NO has a coarser effective vertical resolution (~2.5 km) than the other species. A detailed description of SOFIE NO

measurements, signal corrections, and retrievals was provided by *Gomez-Ramirez et al.,* (2013). Validation papers of the SOFIE products used are available - temperature (*Stevens et al.,* 2012); NO (*Hervig et al.,* 2019); CH_4 (*Rong et al.,* 2016), and H_2O (*Rong et al.,* 2010). This work used version 1.3 SOFIE data.

The ACE-FTS (*Bernath.,* 2001; *Bernath et al.,* 2005; *Boone et al.,* 2005) is a solar occultation instrument on the Canadian SciSat spacecraft and succeeds the ATOMS (Atmospheric Trace Molecule Spectroscopy) experiment (*Gunson et al.,* 1996). ACE was launched to 650 km at 74^o inclination and measured minor atmospheric species in the Earth's atmosphere. ACE measures high-resolution (0.02 cm^{-1}) spectra of the Earth's atmosphere in the medium-long infrared range of 2.2-13 μm (*Bernath et al.,* 2005). ACE data include temperature, pressure, and volume mixing ratios (VMRs) of the species retrieved from the occultation spectra. Due to the lack of sufficiently accurate meteorological data from the complete range of altitudes, ACE temperatures are derived directly from the ACE spectra as the first step, followed by the calculation of synthetic spectra in the global fitting procedure to retrieve the VMRs of target species. ACE NO measurements span ~ 6 to 107 km in altitude with a vertical resolution of ~ 3.5 km, and retrievals are reported at the oversampled vertical interval of 1 km. In this study, we use ACE version 4.1 data. ACE data products used in this study are temperature (*Sica et al.,* 2008), NO (*Kerzenmacher et al.,* 2008; *Sheese et al.,* 2016), H_2O (*Carleer et al.,* 2008; *Waymark et al.,* 2013); CH_4 (*De Mazière et al.,* 2008; *Waymark et al.,* 2013) and O_3 (*Walker et al.,* 2005; *Petelina et al.,* 2005a; *Fussen et al.,* 2005; *McHugh et al.,* 2005; *Kerzenmacher et al.,* 2005; *Cortesi et al.,* 2007; *Froidevaux et al.,* 2008; *E.Dupuy et al.,* 2009).

Comparison of ACE and SOFIE NO measurements indicate mean differences of less than ~50% for altitudes from roughly 50 to 140 km for SOFIE sunsets, i.e., in the northern hemisphere (NH)

(*Hervig et al.,* 2019). SOFIE H_2O observations have a precision of ~0.2% - 2.5% between 45 – 80 km and showed an agreement to ~ 5 – 10% below 80 km (*Rong et al.,* 2010). CH_4 observations, when compared to ACE observations, showed an agreement of ~ 15% between ~30 - 60 km above which the agreement deteriorates (*Rong et al.,* 2016). *Smith et al.,* (2013) used SOFIE O_3 observations at sunrise and sunset to study O_3 in the upper mesosphere, where Sounding of the Atmosphere using Broadband Emission Radiometry (SABER) was the primary instrument (*Esplin et al.,* 1994; *Staunder et al.,* 1998; *Russell III et al.,* 1994,1999).

This paper uses ACE measurements to track temperature variation and the transport of species when SOFIE data are unavailable (during 2004 and 2006) (Figure 21, Figure 22, and Figure 24). As the thrust of this paper is studying the climatological variation in composition after SSWs in the stratosphere and MLT, and not the validation of SOFIE results against ACE; we retain a maximum number of vertical profiles by averaging both datasets in the same latitude range (65^o – 85^o N), although at different longitudes and times. Typically, local time coincidences (not shown) are in concert between SOFIE and ACE as they both measure at sunrise and sunset. As SOFIE and ACE can measure at only one latitude per day, we assume zonal averages can provide reasonable estimates for all species.

4.5 Results

Several SSW events have been recorded in the NH during the last three decades (*Butler et al.,* 2017). However, only some of these have triggered major descent events in the NH. These SSWs are distinguished from the rest by their distinctly elevated stratopause structures, the sharp reversals in the zonal mean zonal wind speed, and the short periods in which these dynamics occur (*Randall et al.,* 2006, 2009; *Bailey et al.,* 2014). This section discusses the five major descent

events from 2004 onwards that have led to strong transport events. For 2004 and 2006, we used ACE data and SOFIE measurements for other years (2009, 2013, and 2019).

In Figure 21, from the top left to bottom right, ACE and SOFIE temperature measurements (K) averaged over daily values are plotted as altitude- time series for 2004, 2006, 2009, 2013, and 2019. The black dashed lines are used to indicate the date of the SSW. ACE data in 2004 was available only from March onwards, and hence, the stratopause behavior before this period is unavailable. However, with the existing ACE data for 2004, it can be inferred that the stratopause rose several kilometers higher than its usual climatological altitude. The stratopause is typically located between 50 and 60 km. A common indicator of major SSWs in all four years is the gradual descent of the stratopause preceding the date of the SSW and indicating its onset.

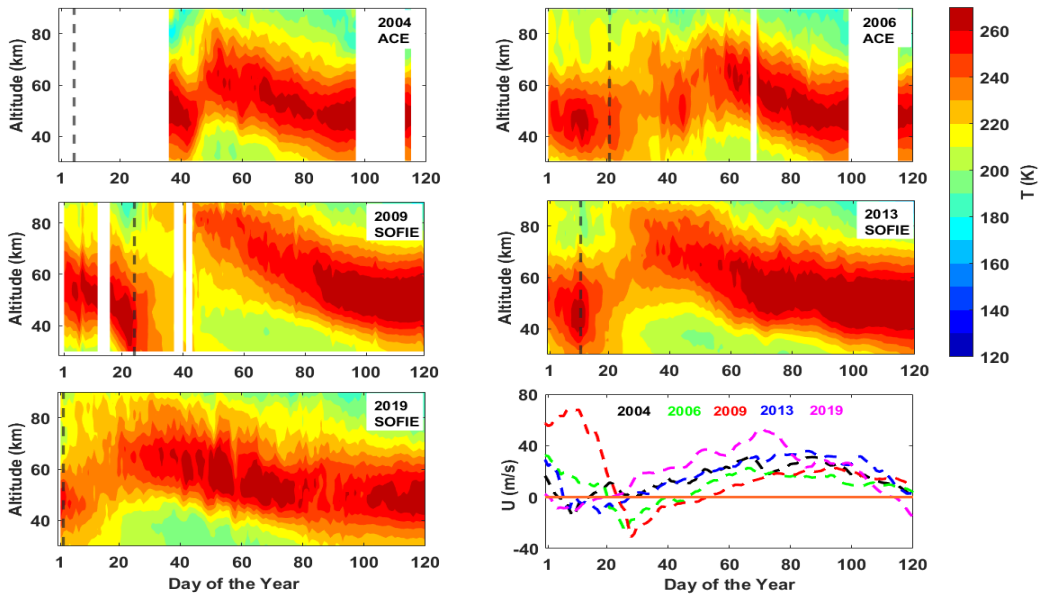

Figure 21. (Top left to bottom right) Contour plots of temperature (K) during JFMA, NH for ACE in 2004 and 2006; SOFIE in 2009, 2013, and 2019 where the dashed black lines indicate the date of SSW; and MERRA -2 Zonal Mean Zonal Wind at 60^{o} N, 10 hPa for these years.

Soon after the date of the SSW, the stratopause rises by ~ 20-30 km above its typical altitude and remains elevated for the succeeding weeks. An interesting feature observed during these events is the mesosphere's cooling before the elevated stratopause formation. These structures were more enhanced in 2006 and 2009 and indicated a possibly close relationship between SSWs and mesospheric cooling. After staying elevated for a few weeks post the SSW event, the elevated stratopause gradually descends back to its usual climatological altitude. The bottom right panel shows the zonal mean zonal wind (m/s) reversal using MERRA-2 data at 10 hPa and 60^{o}N. The date the zonal mean zonal winds reversed from westward to eastward is treated as the date of the SSW (*Charlton and Polvani*, 2007). While sharp reversal in the zonal mean zonal wind values is seen in all years, the earliest reversal occurred in 2019 and 2004. The SSW dates determined from the reversal values are 5 January 2004, 21 January 2006, 24 January 2009, 11 January 2013, and 2 January 2019.

As discussed in Section 4.3, SSWs strongly impact the circulation, dynamics, and transport of species from the MLT to the stratosphere. These transport events carry large tongues of air consisting of different atmospheric species in varying concentrations. Past studies investigated the transport of NO from the MLT to the stratosphere in 2004 (*Jin et al.,* 2005; *Randall et al.,* 2005; *Hauchecorne et al.,* 2007; *Manney et al.,* 2005, 2008a), 2006 (*Randall et al.,* 2006; *Siskind et al.,* 2007; *Manney et al.,* 2008a, 2008b), 2009 (*Randall et al.,* 2009) and 2013 (*Bailey et al.,* 2014). In Figure 22, the left panels show the descent of NO (ppbv) in all five winters. The black dashed lines indicate the date of the SSW, and the red dashed lines at 40 and 50 km are used to track the extent of the descent in terms of how far the NO was transported. In all years, tongues of air rich in NO were transported from the upper mesosphere and lower thermosphere to the stratosphere. The stratosphere extends up to at least 50 km, and thus, any descent below this altitude is treated as

'stratospheric descent.' Two questions to investigate regarding the descent events: 1) how far into the stratosphere is NO transported, and 2) what is the amount of NO that enters the stratosphere at ~ 50 km (edge of the stratosphere)?

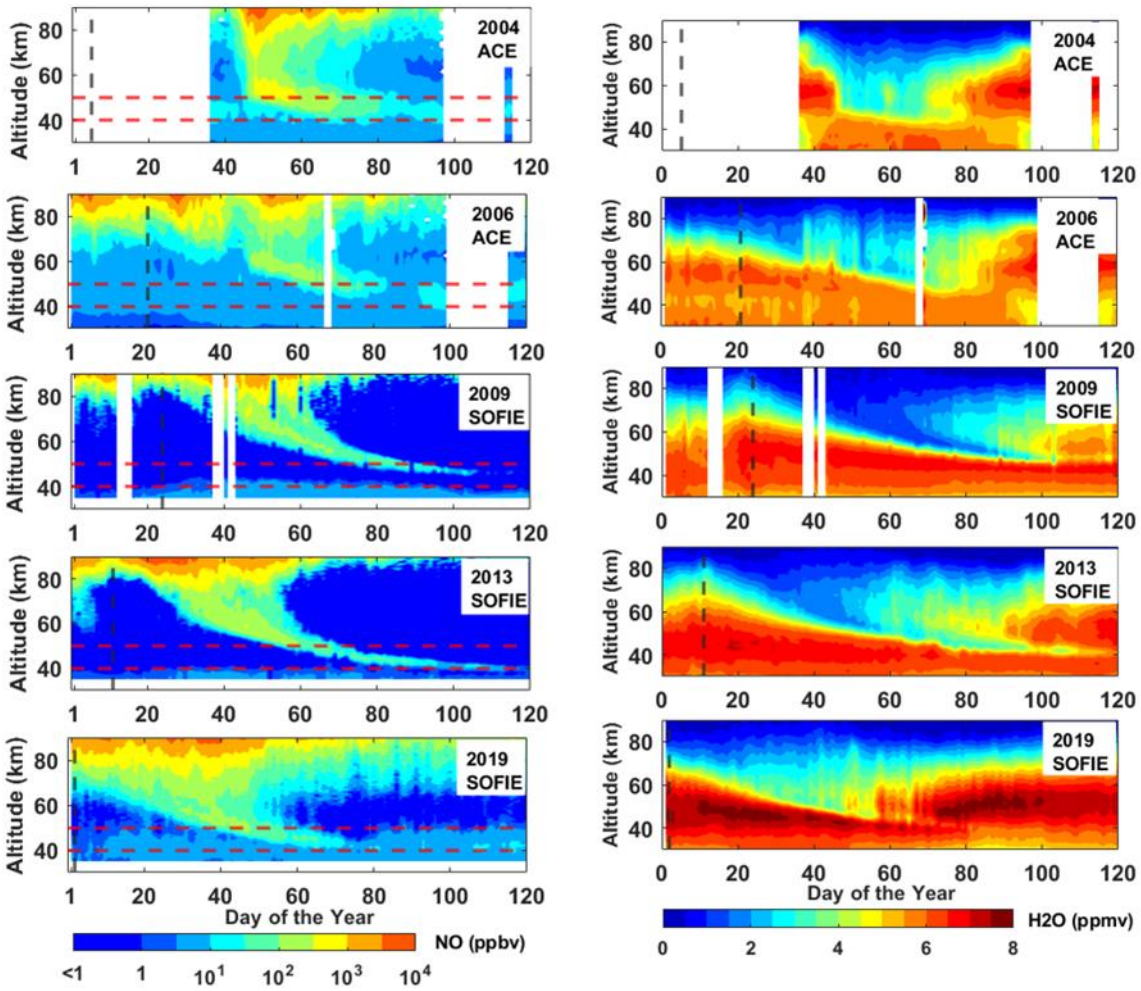

Figure 22. (Left panels) Contour plots of NO (ppbv, dashed red lines are plotted to mark 40 and 50 km) and (right panels) H_2O (ppmv) during JFMA, NH for ACE in 2004 and 2006; SOFIE in 2009, 2013, and 2019. Dashed black lines indicate the SSW date.

While all years indicate a descent below 50 km, the descent goes farther than 40 km in 2004, 2013, and 2019. This is indicated by distinct tongues on NO present below the red dashed line indicating the 40 km altitude. In 2006, although NO is transported below 50 km, it is not transported below

40 km and is transported as low as ~ 43 km. In 2009, NO was transported well below 50 km, but there is no visible NO at 40 km due to transport from the MLT, and any NO measured at this altitude can be treated as that preexistent in the atmosphere, i.e., locally produced by the reactions of N_2O which is originally created on the earth's surface and has a sufficiently long lifetime to reach the stratosphere as it is unreactive in the troposphere (*Crutzen* 1970). Although our results suggest that NO from SOFIE traveled below 50 km in 2009, the ACE measurements indicate that NO is transported below 50 km in meager amounts, and the lowest part of the NO tongue touches ~ 50 km (not shown). However, for consistency, we use ACE measurements for all years (2009, 2013, and 2019 not shown as contour plots) to report the extent of descent and the amount of NO crossing ~ 50 km as SOFIE (was not launched until 2007 and thus,) did not make measurements in 2004 and 2006. While in 2013, the NO descended below 40 km very slightly, in 2004, it reached as low as ~ 37. 5 km, and in 2019 it reached ~ 36.5 km. Thus, in all five winters, 2019 had the farthest transport of NO into the stratosphere. The NO concentration entering the stratosphere is approximated by calculating the averaged NO at ~ 50 km during the first four months of the year and listed for ACE in Table 3.

Table 3. 30-day mean Ap values centered on the day of the SSW and the corresponding NO average at ~ 50 km during JFMA in 2004, 2006, 2009, 2013, and 2019

Year	Mean Ap Values	NO (ppbv) at ~50 km
2004	14.7	198.64
2006	6.5	24.45
2009	4.0	5.79
2013	4.3	36.95
2019	5.8	19.38

The planetary auroral power (Ap) level data provided by the *Geo Forschungs Zentrum German Research Center for Geosciences* is also plotted in Table 3 and indicates the level of geomagnetic activity using the 30-day mean Ap centered on the day of the SSW. The NO measurements at ~ 50 km indicate that the highest amount of NO entering the stratosphere was in 2004 and the lowest in 2009. The 2004 event, which shows the largest amount of NO transported to date, has a moderate mean-Ap value of 14.7, while the 2006, 2009, 2013, and 2019 events occurred during periods of relatively lower geomagnetic values. Low Ap values in all years except 2004 indicate that the NO enhancements in these years are strongly attributed to the dynamical transport events.

Figure 22 (right panels) shows the daily averaged vertical profiles of H_2O (ppmv) plotted as altitude time series for the same parameters as NO (left panels) with the SSW dates marked by dashed black lines. The tongues of air carry air with low amounts of H_2O from the MLT to the stratopause. During polar winters, H_2O mixing ratios decrease with increasing altitudes, and thus low H_2O values indicate air transported from higher altitudes. The polar winter NO mixing ratios are higher above 55 km only during periods when EPP produces the NO. From the above phenomena, a negative correlation between NO and H_2O can be used to indicate the presence of EPP-NO.

In Figure 23, we quantify the amount of NO at 55 km and verify its production by EPP. This procedure has been used by *Bailey et al.*, (2014) and by *Randall et al.*, (2006, 2009) for NO_X and CH_4. In Figure 23, the volume mixing ratios (vmrs) of H_2O and corresponding NO are plotted for ACE and SOFIE. For the same amount of NO at ~ 55 km, the H_2O values are much smaller in 2004,2006, 2009, and 2013 than in 2019. The minimum observed H_2O measured by SOFIE (ACE) varies from ~ 1.3 ppmv (~ 1.9 ppmv) in 2009 to ~ 3.4 ppmv (~ 3.6 ppmv) in 2019. This suggests that the descent at ~ 55 km was most ‘intense’ in 2009 and least in 2019 and that the EPP-NO

detected in 2019 originated from a lower altitude than in other years. The values from SOFIE are inconsistent with ACE and show smaller values. This can be attributed to the difference in viewing latitudes where SOFIE views higher latitudes (SOFIE looks at 65°N - 88°N and ACE at 65°N - 80°N).

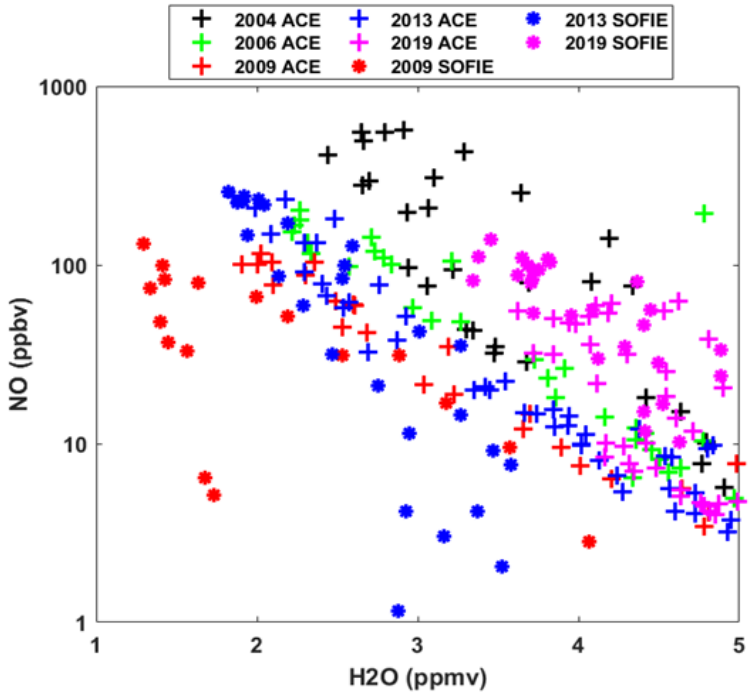

Figure 23. H_2O vs NO for ACE and SOFIE poleward of 65° N at ~55km in JFMA for 2004, 2006, 2009, 2013 and, 2019.

Other reasons for the disagreement possibly include the spatial variability in NO production and the loss of H_2O, highlighting the need for observations at constant latitude. There are large NO discrepancies between SOFIE and ACE in 2009 for $H_2O < 2$ ppmv (*Bailey et al.*, 2014). A possible explanation is the photochemical loss of NO during transport, which has a higher chance of occurrence at high altitudes due to a shorter NO lifetime. The inhomogeneous distribution of NO is, thus, a possible result of photochemical loss attributed to small variations in exposure to sunlight. Note that while Figure 23 addresses the 'intensity' of the transport at ~ 55 km (stratopause

region), it is not to be confused with the parameters used earlier to quantify the events in terms of how far NO is transported into the stratosphere and the total NO concentration entering the stratosphere during JFMA. Although the 2009 event was the most intense of all at 55 km, the lowest part of the EPP-NO tongue in 2009 did not extend as far in altitude as the other four years.

Figure 24 (left panels) shows the altitude-time series of CH_4 (ppmv) for the same parameters as Figure 22. Like H_2O, CH_4 mixing ratios during polar winters decreases with increasing altitude. Thus, low CH_4 indicates air transported from higher altitudes. Typically, CH_4 is used as an important tracer in determining the intensity of EPP-NO at ~ 55 km, with the lowest CH_4 corresponding to the highest NO.

Between 20-25 km, the stratosphere is the largest reservoir of O_3 in the atmosphere. In the upper mesosphere, the region between ~ 85 and 95 km, the concentration of O_3 is the second highest and is therefore called the secondary O_3 maximum (*Smith et al.,* 2009, 2011). *Smith et al.,* (2009), and *Tweedy et al.,* (2013) demonstrated a decrease in the O_3 concentration during nighttime at the secondary maximum following SSW events. This applies to daytime O_3 at the secondary maximum (not shown). Atomic oxygen (O) is important to the chemistry of the mesopause region (~ 80-100 km) and strongly influences the photochemistry of this region (*Smith et al.,* 2010, 2011). It is a long-lived species in the mesopause. *Tweedy et al.,* (2013) described the role of O in influencing the secondary O_3 maximum at nighttime during SSWs while also demonstrating the negative correlation between temperature and O_3. Previously, *Smith et al.,* (2009) inferred that during SSWs, the secondary O_3 concentration decreases with the elevation of the stratopause and the increase in temperature. During the daytime, O in the mesopause is supplemented by eddy and molecular diffusion besides what is locally produced, thus, increasing the O_3 in the secondary maximum (*Smith et al.,* 2005). SSWs perturb the chemistry and dynamics of the atmosphere and

result in important changes in O that impact the O_3 secondary maximum concentration (*Kvissel et al.*, 2012, *Smith et al.*, 2012). These occurrences are alongside the impacts of tidal variations in temperature and winds that influence O and O_3 during the daytime. The variation in O above ~ 97 km is much less, and the secondary O_3 maximum is influenced more strongly by temperature variations above this altitude. However, in the mesopause, typically between ~ 83 and 95 km, O_3 responds strongly to O variations, thus, making it important to quantify the role of O in the MLT after SSWs.

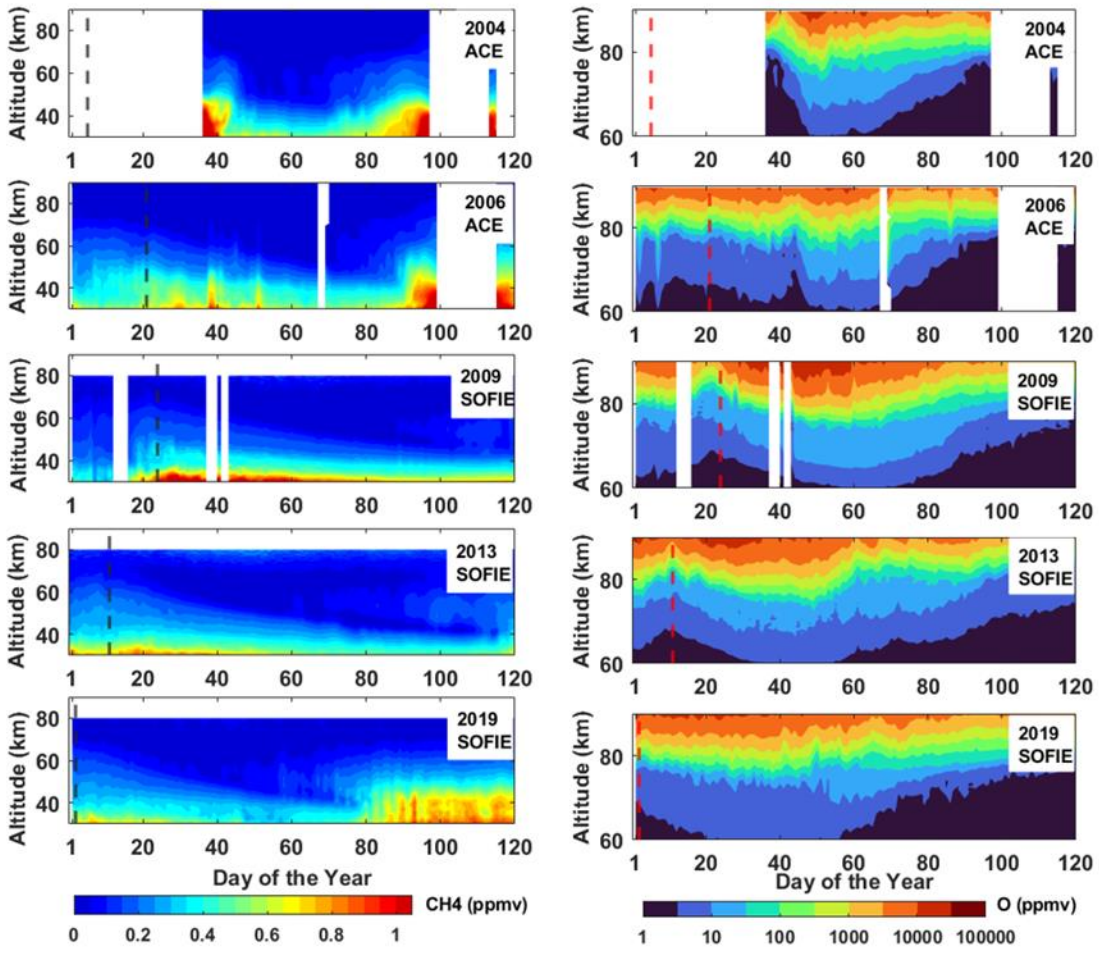

Figure 24. (Left panels) Contour plots of CH_4 (ppmv) and (right panels) O (ppmv) during JFMA, NH for ACE in 2004 and 2006; SOFIE in 2009, 2013, and 2019. Black and red dashed lined for CH_4 and O, respectively denote the SSW date.

In the weeks following the SSW, tongues of air carrying O are transported from the upper mesosphere and lower thermosphere. The direct measurement of O is difficult; thus, O is derived for the daytime from ACE O_3, and SOFIE O_3, measured at 0.291 μm. The production and loss of O_3 assume photochemical equilibrium (*McDade et al.,* 1985; *Evans et al.,* 1988; *Llewellyn et al.,* 1993; *Llewellyn and McDade,* 1996; *Mlynczak et al.,* 2007) and is formulated based on the Chapman equations (*Chapman.,* 1930). Using the method described by *Smith et al.,* (2010), and equating O_3 production and loss, daytime O is calculated as

$$O_{Daytime} = \left[J_{O_3} * O_3\right] / \left[k_{o-o_2} * O_2 . n^2\right]$$

where O, O_2, and O_3 are the mixing ratios, T is the temperature, $k_{o-o_2} = 6\times10^{-34}(300/T)^{2.4}$ is the *reaction rate* of the reaction (*Sander et al.,* 2006), J_{O3} is the photolysis rate of O_3 estimated using the TUV (Tropospheric Ultraviolet-Visible) model (*Madronich and Flocke,* 1998), n is the atmospheric number density calculated using the ideal law.

Figure 24 (right panels) shows the derived O from ACE and SOFIE for the same parameters as Figure 22. The red dashed lines indicate the date of the SSW. High amounts of O in the order of ~10^3 (or higher with increasing altitude) are present at ~ 80 km and above and typically decrease by several orders of magnitude with altitude, reaching as low as 1-10 ppmv at ~ 60 km. However, during the five SSWs, large amounts of O in the orders of $10^2 – 10^4$ ppmv were transported from mesopause to ~ 70 km with consistently decreasing values. The O concentration reached ~ 10 ppmv upon reaching ~ 60 km. In the weeks following the O transport to the mesosphere, the O concentration at altitudes below ~ 80 km returns to its usual values. This indicates that during the five SSWs, enhanced amounts of O were transported to altitudes below ~ 80 km, which are regions with typically low O concentrations.

In the stratosphere, there is an anti-correlation between NO and O_3, where O_3 is catalytically destroyed by NO. This correlation becomes important at ~ 45 km and below. In the years that NO travels far into the stratosphere with high concentrations, a reduction in the O_3 concentration is expected, theoretically. In Figure 25, the panels show the time series of NO and O_3 at coincident points during JFMA at ~ 45 km in the 65°-85° N latitude range for 2004, 2006, 2009, 2013, and 2019. ACE measurements for NO and O_3 were used for 2004 and 2006. In 2009, the O_3 measurements at 45 km were unavailable for SOFIE. Thus, ACE measurements of NO and O_3 were used in 2009. Note that, in 2004, ACE O_3 data was unavailable in January and after March. In 2006 and 2009, ACE data are unavailable after March as ACE views altitudes lower than 65° during this time. The y-axes for NO and O_3 vary for all years and have been plotted at inconsistent values as the two species vary largely during the same period in different years depending on the amount of NO reaching ~ 45 km and the corresponding O_3 decrease. For example, in 2004, large amounts of NO, higher than 200 ppbv, reached ~ 45 km, whereas, in 2009, the highest recorded value was less than 8 ppbv. Plotting these values on a common-valued axis would diminish the representation of NO in 2009 and, thus, underestimate the negative correlation between NO and O_3.

As seen in Figure 22 (left panels), the tip of the descent tongue transported NO well into the stratosphere in 2004 and 2019. High amounts of NO are recorded in both years, and the corresponding O_3 values decrease dip significantly during the peak in NO concentration. In 2004, during early March, the NO values were very high (reached ~227 ppbv), and the O_3 measurement at the same coincidence was ~ 3 ppmv. In 2019, the NO value in late February peaked at ~ 65 ppbv, and the O_3 value at the same coincidence was ~ 2.6 ppmv. In 2006, during mid-March, the NO concentration peaked having a value of ~ 25.6 ppbv, and the coincident O_3 measurement was

~ 4 ppmv. Thus, strong NO peaks in 2004, 2006, and 2019 indicate periods after the SSWs where the transport event enhanced NO in the stratosphere and a sharp decline in O_3 with increasing NO.

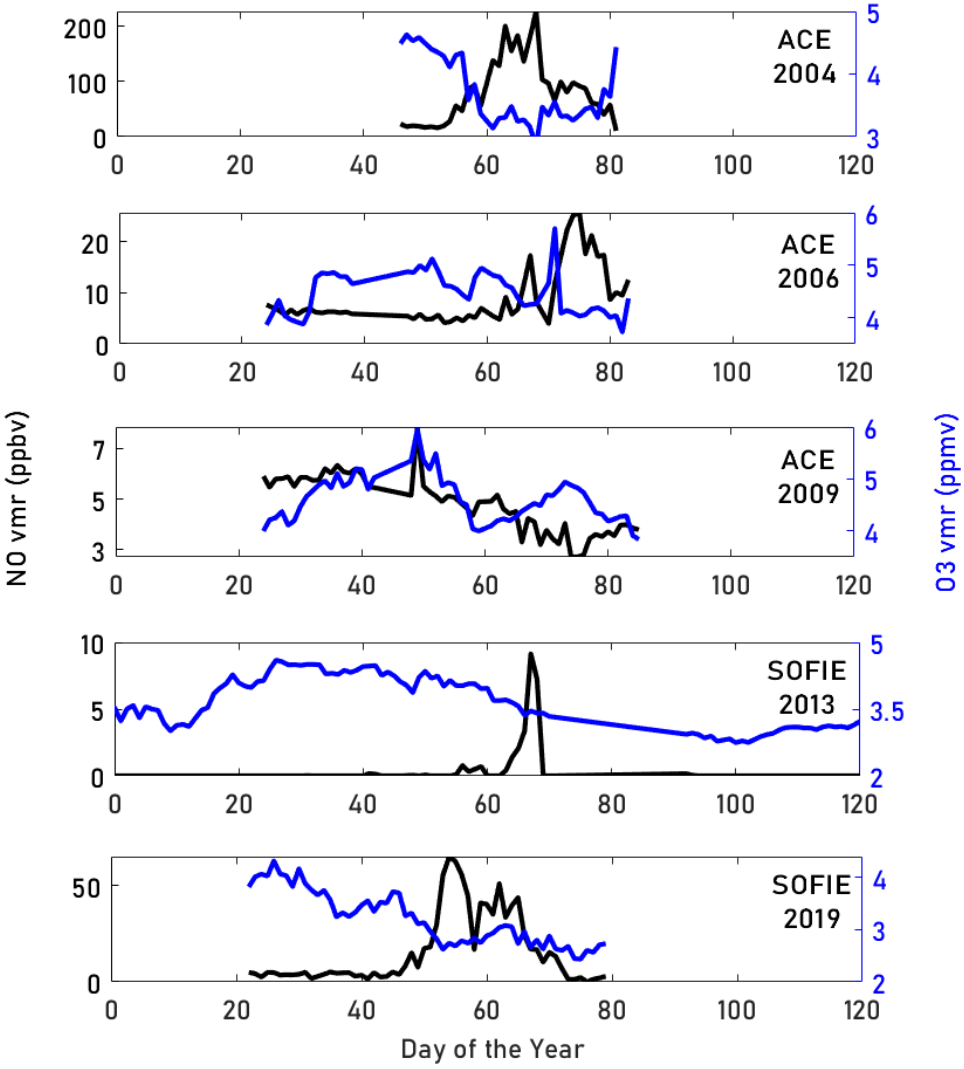

Figure 25. Time-series showing the correlation between NO (ppbv, black solid lines) and O_3 (ppmv, blue solid lines) during JFMA, between 65° – 85° N at ~ 45km for ACE (2004, 2006, and 2009) and SOFIE (2013, and 2019).

In 2013, the second-lowest descent of NO to ~ 45 km was reported. In early March, the NO peak attained the value of ~ 9.1 ppbv, and the coincident O_3 measurement was ~ 3.5 ppmv. It is also evident that the O_3 in 2013 was consistently stable and gradually decreased after NO peaked. In

all five years, the lowest NO values were reported at ~ 45 km in 2009, and the tip of the NO descent tongue did not travel into the stratosphere as per ACE measurements. Although SOFIE measurements observed the transport of the tip of the NO descent tongue into the stratosphere (Figure 22 (third figure in the left panels)), we use ACE measurements for NO and O_3 for consistency due to the unavailability of coincident SOFIE O_3 measurements in 2009. The NO during mid-February was under ~ 8 ppbv, and the coincident O_3 value was ~ 6 ppmv. Since ACE did not report the transport of NO to ~ 45 km, the NO measured at this altitude is attributed to what is already present in the atmosphere. NO is continuously being created, destroyed, or transported. Thus, the preexisting NO in the stratosphere can be possibly attributed to that transported previously from higher altitudes. However, it is most likely associated with the NO locally formed in the stratosphere from reactions of N_2O originally generated at the earth's surface and transported to the stratosphere through the troposphere (where N_2O is unreactive) (*Crutzen* 1970).

The NO and coincident O_3 measurements suggest that in all years, there was a strong negative correlation between NO and O_3 with particularly low O_3 values during very high NO, like in 2004 and 2019. The O_3 values were very high during periods of consistently low NO, observed very distinctly in 2009 and 2013. It is thus established that the negative correlation between NO and O_3 at and below 45 km is unmistakable (*Randall et al.,* 2005).

So far, we have established that the five major SSW-triggered descent events transported enhanced NO to the stratosphere, assessed the correlation of NO with H_2O, and discussed the relation between NO and O_3 below 45 km. These occurrences impact the chemistry and composition from the lower thermosphere to the stratosphere. The most recent event of 2019 transported NO farthest in altitude (i.e., the end of the tongue reached the farthest into the stratosphere of all years). We

now evaluate the descent rate to understand the pace of the varying chemistry in the MLT and stratosphere in 2019.

In Figure 26 - Figure 30, the vertical transport rates of 2004, 2006, 2009, 2013, and 2019, respectively events are plotted. These estimates of the vertical transport rates are calculated using the procedure first used by *Schoeberl et al.*, (1992) and have been used by Lee et al., (2011) for CO and H_2O. These estimates are carried out using the mixing ratios of NO, H_2O, and CH_4. While the thrust of calculating the vertical transport rate is to understand the descent in 2019, we also plot results calculated for the past events and evaluate their behavior compared to 2019.

In 2019, for forty days starting from the SSW date, i.e., 2 January 2019, we track the mixing ratios of 100 different and equally spaced values of NO (between 0.1 to 1000 ppbv), H_2O (1 to 7 ppmv), and CH_4 (0.1 to 0.5 ppmv). We divide the forty days into four ten-day bins and record the altitude at which each value was observed per ten-day bin. A line is fit into the altitudes as a function of day, and the slope of the line is the vertical descent rate. A similar approach is used for all other years, except, the mixing ratio ranges vary for different years.

In 2004, ACE data was unavailable for the first thirty-five days of the year. Thus, the transport from day 31 until day 60 from the SSW date is tracked in an effort to capture the final stages of the descent and plotted as three ten-day bins in Figure 26. Days 31 to 40 indicate a peak in CH_4 near ~ 57 km, which is not visible from days 41 to 50. However, H_2O and CH_4 are distinct, with small peaks between 44 and 45 km on days 51 and 60.

The SSW event took place on 21 January in 2006. However, the transport of the tongue of air is more visibly evident starting from mid-late February, as seen in Figure 27 and also seen in Figure 22 (second figure in the left panels). Since ACE, like SOFIE, provides information about one

latitude per day, it is possible that there is a descent at other latitudes that ACE does not capture, although we assume that the zonal averages give a reasonable estimate for the NO enhancements. Since the transport event is more vigorous towards the end of February, we track the vertical transport rate for the first eighty days starting from the SSW date as eight ten-day bins. The transport of NO, H_2O, and CH_4 is not very distinct during the first forty days. A peak in H_2O concentration is observed at ~ 67 km during days 50 to 59. In the following 10 days, two H_2O peaks are visible at ~ 56 and 48 km, after which there are no distinct peaks during the last ten days.

In 2009, SOFIE measurements reported transport into the stratosphere. In Figure 28, in the first ten days starting from the SSW date, traces of NO and a defined transport of H_2O and CH_4 are observed. A small peak in H_2O is visible at ~ 78 km and a distinct one in CH_4 at ~ 53 km. Between days 20 and 29, the CH_4 peak travels to ~ 47 km and to ~ 42 km the following ten days.

In Figure 29, the 2013 vertical descent rate shows a well-defined peak in H_2O at ~ 80 km during the first ten days starting from the descent. Two peaks from tracking H_2O are recorded in the next ten days. A peak in CH_4 is observed at ~ 43 km during days 30 to 39 from the SSW date, and no distinct peak is recorded in the last ten days, although there is a visible descent. *Bailey et al.,* (2014) analyzed this in greater detail.

For 2019, Figure 30 shows that the NO descent was very strong during the first ten days and began at high altitudes after the SSW. Two peaks in H_2O are recorded at ~ 74 km and ~ 68 km with a descent rate of ~ -0.4 cm/s. In the second bin, the NO peak descended to ~ 72 km at ~ -1.2 cm/s, and the H_2O peak descended to ~ 63 km at ~ -0.7 cm/s. In the third bin, the NO peak is less distinct than before and moves further down, while new NO formation was recorded at high altitudes, as shown in Figure 22 (bottom figure in the left panels). New NO with values as those chosen for

tracking purposes (for vertical transport rate determination) lead to new NO representation at high altitudes in the third bin. There were no visible peaks for any species in the fourth bin, and the descent decreases upon reaching below ~ 55 km.

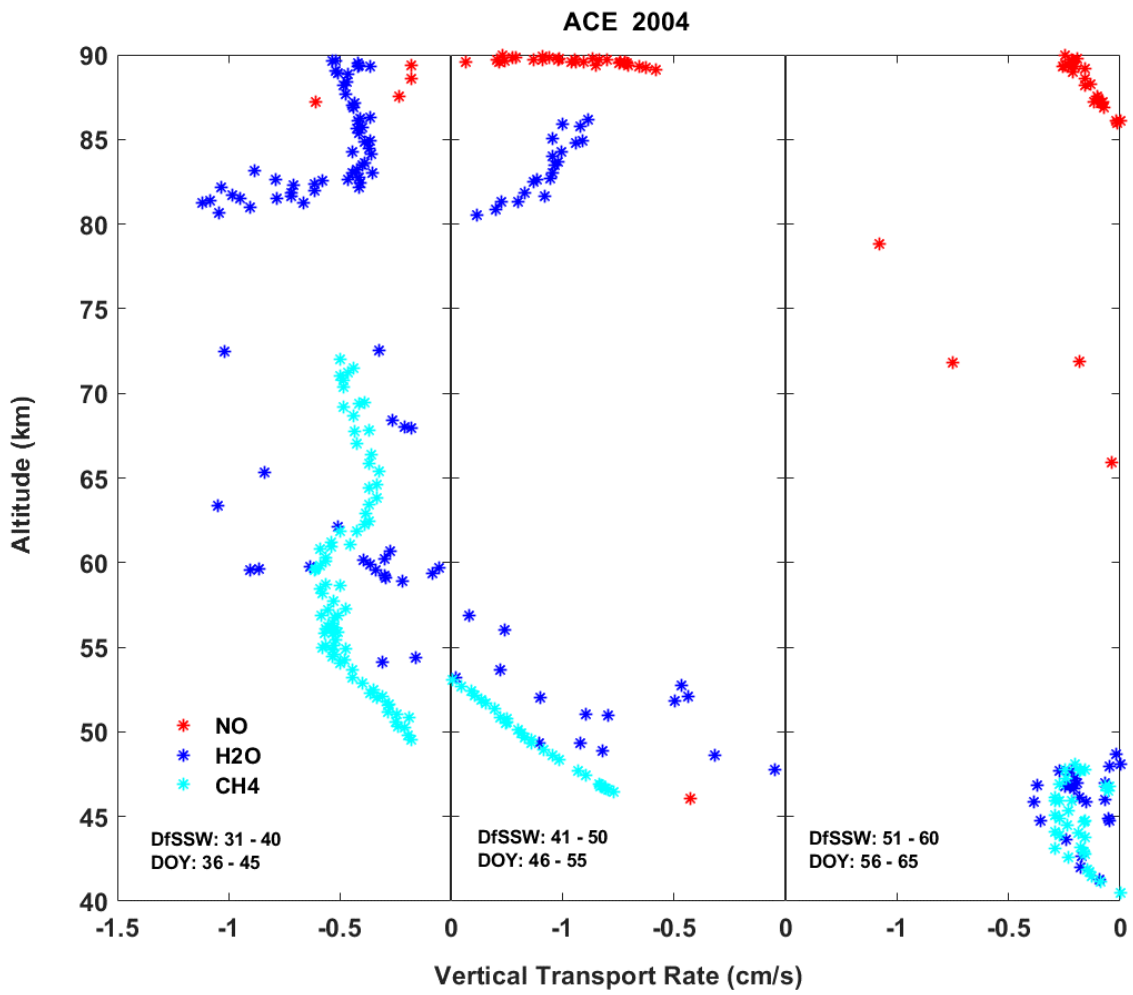

Figure 26. Vertical transport rates estimated by tracking constant mixing ratios of NO, H_2O, and CH_4 from ACE data. Each panel represents vertical transport rates at 10 successive day intervals starting with the 31st day immediately after the SSW (Days from SSW – DfSSW) on 5 January 2004 (Day of Year – DOY 5).

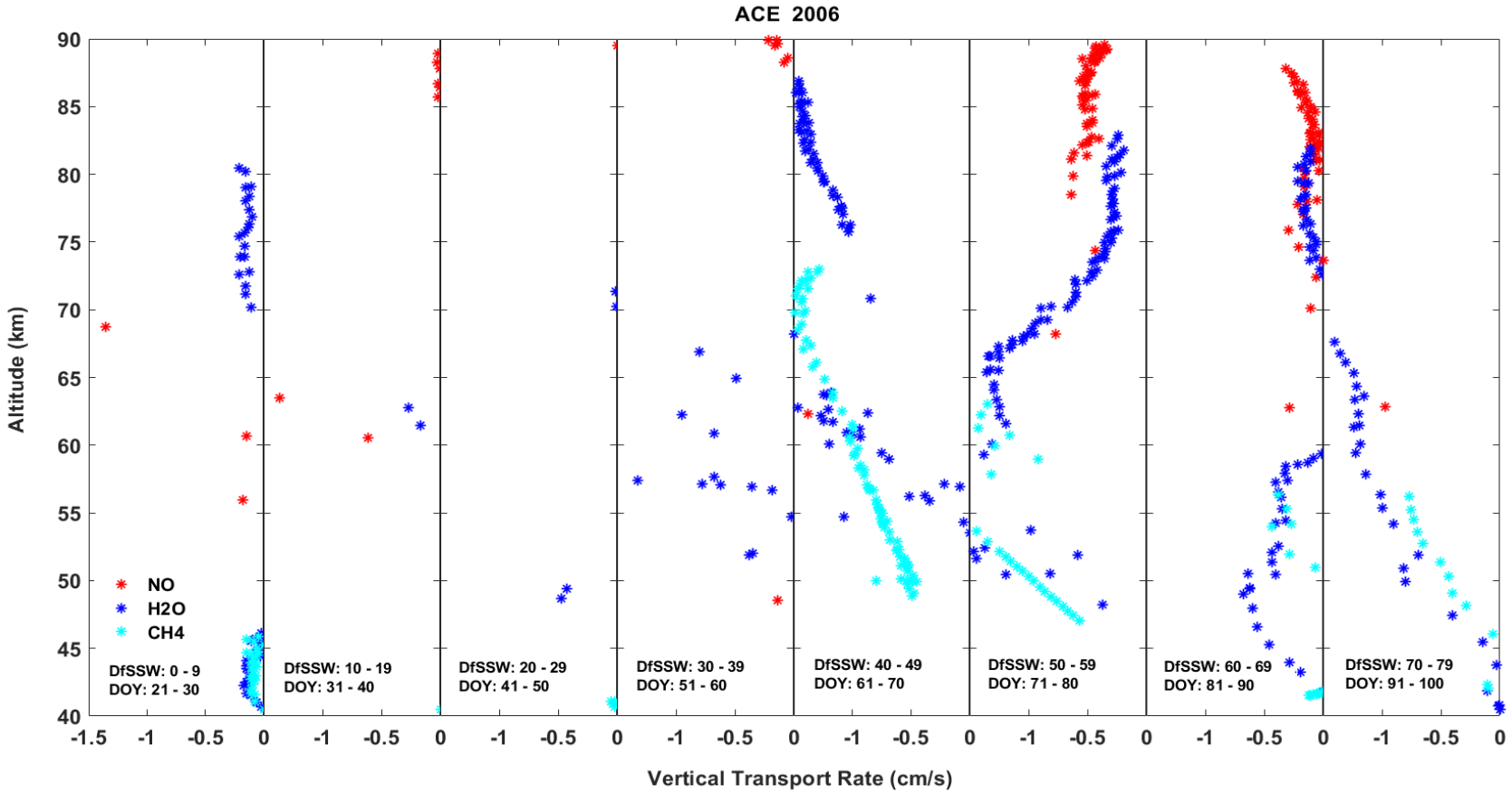

Figure 27. Same as Figure 26, but starting with the first 10 days immediately after the SSW (0 – 10 days from SSW – DfSSW) on 21 January 2006 (Day of Year - DOY 21).

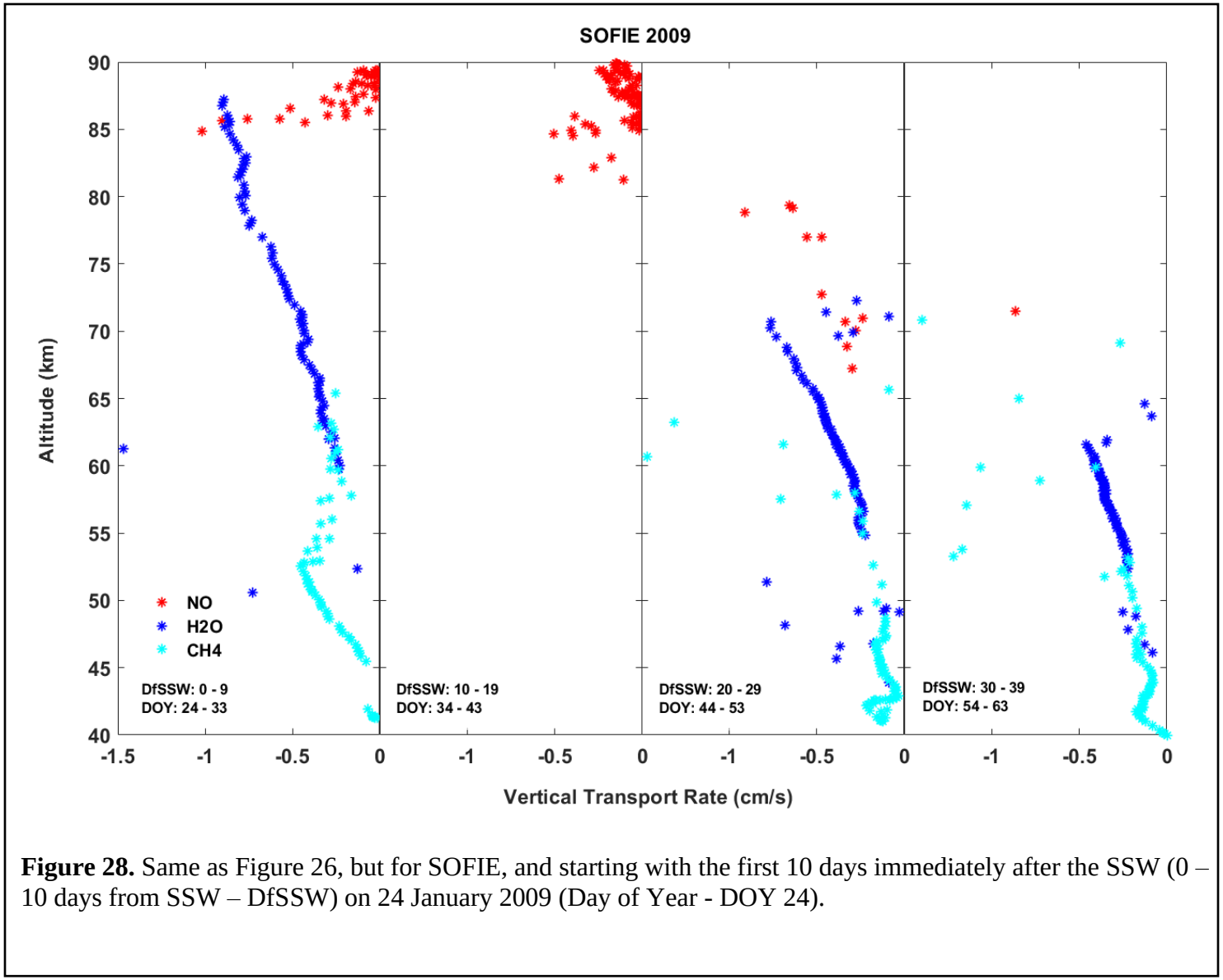

Figure 28. Same as Figure 26, but for SOFIE, and starting with the first 10 days immediately after the SSW (0 – 10 days from SSW – DfSSW) on 24 January 2009 (Day of Year - DOY 24).

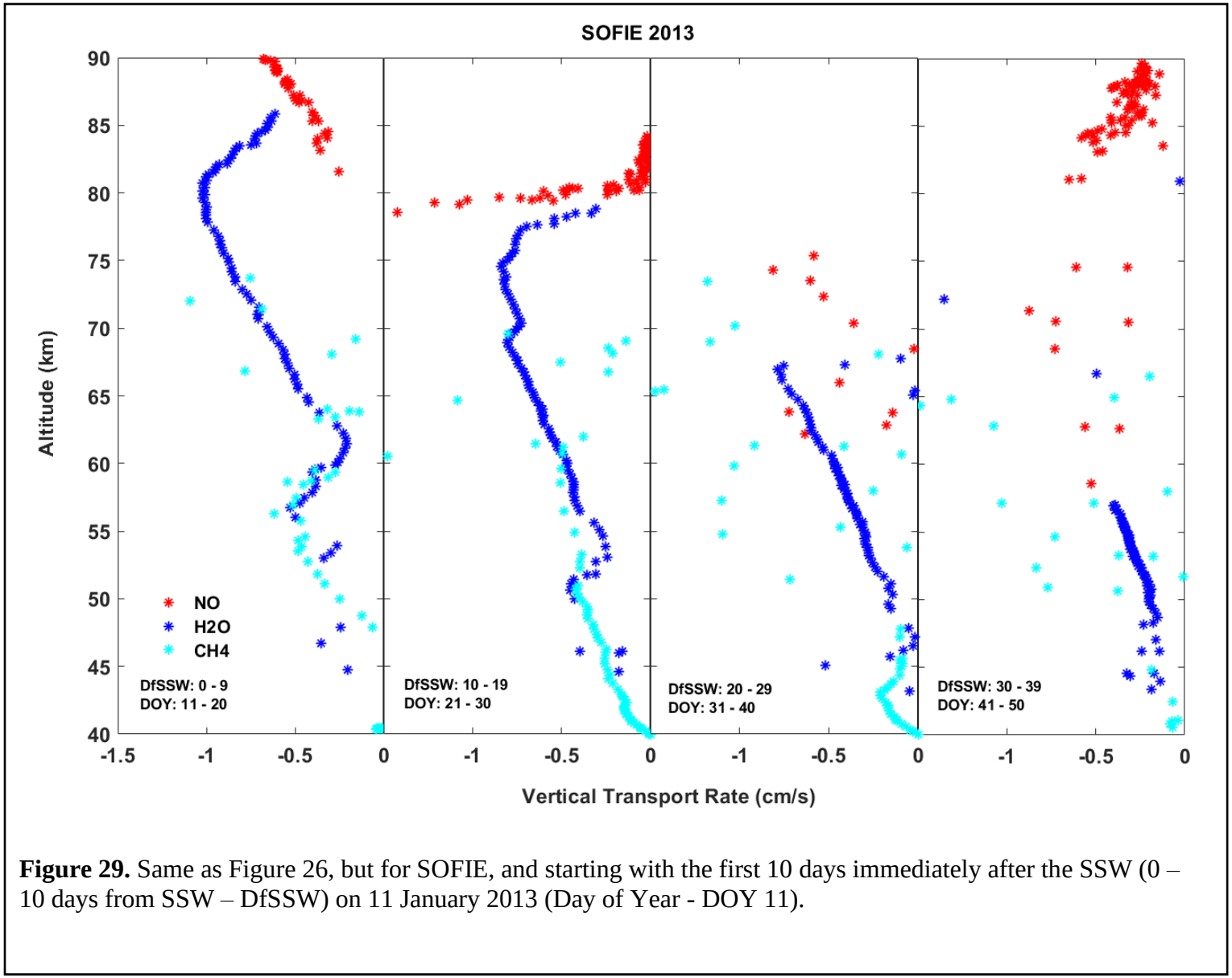

Figure 29. Same as Figure 26, but for SOFIE, and starting with the first 10 days immediately after the SSW (0 – 10 days from SSW – DfSSW) on 11 January 2013 (Day of Year - DOY 11).

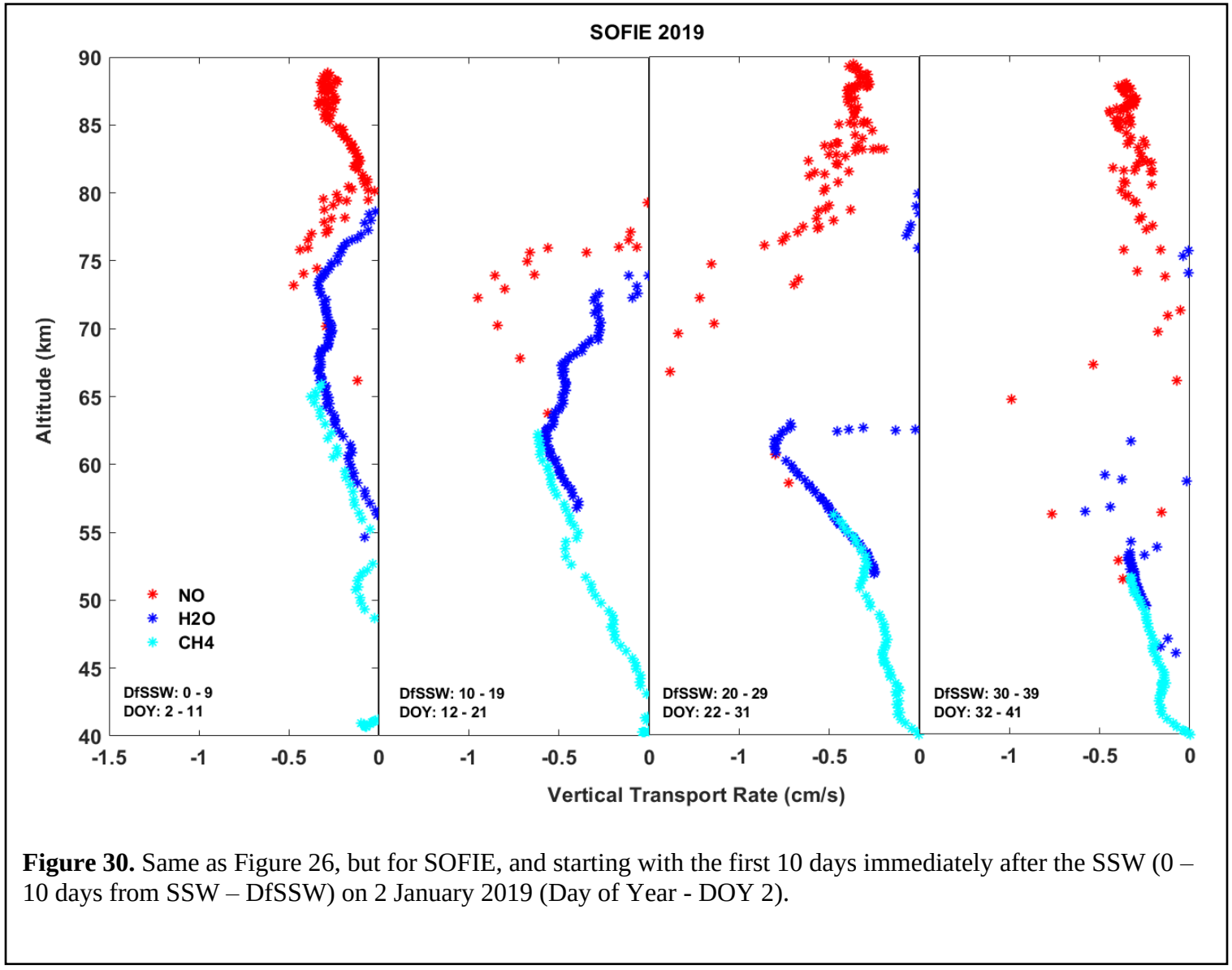

Figure 30. Same as Figure 26, but for SOFIE, and starting with the first 10 days immediately after the SSW (0 – 10 days from SSW – DfSSW) on 2 January 2019 (Day of Year - DOY 2).

4.6 Discussion

In this paper, we look at the five SSWs since 2004 that led to major transport events to the stratosphere and investigate the composition response of the MLT and the stratosphere. ACE measurements are used when SOFIE data are unavailable and to compare the descent at certain altitudes. The results in Section 4.5 indicate that 2004, 2006, 2009, 2013, and 2019 are associated with unusual meteorology and planetary wave activity. Previous efforts have also concluded similar results (*Hauchecorne et al.,* 2007; *Manney et al.,* 2008a, 2008b; *Sathishkumar and Sridharan,* 2009; *Siskind et al.,* 2007; *Winick et al.,* 2009; *Randall et al.,* 2009; *Bailey et al.,* 2014). The 2019 transport event is the most recent major transport event and stands in the ranks of the other four major transport events discussed. A thorough analysis of the 2019 event and comparison with other transport years indicate similarities between these events, such as usually strong and persistent SSWs in January, following an elevated stratopause and NO descent to the stratosphere. In all years except 2004, for which data is unavailable before 21 February, all NO decent events coincide with the elevated stratopause formation. To make a wholistic comparison between all five events, we evaluate them based on different parameters such as the farthest descent in altitude, the amount of NO entering the stratosphere (at ~ 50 km), and the intensity of the event at 55 km, where an anti-correlation with H_2O is used.

Of all years, the 2019 descent reached the farthest altitude into the stratosphere, with the end of the NO tongue located at ~ 36.5 km, followed by 2004 (at ~ 37.5 km). For a fair comparison, all five years are evaluated from ACE data. Upon descending into the stratopause region, the intensity of the descent is determined using H_2O as a tracer. The established negative correlation with NO during SSWs is used to infer that at ~ 55 km, the strength of the 2009 event was the highest (lowest minimum H_2O reported) the 2019 event was the lowest (highest minimum H_2O reported). The

intensities of the descent at ~ 55 km are indicators of how far in altitude the EPP-NO originated. It can be concluded that the NO in 2019 emerged at much lower altitudes than in other years. Figure 22 (left panels) shows that the 2009 tongue at 50 km has the narrowest width (indicating the shortest temporal existence) of all years. For fairness, NO descents for all years from ACE were compared (but not plotted). As per ACE measurements, the end part of the NO tongue in 2009 did not travel farther than 50 km, which is inconsistent with SOFIE. This inconsistency is addressed in Section 4.5 but at ~ 55 km. We believe the discrepancies at both altitudes emerge from the same reasons. From ACE measurements, the highest NO concentration at ~ 50 km was recorded in 2004 and the lowest in 2009. This also indicates that while the 2009 event was the most intense descent event at 55 km, its intensity receded upon descent to ~ 50 km. At altitudes where stratospheric O_3 is vulnerable to catalytic destruction, NO and O_3 variations at ~ 45 km indicated that NO peaks in 2004, 2013, and 2019 during JFMA led to a sharp decrease in coincident O_3 profiles. The descent rate was high in 2019 and the peak descended by ~ 5-6 km every ten days. Although ACE data during January 2004 was unavailable and thus, the descent rate for 2004 for a few weeks after the SSW event could not be calculated, other years indicate that the descent speeds were largest in the events where descent travelled the farthest. The 2019 event bolsters the inference that the enhanced amount of NO reaching the NH was controlled not just by the EPP before and at the time of the SSW but also by meteorology.

Before quantifying the total entrainment of upper atmospheric NO transported to the stratosphere, issues concerning meteorology need to be addressed. *Bailey et al.*, (2002) and *Barth et al.*, (2003) reported that the NO concentrations peak above 100 km during sunlit conditions. *Smith et al.*, (2011) found that above 90 km, there is not much extension in the downward branch of the residual circulation and stated the uncertainty in the roles of diffusive and advective transport in bringing

NO to lower altitudes from the upper atmosphere. They indicated that the MLT transitions from downwelling below 90-95 km and upwelling at higher altitudes at the winter pole. Further, they found that the transport due to upward motion at these altitudes has little to no effect on the vertical distribution of the NO mixing ratio. *Sheese et al.,* (2013) indicate that nighttime NO peak heights descend above and from 100 km during the beginning of autumn to near 90-95 km during the winter solstice. *Sheese et al.,* (2011) discussed the descent with temperature investigations and a decrease in mesopause height, suggesting a net downward advection in this region. These studies suggest that eddy and molecular diffusion are the most probable causes of the downward transport of NO. Although these possibilities are uncertain, further analysis is necessary. *Bailey et al.,* (2022) discussed the contributions of eddy diffusion and advection in transport and suggested that diffusion may be important at the highest altitudes during the SSW-triggered events. It is important to note here that the air transporting NO and H_2O is rich in the former but transports poor amounts of the latter. This suggests that the NO transport is more strongly attributed to advection as diffusion would be inclined to uniformly mix the air. While advection can be considered the more dominant feature corresponding to the transport of NO to the stratosphere, the role of diffusion may be important in getting the NO to an altitude where the advection is strong enough to transport it to the rest of the way into the stratosphere. Thus, a pertinent question open for future research within the science community is to identify the individual contributions of advection and diffusion in transporting NO from the lower thermosphere into the stratosphere. Future SSW-triggered studies will then have to consider the roles of advection and diffusion and independently identify their altitude-specific dominance as possible sources of high NO mixing ratios in the stratosphere.

The other issue is that SOFIE observes just outside the polar night. Thus, the enhancements recorded by SOFIE may not be an absolute representation of the entire polar region. The

photochemical lifetime across the polar night boundary varies rapidly, with a strong dependence on the extent of the meridional transport. Thus, it is likely for the NO abundance to have a sharp gradient while moving towards higher latitudes. Further investigation needs to be done to understand the complete NO profile in the MLT (and the stratosphere) to understand the coupling between upper and middle atmospheric NO. New and comprehensive approaches, including reevaluations of current procedures, are necessary to address significant disagreements in the extant observational NO database.

4.7 Conclusion

The 2019 SSW-triggered NO transport event is significant to the chemistry of the MLT and the stratosphere. This study investigated the 2019 SSW and the transport event that followed. We compare our findings from 2019 with those of the previous major transport events since 2004 and report the key findings.

The 2019 SSW led to a large amount of NO transport into the stratosphere and was comparable to the previous four major transport events. The NO at ~ 55 km recorded in anti-correlation to H_2O concluded that the 2019 transport event was the fifth most intense since 2004. The end part of the NO tongue in 2019 traveled the farthest in the stratosphere in the last 19 years. The NO recorded at ~ 50 km in 2019 was higher than in 2009 when geomagnetic activity was slightly higher or comparable. The 2019 event reaffirms that the enhanced NO reaching the stratosphere was not just attributed to EPP before and during the SSW but also to the unusual meteorology. Higher than usual amounts of O were reported in the mesosphere due to SSW-triggered transport in 2019, just as in other descent years.

The thrust of this study has been to investigate the dynamics of the five major SSWs and the transport events that transported enhanced NO to the stratosphere, impacting the chemistry and

composition of the MLT to the stratosphere. We conclude that the 2019 SSW event was similar to the four major events of the past and unusual meteorology played an important role in the transport activity. High descent rates were recorded for events where the descent travelled the farthest. While we report our observations from the five major transport events, focusing on the 2019 event, we also evaluate the limitations and discrepancies that need to be addressed in future studies.

4.8 Acknowledgments

This research is funded by AIM through the NASA Small Explorer program. We acknowledge the AIM and SOFIE operation teams for their excellent support with this work. We thank the ACE team for their data. We thank the Geo Forschungs Zentrum (GFZ) German Research Center for Geosciences and NASA's Modern-Era Retrospective analysis for Research and Applications (MERRA-2).

4.9 Open Research

The SOFIE Version 1.3 data for temperature, NO, H_2O, and O_3, and documentation are publicly available at the SOFIE website - http://sofie.gats-inc.com/getdata . ACE Version 4.1 temperature, NO, H_2O, and O_3 data are available upon request at the ACE website https://databace.scisat.ca/level2/ace_v4.1_v4.2/ . GFZ German Research Center for Geosciences Ap index data are available at https://www.gfz-potsdam.de/en/section/geomagnetism/data-products-services/ and NASA's MERRA-2 zonal wind data are available at https://acd-ext.gsfc.nasa.gov/Data_services/met/ .

References

Andrews, D.G., Holton, J.R. and Leovy, C.B., 1987. Middle atmosphere dynamics (No. 40). Academic press.

Bailey, S.M., Thurairajah, B., Randall, C.E., Holt, L., Siskind, D.E., Harvey, V.L., Venkataramani, K., Hervig, M.E., Rong, P. and Russell III, J.M., 2014. A multi tracer analysis of thermosphere to stratosphere descent triggered by the 2013 Stratospheric Sudden Warming. *Geophysical Research Letters,* 41(14), pp.5216-5222. https://doi.org/10.1002/2014GL059860

Bailey, S.M., McClintock, W.E., Carstens, J.N., Thurairajah, B., Das, S., Randall, C.E., Harvey, V.L., Siskind, D.E., Stevens, M.H. and Venkataramani, K., 2022. Sounding Rocket Observation of Nitric Oxide in the Polar Night. *Journal of Geophysical Research: Space Physics*, 127(6), p.e2021JA030257. https://doi.org/10.1029/2021JA030257

Baldwin, M.P., Ayarzagüena, B., Birner, T., Butchart, N., Butler, A.H., Charlton-Perez, A.J., Domeisen, D.I., Garfinkel, C.I., Garny, H., Gerber, E.P. and Hegglin, M.I., 2021. Sudden stratospheric warmings. *Reviews of Geophysics*, 59(1), p.e2020RG000708. https://doi.org/10.1029/2020RG000708

Bernath, P., 2001. Atmospheric chemistry experiment (ACE): An overview. *Spectroscopy from Space*, pp.147-160. https://doi.org/10.1007/978-94-010-0832-7_9

Barth, C.A. and Bailey, S.M., 2004. Comparison of a thermospheric photochemical model with Student Nitric Oxide Explorer (SNOE) observations of nitric oxide. *Journal of Geophysical Research: Space Physics*, 109(A3).doi:10.1029/2003JA010227.

Bernath, P.F., McElroy, C.T., Abrams, M.C., Boone, C.D., Butler, M., Camy-Peyret, C., Carleer, M., Clerbaux, C., Coheur, P.F., Colin, R. and DeCola, P., 2005. Atmospheric chemistry experiment (ACE): mission overview. *Geophysical research letters*, 32(15). doi: 10.1029/2005GL022386.

Boone, C.D., Nassar, R., Walker, K.A., Rochon, Y., McLeod, S.D., Rinsland, C.P. and Bernath, P.F., 2005. Retrievals for the atmospheric chemistry experiment Fourier-transform spectrometer. *Applied optics*, 44(33), pp.7218-7231. https://doi.org/10.1364/AO.44.007218

Butler, A.H., Seidel, D.J., Hardiman, S.C., Butchart, N., Birner, T. and Match, A., 2015. Defining sudden stratospheric warmings. *Bulletin of the American Meteorological Society*, 96(11), pp.1913-1928. https://doi.org/10.1175/BAMS-D-13-00173.1

Butler, A.H., Sjoberg, J.P., Seidel, D.J. and Rosenlof, K.H., 2017. A sudden stratospheric warming compendium. *Earth System Science Data*, 9(1), pp.63-76. https://doi.org/10.5194/essd-9-63-2017

Carleer, M.R., Boone, C.D., Walker, K.A., Bernath, P.F., Strong, K., Sica, R.J., Randall, C.E., Vömel, H., Kar, J., Höpfner, M. and Milz, M., 2008. Validation of water vapour profiles from the Atmospheric Chemistry Experiment (ACE). *Atmospheric Chemistry and Physics Discussions*, 8(2), pp.4499-4559. https://doi.org/10.5194/acpd-8-4499-2008

Chandran, A., Garcia, R.R., Collins, R.L. and Chang, L.C., 2013. Secondary planetary waves in the middle and upper atmosphere following the stratospheric sudden warming event of January 2012. *Geophysical Research Letters*, 40(9), pp.1861-1867. https://doi.org/10.1002/ grl.50373

Chandran, A., Collins, R.L. and Harvey, V.L., 2014. Stratosphere-mesosphere coupling during stratospheric sudden warming events. *Advances in Space Research*, 53(9), pp.1265-1289. https://doi.org/10.1016/j.asr.2014.02.005

Charlton, A.J. and Polvani, L.M., 2007. A new look at stratospheric sudden warmings. Part I: Climatology and modeling benchmarks. *Journal of climate*, 20(3), pp.449-469. https://doi.org/10.1175/JCLI3996.1

Cortesi, U., Lambert, J.C., De Clercq, C., Bianchini, G., Blumenstock, T., Bracher, A., Castelli, E., Catoire, V., Chance, K.V., De Maziere, M. and Demoulin, P., 2007. Geophysical validation of MIPAS-ENVISAT operational ozone data. *Atmospheric Chemistry and Physics*, 7(18), pp.4807-4867. https://doi.org/10.5194/acp-7-4807-2007

Crutzen, P.J., 1970. The influence of nitrogen oxides on the atmospheric ozone content. *Quarterly Journal of the Royal Meteorological Society*, 96(408), pp.320-325. https://doi.org/10.1002/qj.49709640815

De Mazière, M., Vigouroux, C., Bernath, P.F., Baron, P., Blumenstock, T., Boone, C., Brogniez, C., Catoire, V., Coffey, M., Duchatelet, P. and Griffith, D., 2008. Validation of ACE-FTS v2. 2 methane profiles from the upper troposphere to the lower mesosphere. *Atmospheric Chemistry and Physics*, 8(9), pp.2421-2435. https://doi.org/10.5194/acp-8-2421-2008

Dupuy, E., Walker, K.A., Kar, J., Boone, C.D., McElroy, C.T., Bernath, P.F., Drummond, J.R., Skelton, R., McLeod, S.D., Hughes, R.C. and Nowlan, C.R., 2009. Validation of ozone measurements from the Atmospheric Chemistry Experiment (ACE). *Atmospheric Chemistry and Physics*, 9(2), pp.287-343. https://doi.org/10.5194/acp-9-287-2009

Esplin, R.W., Batty, J.C., Jensen, M.A., McLain, D., Stauder, J.L., Jensen, S.M., Stump, C., Robinson, D.M. and Dodgen, J., 1994, September. Sounding of the atmosphere using broadband emission radiometer (SABER): sensor system overview. In *Infrared Spaceborne Remote Sensing II* (Vol. 2268, pp. 207-217). SPIE. https://doi.org/10.1117/12.185831

Evans, W.F.J., McDade, I.C., Yuen, J. and Llewellyn, E.J., 1988. A rocket measurement of the O2 infrared atmospheric (0–0) band emission in the dayglow and a determination of the mesospheric ozone and atomic oxygen densities. *Canadian Journal of Physics*, 66(11), pp.941-946. https://doi.org/10.1139/p88-151

PF, B., CD, W., KA, F., MJ, H., RS, F., RA, M., GL, S., MJ, D., WH, D., BJ, C. and RE, C., RP, and Wagner, PA: Validation of Aura Microwave Limb Sounder stratospheric ozone measurements. *J. Geophys. Res.-Atmos*, 113, p.D15S20.https://doi.org/10.1029/2007JD008771, 2008.

Funke, B., López-Puertas, M., Gil-López, S., Von Clarmann, T., Stiller, G.P., Fischer, H. and Kellmann, S., 2005. Downward transport of upper atmospheric NOx into the polar stratosphere and lower mesosphere during the Antarctic 2003 and Arctic 2002/2003 winters. *Journal of Geophysical Research: Atmospheres*, 110(D24). https://doi.org/10.1029/2005 JD006463

Funke, B., López-Puertas, M., García-Comas, M., Stiller, G.P., Von Clarmann, T., Höpfner, M., Glatthor, N., Grabowski, U., Kellmann, S. and Linden, A., 2009. Carbon monoxide distributions from the upper troposphere to the mesosphere inferred from 4.7 μm non-local thermal equilibrium emissions measured by MIPAS on Envisat. *Atmospheric Chemistry and Physics*, 9(7), pp.2387-2411. https://doi.org/10.5194/acp-9-2387-2009

Fussen, D., Vanhellemont, F., Dodion, J., Bingen, C., Walker, K.A., Boone, C.D., McLeod, S.D. and Bernath, P.F., 2005. Initial intercomparison of ozone and nitrogen dioxide number density profiles retrieved by the ACE-FTS and GOMOS occultation experiments. *Geophysical research letters*, 32(16). https://doi.org/10.1029/2005GL022468

Gómez-Ramírez, D., McNabb, J.W., Russell, J.M., Hervig, M.E., Deaver, L.E., Paxton, G. and Bernath, P.F., 2013. Empirical correction of thermal responses in the Solar Occultation for Ice Experiment nitric oxide measurements and initial data validation results. *Applied optics*, 52(13), pp.2950-2959. https://doi.org/10.1364/AO.52.002950

Gordley, L.L., Hervig, M.E., Fish, C., Russell III, J.M., Bailey, S., Cook, J., Hansen, S., Shumway, A., Paxton, G., Deaver, L. and Marshall, T., 2009. The solar occultation for ice experiment. *Journal of Atmospheric and Solar-Terrestrial Physics*, 71(3-4), pp.300-315.doi:10.1016/j.jastp.2008.07.012.

Greer, K., Thayer, J.P. and Harvey, V.L., 2013. A climatology of polar winter stratopause warmings and associated planetary wave breaking. *Journal of Geophysical Research: Atmospheres*, 118(10), pp.4168-4180.doi:10.1002/jgrd.50289.

Gunson, M.R., Abbas, M.M., Abrams, M.C., Allen, M., Brown, L.R., Brown, T.L., Chang, A.Y., Goldman, A., Irion, F.W., Lowes, L.L. and Mahieu, E., 1996. The Atmospheric Trace Molecule Spectroscopy (ATMOS) experiment: Deployment on the ATLAS space shuttle missions. *Geophysical Research Letters*, 23(17), pp.2333-2336. https://doi.org/10.1029/96GL01569

Guttu, S., Orsolini, Y., Stordal, F., Limpasuvan, V. and Marsh, D.R., 2020. WACCM simulations: Decadal winter-to-spring climate impact on middle atmosphere and troposphere from medium energy electron precipitation. *Journal of Atmospheric and Solar-Terrestrial Physics*, 209, p.105382. https://doi.org/10.1016/j.jastp.2020.105382

Hauchecorne, A., Bertaux, J.L., Dalaudier, F., Russell III, J.M., Mlynczak, M.G., Kyrölä, E. and Fussen, D., 2007. Large increase of NO2 in the north polar mesosphere in January–February 2004: Evidence of a dynamical origin from GOMOS/ENVISAT and SABER/TIMED data. *Geophysical Research Letters*, 34(3).doi:10.1029/2006GL027628

Hervig, M.E., Marshall, B.T., Bailey, S.M., Siskind, D.E., Russell III, J.M., Bardeen, C.G., Walker, K.A. and Funke, B., 2019. Validation of Solar Occultation for Ice Experiment (SOFIE)

nitric oxide measurements. *Atmospheric Measurement Techniques,* 12(6), pp.3111-3121.doi:10.5194/amt-2019-56.

Hoffmann, P., Singer, W., Keuer, D., Hocking, W.K., Kunze, M. and Murayama, Y., 2007. Latitudinal and longitudinal variability of mesospheric winds and temperatures during stratospheric warming events. *Journal of Atmospheric and Solar-Terrestrial Physics*, 69(17-18), pp.2355-2366. https://doi.org/10.1016/j.jastp.2007.06.010

Holt, L.A., Randall, C.E., Harvey, V.L., Remsberg, E.E., Stiller, G.P., Funke, B., Bernath, P.F. and Walker, K.A., 2012. Atmospheric effects of energetic particle precipitation in the Arctic winter 1978–1979 revisited. *Journal of Geophysical Research: Atmospheres,* 117(D5).doi:10.1029/2011JD016663.

Holt, L.A., Randall, C.E., Peck, E.D., Marsh, D.R., Smith, A.K. and Harvey, V.L., 2013. The influence of major sudden stratospheric warming and elevated stratopause events on the effects of energetic particle precipitation in WACCM. *Journal of Geophysical Research: Atmospheres,* 118(20), pp.11-636. https://doi.org/10.1002/2013JD020294

Jackman, C.H., Marsh, D.R., Vitt, F.M., Garcia, R.R., Fleming, E.L., Labow, G.J., Randall, C.E., López-Puertas, M., Funke, B., Von Clarmann, T. and Stiller, G.P., 2008. Short-and medium-term atmospheric constituent effects of very large solar proton events. *Atmospheric Chemistry and Physics,* 8(3), pp.765-785. https://doi.org/10.5194/acp-8-765-2008

Jin, J.J., Semeniuk, K., Jonsson, A.I., Beagley, S.R., McConnell, J.C., Boone, C.D., Walker, K.A., Bernath, P.F., Rinsland, C.P., Dupuy, E. and Ricaud, P., 2005. Co-located ACE-FTS and Odin/SMR stratospheric-mesospheric CO 2004 measurements and comparison with a GCM. *Geophysical research letters,* 32(15). https://doi.org/10.1029/2005GL022433

Kerzenmacher, T.E., Walker, K.A., Strong, K., Berman, R., Bernath, P.F., Boone, C.D., Drummond, J.R., Fast, H., Fraser, A., MacQuarrie, K. and Midwinter, C., 2005. Measurements of O3, NO2 and temperature during the 2004 Canadian Arctic ACE Validation Campaign. *Geophysical Research Letters,* 32(16). https://doi.org/10.1029/2005GL023032

Kerzenmacher, T., Wolff, M.A., Strong, K., Dupuy, E., Walker, K.A., Amekudzi, L.K., Batchelor, R.L., Bernath, P.F., Berthet, G., Blumenstock, T. and Boone, C.D., 2008. Validation of NO 2 and NO from the Atmospheric Chemistry Experiment (ACE). *Atmospheric Chemistry and Physics,* 8(19), pp.5801-5841.https://doi.org/10.5194/acp-8-5801-2008

Kvissel, O.K., Orsolini, Y.J., Stordal, F., Limpasuvan, V., Richter, J. and Marsh, D.R., 2012. Mesospheric intrusion and anomalous chemistry during and after a major stratospheric sudden warming. *Journal of atmospheric and solar-terrestrial physics*, 78, pp.116-124. https://doi.org/10.1016/j.jastp.2011.08.015

Labitzke, K., 1981. Stratospheric-mesospheric midwinter disturbances: A summary of observed characteristics. *Journal of Geophysical Research: Oceans*, 86(C10), pp.9665-9678. https://doi.org/10.1029/JC086iC10p09665

Labitzke, K., 1982. On the interannual variability of the middle stratosphere during the northern winters. *Journal of the Meteorological Society of Japan. Ser. II*, 60(1), pp.124-139. https://doi.org/10.2151/jmsj1965.60.1_124

Lee, S.H. and Butler, A.H., 2020. The 2018–2019 Arctic stratospheric polar vortex. *Weather*, 75(2), pp.52-57. https://doi.org/10.1002/wea.3643

Limpasuvan, V., Orsolini, Y.J., Chandran, A., Garcia, R.R. and Smith, A.K., 2016. On the composite response of the MLT to major sudden stratospheric warming events with elevated stratopause. *Journal of Geophysical Research: Atmospheres*, 121(9), pp.4518-4537. https://doi.org/10.1002/2015JD024401

Liu, H.L. and Roble, R.G., 2002. A study of a self-generated stratospheric sudden warming and its mesospheric–lower thermospheric impacts using the coupled TIME-GCM/CCM3. *Journal of Geophysical Research: Atmospheres*, 107(D23), pp.ACL-15. https://doi.org/10.1029/2001JD001533

Llewellyn, E.J., McDade, I.C., Moorhouse, P. and Lockerbie, M.D., 1993. Possible reference models for atomic oxygen in the terrestrial atmosphere. *Advances in Space Research*, 13(1), pp.135-144. https://doi.org/10.1016/0273-1177(93)90013-2

Llewellyn, E.J. and McDade, I.C., 1996. A reference model for atomic oxygen in the terrestrial atmosphere. *Advances in Space Research*, *18*(9-10), pp.209-226. https://doi.org/10.1016/0273-1177(96)00059-2

López-Puertas, M., Funke, B., Clarmann, T.V., Fischer, H. and Stiller, G.P., 2007. The stratospheric and mesospheric NO y in the 2002–2004 polar winters as measured by MIPAS/Envisat. *Solar Variability and Planetary Climates*, pp.403-416.doi:10.1007/s11214-006-9073-2

Madronich, S. and Flocke, S., 1999. The role of solar radiation in atmospheric chemistry. In Environmental photochemistry (pp. 1-26). *Springer, Berlin, Heidelberg*. DOI: 10.1007/978-3-540-69044-3_1

Manney, G.L., Daffer, W.H., Strawbridge, K.B., Walker, K.A., Boone, C.D., Bernath, P.F., Kerzenmacher, T., Schwartz, M.J., Strong, K., Sica, R.J. and Krüger, K., 2008. The high Arctic in extreme winters: vortex, temperature, and MLS and ACE-FTS trace gas evolution. *Atmospheric Chemistry and Physics*, 8(3), pp.505-522. https://doi.org/10.5194/acp-8-505-2008

Manney, G.L., Krüger, K., Pawson, S., Minschwaner, K., Schwartz, M.J., Daffer, W.H., Livesey, N.J., Mlynczak, M.G., Remsberg, E.E., Russell III, J.M. and Waters, J.W., 2008. The evolution of the stratopause during the 2006 major warming: Satellite data and assimilated meteorological analyses. *Journal of Geophysical Research: Atmospheres*, 113(D11). doi:10.1029/2007JD009097

Manney, G.L., Schwartz, M.J., Krüger, K., Santee, M.L., Pawson, S., Lee, J.N., Daffer, W.H., Fuller, R.A. and Livesey, N.J., 2009. Aura Microwave Limb Sounder observations of dynamics

and transport during the record-breaking 2009 Arctic stratospheric major warming. *Geophysical Research Letters*, 36(12). https://doi.org/10.1029/2009GL038586

Marsh, D., Smith, A., Brasseur, G., Kaufmann, M. and Grossmann, K., 2001. The existence of a tertiary ozone maximum in the high-latitude middle mesosphere. *Geophysical Research Letters*, 28(24), pp.4531-4534. https://doi.org/10.1029/2001GL013791

Matsuno, T., 1971. A dynamical model of the stratospheric sudden warming. *Journal of Atmospheric Sciences*, 28(8), pp.1479-1494. https://doi.org/10.1175/1520-0469(1971)028<1479:ADMOTS>2.0.CO;2

McDade, I.C., Llewellyn, E.J. and Harris, F.R., 1985. Atomic oxygen concentrations in the lower auroral thermosphere. *Advances in space research*, 5(7), pp.229-232. https://doi.org/10.1016/0273-1177(85)90379-5

McHugh, M., Magill, B., Walker, K.A., Boone, C.D., Bernath, P.F. and Russell III, J.M., 2005. Comparison of atmospheric retrievals from ACE and HALOE. *Geophysical Research Letters*, 32(15). https://doi.org/10.1029/2005GL022403

McInturff, R.M., 1978. Stratospheric warmings: Synoptic, dynamic and general-circulation aspects (No. NASA-RP-1017).

Mlynczak, M.G., Marshall, B.T., Martin-Torres, F.J., Russell III, J.M., Thompson, R.E., Remsberg, E.E. and Gordley, L.L., 2007. Sounding of the Atmosphere using Broadband Emission Radiometry observations of daytime mesospheric O2 (1Δ) 1.27 μm emission and derivation of ozone, atomic oxygen, and solar and chemical energy deposition rates. *Journal of Geophysical Research: Atmospheres*, 112(D15). https://doi.org/10.1029/2006JD008355

Orsolini, Y.J., Limpasuvan, V., Pérot, K., Espy, P., Hibbins, R., Lossow, S., Larsson, K.R. and Murtagh, D., 2017. Modelling the descent of nitric oxide during the elevated stratopause event of January 2013. *Journal of Atmospheric and Solar-Terrestrial Physics*, 155, pp.50-61. https://doi.org/10.1016/j.jastp.2017.01.006

Pérot, K., Urban, J. and Murtagh, D.P., 2014. Unusually strong nitric oxide descent in the Arctic middle atmosphere in early 2013 as observed by Odin/SMR. *Atmospheric Chemistry and Physics*, 14(15), pp.8009-8015. https://doi.org/10.5194/acp-14-8009-2014

Pérot, K. and Orsolini, Y.J., 2021. Impact of the major SSWs of February 2018 and January 2019 on the middle atmospheric nitric oxide abundance. *Journal of Atmospheric and Solar-Terrestrial Physics*, 218, p.105586. https://doi.org/10.1016/j.jastp.2021.105586

Petelina, S.V., Llewellyn, E.J., Walker, K.A., Degenstein, D.A., Boone, C.D., Bernath, P.F., Haley, C.S., Von Savigny, C., Lloyd, N.D. and Gattinger, R.L., 2005. Validation of ACE-FTS stratospheric ozone profiles against Odin/OSIRIS measurements. *Geophysical research letters*, 32(15). https://doi.org/10.1029/2005GL022377

Randall, C.E., Rusch, D.W., Bevilacqua, R.M., Hoppel, K.W. and Lumpe, J.D., 1998. Polar ozone and aerosol measurement (POAM) II stratospheric NO2, 1993–1996. *Journal of*

Geophysical Research: Atmospheres, 103(D21), pp.28361-28371. https://doi.org/10.1029/98JD02092

Randall, C.E., Siskind, D.E. and Bevilacqua, R.M., 2001. Stratospheric NOx enhancements in the southern hemisphere vortex in winter/spring of 2000. *Geophysical Research Letters*, 28(12), pp.2385-2388. https://doi.org/10.1029/2000GL012746

Randall, C.E., Harvey, V.L., Manney, G.L., Orsolini, Y., Codrescu, M., Sioris, C., Brohede, S., Haley, C.S., Gordley, L.L., Zawodny, J.M. and Russell III, J.M., 2005. Stratospheric effects of energetic particle precipitation in 2003–2004. *Geophysical Research Letters*, 32(5).doi:10.1029/004GL022003.

Randall, C.E., Harvey, V.L., Singleton, C.S., Bernath, P.F., Boone, C.D. and Kozyra, J.U., 2006. Enhanced NOx in 2006 linked to strong upper stratospheric Arctic vortex. *Geophysical Research Letters*, 33(18).doi:10.1029/2006GL027160.

Randall, C.E., Harvey, V.L., Singleton, C.S., Bailey, S.M., Bernath, P.F., Codrescu, M., Nakajima, H. and Russell III, J.M., 2007. Energetic particle precipitation effects on the Southern Hemisphere stratosphere in 1992–2005. *Journal of Geophysical Research: Atmospheres*, 112(D8). https://doi.org/10.1029/2006JD007696

Randall, C.E., Harvey, V.L., Siskind, D.E., France, J., Bernath, P.F., Boone, C.D. and Walker, K.A., 2009. NOx descent in the Arctic middle atmosphere in early 2009. *Geophysical Research Letters*, 36(18).doi:10.1029/2009GL039706.

Rong, P., Russell III, J.M., Gordley, L.L., Hervig, M.E., Deaver, L., Bernath, P.F. and Walker, K.A., 2010. Validation of v1. 022 mesospheric water vapor observed by the Solar Occultation for Ice Experiment instrument on the Aeronomy of Ice in the Mesosphere satellite. *Journal of Geophysical Research: Atmospheres*, 115(D24).doi:10.1029/2010JD014269.

Rong, P.P., Russell III, J.M., Marshall, B.T., Siskind, D.E., Hervig, M.E., Gordley, L.L., Bernath, P.F. and Walker, K.A., 2016. Version 1.3 AIM SOFIE measured methane (CH4): Validation and seasonal climatology. *Journal of Geophysical Research: Atmospheres*, 121(21), pp.13-158.doi:10.1002/2016JD025415.

Russell III, J.M., Mlynczak, M.G. and Gordley, L.L., 1994, September. Overview of the sounding of the atmosphere using broadband emission radiometry (saber) experiment for the thermosphere-ionsphere-mesosphere energetics and dynamics (timed) mission. *In Optical Spectroscopic Techniques and Instrumentation for Atmospheric and Space Research* (Vol. 2266, pp. 406-415). SPIE. https://doi.org/10.1117/12.187579

Russell III, J.M., Mlynczak, M.G., Gordley, L.L., Tansock Jr, J.J. and Esplin, R.W., 1999, October. Overview of the SABER experiment and preliminary calibration results. In *Optical spectroscopic techniques and instrumentation for atmospheric and space research III* (Vol. 3756, pp. 277-288). SPIE. https://doi.org/10.1117/12.366382

Russell III, J.M., Bailey, S.M., Gordley, L.L., Rusch, D.W., Horányi, M., Hervig, M.E., Thomas, G.E., Randall, C.E., Siskind, D.E., Stevens, M.H. and Summers, M.E., 2009. The Aeronomy of Ice in the Mesosphere (AIM) mission: Overview and early science results. *Journal of Atmospheric and Solar-Terrestrial Physics*, 71(3-4), pp.289-299.doi:10.1016/j.jastp.2008.08.011.

Salmi, S.M., Verronen, P.T., Thölix, L., Kyrölä, E., Backman, L., Karpechko, A.Y. and Seppälä, A., 2011. Mesosphere-to-stratosphere descent of odd nitrogen in February–March 2009 after sudden stratospheric warming. *Atmospheric Chemistry and Physics*, 11(10), pp.4645-4655.doi:10.5194/acp-11-4645-2011.

Sander, S.P., Friedl, R.R., DeMore, W.B., Golden, D.M., Kurylo, M.J., Hampson, R.F., Huie, R.E., Moortgat, G.K., Ravishankara, A.R., Kolb, C.E. and Molina, M.J., 2000. Chemical kinetics and photochemical data for use in stratospheric modeling. Evaluation Number 13.

Sathishkumar, S. and Sridharan, S., 2009. Planetary and gravity waves in the mesosphere and lower thermosphere region over Tirunelveli (8.7 N, 77.8 E) during stratospheric warming events. *Geophysical Research Letters*, 36(7).doi:10.1029/2008GL037081

Scherhag, R., 1952. Die explosionartigen stratospharenwarmungen des spatwinters 1951-1952. Ber. Deut. Wetterd., 6, pp.51-63. CRID:1573950399672518528

Schoeberl, M.R., Lait, L.R., Newman, P.A. and Rosenfield, J.E., 1992. The structure of the polar vortex. *Journal of Geophysical Research: Atmospheres*, 97(D8), pp.7859-7882. https://doi.org/10.1029/91JD02168

Sheese, P.E., Gattinger, R.L., Llewellyn, E.J., Boone, C.D. and Strong, K., 2011. Nighttime nitric oxide densities in the Southern Hemisphere mesosphere–lower thermosphere. Geophysical Research Letters, 38(15).

Sheese, P.E., Strong, K., Gattinger, R.L., Llewellyn, E.J., Urban, J., Boone, C.D. and Smith, A.K., 2013. Odin observations of Antarctic nighttime NO densities in the mesosphere–lower thermosphere and observations of a lower NO layer. Journal of Geophysical Research: Atmospheres, 118(13), pp.7414-7425.

Sheese, P.E., Walker, K.A., Boone, C.D., McLinden, C.A., Bernath, P.F., Bourassa, A.E., Burrows, J.P., Degenstein, D.A., Funke, B., Fussen, D. and Manney, G.L., 2016. Validation of ACE-FTS version 3.5 NO y species profiles using correlative satellite measurements. *Atmospheric Measurement Techniques*, 9(12), pp.5781-5810.https://doi.org/10.5194/amt-9-5781-2016, 2016.

Shi, Y., Shulga, V., Ivaniha, O., Wang, Y., Evtushevsky, O., Milinevsky, G., Klekociuk, A., Patoka, A., Han, W. and Shulga, D., 2020. Comparison of major sudden stratospheric warming impacts on the mid-latitude mesosphere based on local microwave radiometer CO observations in 2018 and 2019. *Remote Sensing*, 12(23), p.3950. https://doi.org/10.3390/rs12233950

Shepherd, M.G., Meek, C.E., Hocking, W.K., Hall, C.M., Partamies, N., Sigernes, F., Manson, A.H. and Ward, W.E., 2020. Multi-instrument study of the mesosphere-lower thermosphere dynamics at 80 N during the major SSW in January 2019. *Journal of Atmospheric and Solar-Terrestrial Physics,* 210, p.105427. https://doi.org/10.1016/j.jastp.2020.105427

Sica, R.J., Izawa, M.R.M., Walker, K.A., Boone, C., Petelina, S.V., Argall, P.S., Bernath, P., Burns, G.B., Catoire, V., Collins, R.L. and Daffer, W.H., 2008. Validation of the Atmospheric Chemistry Experiment (ACE) version 2.2 temperature using ground-based and space-borne measurements. *Atmospheric Chemistry and Physics,* 8(1), pp.35-62. https://doi.org/10.5194/acp-8-35-2008

Siskind, D.E., Eckermann, S.D., Coy, L., McCormack, J.P. and Randall, C.E., 2007. On recent interannual variability of the Arctic winter mesosphere: Implications for tracer descent. *Geophysical Research Letters,* 34(9).doi:10.1029/2007GL029293.

Siskind, D.E., Eckermann, S.D., McCormack, J.P., Coy, L., Hoppel, K.W. and Baker, N.L., 2010. Case studies of the mesospheric response to recent minor, major, and extended stratospheric warmings. *Journal of Geophysical Research: Atmospheres,* 115(D3).doi:10.1029/2010JD014114.

Smith, A.K. and Marsh, D.R., 2005. Processes that account for the ozone maximum at the mesopause. *Journal of Geophysical Research: Atmospheres,* 110(D23). https://doi.org/10.1029/2005JD006298

Smith, A.K., López-Puertas, M., García-Comas, M. and Tukiainen, S., 2009. SABER observations of mesospheric ozone during NH late winter 2002–2009. *Geophysical Research Letters,* 36(23). https://doi.org/10.1029/2009GL040942

Smith, A.K., Marsh, D.R., Mlynczak, M.G. and Mast, J.C., 2010. Temporal variations of atomic oxygen in the upper mesosphere from SABER. *Journal of Geophysical Research: Atmospheres,* 115(D18). https://doi.org/10.1029/2009JD013434

Smith, A.K., Marsh, D.R., Mlynczak, M.G., Russell, J.M. and Mast, J.C., 2011. SABER observations of daytime atomic oxygen and ozone variability in the mesosphere. In *Aeronomy of the Earth's Atmosphere and Ionosphere* (pp. 75-82). Springer, Dordrecht. DOI: 10.1007/978-94-007-0326-1_5

Smith, A.K., Harvey, V.L., Mlynczak, M.G., Funke, B., García-Comas, M., Hervig, M., Kaufmann, M., Kyrölä, E., López-Puertas, M., McDade, I. and Randall, C.E., 2013. Satellite observations of ozone in the upper mesosphere. *Journal of Geophysical Research: Atmospheres,* 118(11), pp.5803-5821. https://doi.org/10.1002/jgrd.50445

Solomon, S., Crutzen, P.J. and Roble, R.G., 1982. Photochemical coupling between the thermosphere and the lower atmosphere: 1. Odd nitrogen from 50 to 120 km. *Journal of Geophysical Research: Oceans,* 87(C9), pp.7206-7220.doi:10.1029/JC087iC09p07206

Stauder, J.L. and Esplin, R.W., 1998, November. Stray light design and analysis of the Sounding of the Atmosphere using Broadband Emission Radiometry (SABER) telescope. In *Infrared Spaceborne Remote Sensing VI* (Vol. 3437, pp. 52-59). SPIE. https://doi.org/10.1117/12.331334

Stevens, M.H., Deaver, L.E., Hervig, M.E., Russell III, J.M., Siskind, D.E., Sheese, P.E., Llewellyn, E.J., Gattinger, R.L., Höffner, J. and Marshall, B.T., 2012. Validation of upper mesospheric and lower thermospheric temperatures measured by the Solar Occultation for Ice Experiment. *Journal of Geophysical Research: Atmospheres*, 117(D16). https://doi.org/10.1029/2012JD017689

Walker, K.A., Randall, C.E., Trepte, C.R., Boone, C.D. and Bernath, P.F., 2005. Initial validation comparisons for the Atmospheric Chemistry Experiment (ACE-FTS). *Geophysical research letters*, 32(16). https://doi.org/10.1029/2005GL022388

Waymark, C., Walker, K.A., Boone, C.D. and Bernath, P.F., 2013. ACE-FTS version 3.0 data set: validation and data processing update. *Annals of Geophysics*, 56. doi: 10.4401/ag-6339

Winick, J.R., Wintersteiner, P.P., Picard, R.H., Esplin, D., Mlynczak, M.G., Russell III, J.M. and Gordley, L.L., 2009. OH layer characteristics during unusual boreal winters of 2004 and 2006. *Journal of Geophysical Research: Space Physics*, 114(A2). doi:10.1029/2008JA013688.

5. Ozone Enhancement During the 2019 Sudden Stratospheric Warming in the Southern Hemisphere from Multi-Instrument Analysis

Das, Saswati, et al. “Ozone Enhancement During the 2019 Sudden Stratospheric Warming in the Southern Hemisphere from Multi-Instrument Analysis.” *Journal of Geophysical Research-Atmospheres (Under Review By Co-authors)*

5.1 Abstract

The sudden stratospheric warming (SSW) event that occurred in August 2019 in the southern hemisphere was the strongest event since 2002. Using measurements from NASA's ozone watch, we infer that the 2019 SSW led to large enhancements in stratospheric ozone and an ozone hole smaller than that recorded in 2002. Using zonal wind, temperature, and wave 1 and 2 amplitude of geopotential height from MERRA -2, we compare the 2019 event to that of 2002. We investigate the role of polar stratospheric clouds (PSC) in the ozone loss process and use ground station data to detect PSC presence before and after the 2019 SSW. Using satellite data from three different instruments that complement each other, we present the temporal variation of the chlorine reservoir species and the ozone-depleting active form. We also use satellite data for temperature and to investigate the enhancement in ozone and nitric acid. Our results show that there is a positive anomaly in temperature and ozone measurements that are enhanced after the SSW event. A decrease in PSC concentration is observed around the start of the SSW as a result of PSC evaporation due to the increase in the stratospheric temperature. Consequentially, lower ozone and nitric acid loss are reported after the SSW. This study investigates, using ground-based, satellite, and reanalysis data, the 2019 Antarctic ozone enhancement that occurred as a result of the SSW event and evaluates the role of PSC reduction in the reduction in the ozone hole size in 2019.

5.2 Plain Language Summary

Ozone in the stratosphere is destroyed by the presence of polar stratospheric clouds (PSCs), which provide their surface for the conversion of halogen reservoir species into reactive ozone-destroying forms. Sudden stratospheric warmings (SSWs) are rare in the southern hemisphere (SH) due to the absence of highly varying topography. Thus, the 2019 SSW event during the SH winter was a rare occurrence that led to enhanced temperatures, which evaporated the PSCs. In the absence of PSCs, there was no surface for halogen reservoir species to convert into ozone-destroying reactive forms. Further, PSCs lead to nitric acid reduction through uptake, in the absence of which there is delayed halogen deactivation. Thus, through multi-instrument and lidar measurements, the PSC presence and variation in the concentration of ozone, halogen reservoir, and reactive species are tracked alongside temperature and nitric acid. We investigate the dynamics and chemistry associated with the ozone enhancement and small ozone hole in 2019.

5.3 Introduction

Sudden stratospheric warming (SSW) events in recent times have gathered considerable attention from the scientific community. SSWs play an important role in the changing climate of the Earth's atmosphere (*Pedatella et al.,* 2018). SSW events are identified by the weakening or reversal in the zonal winds at 10 hPa and 60^{o} N/S around the polar vortex region. This is associated with temperature gradient reversal at 10 hPa and poleward of 60^{o} N/S (*Scherhag,* 1952; *WMO,* 1978; *Andrews et al.,* 1987). SSW events are driven by the dynamics that occur when large-scale planetary waves are generated in the troposphere as a result of large-scale topography (mountains, the difference in temperatures between warm ocean and cold land interfaces). These planetary waves occur over different spatial and temporal scales. The stratosphere acts as a filter and allows only the larger waves to propagate into the stratosphere, which does so only during the wintertime.

The breaking of the planetary waves in the stratosphere decelerates the polar vortex circulation and results in a sharp increase in the polar stratospheric temperature (*Butler et al.,* 2015).

SSW events are more common in the northern hemisphere (NH) as there is more variable topography. Thus, the north polar vortex is typically more disturbed by planetary wave activity, and SSWs are reported to occur once every two years, on average, in the NH (*Charlton & Polvani,* 2007; *Blume et al.,* 2012; *Butler et al.,* 2017; *Wang et al.,* 2019). The SH, however, is not home to drastically varying geographical conditions, and thus, very few SSW events have been reported in the SH. Documented SSW events in the SH include that of 2002 (*WMO,* 2002; *Baldwin et al.,* 2003; *Varotsos,* 2003; *Cho et al.,* 2004; *Dowdy et al.,* 2004*; Krüger et al.,* 2005), 2010 (*de Laat & van Weele,* 2011; *Eswaraiah et al.,* 2016, 2017, 2018) and the most recent one in 2019 (*Eswaraiah et al.,* 2020; *Safieddine et al.,* 2020; *Yamazaki et al.,* 2020). By the definition established by the WMO/IQSY (World Meteorological Organization/International Years of the Quiet Sun) for major SSWs (*WMO/IQSY,* 1964), the 2019 SSW can be classified as a major one like the 2002 SSW event, while the 2010 SSW was a minor one.

SSW events lead to enhanced mixing at the polar vortex edge. This is important to the concentration of ozone (O_3) as strong depletion in its concentration occurs inside the polar vortex. This depletion is directly related to the permeability and stability of the polar vortex (*Holton et al.,* 1995). The depletion of polar O_3 in the SH has a strong correlation with temperature. Polar stratospheric clouds (PSCs) play an important role in the destruction of stratospheric O_3 during the winter and spring at high latitudes (*Tritscher et al.,* 2021). PSCs provide sites for heterogenous reactions that convert stable chlorine reservoir species into O_3-destroying reactive forms catalytically (*Solomon,* 1999; *Solomon et al.,* 1986). PSCs delay chlorine deactivation through the removal of gas-phase HNO_3 (nitric acid) and H_2O (water) by the sedimentation of large nitric acid

tetrahydrate (NAT), which leads to prolonged O_3 depletion in the stratosphere. A detailed analysis of the mechanism of O_3 destruction by PSCs is provided in Section 5.5.

During the 2019 SSWs, large temperature increments in the polar stratosphere led to the evaporation of the PSCs and, thus, led to an absence of surface for the chlorine reservoirs to convert into reactive O_3 -destroying reactive forms. Large enhancements in Antarctic O_3 were observed in 2019. The concentrations of Arctic O_3 have been reported to increase in the wintertime during SSWs since the O_3 loss depends on the timing and intensity of the SSW event (*Kuttippurath & Nikulin,* 2012). Faster downward motions during SSWs carry O_3-rich air from above and outside the vortex, thus, strongly impacting the polar stratospheric O_3 depletion (*Solomon,* 1999). Past studies have shown that SSW events lead to circulation anomalies in both hemispheres and can propagate to the troposphere and impact the tropospheric circulation (*Baldwin & Dunkerton,* 1999; *Baldwin,* 2003; *Cohen et al.,* 2007; *Kidston et al.,* 2015; *Lim et al.,* 2018, 2020). O_3 hole characteristics such as size, location, and duration are directly affected by the SSW events.

In this study, we investigate the 2019 SSW event that occurred in late August. The 2019 event was comparable to that of the 2002 event (*Hendon et al.,* 2019) and showed strong stationary planetary wave activity (*Yamazaki et al.,* 2020). We evaluate the O_3 enhancement in the stratosphere and the variation in the halogen reservoir and reactive-halogen species, along with the variation in the HNO_3 concentration. We use ground-based lidar measurements for determining PSC occurrences; NASA O_3 watch data for quantifying the O_3 hole area and polar cap O_3; satellite measurements of temperature, O_3, HNO_3, H_2O, $ClONO_2$ (chlorine nitrate), HCl (hydrochloric acid), ClO (chlorine monoxide) and reanalysis data for temperature, zonal winds and wave 1 and 2 amplitudes of geopotential height. The paper is arranged as follows: data are explained in Section 5.4, O_3 loss

mechanism is explained in Section 5.5, results are presented in Section 5.6 and discussed and summarized in Section 5.7.

5.4 Data Sets

Data from five different sources are used in this study. MERRA-2 is used for SSW analysis, ground station data has been used for the estimation of PSC concentration, and O_3 measurements from NASA O_3 Watch are used to study the varying O_3 hole in the last 43 years (1979 – 2021). The data from three satellite instruments are used to study and varying chemistry of the stratosphere and quantify the corresponding O_3 loss during the 2019 SSW. This is due to two reasons. First, the satellite instruments view different latitudes from August to November. Thus, to have continuous measurements during the four-month period, observations from three instruments are simultaneously used to ensure that measurements from at least one instrument are available at a given time from August to November. Second, the interaction between several chemical species is important for the understanding of the chemistry that triggers O_3 loss. Not all species are observed by a single instrument. Thus, it is necessary to make collective use of data from all three instruments.

5.4.1 SOFIE: Temperature, O_3, H_2O, and NO

SOFIE (*Gordley et al.*, 2009) is a solar occultation instrument onboard the AIM (Aeronomy of Ice in the Mesosphere) (*Russell et al.*, 2009) spacecraft. SOFIE was launched in 2007 with the goal of determining PMC (Polar Mesospheric Clouds) particle characteristics, meteoric particles, and atmospheric waves. SOFIE measures the solar energy passing through the limb of the earth's atmosphere at sunrise/sunset relative to the spacecraft. SOFIE makes observations at 16 wavelengths from 0.29 μm to 5.26 μm and retrieves profiles of temperature, O_3, CH_4, NO, H_2O, and CO_2, with a vertical resolution of ~1.8 km. Typically, SOFIE makes high latitude

measurements between 65°-85° in both hemispheres. In 2017, the SOFIE sunrise/sunset hemispheres switched, due to which there is no data in the SH from 2017 until late 2018. In 2019, SOFIE resumed measuring in the SH. However, it viewed low-mid latitudes and did not start operating at its usual SH latitudes until almost 2021. Thus, the latitudes viewed by SOFIE during our period of interest (ASON) are always north of – 65°S. In this study, we use SOFIE version 1.3 temperature (*Stevens et al.,* 2012), NO (*Hervig et al.,* 2019), H_2O (*Rong et al.,* 2010), and O_3 (*Smith et al.,* 2013; *Das et al. (under review)*) retrievals.

5.4.2 ACE: Temperature, O_3, HNO_3, ClO, $ClONO_2$, and HCl

ACE-FTS (*Bernath.,* 2001, 2005; *Boone et al.,* 2005) is a solar occultation instrument that flies onboard the Canadian SciSat spacecraft. It was preceded by the ATOMS (Atmospheric Trace Molecule Spectroscopy) experiment (*Gunson et al.,* 1996). ACE was launched at 650 km and 74° inclination into the low earth orbit. It measures minor atmospheric species in the earth's atmosphere at a high resolution (0.02 cm^{-1}) spectra in the medium-long infrared range of 2.2-13 μm (*Bernath et al.,* 2005). Data recorded by ACE include temperature, pressure, and the volume mixing ratios (VMRs) of the species retrieved from the occultation spectra. In the absence of sufficiently accurate meteorological data from the full range of altitudes, temperature measurements of ACE are derived directly from the ACE spectra, followed by the calculation of the synthetic spectra in the global fitting procedure to retrieve the VMRs of the target species. In this study, we use ACE version 4.1 data for temperature (*Sica et al.,* 2008), O_3 (*Walker et al.,* 2005; *Petelina et al.,* 2005a; *Fussen et al.,* 2005; *McHugh et al.,* 2005; *Kerzenmacher et al.,* 2005; *Cortesi et al.,* 2007; *Froidevaux et al.,* 2008; *E.Dupuy* et al., 2009), HNO_3, ClO, $ClONO_2$ (*Wolff et al.,* 2008; *Batchelor et al.,* 2010; *Waymark et al.,* 2013) and HCl (*Mahieu et al.,* 2008).

5.4.3 SMR: O_3, HNO_3, and ClO

Odin (*Murtagh et al.,* 2002) was built in cooperation between Sweden, Canada, France, and Finland and launched in February 2001 into a sun-synchronous 18:00 ascending node orbit, carrying two co-aligned limb-sounding instruments. SMR (Sub-Millimeter wave Radiometer) is one of the two instruments. It is a passive microwave limb sounder. The Odin/SMR package is variable. The four main receiver chains can be tuned to cover frequencies that lie in the ranges of 486–504 GHz and 541–581 GHz; however, the total instantaneous bandwidth is 1.6 GHz. Odin/SMR has a diameter of 1.1 m and gives a vertical resolution of ~ 2 km at the tangent point. The lower end of the scan (during upward and downward scanning) is typically at ~ 7 km, and the upper end varies between 70 km and 110 km (depending on the observation mode). The horizontal sampling can range from 1 scan per 600 km to 1 scan per 1000 km. The latitudinal range spans from 82.5^{o}S to 82.5^{o}N. The main products of SMR are retrieved from the 'stratospheric' observation mode, and SMR covers this region during ~ 50 % of its observation time. In this mode, the spectra in frequency bands ~ 501 and 544 GHz are collected. The main data products include O_3 (*Massart et al.,* 2007), ClO, N_2O, and HNO_3 (*Urban et al.,* 2005). The science data are gathered from less frequently applied observation modes and include H_2O, CO, NO, and isotopologues of H_2O and O_3 as science data products. In this study, we used SMR version data for HNO_3, O_3, and ClO.

5.4.4 MERRA-2: Zonal Wind, Temperature, and Wave 1, 2 Amplitude of Geopotential Height

MERRA-2 (Modern Era Retrospective Analysis and Applications, version 2) (*Gelaro et al.,* 2017) is the latest atmospheric analysis of the modern era, produced by GMAO (Global Modeling and Assimilation Office) and an intended development milestone for a future integrated Earth system analysis (IESA). MERRA-2 is an upgradation to its predecessor (MERRA) and successfully

assimilates observation types unavailable to MERRA, including updates to GOES (Goddard Earth Observing System) model and analysis scheme, with the ability to provide a suitable ongoing climate analysis beyond MERRA's terminus. MERRA-2 data are used in this study to quantify the dynamics of the SSWs that took place from 2002 to 2021 in the SH. Data used are for the zonal mean zonal wind (U (m/s)) at 60°S, average temperature (K) from 60°-90°S, and Wave 1 and 2 amplitudes of geopotential height at 60°S in the stratosphere (10 hPa).

5.4.5 NASA O_3 Watch

The National Aeronautical and Space Administration monitors the O_3 over the Antarctic layer with a focus on the O_3 hole. Satellite instruments monitor the O_3 layer, and the NASA O_3 watch uses their data to create images and depicts the amount of O_3. In this study, we use the data for O_3 hole area, O_3 mass deficit, polar cap O_3, and mean O_3 at high latitudes (60°-90° S) from 1979 to 2021. TOMS (Total Ozone Mapping Spectrometer) (*Krueger*, 1989), OMI (Ozone Monitoring Instrument) (*Veefkind et al.*, 2006), and OMPS (Ozone Mapping and Profiler Suite) (*Kramarova et al.*, 2014) satellite data are used to determine the NASA O_3 watch data. O_3 missing areas are filled using assimilated O_3 data from GOES DAS (Goddard Earth Observing System Data Assimilation System). The assimilated O_3 data is primarily from MERRA, MERRA-2, and GOES FP (Forward Processing).

5.4.6 Dumont d'Urville Ground-Based Measurements

The French Antarctic station Dumont d'Urville (DDU), located at 66°S,140°E, carries out measurements from 1989 with support from the French Polar Institute. This is carried out as a part of the NDAAC (Network for the Detection of Atmospheric Composition Change) framework. At DDU, measurements are made by lidar (Raman/Mie/Rayleigh instrument) during the nighttime, typically from March to October. These measurements are carried out to understand the optical

properties of aerosol layers, tropopause cirrus clouds (clouds with their base above 14.5 km) (*Tseng and Fu,* 2017), and PSCs (*David et al.,* 1998, 2012; *Tritscher et al.,* 2021). The lidar emits at 532 nm and retrieves backscattered light in the 6-40 km altitude range with orthogonal polarization. It has vertical and time resolutions of 60 km and 3 minutes, respectively. We treat the 532 nm attenuated backscatter as an indicator of cloud presence in the stratosphere. Data are summed according to the dynamics of the SNR (signal-to-noise ratio) and particle presence. The backscatter data is retrieved (assuming non-absorbing particles) after the removal of background and molecular scattering. Fully corrected scattering ratio time series data are available as monthly files at the NDAAC data archive.

Figure 31 shows the time series of the latitudes observed by SOFIE, ACE, and SMR during the period from 1 August to 30 November in 2019 in the SH. As described in Section 5.4.1, SOFIE's switching of the sunrise and sunset hemispheres in 2017 led to no SH measurements until late 2018, and in 2019, SOFIE did not view latitudes poleward of 65^{o}S during ASON. SOFIE latitude coverage goes northward, starting at ~ 63^{o}S, and moves to lower latitudes below ~ 50^{o} S by mid-October. Thus, for SOFIE, we use data measured at latitudes poleward of 50^{o} S, assuming there is less variation in O_3 between 50^{o}S and 60^{o}S. Although this is not a perfect assumption, as O_3 at mid-latitudes (30^{o} – 60^{o} S) is typically higher than that at high latitudes (60^{o} – 90^{o} S) during ASON (except in November during certain years) as reported by NASA O_3 watch, we include latitudes from 50^{o} to 60^{o} S with the understanding that SOFIE is biased towards mid-latitudes. ACE observes high latitudes during August and September but observes mid and low latitudes during late September to mid-November. However, SMR observes high latitudes during the period ACE views mid-low latitudes, although the overall number of high latitude observations by SMR is low.

5.5 Mechanism of Occurrence

Polar O_3 depletion is driven by the enhancement of ClO that is produced by the heterogeneous reactions on the surface of PSC particles (*Solomon et al.,* 1986; McElroy, *Salawitch, & Wofsy et al.,* 1986*; McElroy, Salawitch, Wofsy, & Logan,* 1986). *Molina and Molina,* (1987) concluded that almost all of the springtime chemical loss of O_3 occurs through a catalytic cycle that starts with the self-reaction of ClO or alternatively through other cycles that begin with the reaction of ClO with BrO (*McElroy, Salawitch, Wofsy, & Logan et al.,* 1986). During the springtime, temperatures are low. HCl and $ClONO_2$ are converted to highly reactive ClO, and HNO_3 is removed due to the gravitational settling of PSC particles. During mid-September, ClO is present at the South Pole in low amounts due to limited sunlight, necessary for the photolysis of Cl_2 and ClOOCl to form ClO. Towards the edge of the polar vortex, high amounts of ClO are spread over extensive areas. These areas sometimes cover the Antarctic continent and can sustain for many months, leading to the efficient destruction of O_3 in sunlit regions. The chemical destruction of O_3 is an ongoing process during this time since O_3 typically attains minimum values in early to mid-October.

PSC surfaces act as suitable grounds for the occurrence of heterogeneous chemical reactions that trigger chlorine activation. $ClONO_2$ and HCl are treated as reservoir species (*Solomon,* 1988; *Wilmouth et al.,* 2006) as they almost entirely store inorganic chlorine (Cl_y) in the lower stratosphere of the polar vortices. However, they themselves are not reactive toward O_3. BrO constitutes almost half of the inorganic bromine (Br_y) that is in the stratosphere during sunlit conditions. ClO/Cl_y is present in much-reduced quantities than BrO/Br_y as the HCl (produced by $Cl + CH_4 \rightarrow HCl + CH_3$ (exothermic)) is more stable than HBr (produced by $Br + CH_4 \rightarrow HBr + CH_3$ (endothermic)).

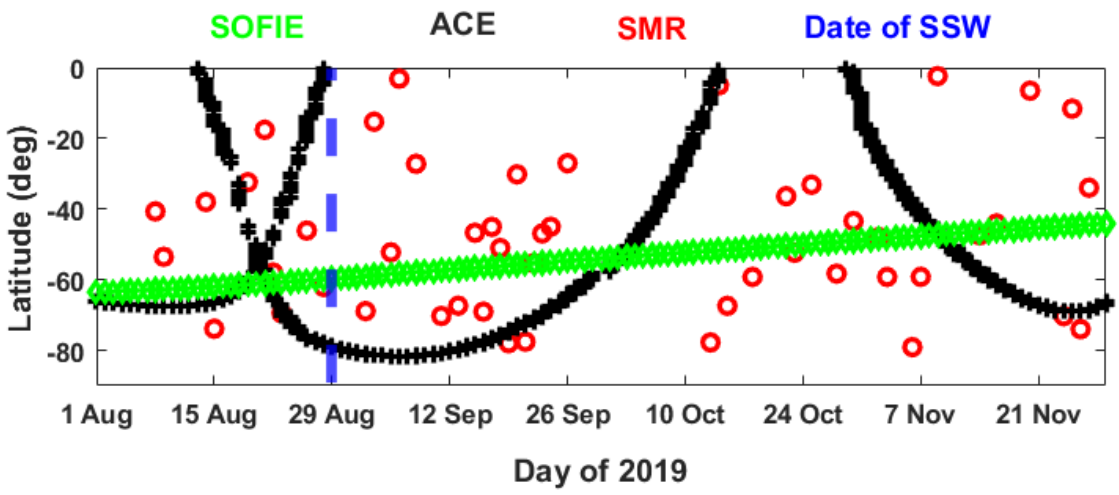

Figure 31. Latitudinal coverage of SOFIE, ACE, and SMR during ASON in the SH. Blue dashed line indicates the start date of the SSW (29 August 2019).

The reactions that take place on the surface or in the bulk of the PSC are crucial in understanding polar O_3 depletion. HCl and $ClONO_2$ are the two primary inorganic chlorine reservoirs present in the initial phase of the wintertime polar vortex. In the stratosphere, these compounds do not react in the gas phase. The heterogeneous reactions are:

$$ClONO_2 + HCl(C) \rightarrow HNO_3(C) + Cl_2, \quad (1)$$

$$ClONO_2 + H_2O(C) \rightarrow HNO_3(C) + HOCl, \quad (2)$$

$$HOCl + HCl(C) \rightarrow H_2O(C) + Cl_2, \quad (3)$$

$$N_2O_5 + H_2O(C) \rightarrow HNO_3(C) + HNO_3, \quad (4)$$

These reactions take place on the surface of PSCs. The Cl-bearing products are photolabile, i.e., they are susceptible to change under the influence of radiant energy or light. These Cl-bearing species readily react with O_3 in catalytic cycles. (C) indicates the condensed phase in which the

HNO_3 and H_2O exist (*Abbatt & Molina,* 1992a, 1922b; *Crutzen & Arnold,* 1986; *McElroy, Salawitch, & Wofsy et al.,* 1986; *Solomon,* 1988; *Solomon et al.,* 1986). Reactions (1) and (2) lead to the greatest amount of Chlorine activation, followed by the conversion of chlorine reservoirs HCl and $ClONO_2$ into active chlorine ClO_X. Reaction (3) activates chlorine in regions of particularly low $ClONO_2$, and reaction (4) leads to the conversion of NO_X into HNO_3, typically during early winter polar nights. Earlier, reactions (1) and (2) were inferred to be very effective on ice and on ice surfaces containing HNO_3/H_2SO_4 during periods of low temperature during wintertime in the polar stratosphere (*Leu,* 1988; *Tolbert et al.,* 1987). More recent studies acknowledged that these reactions on/in liquid droplets occur at a similar rate (per unit surface area density, SAD). As the SAD of liquid PSCs is more than the SAD of solids, typically; thus, liquid PSCs dominate the winter chlorine activation (*Tritscher et al.,* 2021).

5.6 Results

5.6.1 Reduced O_3 Hole Area

Figure 32 (top panel) shows the average O_3 hole area (million km^2) from NASA O_3 watch for August (red), September (blue), October (black), and November (green) (jointly termed ASON herein) from 1979 to 2021. The O_3 hole area is defined as the region where the O_3 values are below 220 Dobson Unit (DU) and located south of 40^oS. The values below 220 DU represent losses due to anthropogenic factors over Antarctica. Prior to 1979, scientists had not observed O_3 concentrations below 220 DU. However, in the early 1980s, using a combination of ground-based and satellite measurements, they realized a persistent and dramatic thinning over the south-polar region during the spring. Figure 32 (top panel) indicates that over the 43 years (and since the acknowledgment of O_3 loss in the early 1980s) of O_3 measurements, the patterns in O_3 hole area variation during ASON in 1988, 2002, and 2019 were different from the typical O_3 hole area. The

common trend in these three years is the gradual decrease in the O_3 hole area starting from September. The O_3 hole area reaches its lowest value in November and is reported as 0 in all three years. Figure 32 (bottom panel) shows the polar cap O_3 (DU). The total column O_3 is averaged around the polar cap for latitudes poleward of 63°S. The polar cap O_3, as expected, has an opposite behavior to the O_3 hole area. The measurements in 1988, 2002, and 2019 show that the concentration of O_3 in the polar cap gradually increases from August to December. The highest polar cap O_3 was recorded in 1988 during November, while 2002 and 2019 showed comparable O_3 concentrations. 2019 O_3 behavior was very similar to that of 2002, and thus, both years are indicated by the pink dashed-line boxes. Similarities in the SSW events that took place in these years are discussed ahead.

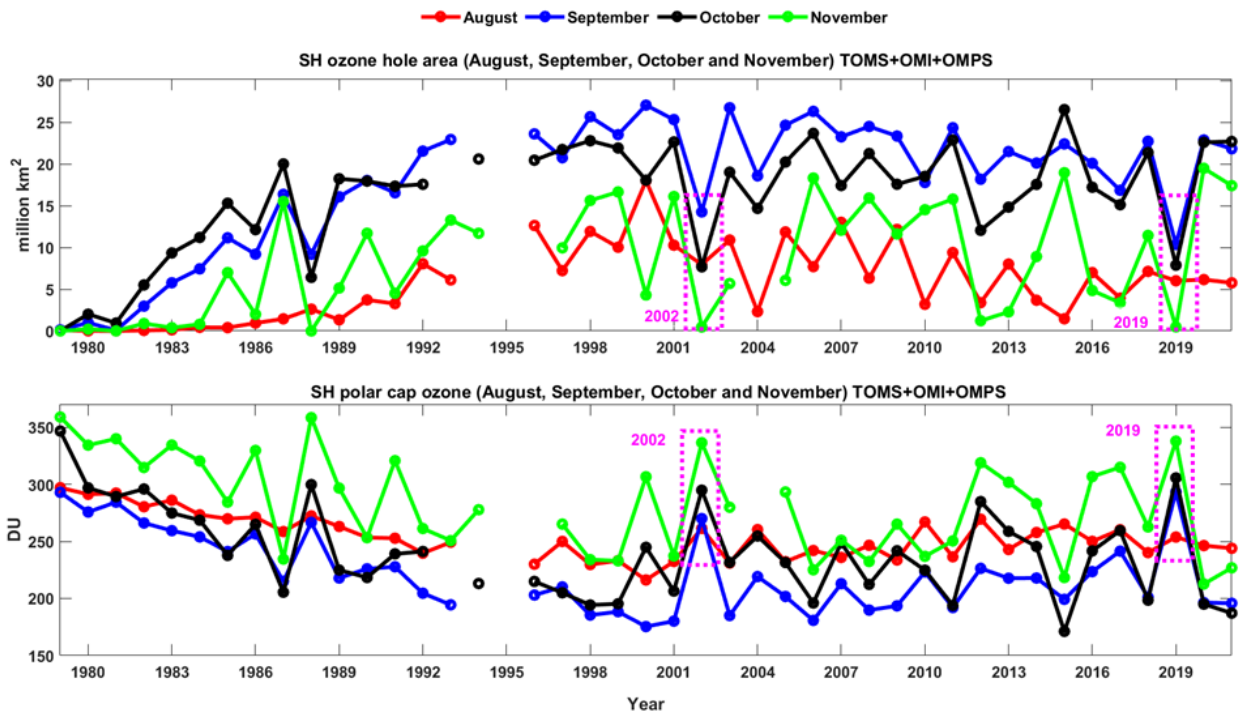

Figure 32. NASA Ozone Watch ozone hole area poleward of 40° S (Top panel) and polar cap ozone poleward of 63° S (Bottom panel) in the southern hemisphere during August, September, October, and November from 1979 to 2021. The data points are disconnected in years where data is unavailable.

The O_3 concentration undergoes strong variations typically during September and October. Figure 33 (left panel) shows the O_3 hole area poleward of 40°S averaged during 7 September – 13 October from 1979 to 2021 from NASA O_3 watch. The red markers indicate the actual recorded data, and the blue bars indicate the maximum and minimum values recorded. The smallest O_3 hole area in the last two decades of observations was recorded in 2002 and 2019, with the O_3 hole area being smaller in 2019 than in 2002. In Figure 33 (right panel), almost simultaneous polar cap O_3 measurements from 13 September – 5 October in the same years indicate that strong O_3 enhancements were observed in 2002 and 2019. In the 43 years of recorded polar cap O_3 measurements, 2019 indicates the highest O_3 values during 13 September – 5 October.

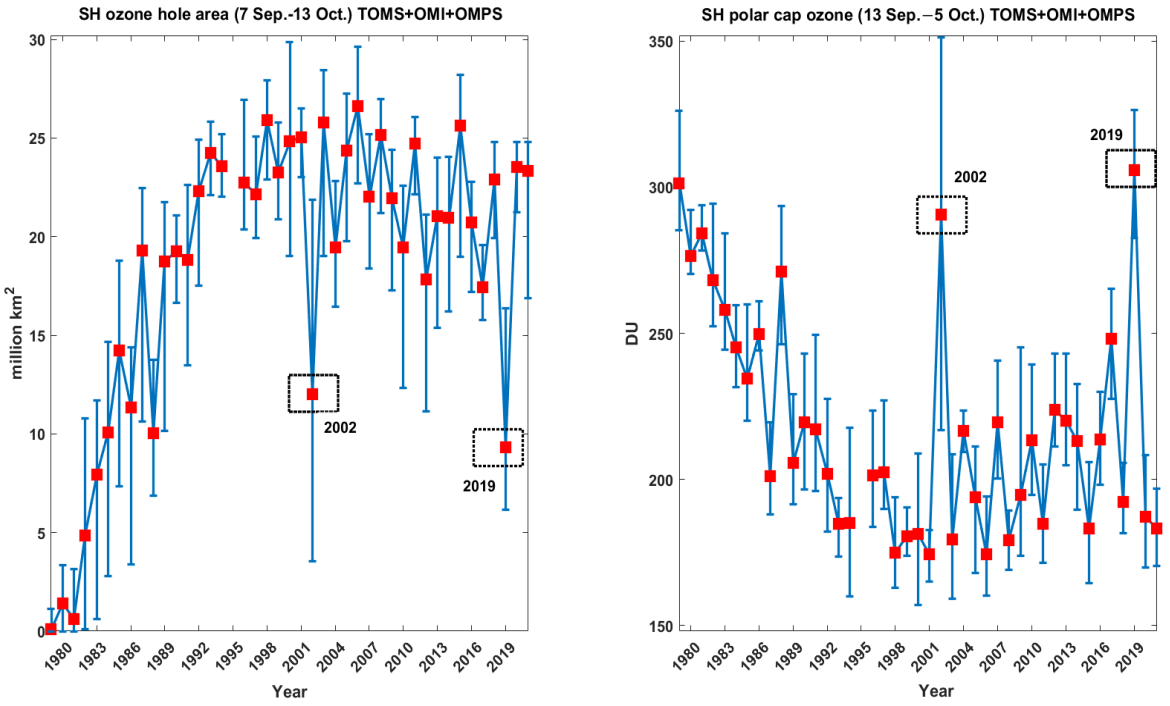

Figure 33. NASA Ozone Watch ozone hole area poleward of 40°S during 7 Sep. – 13 Oct. (Left panel) and polar cap ozone poleward of 63°S during 13 Sep. – 5 Oct. (Right panel) in the southern hemisphere from 1979 to 2021. The red markers indicate the actual averaged data. The blue bars indicate the maximum and minimum values at each data point. The black dashed-line boxes are used to identify the measurements in 2002 and 2019.

5.6.2 2019 SSW Event

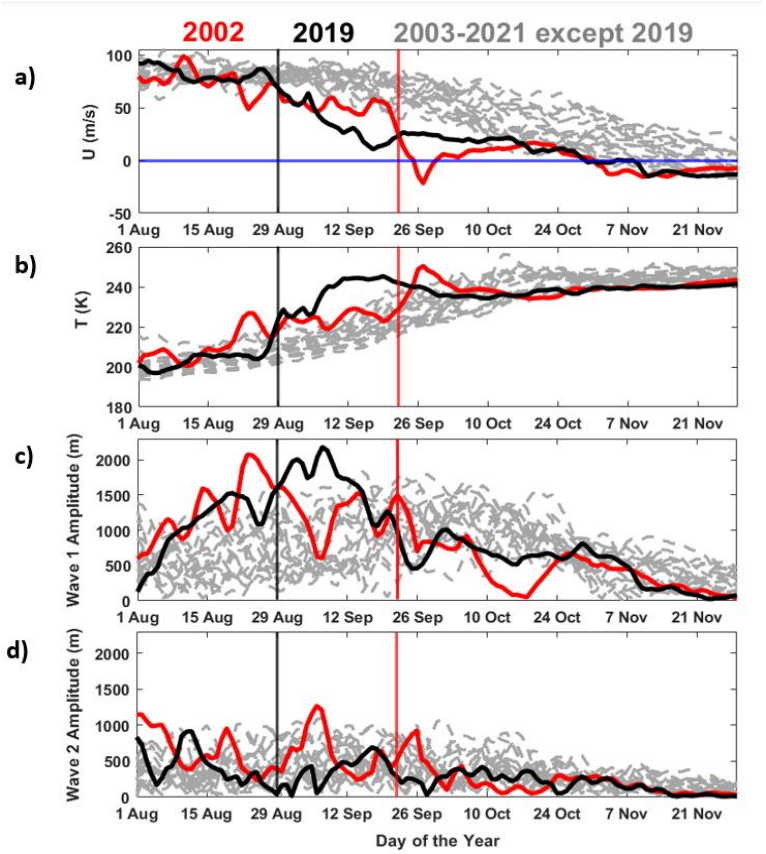

Figure 34. The daily mean variability of the (a) zonal mean zonal wind at 60° S, (b) zonal mean temperature of the stratosphere (60° - 90° S), (c) amplitude of Planetary Wave 1 and (d) amplitude of Planetary Wave 2 at 60° S geopotential height from MERRA-2 for the for the SH. Red lines denote 2019 and black lines denote 2002. Grey lines are for years from 2003 to 2021 (except 2019). Red and black vertical lines represent the start of SSW date for 2002 and 2019, respectively. The blue horizontal line in (a) indicates the zero-wind level. All parameters are at 10 hPa.

Figure 34 shows the SH zonal mean zonal wind, the temperature averaged between 60°S and 90°S, and the amplitudes of Waves 1 and 2 at 10 hPa from MERRA-2. In each plot, the solid red and black lines indicate the parameter for 2002 and 2019, respectively. The vertical red and black lines indicate the SSW date for 2002 and 2019, respectively. While the focus of this study is to

understand the 2019 SSW, we plot results from 2002 for comparison. The grey dashed lines in each panel indicate the corresponding parameters for the years 2003 to 2021 (except 2019).

Figure 34a shows the reversal in the zonal mean zonal wind (U (m/s)) at 60^{o}S, 10 hPa, and Figure 34b shows the stratosphere temperature poleward of 60^{o}S. The onset of the warming was observed on 29 August 2019, indicated by a sudden rise in temperature that gradually attained peak value during mid-September and lasted for several weeks. In 2002, the period of a sharp rise in temperature occurred during the late September/early October period and lasted for a very brief duration (~ one week). The zonal mean zonal wind in 2019 did not reverse but began to weaken during late August and showed receding values on 29 August. However, in 2002, there was a complete reversal in the zonal mean zonal wind, but this occurred much later in the year, towards late September 2002.

Figure 34c and Figure 34d show the growing amplitudes of Wave 1 and Wave 2 at 60^{o}S, respectively. There is anomalous amplification in Wave 1 in 2002 and 2019. In late August, the amplification in 2002 was larger than in 2019. However, during the first two weeks of September, the 2019 Wave 1 amplification is more than that of 2002. Wave 2 values in 2019 were typically lower than in 2002. In 2002, high Wave 2 values were reported from late August until mid-September, with a small peak seen again in late September that decreased in value in the following days. In 2019, Wave 2 values were higher than in 2002 for a very brief period during mid-September. The unusual nature and growth of Wave 1 indicate a strong disturbance in the southern polar vortex (*Watson & Gray,* 2014; *Evtushevsky et al.*, 2019). Typically, the SH warmings occur during late spring (*Allen et al.,* 2003; *Eswaraiah et al.,* 2016). However, the 2019 SSW occurred in early spring. The Wave 1 amplification started in early Spring (not shown), followed by a peak

in early September, and accompanied by a moderate amplification in Wave 2 during August. The Antarctic stratosphere in 2019 was thus unusual and disturbed during the winter and spring.

Although the 2019 SSW event demonstrated sharp temperature increments and Wave 1 amplitude enhancement, there was no reversal in the zonal wind but weakening. Based on the WMO definition of minor SSWs, *Yamazaki et al.,* (2020) classified the 2019 SSW as a minor event. Based on the above analysis, it can be said that while the 2019 SSW event is categorized as a minor event, its behavior was similar to a major SSW event.

5.6.3 Temperature and O_3 Profile Anomalies

The increase in stratospheric temperature in 2019 was more than that of previous years, attributed to the SSW event. To follow the progression of the SSW event, we plot in Figure 35 (top panel), the evolution of the SOFIE temperature profile anomalies in 2019 averaged poleward of 50^{o}S, with respect to the average of 2008-2014. Clear SSW event signatures are seen during late August, starting from 29 August at altitudes $\geq$ 10 hPa. The blue dashed line indicates the start of the 2019 SSW. The temperature anomaly reached very high values during 6 – 25 September, as indicated by the dashed black lines. The average increase in the stratospheric temperature was ~ 34^o during mid-September. Figure 35 (bottom plot) shows the SOFIE O_3 profile anomalies in 2019, averaged poleward of 50^{o}S, with respect to the average of 2008-2014. The blue dashed line indicates the 2019 SSW date. The periods before and after the SSW show a positive O_3 anomaly. There is a negative correlation between temperature and O_3 (*Smith et al.,* 2005, 2009), which is seen by the decrease in positive O_3 anomaly values around the SSW date. However, the evaporation of PSCs due to high temperatures contributes to O_3 retention. The O_3 anomaly is plotted in Figure 35 (bottom plot) and shows the cumulative effect of both processes that occur simultaneously. Overall, the O_3 anomaly in 2019 is typically positive in the stratosphere.

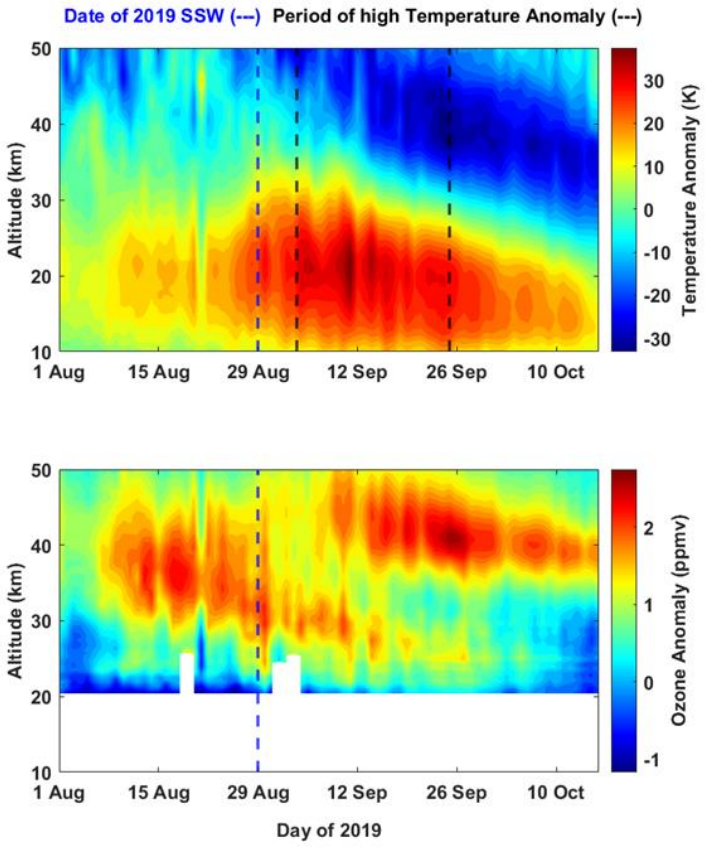

Figure 35. (Top Panel) Temperature anomaly (T_{2019} - $T_{(2008\text{-}2014\ average)}$) and (Bottom Panel) O_3 anomaly ($O_{3\ (2019)} - O_{3\ (2008\text{-}2014\ average)}$) from SOFIE. The blue dashed lines indicate the 2019 SSW date, and the black dashed lines indicate the period where the temperature anomaly is very high in the lower stratosphere. The white area denotes no measurements below ~ 20 km.

5.6.4 Polar Stratospheric Cloud Detection

Figure 36 shows the evolution of PSCs from June through November measured at the DDU station. The 532-nm backscatter ratio is used to measure PSCs qualitatively. The presence of PSCs is treated as positive when the backscatter ratio is higher than 1. A backscatter ratio higher than 1 can also indicate the presence of clouds and aerosols. However, typically, during stratospheric winters, a backscatter ratio value higher than 1 is treated as an indicator of PSC presence. The overall length of the PSC season is an important determinant of O_3 depletion. PSC evolution is regulated by temperature variation. Figure 36 shows a strong and distinct PSC concentration at DDU that started around 20 June. An increase in the temperature of the stratosphere and the SSW

on 29 August led to the evacuation of the PSCs. Thus, the concentration of the PSCs decreases substantially towards late August. This behavior digresses from the typically high PSC values observed during July and August in the SH stratosphere.

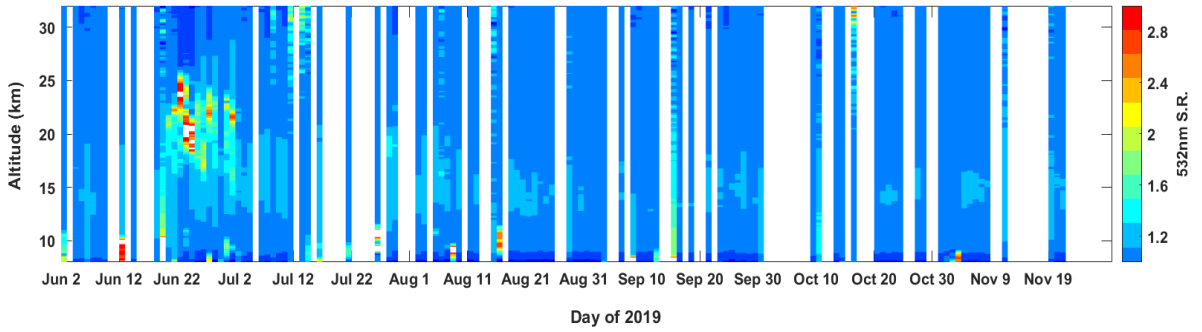

Figure 36. 532-nm attenuated scattering ratio time series using lidar measurements from the Dumont d'Urville ground station during June to November.

5.6.5 Varying Stratospheric Chemistry from ACE, SMR, and SOFIE

5.6.5.1 ACE

As discussed in Section 5.5, the PSC surface allows for the conversion of halogen reservoir species into reactive O_3-destroying forms. The increase in temperature during the 2019 SSW evaporated the PSCs, and thus, in the absence of a surface, the conversion of the halogen reservoir species to reactive-halogen forms was restricted. We verify these theoretical estimations using real-time satellite instrument measurements.

Figure 37 shows ACE measurements of a) temperature, b) $ClONO_2$, c) HCl, d) ClO, e) HNO_3, and e) O_3 poleward of 60°S. The solid red and black lines show measurements for 2019 and the average from 2004 to 2018, respectively. The dashed red and black lines show the measurement errors for 2019 and the average from 2004 to 2018, respectively. For the species that the errors are not calculated or incomplete/biased, the errors have not been plotted. The dashed blue lines indicate the 2019 SSW date. The grey region indicates the period when ACE measures at lower latitudes.

In Figure 37a, the temperature in 2019 increases around the SSW date and is much higher than the 15-year (2004-2018) average. The temperature in 2019 reached as high as ~ 244 K during mid-September which is also observed by MERRA-2 and SOFIE temperature measurements.

In Figure 37b, one of the two chlorine reservoir species, $ClONO_2$, shows an increase in concentration in 2019 around the SSW date and is continuously higher than the 15-year average until late September. This indicates that lower amounts of $ClONO_2$ were converted into reactive-chlorine form, and thus, more $ClONO_3$ was retained. In Figure 37c, the other halogen (chlorine) reservoir species, HCl, is plotted. In theory, the 2019 HCl measurements are expected to be higher than the 15-year average. While both the 2019 and the 15-year average values are close during the SSW date, the 2019 HCl measurement does not exceed the 15-year average. Since the reported error values for HCl are very high, it can be assumed that the actual HCl measurements fluctuate over a broad range of values. Thus, the deviation of the 2019 HCl observations from expected behavior can be attributed to the inconsistencies in measurement.

The chlorine reservoir species react to produce Cl_2, which is eventually converted to ClO, an O_3-destroying reactive form. In Figure 37d, lower ClO is observed in 2019 compared to the 15-year average, starting around the SSW date. This indicates that lower ClO was produced in 2019, suggesting lower conversion of Cl_2 to ClO and, thus, lower production of Cl_2. This corroborates the reasoning that more $ClONO_2$ is retained as very little is converted into Cl_2.

The annual cycle of HNO_3 strongly depends on the evolution of temperature. Before the southern hemispheric winter, HNO_3 columns typically increase over the south pole and gradually decrease from June to September due to the formation of PSCs. The SSW dynamics in 2019 impacted the polar vortex and restricted the persistence of PSCs, leading to lesser denitrification through HNO_3

uptake by PSCs. In Figure 37e, there is a sharp increase in the 2019 HNO_3 starting from the SSW date, and the 2019 HNO_3 measurements are higher than the 15-year average. Thus, the increased temperature in 2019 hindered HNO_3 depletion.

In Figure 37f, O_3 measurements in 2019 are higher than the 15-year average. The enhanced values in 2019 appear a few weeks before the SSW date and continue to increase sharply starting from the SSW date. The lack of O_3-destroying reactive halogen (chlorine) forms like ClO leads to an enhancement in the O_3 concentration.

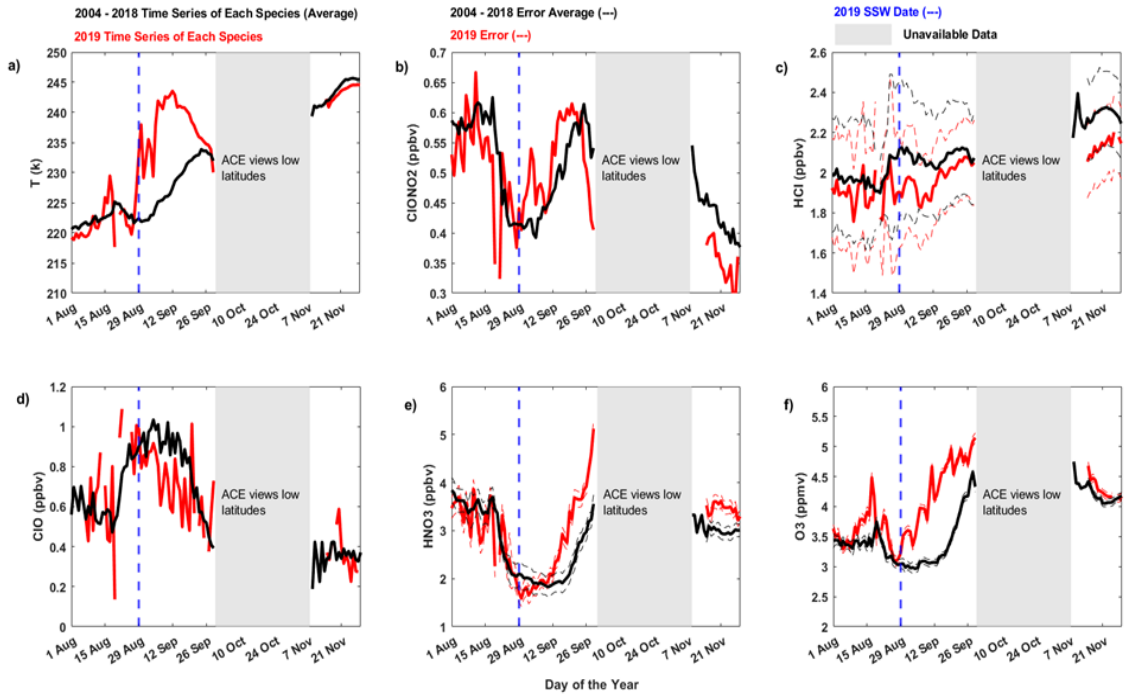

Figure 37. ACE measurements of a) Temperature, b) $ClONO_2$, c) HCl, d) ClO , e) HNO_3 and f) O_3 at latitudes poleward of 60° S. Red and black lines indicate 2019 and 2004-2018 average for each species, respectively. Dashed red and dashed black lines indicate the errors (where available) for 2019 and 2004 - 2018 average, respectively. The blue dashed lines indicate the 2019 SSW date.

5.6.5.2 SMR

ACE measurements from late September to early November are not used because ACE measures at lower latitudes during then. For the sake of completeness, we include observations from SMR that provides consistent measurements from August to November. However, in 2019, SMR made a low number of measurements poleward of 60°S. In Figure 38, we use ClO, HNO_3, and O_3 from SMR to compare the 2019 measurements to the average from 2003-2018 (16-year average). We also plot these species' measurements for 2002 and compare the similarities with 2019. The solid and dashed black lines indicate the 16-year average and their corresponding uncertainty. The green pluses and bars indicate 2002 measurements and their corresponding errors. The red pluses and bars indicate 2002 measurements and their corresponding errors. The dashed blue line indicates the 2019 SSW date.

In Figure 38a, the ClO measurement for the 16-year average is much higher than that of 2019 and 2002. Although not many ClO profiles from 2019 are available just after the SSW start date, the ClO in 2019 is typically lower than the 16-year average after the SSW event. Lower ClO in 2019 and 2002 than in the average from 2003 to 2018 indicates that there is lower ClO formation. In Figure 38b, the HNO_3 measurements in 2002 and 2019 were higher than the 16-year average, indicating a lower loss of HNO_3 through denitrification by PSC uptake. In Figure 38c, the O_3 in 2002 and 2019 are typically higher than the 16-year average, indicating higher O_3 preservation. The atmospheric response to the loss of PSCs resulted in similar chemistry in both 2002 and 2019.

5.6.5.3 SOFIE

The SMR instrument provides continuous measurements of O_3 for 2019. However, there are fewer data points in 2019. Thus, the evaluation of O_3 measurements from a diverse range of satellite instruments is useful in corroborating our understanding of O_3 enhancement during the 2019 winter

in the SH. SOFIE observed the 2019 SSW in the SH from August to mid-October between 50° and 90° S. As discussed in Section 5.4.1, SOFIE began measuring in the SH in 2019 after a brief absence during the switching of the sunrise and sunset hemispheres. Due to this transition, SOFIE viewed poleward of 60° S for a short period of time from August to mid-October. We thus include measurements poleward of 50°S in our analysis. SOFIE typically looks at high latitudes, and hence, the observations during 2008-2014 used for comparison fall under latitudes poleward of 60°S. It is assumed that the concentration of species does not have a high variation between 50° and 60° S. We believe this assumption does not impact the overall quality of our results as the purpose of including SOFIE measurements is to study the 2019 trend in the variation of species compared to previous years' average and not a comparison of the species' concentration between different data sets.

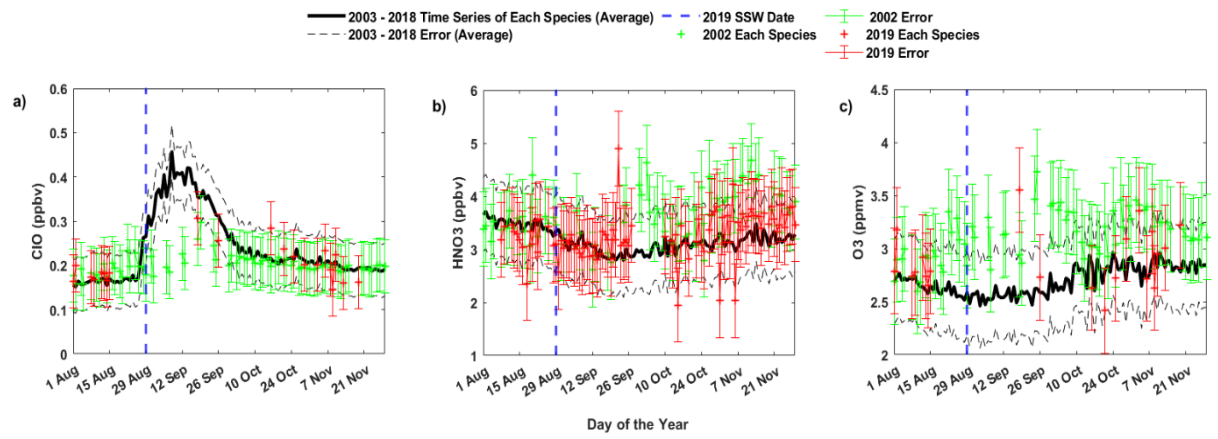

Figure 38. SMR measurements of a) ClO, b) HNO_3, and c) O_3 at latitudes poleward of 65° S. The black solid and dashed lines indicate the 2004 - 2018 values for each species and the corresponding errors, respectively. The red pluses and the red error bars indicate the indicate the 2019 values and the corresponding errors, respectively. The green pluses and the green error bars indicate the 2002 values and the corresponding errors, respectively. The dashed blue lines indicate the 2019 SSW date.

HNO_3 is an important indicator of PSC loss, as seen from ACE and SMR measurements. SOFIE does not measure HNO_3, but the production of HNO_3 involves the contribution of NO (nitric oxide) and H_2O, as shown in equations 5, 6, and 7 below.

$$2\,NO + O_2 \rightarrow 2\,NO_2 \tag{5}$$

$$3\,NO_2 + H_2O \rightarrow 2\,HNO_3 + NO \tag{6}$$

The NO produced in equation 6 is cycled back for reoxidation. If equation 6 takes place in the presence of air, O_2 (molecular oxygen) factors in, and the alternate reaction is equation 7.

$$4\,NO_2 + O_2 + 2\,H_2O \rightarrow 4HNO_3 \tag{7}$$

Thus, we use NO and HO_2 as indicators of HNO_3 presence, assuming a constant supply of O_2.

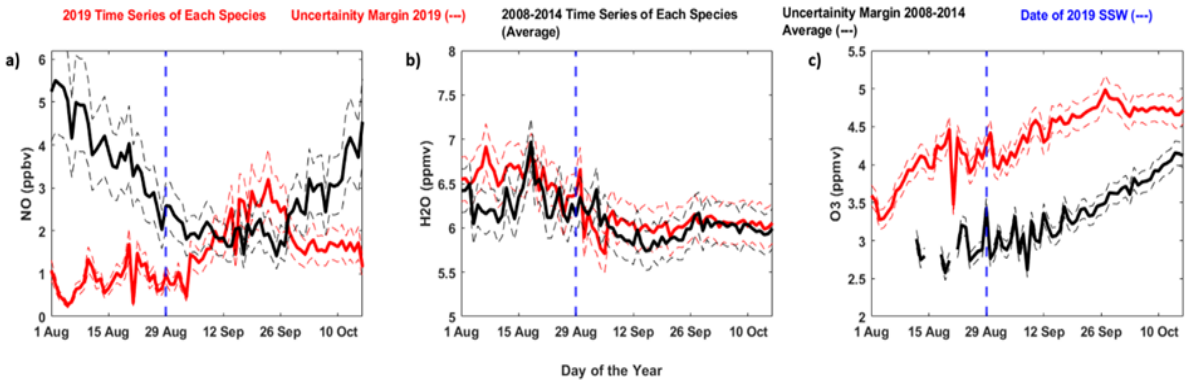

Figure 39. SOFIE a) NO, b) H_2O and c) O_3 measurements poleward of 50° S. The black solid and dashed lines indicate the 2008-2014 values for each species and the corresponding errors respectively. The red solid and dashed lines indicate the 2019 values for each species and the corresponding errors, respectively. The dashed blue lines indicate the 2019 SSW date.

In Figure 39a, Figure 39b, and Figure 39c, we plot SOFIE measurements of NO, H_2O, and O_3, respectively. The red and black solid lines indicate measurement for each species for 2019 and the average for 2008-2014 (7-year average), respectively. The red and black dashed lines indicate the

uncertainty in measurement for each species for 2019 and the 7-year average. The dashed blue lines indicate the 2019 SSW date.

The NO in 2019 indicates an enhancement and increases above the 7-year average for ~ 2 weeks starting a few days after the 2019 SSW date. Increased amounts of H_2O in 2019 are observed compared to the 7-year average, typically throughout the August-mid-October period. However, the increase in H_2O in 2019 for 2 weeks starting a few days after the SSW date is distinctly high. Increased NO and H_2O concentrations after the 2019 SSW indicate that higher HNO_3 was present during these times than the 7-year average.

The concentration of O_3 in 2019 was consistently higher than the 7-year average, even before the SSW date. This was also observed in the ACE O_3 measurements. The weeks before the SSW event led to preconditioning for the retention of O_3. The period after the SSW date led to a sharp increase in the O_3 concentration that continued for several weeks until early October when the O_3 concentration began to stabilize gradually.

5.7 Discussion and Summary

SSW events are a common meteorological feature in the NH but a rare event in the SH. Like the 2002 SSW event in the last two decades, the recent 2019 SSW event in the SH had a strong impact on the concentration of O_3, leading to large enhancements. In this study, we look at the O_3 hole area, and polar cap O_3 from August to November and averaged during September and October from 1979 to 2021 (43 years) from NASA O_3 watch data. While the smallest O_3 hole area identified after the detection of O_3 loss by anthropogenic activity during the early 1980s is for 1988, the more recent small O_3 holes are reported for 2002 and 2019. The O_3 hole area was smaller in 2019 than in 2002. Evaluation of the polar cap O_3 indicates that of all 43 years, the largest O_3 concentration averaged during September and October was in 2019.

MERRA-2 measurements for temperature, zonal mean wind, and the amplitude of the geopotential height (waves 1 and 2), determine the strength of the 2019 SSW and the similarities to the 2002 SSW event. Although per the WMO categorization of SSW events, the 2019 event is classified as a minor one (there was no zonal wind reversal but weakening), it showed a strong and sharp temperature gradient along with an increment in the wave 1 amplitude in early spring than the usual late springtime SSW in the SH. While the onset of the warming was observed on 29 August, it attained peak value during mid-September, and the abnormal growth of waves 1 and 2 in 2019 was the strongest amongst those recorded from 2003 to 2021. Thus, the assessment of these features indicates that the 2019 SSW was an unusual one and the longest warming event on record in the SH.

Temperature and O_3 measurements from SOFIE determine the 2019 anomalies compared to the average from 2008 to 2014. Temperature anomalies are typically high throughout the altitudes between 10 and 30 km, with the vales reaching the highest (~ 34^o) during 6 – 25 September. This long period of high anomaly values indicates that the 2019 SSW led to a prolonged period of high temperatures compared to the previous years' average. O_3 anomalies during the same period indicate that the total O_3 in 2019 was much higher (up to ~ 2.8 ppmv) than the average from 2008 to 2014. Although there is an already established negative correlation between temperature and O_3 concentration, the temperature increase evaporates PSCs that provide a surface for the conversion of halogen reservoirs into O_3-destroying reactive forms. Thus, the increase in temperature leads to both the loss and retention of O_3 and the net effect is seen as O_3 enhancement marked by the large anomaly values in 2019.

Lidar measurements from DDU show that the backscatter ratio used to determine PSC presence was typically > 1 from June to August. PSC concentration during mid-June was very high,

indicated by the large backscatter ratio values. A gradual decrease in the concentration of PSCs was observed during late August, which coincides with the period of increased temperature in the stratosphere. The backscatter ratio in September through November is very occasionally > 1 (and mostly greater by very small numbers). The decrease in PSCs with the SSW event and the increase in temperatures suggests PSC evaporation due to large temperatures. Thus, the absence of PSCs after the SSW event suggests the measurements from ACE, SMR, and SOFIE indicate O_3 enhancements in 2019 when compared to previous years' average. ACE measurements of $ClONO_2$ indicate that in 2019, higher measurement was recorded for the species than from 2004 to 2018 averaged. This indicates a lower loss of $ClONO_2$, a chlorine reservoir species, into a reactive form. HCl, the other chlorine reservoir species, showed lower values in 2019 than the average from 2004 to 2018, which is opposed to the theoretical expectation of higher HCl retention in 2019 due to lower loss to chlorine uptake by the conversion to reactive-chlorine forms. However, the unexpected digression from theoretical expectations in HCl profiles can be attributed to the large uncertainties in the measurements. Lower measurements of ClO were recorded in 2019 compared to the average from 2004 to 2018, corroborating that there was a lower conversion of the reservoir species into reactive chlorine form. Higher HNO_3 in 2019 was reported compared to the average from 2004 to 2018. Lower PSC concentration from August onwards led to lower loss of HNO_3 by the absorption by PSCs. Thus, higher HNO_3 in 2019 is an indicator of lower denitrification through PSC uptake. ACE recorded higher O_3 in 2019 compared to the average from 2004 to 2018.

SMR measurements corroborate the observations from ACE for ClO, HNO_3, and O_3. SMR observations of ClO vary over a smaller range than ACE. One possible reason for this could be the difference in the viewing latitudes from August to November in the SH and the number of measurements made by each instrument. However, further investigation is required. SMR

measurements in 2019 were fewer at high latitudes than in other years. However, the overall behavior of species in 2019 was similar to 2002. Lower ClO than the average from 2003-2018 was recorded in 2002 and 2019 after the SSW event, while larger HNO_3 and O_3 were recorded in both years after the SSW when compared to the 16-year average.

SOFIE measurements of NO and H_2O used as indicators of HNO_3 presence indicate that both species increased after the 2019 SSW event and are higher compared to the average from 2008 to 2014. O_3 measurements in 2019 from SOFIE are higher than the average from 2008 to 2014. Overall, SOFIE measurements corroborate the trend in HNO_3 and O_3 variation from ACE and SMR.

Our observations and interpretations suggest that the unusual warming in the SH polar region in 2019 disturbed the middle atmosphere in serious amounts by anomalously hiking the temperature in the polar stratosphere and abnormal behavior of wave 1 and 2 amplitudes. The 2019 event was comparable to that of 2002 but started earlier in the spring. The evaporation of PSCs with increasing temperature during SSWs took away the surface for conversion of chlorine reservoirs into reactive O_3-destroying forms. Satellite measurements corroborate this by providing real-time records of lower dichlorination in 2019 than in other years and higher HNO_3 due to lower loss through PSC-probed denitrification. All three instruments indicate strong enhancement in O_3 after the SSW event and show strong increments compared to previous years' average. This SSW event stands as a good illustration of the large variability of the O_3 loss governing mechanisms in the polar and near-polar stratosphere.

Our study provides a detailed investigation of the 2019 event in terms of atmospheric dynamics and variation in stratospheric chemistry. The process of O_3 hole recovery is slow (*Wespes et al.,*

2019), and the matching of the springtime O_3 column concentrations to the values in 1980 is expected in the 2060s (*WMO,* 2018). While this is a long process, further extensive studies are encouraged to address the unusual dynamics and chemistry of the stratosphere during the unusual and anomalous SH winters. More attention needs to be paid to the 2019 SSW event because the high O_3 enhancement during this event is significant to future O_3 hole healing.

5.8 Acknowledgments

This research is funded by AIM through the NASA Small Explorer program. We acknowledge the AIM and SOFIE operation teams for their excellent support with this work. We thank the SciSat/ACE and Odin/SMR teams for their data. We thank NASA Ozone Watch, MERRA-2, and DDU station for their data.

5.9 Open Research

SOFIE Version 1.3 temperature, O_3, H_2O, and NO data and documentation are accessible through the SOFIE website - http://sofie.gats-inc.com/. ACE Version 4.1 data for temperature, O_3, $ClONO_2$, HCl, HNO_3, and ClO are available upon request at the ACE website https://databace.scisat.ca/level2/ace_v4.1_v4.2/ . Odin/SMR O_3, HNO_3, and ClO data are available at their website - http://odin.rss.chalmers.se/level2_download/ . DDU lidar data are available at their website - https://www-air.larc.nasa.gov/missions/ndacc/data.html?station=dumont.d.urville/ames/lidar/ . MERRA-2 data for temperature, zonal mean wind, and wave 1 and 2 amplitude are available at https://acd-ext.gsfc.nasa.gov/Data_services/met/ann_data . NASA Ozone watch O_3 hole area and polar cap O_3 data are available at https://ozonewatch.gsfc.nasa.gov/meteorology/SH .

References

Abbatt, J.P.D. and Molina, M.J., 1992a. Heterogeneous interactions of nitryl hypochlorite and hydrogen chloride on nitric acid trihydrate at 202 K. *The Journal of Physical Chemistry*, 96(19), pp.7674-7679. https://dx.doi.org/10.1021/j100198a036

Abbatt, J.P.D. and Molina, M.J., 1992b. The heterogeneous reaction of HOCl+ HCl→ Cl2+ H2O on ice and nitric acid trihydrate: Reaction probabilities and stratospheric implications. *Geophysical research letters*, 19(5), pp.461-464. https://doi.org/10.1029/92GL00373

Allen, D.R., Bevilacqua, R.M., Nedoluha, G.E., Randall, C.E. and Manney, G.L., 2003. Unusual stratospheric transport and mixing during the 2002 Antarctic winter. *Geophysical Research Letters*, 30(12). https://doi.org/10.1029/2003GL017117

Andrews, D.G., Holton, J.R. and Leovy, C.B., 1987. *Middle atmosphere dynamics* (No. 40). Academic press.

Mark, P.B. and Timothy, J.D., 1999. Propagation of the Arctic Oscillation from the stratosphere to the troposphere. *Journal of Geophysical Research: Atmospheres*, 104(D24), pp.30937-30946. https://doi.org/10.1029/1999JD900445

Baldwin, M., 2003. Major stratospheric warming in the Southern Hemisphere in 2002: Dynamical aspects of the ozone hole split. *SPARC newsletter*, 20, pp.24-26.

Batchelor, R.L., Kolonjari, F., Lindenmaier, R., Mittermeier, R.L., Daffer, W., Fast, H., Manney, G., Strong, K. and Walker, K.A., 2010. Four Fourier transform spectrometers and the Arctic polar vortex: instrument intercomparison and ACE-FTS validation at Eureka during the IPY springs of 2007 and 2008. *Atmospheric Measurement Techniques*, 3(1), pp.51-66. https://doi.org/10.5194/amt-3-51-2010

Bernath, P., 2001. Atmospheric chemistry experiment (ACE): An overview. *Spectroscopy from Space*, pp.147-160. DOI: 10.1007/978-94-010-0832-7_9

Bernath, P.F., McElroy, C.T., Abrams, M.C., Boone, C.D., Butler, M., Camy-Peyret, C., Carleer, M., Clerbaux, C., Coheur, P.F., Colin, R. and DeCola, P., 2005. Atmospheric chemistry experiment (ACE): mission overview. *Geophysical research letters*, 32(15). doi:10.1029/2005GL022386.

Boone, C.D., Nassar, R., Walker, K.A., Rochon, Y., McLeod, S.D., Rinsland, C.P. and Bernath, P.F., 2005. Retrievals for the atmospheric chemistry experiment Fourier-transform spectrometer. *Applied optics*, 44(33), pp.7218-7231. https://doi.org/10.1364/AO.44.007218

Blume, C., Matthes, K. and Horenko, I., 2012. Supervised learning approaches to classify sudden stratospheric warming events. *Journal of the atmospheric sciences*, 69(6), pp.1824-1840. https://doi.org/10.1175/JAS-D-11-0194.1

Butler, A.H., Seidel, D.J., Hardiman, S.C., Butchart, N., Birner, T. and Match, A., 2015. Defining sudden stratospheric warmings. *Bulletin of the American Meteorological Society*, 96(11), pp.1913-1928. https://doi.org/10.1175/BAMS-D-13-00173.1

Butler, A.H., Sjoberg, J.P., Seidel, D.J. and Rosenlof, K.H., 2017. A sudden stratospheric warming compendium. *Earth System Science Data*, 9(1), pp.63-76. https://doi.org/10.5194/essd-9-63-2017

Charlton, A.J. and Polvani, L.M., 2007. A new look at stratospheric sudden warmings. Part I: Climatology and modeling benchmarks. *Journal of climate*, 20(3), pp.449-469. https://doi.org/10.1175/JCLI3996.1

Cho, Y.M., Shepherd, G.G., Won, Y.I., Sargoytchev, S., Brown, S. and Solheim, B., 2004. MLT cooling during stratospheric warming events. *Geophysical Research Letters*, 31(10). https://doi.org/10.1029/2004GL019552

Cohen, J., Barlow, M., Kushner, P.J. and Saito, K., 2007. Stratosphere–troposphere coupling and links with Eurasian land surface variability. *Journal of Climate*, 20(21), pp.5335-5343. https://doi.org/10.1175/2007JCLI1725.1

Cortesi, U., Lambert, J.C., De Clercq, C., Bianchini, G., Blumenstock, T., Bracher, A., Castelli, E., Catoire, V., Chance, K.V., De Maziere, M. and Demoulin, P., 2007. Geophysical validation of MIPAS-ENVISAT operational ozone data. *Atmospheric Chemistry and Physics*, 7(18), pp.4807-4867. https://doi.org/10.5194/acp-7-4807-2007

Crutzen, P.J. and Arnold, F., 1986. Nitric acid cloud formation in the cold Antarctic stratosphere: A major cause for the springtime 'ozone hole'. *Nature*, 324(6098), pp.651-655. https://doi.org/10.1038/324651a0

David, C., Bekki, S., Godin, S., Mégie, G. and Chipperfield, M.P., 1998. Polar stratospheric clouds climatology over Dumont d'Urville between 1989 and 1993 and the influence of volcanic aerosols on their formation. *Journal of Geophysical Research: Atmospheres*, 103(D17), pp.22163-22180. https://doi.org/10.1029/98JD01692

David, C., Haefele, A., Keckhut, P., Marchand, M., Jumelet, J., Leblanc, T., Cénac, C., Laqui, C., Porteneuve, J., Haeffelin, M. and Courcoux, Y., 2012. Evaluation of stratospheric ozone, temperature, and aerosol profiles from the LOANA lidar in Antarctica. *Polar Science*, 6(3-4), pp.209-225. https://doi.org/10.1016/j.polar.2012.07.001

DDU (2019). Dumont d'Urville station sonde and lidar data, available at: http://www.ndacc.org, last access: 12 December 2019.

De Laat, A.T.J. and Van Weele, M., 2011. The 2010 Antarctic ozone hole: Observed reduction in ozone destruction by minor sudden stratospheric warmings. *Scientific Reports*, 1(1), pp.1-8. https://doi.org/10.1038/srep00038

Dowdy, A.J., Vincent, R.A., Murphy, D.J., Tsutsumi, M., Riggin, D.M. and Jarvis, M.J., 2004. The large-scale dynamics of the mesosphere–lower thermosphere during the Southern Hemisphere stratospheric warming of 2002. *Geophysical Research Letters*, 31(14). httsp://doi.org/10.1029/2004GL020282

Dupuy, E., Walker, K.A., Kar, J., Boone, C.D., McElroy, C.T., Bernath, P.F., Drummond, J.R., Skelton, R., McLeod, S.D., Hughes, R.C. and Nowlan, C.R., 2009. Validation of ozone measurements from the Atmospheric Chemistry Experiment (ACE). *Atmospheric Chemistry and Physics*, 9(2), pp.287-343. https://doi.org/10.5194/acp-9-287-2009

Eswaraiah, S., Kim, Y.H., Hong, J., Kim, J.H., Ratnam, M.V., Chandran, A., Rao, S.V.B. and Riggin, D., 2016. Mesospheric signatures observed during 2010 minor stratospheric warming at King Sejong Station (62 S, 59 W). *Journal of Atmospheric and Solar-Terrestrial Physics*, 140, pp.55-64. https://doi.org/10.1016/j.jastp.2016.02.007

Eswaraiah, S., Kim, Y.H., Liu, H., Ratnam, M.V. and Lee, J., 2017. Do minor sudden stratospheric warmings in the Southern Hemisphere (SH) impact coupling between stratosphere and mesosphere–lower thermosphere (MLT) like major warmings?. *Earth, Planets and Space*, 69(1), pp.1-8. https://doi.org/10.1186/s40623-017-0704-5

Eswaraiah, S., Kim, Y.H., Lee, J., Ratnam, M.V. and Rao, S.V.B., 2018. Effect of Southern Hemisphere sudden stratospheric warmings on Antarctica mesospheric tides: First observational study. *Journal of Geophysical Research: Space Physics*, 123(3), pp.2127-2140. https://doi.org/10.1002/2017JA024839

Eswaraiah, S., Kim, J.H., Lee, W., Hwang, J., Kumar, K.N. and Kim, Y.H., 2020. Unusual changes in the Antarctic middle atmosphere during the 2019 warming in the Southern Hemisphere. *Geophysical Research Letters*, 47(19), p.e2020GL089199. https://doi.org/10.1029/2020GL089199

Evtushevsky, O.M., Grytsai, A.V. and Milinevsky, G.P., 2019. Decadal changes in the central tropical Pacific teleconnection to the Southern Hemisphere extratropics. *Climate Dynamics*, 52(7), pp.4027-4055. https://doi.org/10.1007/s00382-018-4354-5

Froidevaux, L., Jiang, Y.B., Lambert, A., Livesey, N.J., Read, W.G., Waters, J.W., Browell, E.V., Hair, J.W., Avery, M.A., McGee, T.J. and Tiwgg, L.W., Validation of Aura Microwave Limb Sounder stratospheric and mesospheric ozone measurements. *J. Geophys. Res*, 113. https://doi.org/10.1029/2007JD008771

Fussen, D., Vanhellemont, F., Dodion, J., Bingen, C., Walker, K.A., Boone, C.D., McLeod, S.D. and Bernath, P.F., 2005. Initial intercomparison of ozone and nitrogen dioxide number density profiles retrieved by the ACE-FTS and GOMOS occultation experiments. *Geophysical research letters*, 32(16). https://doi.org/10.1029/2005GL022468

Gelaro, R., McCarty, W., Suárez, M.J., Todling, R., Molod, A., Takacs, L., Randles, C.A., Darmenov, A., Bosilovich, M.G., Reichle, R. and Wargan, K., 2017. The modern-era retrospective analysis for research and applications, version 2 (MERRA-2). *Journal of climate*, 30(14), pp.5419-5454. https://doi.org/10.1175/JCLI-D-16-0758.1

Gordley, L.L., Hervig, M.E., Fish, C., Russell III, J.M., Bailey, S., Cook, J., Hansen, S., Shumway, A., Paxton, G., Deaver, L. and Marshall, T., 2009. The solar occultation for ice experiment. *Journal of Atmospheric and Solar-Terrestrial Physics*, 71(3-4), pp.300-315. doi:10.1016/j.jastp.2008.07.012.

Gunson, M.R., Abbas, M.M., Abrams, M.C., Allen, M., Brown, L.R., Brown, T.L., Chang, A.Y., Goldman, A., Irion, F.W., Lowes, L.L. and Mahieu, E., 1996. The Atmospheric Trace Molecule Spectroscopy (ATMOS) experiment: Deployment on the ATLAS space shuttle missions. *Geophysical Research Letters*, 23(17), pp.2333-2336. https://doi.org/10.1029/96GL01569

Hendon, H.H., Thompson, D.W.J., Lim, E.P., Butler, A.H., Newman, P.A., Coy, L. and Scaife, A., 2019. Rare forecasted climate event under way in the Southern Hemisphere. *Nature*, 573(7775), pp.495-496. https://doi.org/10.1038/d41586-019-02858-0

Hervig, M.E., Marshall, B.T., Bailey, S.M., Siskind, D.E., Russell III, J.M., Bardeen, C.G., Walker, K.A. and Funke, B., 2019. Validation of Solar Occultation for Ice Experiment (SOFIE) nitric oxide measurements. *Atmospheric Measurement Techniques*, 12(6), pp.3111-3121. doi:10.5194/amt-2019-56.

Holton, J.R., Haynes, P.H., McIntyre, M.E., Douglass, A.R., Rood, R.B. and Pfister, L., 1995. Stratosphere-troposphere exchange. *Reviews of geophysics*, 33(4), pp.403-439.

Kerzenmacher, T.E., Walker, K.A., Strong, K., Berman, R., Bernath, P.F., Boone, C.D., Drummond, J.R., Fast, H., Fraser, A., MacQuarrie, K. and Midwinter, C., 2005. Measurements of O3, NO2 and temperature during the 2004 Canadian Arctic ACE Validation Campaign. *Geophysical Research Letters*, 32(16). doi:10.1029/2005GL023032

Kidston, J., Scaife, A.A., Hardiman, S.C., Mitchell, D.M., Butchart, N., Baldwin, M.P. and Gray, L.J., 2015. Stratospheric influence on tropospheric jet streams, storm tracks and surface weather. *Nature Geoscience*, 8(6), pp.433-440. https://doi.org/10.1038/ngeo2424

Kramarova, N.A., Nash, E.R., Newman, P.A., Bhartia, P.K., McPeters, R.D., Rault, D.F., Seftor, C.J., Xu, P.Q. and Labow, G.J., 2014. Measuring the Antarctic ozone hole with the new Ozone Mapping and Profiler Suite (OMPS). *Atmospheric Chemistry and Physics*, 14(5), pp.2353-2361. https://doi.org/10.5194/acp-14-2353-2014

Krueger, A.J., 1989. The global distribution of total ozone: TOMS satellite measurements. *Planetary and Space Science*, 37(12), pp.1555-1565. https://doi.org/10.1016/0032-0633(89)90145-1

Krüger, K., Naujokat, B. and Labitzke, K., 2005. The unusual midwinter warming in the Southern Hemisphere stratosphere 2002: A comparison to Northern Hemisphere phenomena. *Journal of the atmospheric sciences*, 62(3), pp.603-613. https://doi.org/10.1175/JAS-3316.1

Kuttippurath, J. and Nikulin, G., 2012. A comparative study of the major sudden stratospheric warmings in the Arctic winters 2003/2004–2009/2010. Atmospheric Chemistry and Physics, 12(17), pp.8115-8129. https://doi.org/10.5194/acp-12-8115-2012

Leu, M.T., 1988. Laboratory studies of sticking coefficients and heterogeneous reactions important in the Antarctic stratosphere. *Geophysical research letters*, 15(1), pp.17-20. https://doi.org/10.1029/GL015i001p00017

Lim, E.P., Hendon, H.H. and Thompson, D.W.J., 2018. Seasonal evolution of stratosphere-troposphere coupling in the Southern Hemisphere and implications for the predictability of surface climate. *Journal of Geophysical Research: Atmospheres*, 123(21), pp.12-002. https://doi.org/10.1029/2018JD029321

Lim, E.P., Hendon, H.H., Butler, A.H., Garreaud, R.D., Polichtchouk, I., Shepherd, T.G., Scaife, A., Comer, R., Coy, L., Newman, P.A. and Thompson, D.W., 2020. The 2019 Antarctic sudden stratospheric warming. *SPARC newsletter*, 54, pp.10-13. https://doi.org/10.1175/BAMS-D-20-0112.1

Massart, S., Piacentini, A., Cariolle, D., Amraoui, L.E. and Semane, N., 2007. Assessment of the quality of the ozone measurements from the Odin/SMR instrument using data assimilation. *Canadian Journal of Physics*, 85(11), pp.1209-1223. https://doi.org/10.1139/p07-124

Mahieu, E., Duchatelet, P., Demoulin, P., Walker, K.A., Dupuy, E., Froidevaux, L., Randall, C., Catoire, V., Strong, K., Boone, C.D. and Bernath, P.F., 2008. Validation of ACE-FTS v2. 2 measurements of HCl, HF, CCl 3 F and CCl 2 F 2 using space-, balloon-and ground-based instrument observations. *Atmospheric Chemistry and Physics*, 8(20), pp.6199-6221. https://doi.org/10.5194/acp-8-6199-2008

McElroy, M.B., Salawitch, R.J. and Wofsy, S.C., 1986. Antarctic O3: Chemical mechanisms for the spring decrease. *Geophysical research letters*, 13(12), pp.1296-1299. https://doi.org/10.1029/GL013i012p01296

McElroy, M.B., Salawitch, R.J., Wofsy, S.C. and Logan, J.A., 1986. Reductions of Antarctic ozone due to synergistic interactions of chlorine and bromine. *Nature*, 321(6072), pp.759-762. https://doi.org/10.1038/321759a0

McHugh, M., Magill, B., Walker, K.A., Boone, C.D., Bernath, P.F. and Russell III, J.M., 2005. Comparison of atmospheric retrievals from ACE and HALOE. *Geophysical Research Letters*, 32(15). https://doi.org/10.1029/2005GL022403

Molina, L.T. and Molina, M.J., 1987. Production of chlorine oxide (Cl2O2) from the self-reaction of the chlorine oxide (ClO) radical. *Journal of Physical Chemistry*, 91(2), pp.433-436. https://doi.org/10.1021/j100286a035

Murtagh, D., Frisk, U., Merino, F., Ridal, M., Jonsson, A., Stegman, J., Witt, G., Eriksson, P., Jiménez, C., Megie, G. and Noë, J.D.L., 2002. An overview of the Odin atmospheric mission. *Canadian Journal of Physics*, 80(4), pp.309-319. https://doi.org/10.1139/p01-157

Petelina, S.V., Llewellyn, E.J., Walker, K.A., Degenstein, D.A., Boone, C.D., Bernath, P.F., Haley, C.S., Von Savigny, C., Lloyd, N.D. and Gattinger, R.L., 2005. Validation of ACE-FTS stratospheric ozone profiles against Odin/OSIRIS measurements. *Geophysical research letters*, 32(15). https://doi.org/10.1029/2005GL022377

Rong, P.P., Russell III, J.M., Marshall, B.T., Siskind, D.E., Hervig, M.E., Gordley, L.L., Bernath, P.F. and Walker, K.A., 2016. Version 1.3 AIM SOFIE measured methane (CH4): Validation and seasonal climatology. *Journal of Geophysical Research: Atmospheres*, 121(21), pp.13-158. doi:10.1002/2016JD025415.

Russell III, J.M., Bailey, S.M., Gordley, L.L., Rusch, D.W., Horányi, M., Hervig, M.E., Thomas, G.E., Randall, C.E., Siskind, D.E., Stevens, M.H. and Summers, M.E., 2009. The Aeronomy of Ice in the Mesosphere (AIM) mission: Overview and early science results. *Journal of Atmospheric and Solar-Terrestrial Physics*, 71(3-4), pp.289-299. doi:10.1016/j.jastp.2008.08.011.

Safieddine, S., Bouillon, M., Paracho, A.C., Jumelet, J., Tence, F., Pazmino, A., Goutail, F., Wespes, C., Bekki, S., Boynard, A. and Hadji-Lazaro, J., 2020. Antarctic ozone enhancement during the 2019 sudden stratospheric warming event. *Geophysical Research Letters*, 47(14), p.e2020GL087810. https://doi.org/10.1029/2020GL087810

Scherhag, R., 1952. Die explosionartigen stratospharenwarmungen des spatwinters 1951-1952. *Ber. Deut. Wetterd*., 6, pp.51-63.

Sica, R.J., Izawa, M.R.M., Walker, K.A., Boone, C., Petelina, S.V., Argall, P.S., Bernath, P., Burns, G.B., Catoire, V., Collins, R.L. and Daffer, W.H., 2008. Validation of the Atmospheric Chemistry Experiment (ACE) version 2.2 temperature using ground-based and space-borne measurements. *Atmospheric Chemistry and Physics*, 8(1), pp.35-62. https://doi.org/10.5194/acp-8-35-2008

Smith, A.K. and Marsh, D.R., 2005. Processes that account for the ozone maximum at the mesopause. *Journal of Geophysical Research: Atmospheres*, 110(D23). https://doi.org/10.1029/2005JD006298

Smith, A.K., López-Puertas, M., García-Comas, M. and Tukiainen, S., 2009. SABER observations of mesospheric ozone during NH late winter 2002–2009. *Geophysical Research Letters*, 36(23). https://doi.org/10.1029/2009GL040942

Smith, A.K., Harvey, V.L., Mlynczak, M.G., Funke, B., García-Comas, M., Hervig, M., Kaufmann, M., Kyrölä, E., López-Puertas, M., McDade, I. and Randall, C.E., 2013. Satellite observations of ozone in the upper mesosphere. *Journal of Geophysical Research: Atmospheres*, 118(11), pp.5803-5821. doi:10.1002/jgrd.50445

Solomon, S., Garcia, R.R., Rowland, F.S. and Wuebbles, D.J., 1986. On the depletion of Antarctic ozone. *Nature*, 321(6072), pp.755-758.https://doi.org/10.1029/RG026i001p0013110.1038/321755a0

Solomon, S., 1988. The mystery of the Antarctic ozone "hole". *Reviews of Geophysics*, 26(1), pp.131-148. https://doi.org/10.1029/rg026i001p00131

Solomon, S., 1999. Stratospheric ozone depletion: A review of concepts and history. *Reviews of Geophysics*, 37(3), pp.275-316. https://doi.org/10.1029/1999rg900008

Stevens, M.H., Deaver, L.E., Hervig, M.E., Russell III, J.M., Siskind, D.E., Sheese, P.E., Llewellyn, E.J., Gattinger, R.L., Höffner, J. and Marshall, B.T., 2012. Validation of upper mesospheric and lower thermospheric temperatures measured by the Solar Occultation for Ice Experiment. *Journal of Geophysical Research: Atmospheres*, 117(D16). doi:10.1029/2012JD017689

Tolbert, M.A., Rossi, M.J., Malhotra, R. and Golden, D.M., 1987. Reaction of chlorine nitrate with hydrogen chloride and water at Antarctic stratospheric temperatures. *Science*, 238(4831), pp.1258-1260. https://doi.org/10.1126/science.238.4831.1258

Tritscher, I., Pitts, M.C., Poole, L.R., Alexander, S.P., Cairo, F., Chipperfield, M.P., Grooß, J.U., Höpfner, M., Lambert, A., Luo, B. and Molleker, S., 2021. Polar stratospheric clouds: Satellite observations, processes, and role in ozone depletion. *Reviews of geophysics*, 59(2), p.e2020RG000702. https://doi.org/10.1029/2020RG000702

Tseng, H.H. and Fu, Q., 2017. Temperature control of the variability of tropical tropopause layer cirrus clouds. *Journal of Geophysical Research: Atmospheres*, 122(20), pp.11-062. https://doi.org/10.1002/2017JD027093

Urban, J., Lautié, N., Le Flochmoën, E., Jiménez, C., Eriksson, P., de La Noë, J., Dupuy, E., Ekström, M., El Amraoui, L., Frisk, U. and Murtagh, D., 2005. Odin/SMR limb observations of stratospheric trace gases: Level 2 processing of ClO, N2O, HNO3, and O3. *Journal of Geophysical Research: Atmospheres*, 110(D14). https://doi.org/10.1029/2004JD005741

Veefkind, J.P., de Haan, J.F., Brinksma, E.J., Kroon, M. and Levelt, P.F., 2006. Total ozone from the Ozone Monitoring Instrument (OMI) using the DOAS technique. *IEEE transactions on geoscience and remote sensing*, 44(5), pp.1239-1244. DOI: 10.1109/TGRS.2006.871204

Walker, K.A., Randall, C.E., Trepte, C.R., Boone, C.D. and Bernath, P.F., 2005. Initial validation comparisons for the Atmospheric Chemistry Experiment (ACE-FTS). *Geophysical research letters*, 32(16). doi:10.1029/2005GL022388

Wang, Y., Shulga, V., Milinevsky, G., Patoka, A., Evtushevsky, O., Klekociuk, A., Han, W., Grytsai, A., Shulga, D., Myshenko, V. and Antyufeyev, O., 2019. Winter 2018 major sudden stratospheric warming impact on midlatitude mesosphere from microwave radiometer measurements. *Atmospheric Chemistry and Physics*, 19(15), pp.10303-10317. https://doi.org/10.5194/acp-19-10303-2019

Watson, P.A. and Gray, L.J., 2014. How does the quasi-biennial oscillation affect the stratospheric polar vortex?. *Journal of the Atmospheric Sciences*, 71(1), pp.391-409. https://doi.org/10.1175/JAS-D-13-096.1

Waymark, C., Walker, K.A., Boone, C.D. and Bernath, P.F., 2013. ACE-FTS version 3.0 data set: validation and data processing update. *Annals of Geophysics*, 56. doi: 10.4401/ag-6339

Wespes, C., Hurtmans, D., Chabrillat, S., Ronsmans, G., Clerbaux, C. and Coheur, P.F., 2019. Is the recovery of stratospheric O 3 speeding up in the Southern Hemisphere? An evaluation from the first IASI decadal record (2008–2017). *Atmospheric Chemistry and Physics*, 19(22), pp.14031-14056. https://doi.org/10.5194/acp-19-14031-2019

Wilmouth, D.M., Stimpfle, R.M., Anderson, J.G., Elkins, J.W., Hurst, D.F., Salawitch, R.J. and Lait, L.R., 2006. Evolution of inorganic chlorine partitioning in the Arctic polar vortex. *Journal of Geophysical Research: Atmospheres*, 111(D16). https://doi.org/10.1029/2005JD006951

WMO/IQSY. (1964). International Years of the Quiet Sun (IQSY) 1964-65. Alert messages with special references to stratwarms. WMO/IQSY Report No 6, Secretariat of the World Meteorological Organization, Geneva, Switzerland. World Meteorological Organization.

WMO (1978). WMO Commission for Atmospheric Sciences, Abridged Final Report of the Seventh Session, Manila, 27 February-10 March1978. WMO No. 509. (p. 36, item 9.4.4).

WMO (2002). Antarctic ozone hole splits in two. Press Release No. 681, October 1, 2002.

WMO (2018). Scientific assessment of ozone depletion: 2018, Global Ozone Research and Monitoring Project–Report No. 58, 588 pp.,Geneva, Switzerland.

Wolff, M.A., Kerzenmacher, T., Strong, K., Walker, K.A., Toohey, M., Dupuy, E., Bernath, P.F., Boone, C.D., Brohede, S., Catoire, V. and von Clarmann, T., 2008. Validation of HNO 3, ClONO 2, and N 2 O 5 from the Atmospheric Chemistry Experiment Fourier Transform

Spectrometer (ACE-FTS). *Atmospheric Chemistry and Physics*, 8(13), pp.3529-3562. https://doi.org/10.5194/acp-8-3529-2008

Yamazaki, Y., Matthias, V., Miyoshi, Y., Stolle, C., Siddiqui, T., Kervalishvili, G., Laštovička, J., Kozubek, M., Ward, W., Themens, D.R. and Kristoffersen, S., 2020. September 2019 Antarctic sudden stratospheric warming: Quasi-6-day wave burst and ionospheric effects. *Geophysical Research Letters*, 47(1), p.e2019GL086577. https://doi.org/10.1029/2019GL086577

6. Conclusions

Studies presented in this dissertation explore multiple aspects of the middle atmosphere using SOFIE and other datasets. The first study presents SOFIE ozone retrievals that are validated against independent measurements from ACE and MIPAS. The study concludes that the SOFIE ozone data product successfully demonstrates the presence of the primary and secondary ozone maximum layers. The seasonal variability of ozone in the stratosphere is captured by SOFIE, where the springtime maximum and the autumntime minimum are evident. When compared to coincident profiles from ACE and MIPAS, SOFIE shows qualitative and quantitative agreement. SOFIE typically reports lower ozone at most altitudes compared to the other datasets. SOFIE data are divided into winter, spring, summer, and autumn for comparison with other datasets. The presence of higher coincidences in certain months than others captures the seasonal variation of ozone more accurately in some seasons than others. Interhemispheric comparisons for all seasons indicate that although both hemispheres show similar results, the agreement between SOFIE and the other datasets is typically better in the northern hemisphere than the southern hemisphere at most altitudes. Both hemispheres, averaged over all seasons, typically suggest good agreement between ~ 30 and 70 km and at 90 km, indicated by small values of the mean difference and standard deviation of the difference. This is applicable to both coincident datasets; however, the agreement between SOFIE and ACE is slightly better than MIPAS at certain altitudes. The large differences bat ~ 20 km can be attributed to interference by Polar Stratospheric Clouds. Large differences between SOFIE and MIPAS above ~ 70 km are associated with limited coincidences described in Chapter II. However, the seasonal averages for mean differences for both hemispheres at ~ 100 km between SOFIE and MIPAS are better than SOFIE and ACE. Overall, considering the distribution of coincidences, sampling differences, and systematic and random errors between SOFIE and the coincident datasets, the agreements are concluded to be very good. Thus, this study

validates the utility and robustness of the SOFIE ozone data product for use within the science community.

While ozone is an important molecule in the atmosphere and is a key species of interest investigated by several space missions, atomic oxygen plays a very important role in the photochemistry of ozone and is, to date, a poorly understood species. The underlying limitations and technological complexities associated with measuring atomic oxygen through in-situ and remote sensing techniques have resulted in the use of derived measurements and model predictions. Thus, to expand the existing atomic oxygen database and fill existing knowledge gaps pertaining to the species, the second study of this dissertation has used SOFIE ozone retrievals to derive atomic oxygen and validate the results with coincident profiles from SABER and NRLMSIS 2.0. The daytime atomic oxygen is derived using the Chapman equations for ozone production and loss. Coincident measurements with SABER and NRLMSIS 2.0 suggest that in the northern hemisphere, SOFIE shows excellent agreement with both data sets in terms of volume mixing ratio (vmr) and very good agreement in terms of number density. In terms of the latter, SOFIE atomic oxygen is typically slightly lower than the other datasets in some years, particularly above ~ 95 km. In the southern hemisphere, there is typically a good agreement between SOFIE and NRLMSIS 2.0 below ~ 95 km in most years in terms of both vmr and number density. SOFIE agrees with SABER above ~ 85 km in most years. Overall, the agreement in the northern hemisphere is better than in the southern hemisphere. Disagreements between SOFIE and SABER are attributed to limited coincidences, sampling differences, systematic and random errors, and uncertainties associated with individual temperature and ozone retrievals from both instruments. Between SOFIE and NRLMSIS 2.0, there are fewer altitudes of disagreements. These are due to the differences between SOFIE-derived measurements and the NRLMSIS 2.0 atomic oxygen

database comprised of satellite instruments and rocket data. Seasonal variation of atomic oxygen from SOFIE and coincident NRLMSIS 2.0 measurements indicate a wintertime transport to ~ 60 km from the lower thermosphere due to eddy diffusion. Our analysis also indicates that the summer and wintertime atomic oxygen maximums are at ~ 84 and 94 km, respectively. Finally, an interhemispheric variation in atomic oxygen is studied, which suggests that there is a comparable distribution of atomic oxygen in both hemispheres; it is more evenly distributed in the northern hemisphere at ~ 100 km with a slightly higher concentration. Atomic oxygen varies over several orders of magnitude in both hemispheres through 80 to 100 km. This study indicates that the SOFIE-derived atomic oxygen measurements are well with established datasets with justifications for differences. Thus, SOFIE atomic oxygen is of great utility to the extant database and is suitable for scientific use.

The middle atmospheric composition varies regularly in response to changing seasons and recurring atmospheric patterns. However, atmospheric anomalies lead to sudden disturbances that trigger the transport of species from the lower thermosphere to the mesosphere, thereby changing the expected composition of the middle atmosphere. These anomalies, identified as Sudden Stratospheric Warmings (SSWs), marked by a temperature gradient and reversal of zonal mean wind at 10 hPa and 60^{o} N/S, are more typical occurrences in the northern hemisphere. In 2004, 2006, 2009, and 2013, large tongues of air carrying enhanced amounts of nitric oxide produced by Energetic Particle Precipitation were transported from the lower thermosphere into the stratosphere. In the third study, a comparison of the past events is made with the 2019 SSW-triggered descent event, and the 2019 event is studied in detail. In 2019, the SSW event took place on 2 January. It is observed that the 2019 descent event followed a trend very similar to past events and carried enhanced amounts of nitric oxide into the stratosphere. Among all years in 2004, 2006,

2019, 2013, and 2019, nitric oxide was transported the farthest into the stratosphere in 2019. The negative correlation with water vapor also transported during the descent event indicated that at ~ 55 km, the 2019 event was the least intense of all five years, and the nitric oxide descent started from relatively lower altitudes than in other years. This study corroborated the catalytic destruction of stratospheric ozone by nitric oxide. In the descent years where nitric oxide reached ~ 45 km, the concentration of ozone abruptly dropped during coincident periods. Vertical transport rates were calculated for all years for the first forty days starting from the date of descent, and for 2019, the results indicate that the descent peak was transported by ~ 5-6 km every ten days. Low geomagnetic indices for all years except 2004 suggest that the transport event in 2019, much like in other descent years, is strongly attributed to the unusual meteorology.

The last study of this dissertation addresses the 2019 SSW in the southern hemisphere and the subsequent ozone enhancement in the stratosphere. SSW events are rare in the southern hemisphere, with the last major event reported in 2002. In 2010, a minor event was reported. In 2019, an elevated stratopause and slowing of the zonal mean wind at 10 hPa and 60^{o}S indicated the occurrence of an SSW event during the Antarctic winter. Although this event is categorized as a minor one based on the parameters used to determine major and minor SSWs, its nature was close to the 2002 event in terms of temperature gradient and the anomaly in planetary waves 1 and 2 amplitude. The zonal mean wind in 2019 did not reverse direction like in 2002, but the weakening of its speed was reported much earlier than in 2002. The SSW event took place on 29 August 2019. Muti-instrument temperature variations in 2019 compared to the average of past years indicate that the sudden rise in temperature led to Polar Stratospheric Cloud (PSC) evaporation. Lidar backscatter measurements from Dumont d'Urville station indicate that while PSCs are a typical wintertime occurrence in the southern hemisphere, in 2019, their concentration dipped from high

(in June) to low (in August) concentrations, coincident with gradual temperature rise. Complementary measurements from different instruments indicate that there was a lower conversion of halogen reservoir species into reactive forms in 2019 compared to the previous year's average. Lower loss of nitric acid and water through PSC uptake was also reported in 2019 compared to the previous year's average. It is thus suggested that delayed chlorine deactivation through the removal of nitric acid and water by the sedimentation of large nitric acid tetrahydrate (NAT) resulting in prolonged ozone loss does not occur in 2019. High enhancements in ozone concentration from August to November are recorded by multiple instruments in the southern hemisphere. NASA ozone watch data from 1979 to 2021 suggested that the average ozone hole size from early September to mid-October was the smallest in 2019 since 1982. The polar cap ozone average from mid-September to early October indicates that there was a high concentration of ozone in 2019, which exceeded the 2002 average during the same period.

7. Future Work

The dissertation looks at several aspects of the middle atmosphere through SOFIE and other datasets. While we make the best use of SOFIE and other datasets, we also infer that further investigation is necessary to make more conclusive remarks about the composition of the middle atmosphere. The ozone data validation study successfully corroborated the quality and usability of the SOFIE ozone data product. However, continuous and novel measurements are necessary to monitor ozone variation at not just high but all latitudes. Although SOFIE results show excellent agreement with NRLMSIS 2.0 and very good agreement with SABER, future studies need to include novel approaches in expanding the atomic oxygen database. Further investigations are necessary to narrow down the uncertainties and discrepancies associated with different data sets and improve the technique for the determination of atomic oxygen in the mesopause region. In 2019, the Arctic SSW-triggered descent was captured very well by SOFIE. While it is likely that the transport of NO from the lower thermosphere to the stratosphere is a mixed effect of eddy diffusion and advection, it is necessary to identify the individual contributions, extents, and impacts of these occurrences on the NO transport. Furthermore, SOFIE looked just outside the polar night in 2019, and thus, the NO enhancements recorded by SOFIE may not represent the entire polar region. Due to the rapidly varying photochemical lifetime of NO across the polar night boundary, which depends on the extent of the meridional transport, the possibility of a sharp NO gradient while moving toward higher latitudes needs further investigation. The 2019 SSW in the SH led to enormous O_3 enhancement and an O_3 hole smallest since 1982. The 2019 ozone enhancement is thus important to the future of ozone recovery. The breakdown of ozone, a greenhouse gas, has led to an increased cooling effect. The gradual recovery of the ozone layer in the coming decades is expected to recede the cooling effect. Thus, continuous monitoring and

future studies involving the Antarctic ozone concentration and hole size are necessary to predict the period for the complete recovery of the ozone hole.